2011

THE EFFECT OF INLET GEOMETRY ON THE DEVELOPMENT OF A PLANE WALL JET

Rory Peter McIntyre

THE EFFECT OF INLET GEOMETRY ON THE DEVELOPMENT OF A PLANE WALL JET

(Spine title: EFFECT OF INLET GEOMETRY ON THE DEVELOPMENT OF A WALL JET)

(Thesis format: Monograph)

by

Rory P. McIntyre

Graduate Program in Mechanical and Materials Engineering

A thesis submitted in partial fulfillment
of the requirements for the degree of
Master of Engineering Science

The School of Graduate and Postdoctoral Studies
The University of Western Ontario
London, Ontario, Canada

THE UNIVERSITY OF WESTERN ONTARIO
School of Graduate and Postdoctoral Studies

CERTIFICATE OF EXAMINATION

Supervisor

Dr. Eric Savory

Supervisory Committee

Dr. Roi Gurka

Examiners

Dr. Jun Yang

Dr. Roger Khayat

Dr. Craig Miller

The thesis by

Rory Peter McIntyre

entitled:

The effect of inlet geometry on the development of a plane wall jet

is accepted in partial fulfillment of the
requirements for the degree of
Master of Engineering Science

4-21-2011
Date

Dr. James Johnson
Chair of the Thesis Examination Board

Abstract

A turbulent wall jet, jet Reynolds number of 30 7000, issuing from a rectangular nozzle adjacent to a plane surface is experimentally examined for different thicknesses of the nozzle upper boundary and for different heights of the external co-flow above the jet.

The object of the study is to understand the role of nozzle lip thickness and external stream height on the downstream development of the flow. Using cross hot-wire anemometry the velocity, shear stress and normal stress profiles of the flow were measured. The role of the external stream height is primarily to truncate the downstream distance for which a wall jet profile can be measured. No trend exists in the measurements due to increasing the lip thickness and it is postulated that the flow converts from a shear flow to a wake flow with increasing lip thickness.

Keywords

Wall, slot, turbulent, plane, jet, mixing layer, shear layer, wake flow, velocity ratio, confined, hot-wire anemometry

Acknowledgments

I wish to express my gratitude to Dr. E. Savory for his guidance and funding of this research. His insight and interest of the project is much appreciated, as well as his review of this monograph.

I relied on the experience of Dr. W. E. Lin, who was familiar with the wall jet facility and data acquisition apparatus that were employed.

The modifications to the experimental facility were thanks to C. Vandelaar, whose willingness and perseverance allowed the modular inlet cone, among other components, to be constructed.

My parents have been very patient and supportive of my work, for which I am thankful.

Lastly, I value the knowledge and encouragement I received from the Advanced Fluid Mechanics Research Group.

Table of Contents

List of Tables

List of Figures

List of Equations

Nomenclature

A, C, D, a, c, d	General constants to show form of equations
B	Height from lip top of lip to upper boundary, $Y-(t+b)$ [m]
b_Q	Bias or systematic uncertainty of variable Q
b	Height of the slot lip above the wall, [m]
f	Sampling frequency, [Hz]
k^2	Yaw coefficient
k	Turbulent kinetic energy per unit mass, $\frac{1}{2}\left(\overline{uu}+\overline{vv}+\overline{ww}\right)$ [m^2/s^2]
L	Integral length scale, [m]
M	Downstream momentum, $\int_0^\infty \rho U^2 dy$ [kg/s^2]
M_j	Momentum at the jet exit, $\int_0^b \rho U_j^2 dy$ [kg/s^2]
m	Maximum lag number
P	Function made up of J variables X_i
Re_j	Jet Reynolds number, $\frac{U_j b}{\nu}$
r	Lag number
r_Q	Random uncertainty of variable Q
T_E	Integral time scale, [s]
t	Thickness of the slot lip, [m]
Δt	Time interval between sampled data points, $\frac{1}{f}$ [s]
U	Time averaged mean velocity, $\frac{1}{n}\int_{i=0}^{n} u_i(t)dt$ [m/s]

U_E Average co-flow velocity, $\frac{1}{Y}\int_{b+t}^{b+t+Y} U\,dy$ [m/s]

U_j Average jet velocity, $\frac{1}{b}\int_{0}^{b} U\,dy$ [m/s]

U_m Maximum velocity in a vertical velocity profile, [m/s]

U_N Velocity component normal to a hot-wire probe filament, [m/s]

U_T Velocity component tangent to a hot-wire probe filament, [m/s]

ΔU Excess velocity, $U - U_E$ [m/s]

ΔU_M Maximum excess velocity, $U_m - U_E$ [m/s]

u_τ Friction Velocity, $\sqrt{\frac{\bar{\tau}_w}{\rho}}$

u Instantaneous velocity component in the x direction, [m/s]

u' u turbulence intensity, $\sqrt{\overline{uu}}$ [m/s]

U Time averaged mean velocity in x direction, $\frac{1}{n}\int_{i=0}^{n} u_i(t)dt$ [m/s]

v Instantaneous velocity component in the x direction, [m/s]

v' v turbulence intensity, $\sqrt{\overline{vv}}$ [m/s]

v^+ Velocity v in wall coordinates, $\frac{v}{u_\tau}$

U Time averaged mean velocity, $\frac{1}{n}\int_{i=0}^{n} u_i(t)dt$ [m/s]

W Combined uncertainty

W Time averaged mean velocity in z direction, $\frac{1}{n}\int_{i=0}^{n} w_i(t)dt$ [m/s]

W_X Combined uncertainty of variable X_i

w'	w turbulence intensity, $\sqrt{\overline{ww}}$ [m/s]
w	Instantaneous velocity component in the z direction, [m/s]
x	Downstream distance from the lip tip, [m]
Y	Height from wall to upper boundary for x > 0, [m]
y	Vertical location, [m]
y_m	Height of maximum velocity location, [m]
$½\Delta y_M$	Half-height, defined by $U(½\Delta y_M) = ½\Delta U_M$ [m]
$y_{M/2}$	Half-height; defined by $U(y_{M/2}) = ½U_M$ [m]
y_δ	Alternative to half-height, defined by $U(y_\delta) = 0.99U_E$ [m]
y^+	Vertical location in wall coordinates, $\frac{yu_\tau}{\nu}$
$½\Delta y_M^+$	Half-height in wall coordinates, $\frac{½\Delta y_M u_\tau}{\nu}$
Z	Span of tunnel in the z direction, [m]
z	Spanwise distance into the page, [m]
β	Ratio of the co-flow to jet velocity, $\frac{U_E}{U_J}$
τ	Lag time, $r\Delta t$ [s]
ρ	Density, [kg/m^3]
τ_E	Taylor micro time scale, [s]
φ	Power spectral density
ν	Kinematic viscosity, [m^2/s]
τ_w	Shear stress at the wall, defined by $\tau_w(y=0) = \mu\left(\frac{du}{dy}\right)$ [Pa]

HW	Hot-Wire
LDV	Laser Doppler Velocimetry
CFD	Computational Fluid Dynamics

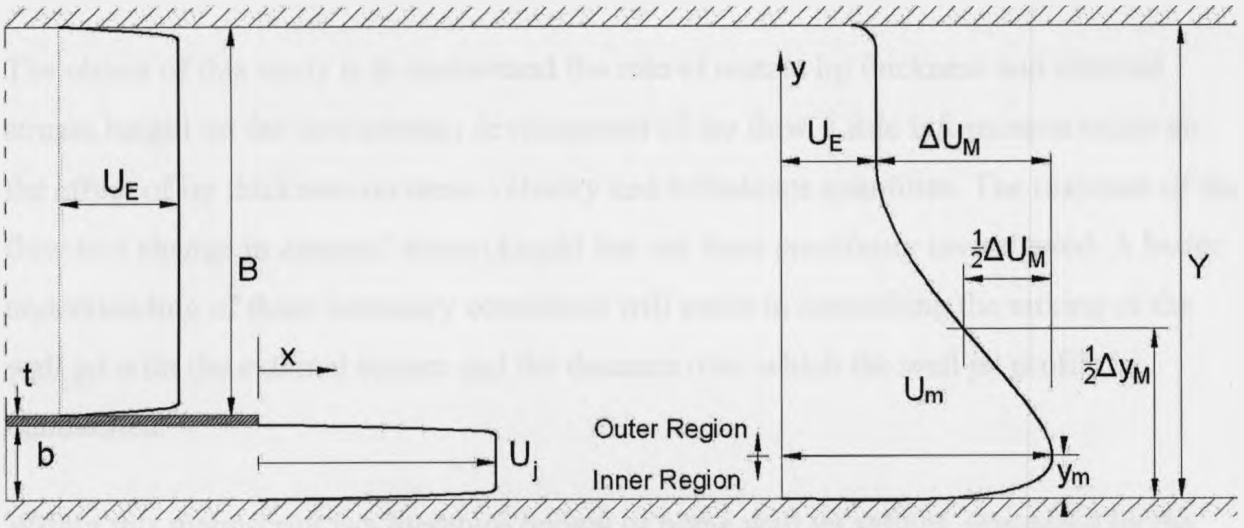

Figure 1: Common wall jet variables

Introduction

A wall jet differs from a free jet in that the fluid stream is tangential to a wall boundary, creating a thin boundary layer, with the maximum velocity of the flow being close to the wall. In industrial processes, wall jets are used for improving heat transfer at solid boundaries and, in the aerospace industry, for controlling boundary layer separation on wings, such as in Short Take-Off and Landing aircraft.

The object of this study is to understand the role of nozzle lip thickness and external stream height on the downstream development of the flow. Little information exists on the effect of lip thickness on mean velocity and turbulence quantities. The response of the flow to a change in external stream height has not been previously investigated. A better understanding of these boundary conditions will assist in controlling the mixing of the wall jet with the external stream and the distance over which the wall jet profile is maintained.

Within this manuscript is a literature review of plane wall jet studies, organized by the different approaches taken in studying plane wall jets. Following that is the experimental method in which modifications to a wall jet wind tunnel are detailed, as well as the validation of the flow in the tunnel. The measuring apparatus and its' calibration is also discussed. In the Appendix is a detailed error analysis. Finally, the results of the investigation are presented and discussed.

1 Literature Review

Encompassed within this review are studies relating to the plane turbulent case. Firstly, analytical techniques of predicting wall jet flow will be examined. Following that, a collection of superficial origin, mass flow rate and momentum methods for scaling wall jet flow will be considered. There are several important aspects of wall jets, including the inner region, jet Reynolds number, velocity ratio and lip thickness, and each will be discussed in turn. Additionally, there is a comparison of computational and experimental methods for studying wall jets. Finally, a comparison of Laser Doppler Velocimetry and Cross Hot-Wire Anemometry for measuring wall jet flows is presented.

1.1 Analytical approaches

Glauert (1956) coined the term 'wall jet' when he performed an analytical study of a jet, in a similar medium, flowing out radially after impinging on a plane surface, without any external stream. The impinging case can also be planar, or alternately the jet can issue adjacent and tangential to a plane surface and still be considered a wall jet, **Figure 2**.

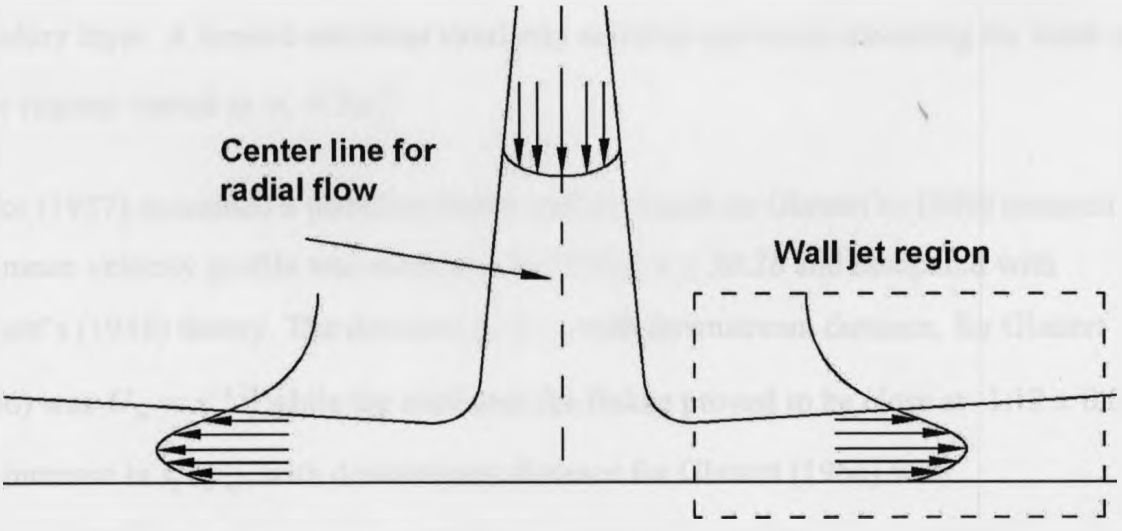

Figure 2: An impinging jet producing a wall jet, a similar cross section exists for the plane and radial cases

Glauert (1956) developed a similarity solution for the laminar situation and found the velocity distributions to be identical in the radial and plane case. In the current

investigation, only the turbulent case will be considered, due to the many studies available for comparison and the diverse applications, Eriksson et al. (1998). In creating a solution for the turbulent case to predict the downstream development, Glauert (1956) found that the flow would be best reproduced by using a constant eddy viscosity (ν_t) model above the maximum velocity (outer region) and a form of Blasius' power-law velocity profile below the maximum velocity (inner region). By making this simplification, a complete similarity solution of the flow was no longer possible, only an estimation of the velocity profile. Glauert (1956) also assumed that the shear stress would be zero at the maximum velocity, but was erroneous in his assumption as the maximum velocity and zero shear stress do not coincide for asymmetrical flows, Beguier et al. (1977). Following the precedent of free jets, Glauert (1956) specified a length scale, $\frac{1}{2}\Delta y_M$, and velocity scale U_m. The length scale was based on the height at which the velocity is half of the maximum in any given downstream vertical profile of mean streamwise velocity. Refer to **Figure 1** for more explanation. Glauert (1956) found that the Blasius' boundary layer varied as $\nu_t \propto \mathrm{Re}_x^{3/4}$ and the outer region varied as $\nu_t \propto \mathrm{Re}_x$, Re_x being the Reynolds number downstream with distance. Because of this, complete similarity of the flows is not possible, assuming the wall jet is comprised of a free jet and boundary layer. A limited turbulent similarity solution was made assuming the inner and outer regions varied as $\nu_t \propto \mathrm{Re}_x^{3/4}$.

Bakke (1957) examined a turbulent radial wall jet based on Glauert's (1956) research. The mean velocity profile was measured for $9.5b \leq x \leq 20.2b$ and compared with Glauert's (1956) theory. The decrease in U_m, with downstream distance, for Glauert (1956) was $U_m \propto x^{-1.14}$ while the exponent for Bakke proved to be close at -1.12 ± 0.03. The increase in $\frac{1}{2}\Delta y_m$, with downstream distance for Glauert (1956) was $\frac{1}{2}\Delta y_m \propto x^{1.02}$ while the exponent of Bakke was 0.94 ± 0.02. Glauert's (1956) assumptions regarding the use of an eddy viscosity model and Blasius' power-law velocity profile were able to be implemented for turbulent flow although the similarity solution was very limited. The use of power law to describe the downstream development of a wall jet was subsequently used by other researchers.

George et al. (2000) did an extensive analytical study of turbulent wall jet flow, without a co-flow, to find a complete similarity solution. The focus was on scaling the mean U velocity profile, the $\overline{uu}$ and $\overline{vv}$ normal stresses and the $\overline{uv}$ shear stress. It was found that the entire wall jet profile cannot be scaled at once, but must be separated, similar to the findings of Glauert (1956). As well, a region exists where the scaling of the inner and outer flows overlap, $30 < y^+ < 0.1\,½\,\Delta y_M^+$. George et al. (2000) used the friction velocity, u_τ, as a key parameter for scaling a wall jet flow and used it as part of a scaling for both the inner and outer flow, refer to **Appendix B** for examples. Earlier studies did not make use of u_τ. George et al. (2000) expressed a desire to better understand what consequence the initial conditions of the flow had on the downstream development of the wall jet; in particular the jet Reynolds number and the velocity profile of the jet at the outlet. In their study, a comparison was made between wall jets and boundary layers. It was found that a wall jet scales in the same way as a conventional boundary layer up to $y^+ = 100$ for u^+ and up to $y^+ = 35$ for $\overline{uv}^+$. George et al. decided from this that it is not the wall, but the outer flow's influence, which causes wall jet profiles to differ from boundary layer profiles.

Within the span of Glauert (1956) and George et al. (2000) a similarity solution has not been discovered for turbulent wall jets. Possibly the flow must be better understood through observation and measurement before an overall solution can be found.

1.2 Use of superficial origins

Schwarz and Cosart (1961) studied a plane wall jet without an external stream and assumed the flow was self-preserving - that a universal scale existed for the flow. They introduced a superficial origin, x_o, to scale the flow development, as opposed to the slot lip tip as the x origin, as in Glauert (1956). The superficial origin concept is used by several researchers to aid in scaling wall jet flows and x_o is found in various ways. Superficial origins arise from analytical solutions of the flow's downstream development. An analytical solution may fit experimental data in such a way that the solution predicts the origin of the flow at x_o as opposed to x. Schwarz and Cosart (1961) found in their theoretical analysis that **Equation 1** describes the half-height increase downstream. The solution, however, dictates that at some x location the half-height must be zero. This is not a physical property of wall jets and the location of this is the superficial origin, refer to **Figure 3** for a schematic.

Equation 1: Dimensionalized half-height development, Schwarz and Cosart (1961)

$$\frac{\frac{1}{2}\Delta y_m}{b} = A\left(\frac{x + x_o}{b}\right)$$

The constant x_o is found, in Schwarz and Cosart's (1961) study, from a least-squares fit of **Equation 1**. Once found, x_o was used to describe the decrease in maximum velocity, with downstream distance, in **Equation 2**.

Equation 2: Dimensionalized maximum velocity development, Schwarz and Cosart (1961)

$$\frac{U_m}{U_j} = B\left(\frac{x + x_o}{b}\right)^a$$

Schwarz and Cosart (1961) demonstrated through a dimensionless analysis that the shear stress, $\overline{uv}$, cannot equal zero at the maximum velocity.

Figure 3: Example of using a superficial origin. (Dashed in red) A wall jet would be developing and the dashed half-height curve is not realistic but a result of the formulae. (Solid in red) A wall jet profile has developed.

Kruka and Eskinazi (1964) also scaled the downstream development using a superficial origin. **Equation 3** was used to translate the superficial origin depending on the strength of the co-flow. In **Equation 3**, the method to determine x_o is different from that of Schwarz and Cosart (1961), the value of x_o is the amount required to shift the curve of $\frac{\frac{1}{2}\Delta y_M}{b}$ versus $\frac{x_t}{b}$ to intercept the origin of the plot.

Equation 3: Superficial origin, Kruka and Eskinazi (1964)

$$x_t = \frac{x_o + x}{1 + \frac{U_E}{(1+a)\Delta U_M}} \quad \text{where} \quad a = \frac{1.06}{(1-\beta)} - 0.5$$

Kruka and Eskinazi's (1964) superficial origin was used to scale the development of a characteristic length scale, $\frac{1}{2}\Delta y_M - y_m$, onto one curve, $\frac{x_t}{b} = (0.0601)\frac{\frac{1}{2}\Delta y_M - y_m}{b}$, as seen in **Figure 4.** The scaling result is shown for the range of jet Reynolds numbers and velocity ratios listed in **Figure 5,** and the resulting scatter in the data is conveyed by the boundaries in **Figure 4**.The x_t variable is used in other scaling methods by Kruka and Eskinazi (1964). In order to scale the decay of velocity downstream two methods are presented; one dependent on β and Re_j and the other independent of β and Re_j. The dependent method uses x_t versus ΔU_M, **Figure 5**,and each combination of β and Re_j scales separately on a logarithmic plot.

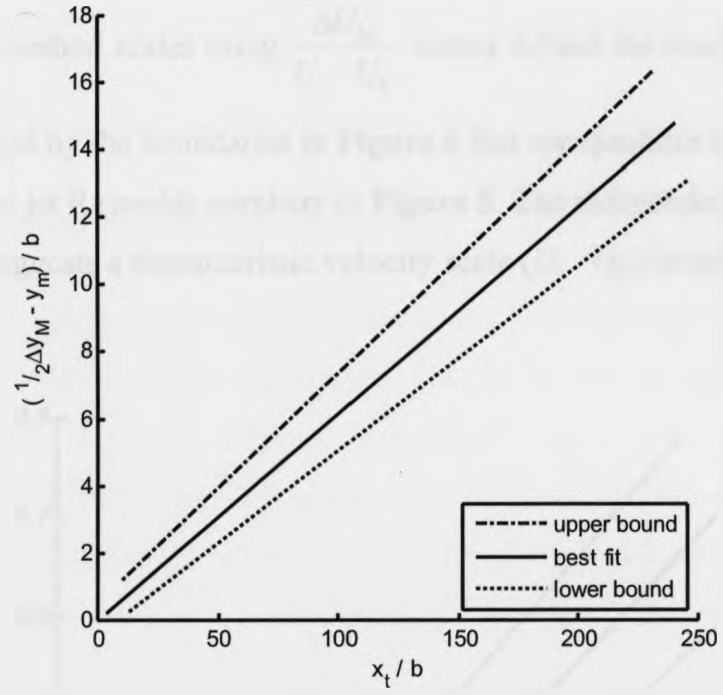

Figure 4: Scaling of characteristic length scale

(Adapted from scatter plot of Kruka & Eskinazi (1964))

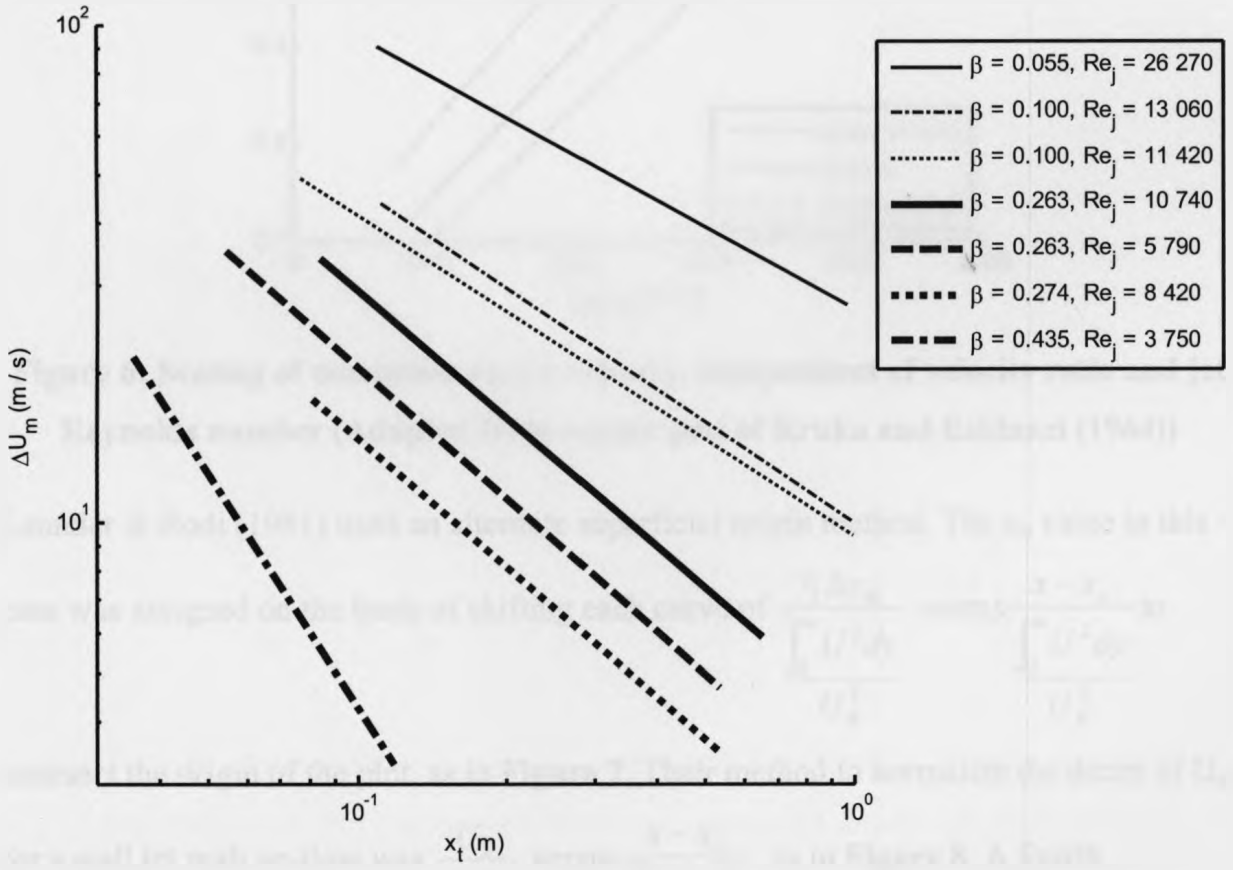

Figure 5: Scaling of maximum excess velocity dependant on velocity ratio and jet Reynolds number (Adapted from Kruka and Eskinazi (1964))

The independent method scales using $\frac{\Delta U_M}{U_j - U_E}$ versus bx_t^a and the result has a fair amount of scatter, conveyed by the boundaries in **Figure 6** that encapsulates data for the range of velocity ratios and jet Reynolds numbers in **Figure 5**. The independent method is interesting as it suggests a characteristic velocity scale (U_j - U_E) to remove the co-flow effect.

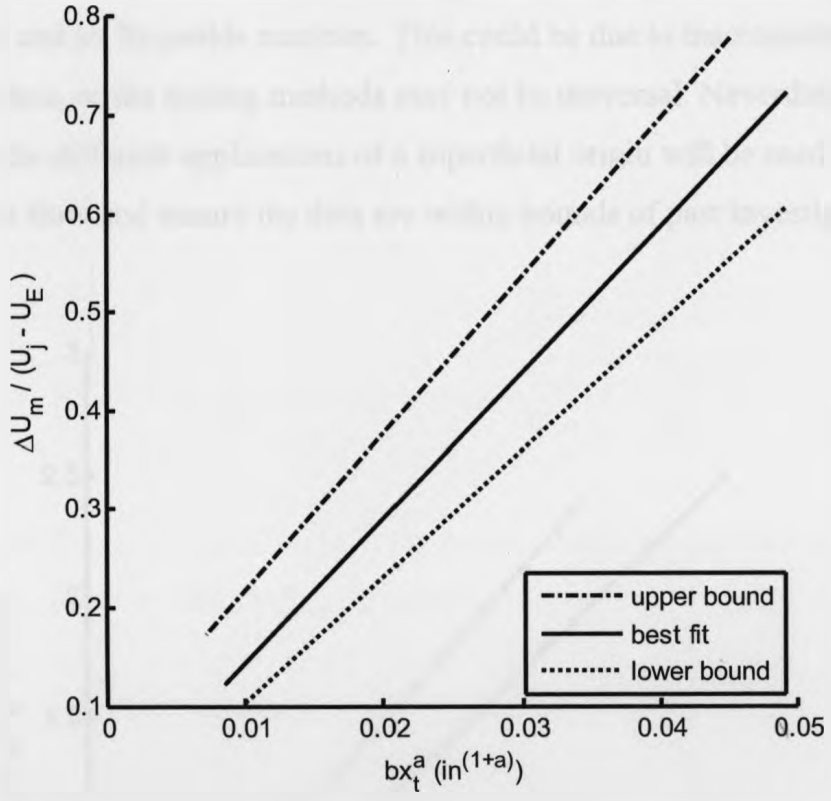

Figure 6: Scaling of maximum excess velocity, independent of velocity ratio and jet Reynolds number (Adapted from scatter plot of Kruka and Eskinazi (1964))

Launder & Rodi (1981) used an alternate superficial origin method. The x_o value in this case was assigned on the basis of shifting each curve of $\frac{\frac{1}{2}\Delta y_M}{\frac{\int_0^\infty U^2 dy}{U_E^2}}$ versus $\frac{x - x_o}{\frac{\int_0^\infty U^2 dy}{U_E^2}}$ to intersect the origin of the plot, as in **Figure 7**. Their method to normalize the decay of U_m for a wall jet with co-flow was $\frac{U_E}{\Delta U_M}$ versus $\frac{x - x_o}{\frac{\int_0^\infty U^2 dy}{U_E^2}}$, as in **Figure 8**. A fourth

superficial origin is by Wygnanski et al. (1992) which requires that for $\left(\frac{U_m}{U_j}\right)^2$ versus $\frac{x-x_o}{b}$, x_o must shift the curves so that $\frac{U_m}{U_j}=1$ at $x=x_o$. This will be explored more in the section on the **Section 1.5**.

Evidently, using a superficial origin can assist in collapsing length and velocity scales onto a single curve. The figures showed thus far do not scale perfectly for different velocity ratios and jet Reynolds numbers. This could be due to inaccuracies in experimental data, or the scaling methods may not be universal. Nevertheless, in the current study the different applications of a superficial origin will be used to understand more about the flow and ensure the data are within bounds of past investigations.

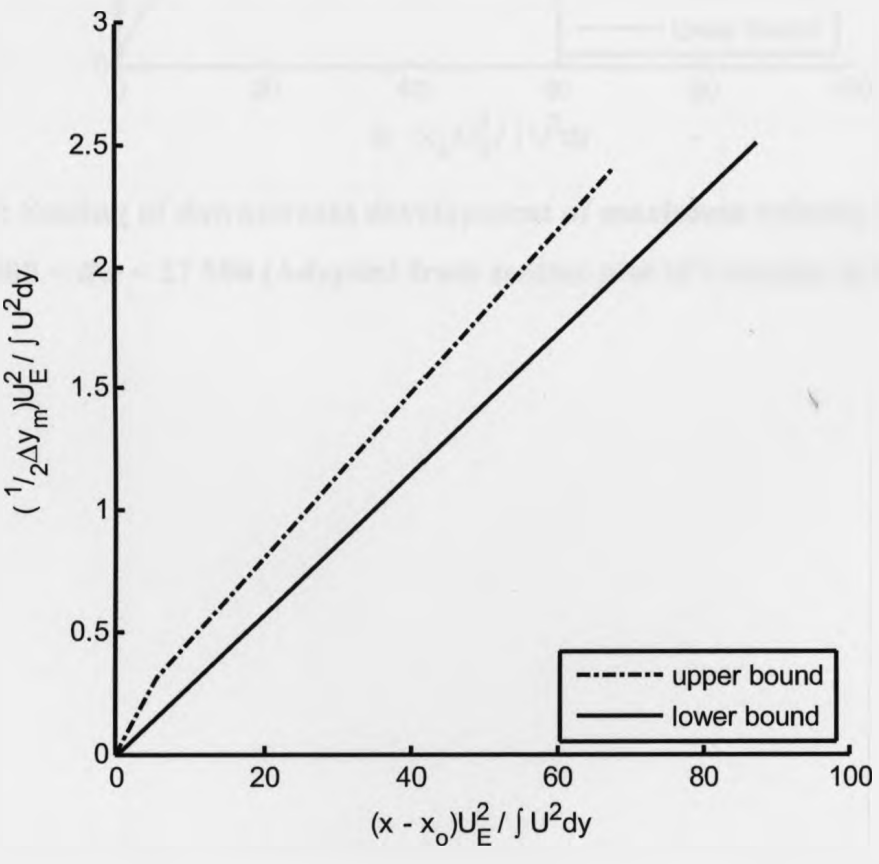

Figure 7: Scaling of downstream development of half-height, $0.055 < \beta < 0.487$, $3\,000 < Re_j < 27\,500$ (Adapted from scatter plot of Launder & Rodi (1981))

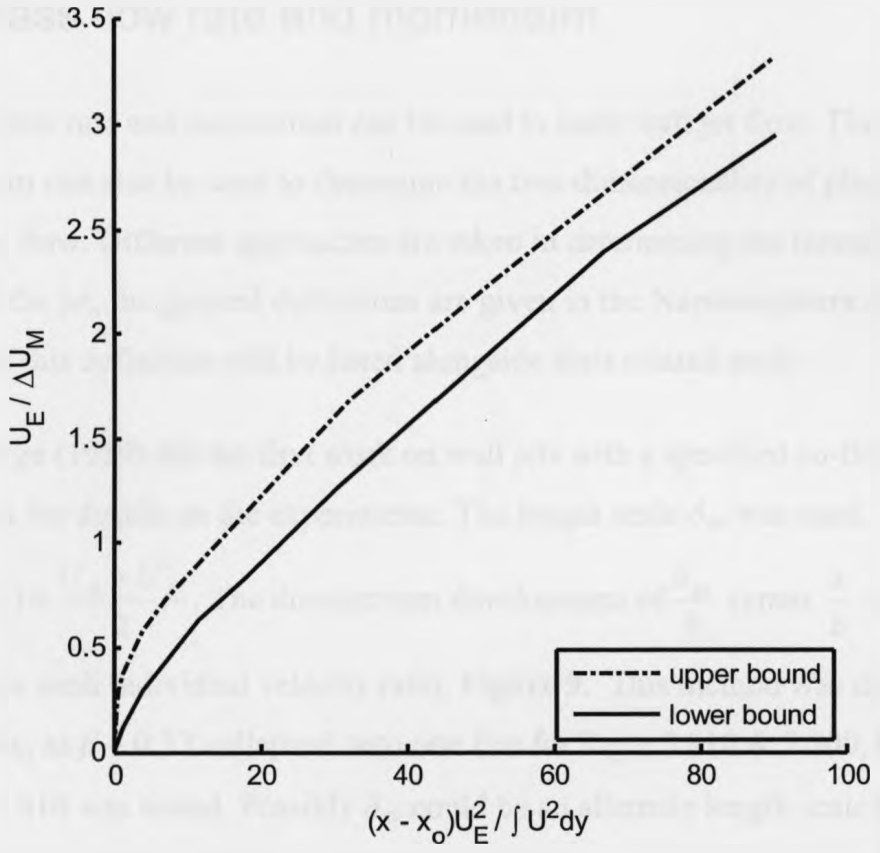

Figure 8: Scaling of downstream development of maximum velocity, $0.055 < \beta < 0.487$, $3\,000 < Re_j < 27\,500$ (Adapted from scatter plot of Launder & Rodi (1981))

1.3 Mass flow rate and momentum

Both mass flow rate and momentum can be used to scale wall jet flow. The conservation of momentum can also be used to determine the two-dimensionality of plane two-dimensional flow. Different approaches are taken in determining the momentum of the flow and of the jet, the general definitions are given in the **Nomenclature** section and variations of this definition will be listed alongside their related study.

George (1959) did the first work on wall jets with a specified co-flow; refer to **Appendix A** for details on the experiments. The length scale δ_{av} was used, where $U(\delta_{av}) = \frac{U_m + U_E}{2}$. The downstream development of $\frac{\delta_{av}}{b}$ versus $\frac{x}{b}$ scaled separately for each individual velocity ratio, **Figure 9**. This method was dependent on β but not on Re_j as $\beta = 0.33$ collapsed onto one line for Re_j = 3 810 & 7 500, for $\beta = 0.66$ only Re_j = 3 810 was tested. Possibly δ_{av} could be an alternate length scale to $\frac{1}{2}\Delta y_m$, although the determination of this quantity is difficult.

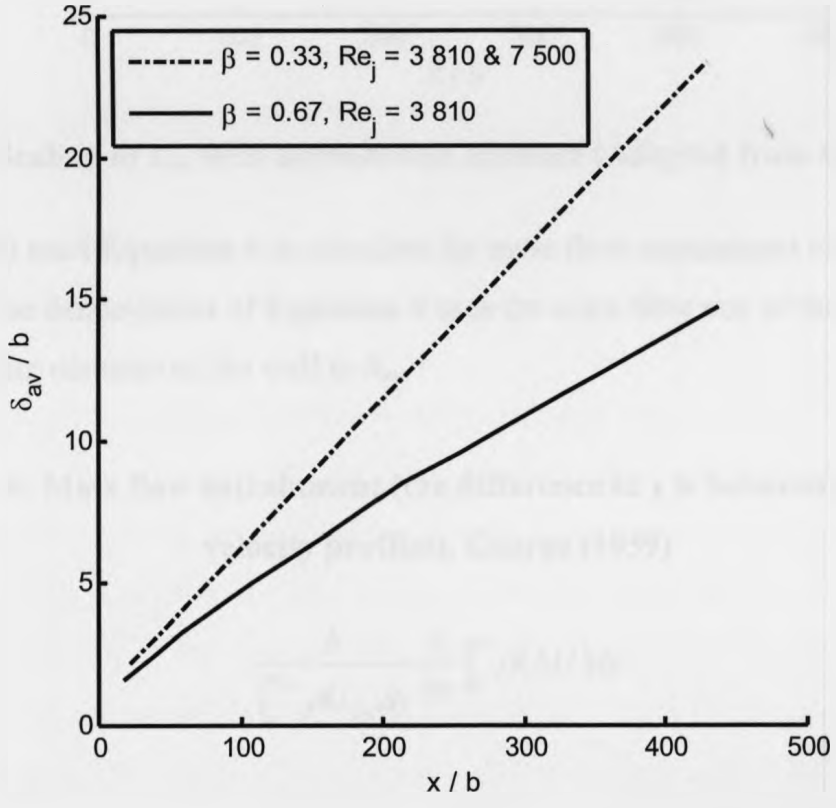

Figure 9: Scaling of δ_{av} with downstream distance (Adapted from George (1959))

George (1959) scaled $\frac{U_m}{U_E}$ versus $\frac{x}{b}$, and the maximum velocity proved to also be dependent on β with this scaling method, **Figure 10**, but not on Re_j.

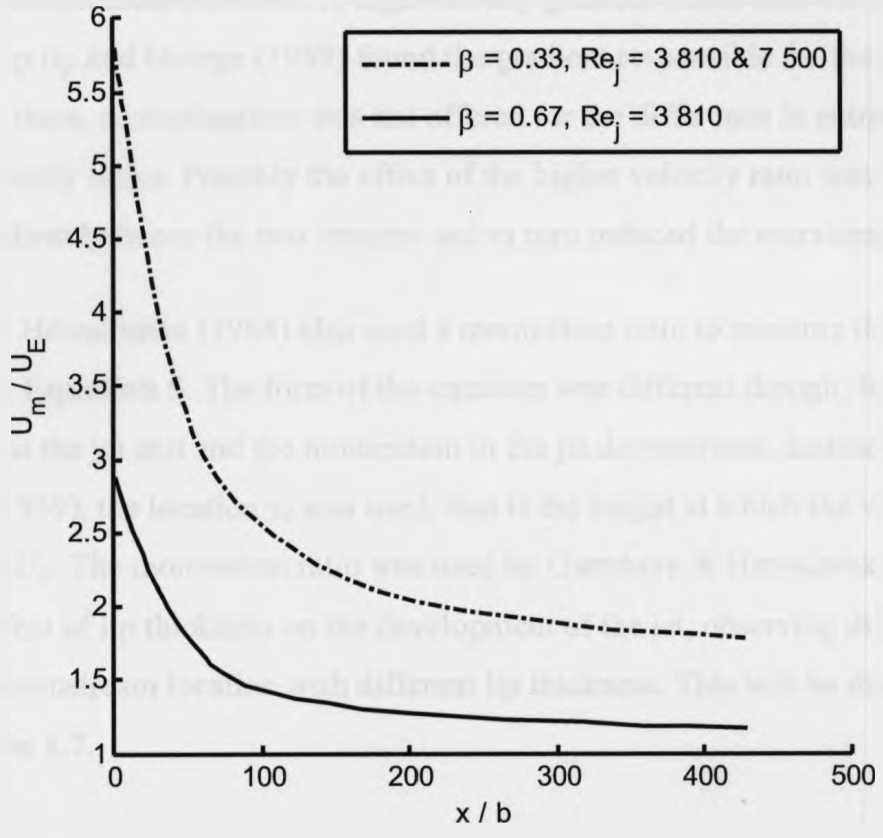

Figure 10: Scaling of U_m with downstream distance (Adapted from George (1959))

George (1959) used **Equation 4** to calculate the mass flow entrainment of the co-flow into the jet. The denominator of **Equation 4** uses the mass flow rate of the jet integrated over the varying distance of the wall to δ_{av}.

Equation 4: Mass flow entrainment (the difference in x is between neighboring velocity profiles), George (1959)

$$\frac{b}{\int_0^{\delta_{av}} \rho U_{jet} dy} \frac{\partial}{\partial x} \int_0^{\infty} \rho(\Delta U) dy$$

It was found the mass flow entrainment was greatest near the jet exit with $m \approx 0.030$, for $\beta = 0.33$ and $Re_j = 3\ 810$ & $7\ 500$. The mass flow entrainment dropped to $m \approx 0.005$ at $x = 40b$ and remained at that level for the subsequent measurements up to $x = 400$b. For $\beta = 0.67$, $m \approx 0.030$ at the jet exit but dropped to $m \approx 0$ at $40b$ and remained there for the rest of the downstream measurements. A high velocity gradient exists between the jet and co-flow at the lip tip and George (1959) found the gradient responsible for the high entrainment there, an explanation was not offered for the difference in entrainments for different velocity ratios. Possibly the effect of the higher velocity ratio was to reduce the velocity gradient between the two streams and in turn reduced the entrainment.

Gartshore & Hawaleshka (1964) also used a momentum ratio to measure the mass flow entrainment, **Equation 5**. The form of the equation was different though, focusing on the momentum at the jet exit and the momentum in the jet downstream. Instead of using δ_{av} as George (1959), the location y_δ was used, that is the height at which the velocity reaches $0.99U_E$. The momentum ratio was used by Gartshore & Hawaleshka (1964) to study the effect of lip thickness on the development of the jet, observing different ratios at a single downstream location with different lip thickness. This will be discussed further in the **Section 1.7**.

Equation 5: Momentum ratio, Gartshore & Hawaleshka (1964)

$$\frac{\int_0^{y_\delta} \rho U^2 dy}{\int_0^b \rho U_j^2 dy}$$

Patel (1971) focused on wall jets with a co-flow. His goal was to predict the downstream development of $½\Delta y_M$ and ΔU_M with a single experimental constant. Patel also makes reference to Patel (1970) in which he notes that the behaviour of a wall jet, with $\beta < 1/6$, behaves like a wall jet in still air. Data from several published wall jet studies were used in the analysis. Patel's (1971) approach for wall jet development follows Abramovich's (1963) method involving an integral momentum equation for a free jet. A relation for the velocity scale ΔU_M, **Equation 6**, and a relation for the length scale $½\Delta y_m$, **Equation 7**,

was created. Patel applies this with reasonable success for 5 000 < Re_j < 12 000 and 0.1 < β < 0.487, refer to **Figures 11 & 12**. The superficial origin, x_o, in **Equation 6**, translates the data in order for the curves to pass through the origin of the plot. The plot of **Equation 7** can be described by a straight line, but the plot of **Equation 6** requires an extensive formula to describe the curve, which will not be reprinted here but can be viewed in Patel (1971).

Equation 6: Velocity scale development downstream, Patel (1971)

$$\frac{x - x_o}{\int_0^{\infty} \frac{U}{U_E}\left(\frac{U}{U_E} - 1\right) dy} \quad \textbf{versus} \quad \frac{U_E}{\Delta U_M}$$

Equation 7: Length scale development downstream, Patel (1971)

$$\frac{U_E^2 / \Delta U_M^2}{0.724 + \frac{U_E}{U_M}} \quad \text{versus} \quad \frac{\frac{1}{2}\Delta y_M}{\int_0^{\infty} \frac{U}{U_E}\left(\frac{U}{U_E} - 1\right) dy}$$

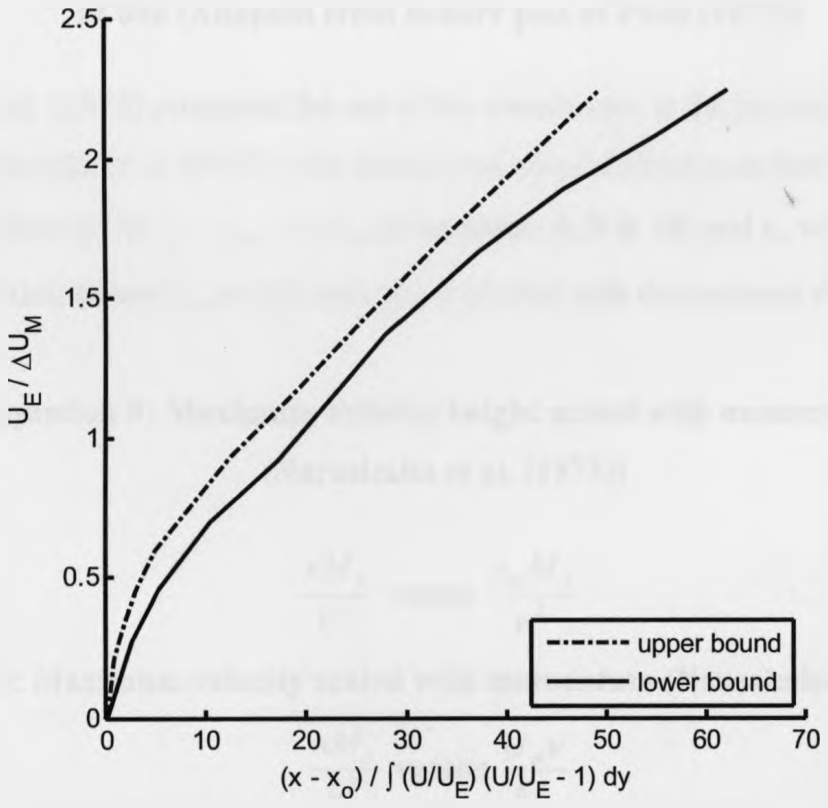

Figure 11: Downstream development of ΔU_M for = 0.100 < β < 0.376, 5 000 < Re_j < 12 000 (Adapted from scatter plot of Patel (1971))

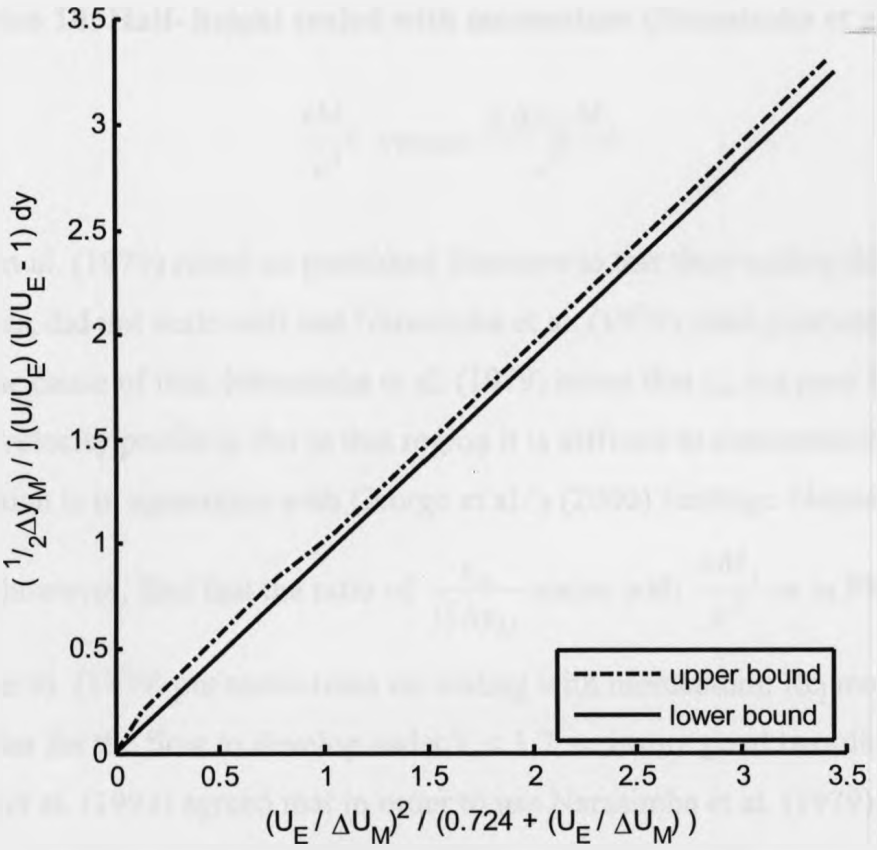

Figure 12: Downstream development of $\frac{1}{2}\Delta y_M$ for = 0.168 < β < 0.376, 5 000 < Re_j < 12 000 (Adapted from scatter plot of Patel (1971))

Narasimha et al. (1973) promoted the use of the momentum at the jet nozzle, M_j, to scale the flow. Narasimha et al. (1973) only considered cases without a co-flow. Relations scaling the values of ΔU_M, y_M, $\frac{1}{2}\Delta y_M$ (**Equations 8, 9 & 10**) and τ_w were developed. All the quantities, except τ_w, scaled well when plotted with downstream distance, **Figures 13, 14 & 15**.

Equation 8: Maximum velocity height scaled with momentum, (Narasimha et al. (1973))

$$\frac{xM_j}{\nu^2} \text{ versus } \frac{y_m M_j}{\nu^2}$$

Equation 9: Maximum velocity scaled with momentum (Narasimha et al. (1973))

$$\frac{xM_j}{\nu^2} \textbf{ versus } \frac{U_m \nu}{M_j}$$

Equation 10: Half- height scaled with momentum (Narasimha et al. (1973))

$$\frac{xM_j}{\nu^2} \text{ versus } \frac{\frac{1}{2}\Delta y_M M_j}{\nu^2}$$

Narasimha et al. (1979) relied on published literature to test their scaling theories. The wall stress, τ_w, did not scale well and Narasimha et al. (1979) cited poor experimental data to be the cause of this. Narasimha et al. (1979) noted that y_m is a poor length scale to use. As the velocity profile is flat in that region it is difficult to determine the height location, which is in agreement with George et al.'s (2000) findings. Narasimha et al. (1979) did, however, find that the ratio of $\frac{y_m}{\frac{1}{2}\Delta y_M}$ scales with $\frac{xM_j}{\nu^2}$ as in **Figure 15.**

Narasimha et al. (1979) put restrictions on scaling with momentum; Re_j must be large, $x > 30b$ in order for the flow to develop and $x/L < 1.7$, to insure good two-dimensionality. Wygnanski et al. (1992) agreed that in order to use Narasimha et al. (1979) scaling methods must be large, found to be $Re_j > 5\ 000$, and that the wall jet can only be scaled for $x > 30b$.

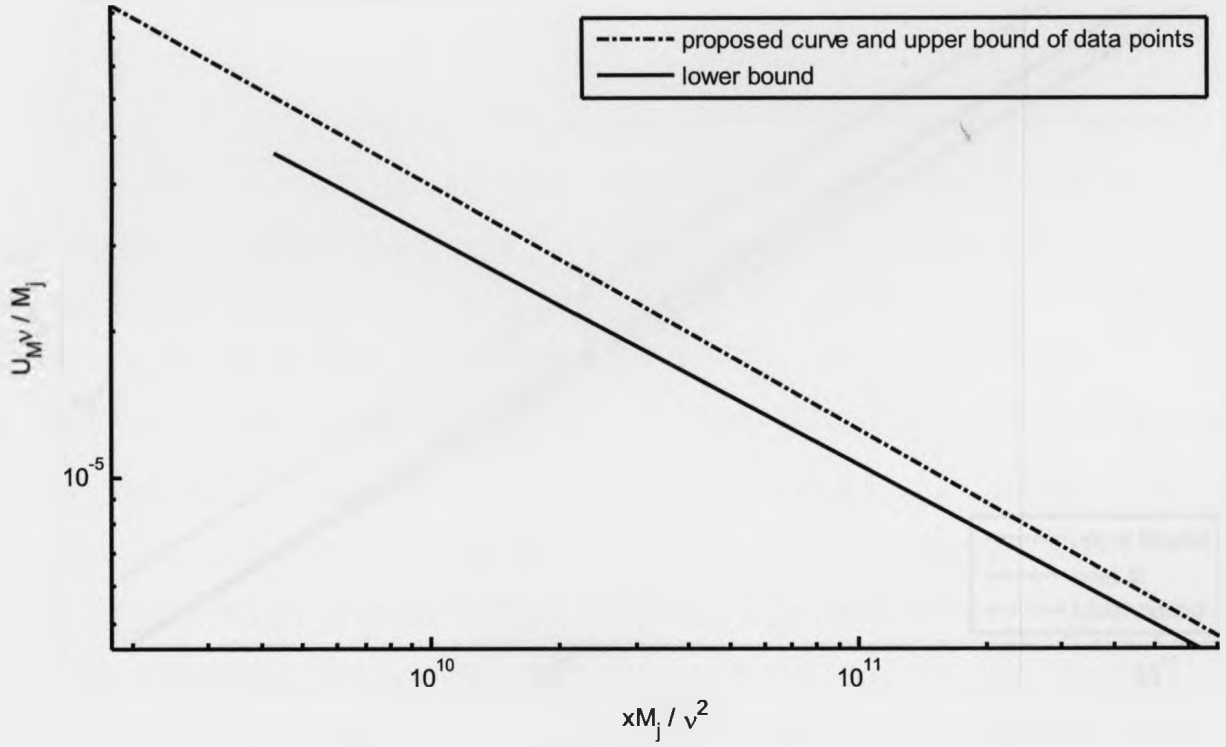

Figure 13: Downstream development of U_M (Narasimha et al. (1973))

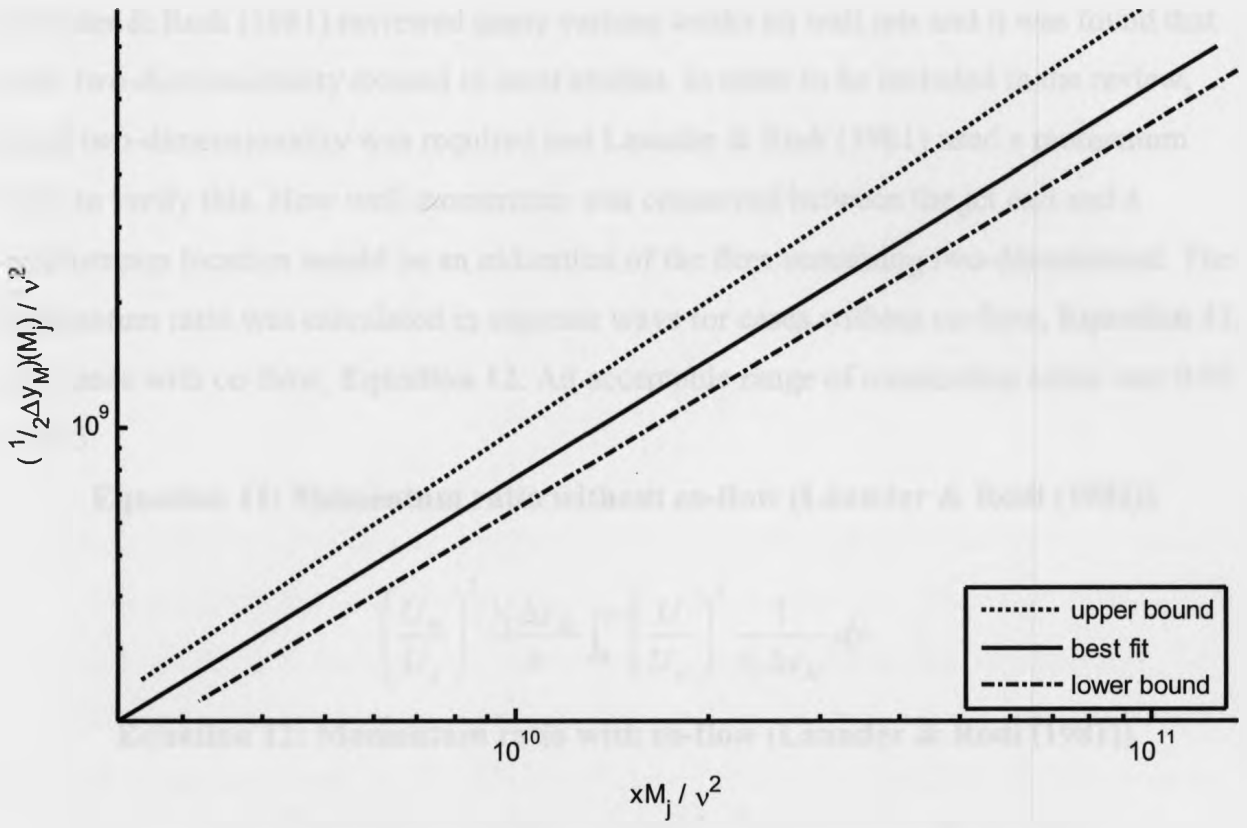

Figure 14: Downstream development of ½Δy_M (Narasimha et al. (1973))

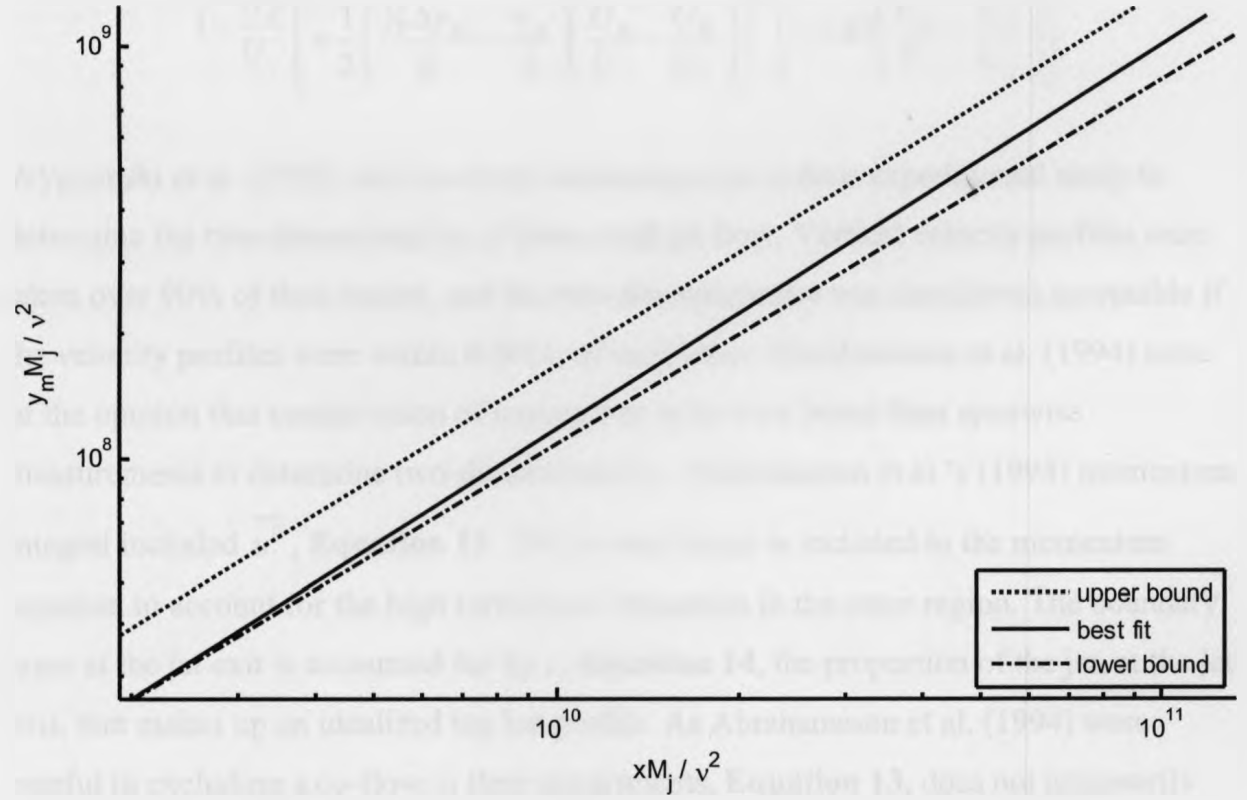

Figure 15: Downstream development of y_m (Narasimha et al. (1973))

Launder & Rodi (1981) reviewed many various works on wall jets and it was found that poor two-dimensionality existed in most studies. In order to be included in the review, good two-dimensionality was required and Launder & Rodi (1981) used a momentum ratio to verify this. How well momentum was conserved between the jet exit and a downstream location would be an indication of the flow remaining two-dimensional. The momentum ratio was calculated in separate ways for cases without co-flow, **Equation 11**, and cases with co-flow, **Equation 12**. An acceptable range of momentum ratios was 0.95 – 0.75.

Equation 11: Momentum ratio without co-flow (Launder & Rodi (1981))

$$\left(\frac{U_m}{U_j}\right)^2 \frac{½\Delta y_M}{b} \int_0^{y_\delta} \left(\frac{U}{U_m}\right)^2 \frac{1}{½\Delta y_M} dy$$

Equation 12: Momentum ratio with co-flow (Launder & Rodi (1981))

$$\frac{1}{1-\frac{U_E}{U_j}} \left[\begin{array}{l} \frac{y_m}{b}\frac{U_m}{U_j}\left(0.83\frac{U_m}{U_j} - 0.91\frac{U_E}{U_j}\right) \\ +\frac{1}{2}\left(\frac{½\Delta y_M}{b} - \frac{y_m}{b}\right)\left(\frac{U_m}{U_j} - \frac{U_E}{U_j}\right) \end{array} \right] \times \left[\begin{array}{c} 2.025\frac{U_E}{U_j} \\ +1.47\left(\frac{U_m}{U_j} - \frac{U_E}{U_j}\right) \end{array} \right]$$

Wygnanski et al. (1992) used spanwise measurements in their experimental study to determine the two-dimensionality of plane wall jet flow. Vertical velocity profiles were taken over 90% of their tunnel, and the two-dimensionality was considered acceptable if the velocity profiles were within $0.04U_m$ of each other. Abrahamsson et al. (1994) were of the opinion that conservation of momentum tests were better than spanwise measurements to determine two-dimensionality. Abrahamsson et al.'s (1994) momentum integral included $\overline{u^2}$, **Equation 13**. The normal stress is included in the momentum equation to account for the high turbulence intensities in the outer region. The boundary layer at the jet exit is accounted for by *c*, **Equation 14**, the proportion of the jet, at the jet exit, that makes up an idealized top hat profile. As Abrahamsson et al. (1994) were careful in excluding a co-flow in their experiments, **Equation 13**, does not necessarily hold for flow including a co-flow.

Equation 13: Momentum ratio without co-flow (Abrahamsson et al. (1994))

$$\frac{1}{c}\left(\frac{\Delta U_M}{U_j}\right)^2 \frac{\frac{1}{2}\Delta y_M}{b}\int_0^{\infty}\left(\frac{U^2}{\Delta U_M^2}+\frac{\overline{u^2}}{\Delta U_M^2}\right)\frac{1}{\frac{1}{2}\Delta y_M}dy$$

Equation 14: Jet mass flow rate coefficient, (Abrahamsson et al. (1994))

$$c=\frac{\int_0^b \rho U dy_{\,jet\ exit}}{\rho b U_{j,\max}}$$

The momentum ratios found by Abrahamsson et al. (1994) using **Equation 13**, were 1.0 – 0.8. These momentum ratios were compared to momentum ratios expected from considering only wall friction, not viscous losses; note that **Equation 13** inherently includes the loss due to friction. The method to find the friction loss was cited as being found through Launder & Rodi (1981), unfortunately the exact method was not given by Abrahamsson et al. (1994) but was likely Bradshaw & Gee's (1961) method due to Launder & Rodi's (1981) recommendation of it. This friction formula can be found in **Equation 16** in the **Section 1.4**. Abrahamsson et al. (1994) found that up to distances of 150b the two different momentum ratios are of similar magnitude. Abrahamsson et al. (1994) inferred from this that up to x = 150b the reduction of the momentum ratio was primarily due to friction, and not from poor two-dimensionality. For $x > 150b$, the expected loss due to friction was less than that calculated through momentum, which Abrahamsson et al. (1994) concluded was a breakdown of two-dimensionality.

Schneider & Goldstein (1994) used a momentum ratio variation, **Equation 15**, in which the wall shear stress, τ_w, appears. In order to determine the stress, Kobayahsi's (1983) formula is used, where the local skin friction coefficient is $c_f = 0.117\left(\frac{U_m y_m}{\nu}\right)^{-0.31}$. It was found that 13% of the momentum was lost due to wall friction by $x = 45b$ and 17% by $x = 109b$.

Equation 15: Momentum ratio, (Schneider & Goldstein (1994))

$$\frac{\rho b U_j^2 - \int_0^x \tau_w dx}{\rho U_j^2 b}$$

As discussed, mass and momentum are very powerful tools to analyze and scale wall jet flows. Momentum can be used to estimate the mixing between the inner and outer layers, as well testing the two-dimensionality of the flow. George (1959), Patel (1971) and Launder & Rodi (1981) provide methods to use momentum for situations that include a co-flow. However, reiterating Patel (1971), if $\beta < 1/6$, a wall jet behaves as though a co-flow does not exist. This means that, depending on the velocity ratio, Narasimha et al. (1979), Schneider & Goldstein (1994) and Abrahamsson et al.'s (1994) momentum methods may also work for flows that include a co-flow. Of the methods to calculate momentum ratio, Abrahamsson et al.'s (1994) method would appear to encompass the most variables of the flow, through including the normal streamwise stress and the jet mass flow rate coefficient. Launder & Rodi (1981) also uses many aspects of the flow, but experimental constants are used in the formula that includes co-flow and the applicability of the constants may not be universal.

1.4 Inner region

The inner region of the wall jet, **Figure 1**, is of interest as it does not develop similar to a conventional boundary layer. In comparing free jets and a wall jets, Narasimha et al. (1979) found that, with similar jet momentum values, the maximum velocity is greater in the wall jet. Narasimha et al. (1979) cited this as being due to a reduction in mixing by the wall. Evidently, a better understanding of the inner region will allow a better explanation of the uniqueness of wall jet flow.

Launder & Rodi (1983) noted that the logarithmic region of the conventional boundary layer increases with downstream distance, but in a wall jet the logarithmic region remains constant or decreases, similar to findings by George et al. (2000). Launder & Rodi (1983) considered this to be due to the wall shear stress decreasing at a greater rate downstream than the shear in the outer region, and that the maximum shear stress in the outer region is several times the magnitude of the shear stress at the wall and of opposite sign. Erikkson et al. (1998) performed a high resolution experiment in order to capture the flow in the near wall region. Despite the high quality data of the inner region, there was no expansion on Launder & Rodi's (1983) theory regarding the influence of the wall and is something that requires further exploration.

In order to scale within the inner region y_m has been found to be an effective length scale. In the **Section 1.3** the validity of using y_m was questioned due to the difficulty in determining its' location, but y_m has been used as a length scale in several studies, refer to **Appendix B** for additional examples. Kruka and Eskinazi (1964) used $\frac{U}{U_m}$ versus $\frac{y}{y_m}$, with little scatter, for a range of downstream distances as can be seen in **Figure 16**. Unfortunately, other studies were non-dimensionalized such that they could not be scaled in this way, in order to compare alternate velocity ratios and jet Reynolds numbers.

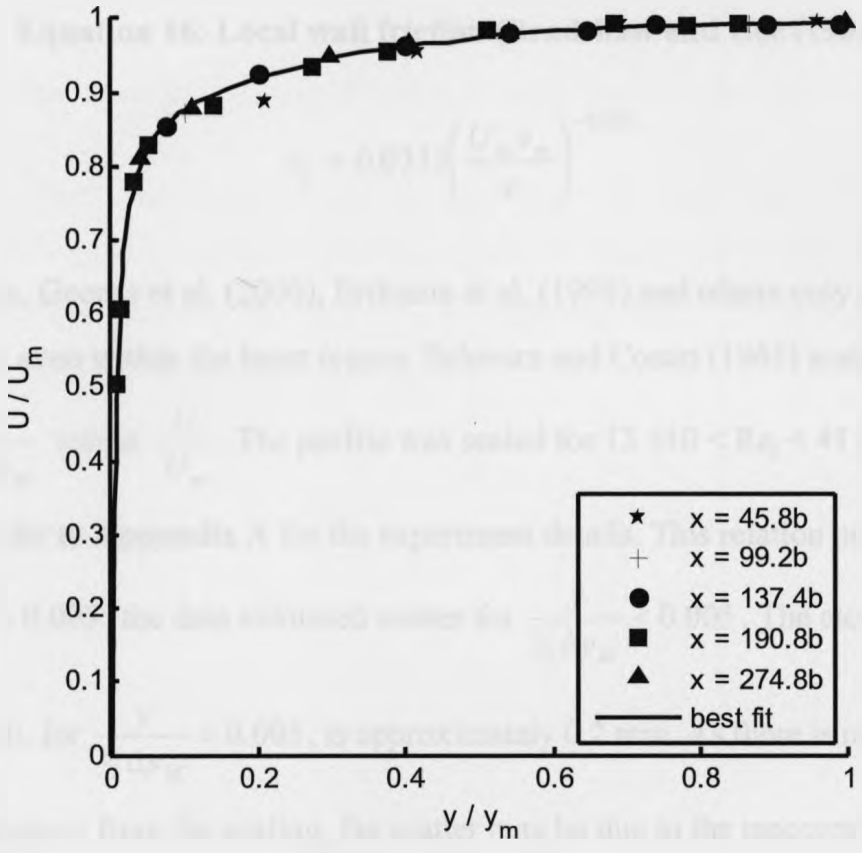

Figure 16: Velocity profile with inner scaling, $\beta = 0.1$ and $Re_j = 13\ 060$ (Kruka and Eskinazi (1964))

An early study that included shear stress values in their wall jet experiments was Bradshaw and Gee (1960). They developed a formula for wall friction, **Equation 16**. In Launder & Rodi's (1981) review of wall jet studies **Equation 16** was found to be the best method for estimating wall friction and that it was applicable for $3000 < \frac{U_m y_m}{\nu} < 40\ 000$. **Equation 16** includes U_m and y_m in the formula, these are the same scales used in **Figure 16**. In **Section 1.1**, George et al. (2000) determined that u_τ was an important velocity scale in both the inner and outer regions. However, over the whole vertical profile a better collapse of data was found in their study using U_m to scale the normal stresses ($\overline{uu}$ & $\overline{vv}$) and using u_τ to scale $\overline{uv}$. Evidently U_m and y_m are important velocity and length scales in the inner region, but u_τ should be considered as well.

Equation 16: Local wall friction (Bradshaw and Gee (1964))

$$c_f = 0.0315\left(\frac{U_m y_m}{\nu}\right)^{-0.182}$$

Many studies, George et al. (2000), Eriksson et al. (1998) and others only used $\frac{1}{2}\Delta y_M$ to scale height, even within the inner region. Schwarz and Cosart (1961) scaled the velocity profile $\frac{y}{\frac{1}{2}\Delta y_M}$ versus $\frac{U}{U_m}$. The profile was scaled for 13 510 < Re_j < 41 600 within $29b \leq x \leq 85b$, refer to **Appendix A** for the experiment details. This relation proved to hold for $\frac{y}{\frac{1}{2}\Delta y_M} > 0.005$, the data exhibited scatter for $\frac{y}{\frac{1}{2}\Delta y_M} < 0.005$. The closest distance from the wall, for $\frac{y}{\frac{1}{2}\Delta y_M} = 0.005$, is approximately 0.2 mm. As there is no obvious trend in the discrepancy from the scaling, the scatter may be due to the inaccuracies of using a hot-wire probe that close to the wall, Bruun (1995). Wygnanski et al. (1992) found that $\frac{y}{\frac{1}{2}\Delta y_M}$ versus $\frac{U}{U_m}$ exhibited a divergence as opposed to scatter, for Re_j = 19 000 & 3 700 in the velocity profiles for $\frac{y}{\frac{1}{2}\Delta y_M} < 0.20$. This will be discussed further in **Effect of jet Reynolds number** for **Figure 17**. Subsequently, Wygnanski et al. (1992) recommended the use of $\frac{1}{2}\Delta y_M$ to scale the outer region only.

Both y_m and $\frac{1}{2}\Delta y_M$ are able to scale the inner region of the wall jet. This may be due to the relation found between y_m and $\frac{1}{2}\Delta y_M$, and it is possible the length scales are interchangeable. Launder & Rodi (1981) tabulated data of the ratio $\frac{y_m}{\frac{1}{2}\Delta y_M}$, for cases without a co-flow, and found that $\frac{y_m}{\frac{1}{2}\Delta y_M} \approx 0.15$. Wygnanski et al. (1992) surmised that

as $\frac{y_m}{\frac{1}{2}\Delta y_M} \approx 0.15$ holds for many experiments, despite varying turbulence levels in the outer region, therefore $\frac{1}{2}\Delta y_M$ must be a robust length scale for the outer region.

Other than Kruka & Eskinazi (1964), scaling of the inner region with y_m has not been used. If a method were found that was able to accurately determine its' location, y_m could prove to be a valuable length scale. The most important velocity scale is clearly U_m and the most common length scale is $\frac{1}{2}\Delta y_M$.

1.5 Effect of jet Reynolds number

An important parameter in classifying wall jets is the jet Reynolds number, $\mathrm{Re}_j = \frac{U_j b}{\nu}$.

The transition of a laminar to a turbulent wall jet ocurs at $\mathrm{Re_j} \approx 2\,200$, Gogineni & Shih (1997). Wygnanski et al. (1990) found the wall jet to be fully turbulent for $\mathrm{Re_j} = 3\,700$. As the fluid medium remains constant in each study, the jet height, b, and the jet velocity, U_j, are the primary variables to control $\mathrm{Re_j}$.

Wygnanski et al.'s (1992) wall jet research was on how the growth of half-height and the decay of maximum velocity were dependent on Re_j, as this dependence is not found in comparable free jets. Their experiments did not include a specified co-flow; however an entrained co-flow was allowed to mix with the jet. The entrained air was not accounted for through ΔU_M or a similar method, and this may have affected their scaling methods. The U_j was unchanged for different b values, and vice versa, allowing a parametric investigation of the effect of momentum and $\mathrm{Re_j}$, refer to **Appendix A** for more experimental details. For plots of $\frac{y}{\frac{1}{2}\Delta y_M}$ versus $\frac{U}{U_m}$ with the same value of b, but $\mathrm{Re_j} = 10\,000$ & $19\,000$, a divergence above $y = \frac{1}{2}\Delta y_M$ was observed. The plots did however scale for different downstream profiles, $30b < x < 140b$. The values of $\mathrm{Re_j} = 10\,000$ lay above the values of $\mathrm{Re_j} = 19\,000$, refer to **Figure 17**. This shows that there was a $\mathrm{Re_j}$ dependence existing in the outer portion of the jet. As well, by looking closely at **Figure 17**, shown expanded in **Figure 18**, it is seen that a $\mathrm{Re_j}$ dependence exists in the inner region and that the higher $\mathrm{Re_j}$ values appear closer to the wall. The dependence on $\mathrm{Re_j}$ is contrary to that found by Schwarz and Cosart (1961), discussed in **Section 1.4**. Possibly a threshold exists at which the effect of $\mathrm{Re_j}$ is not discernable from the published plots, as the range of $13\,510 < \mathrm{Re_j} < 41\,600$ for Schwarz and Cosart (1961) was higher overall compared to $3\,700 < \mathrm{Re_j} < 19\,000$ for Wygnanski et al. (1992).

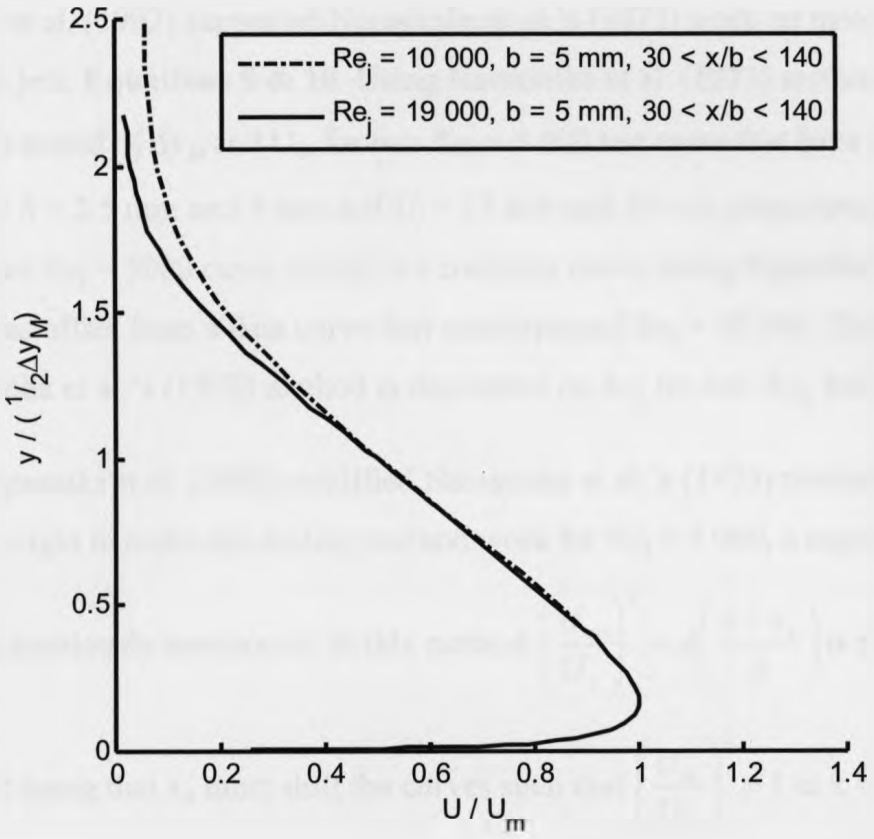

Figure 17: Velocity profiles $30b < x < 140b$ (Wygnanski et al. (1992))

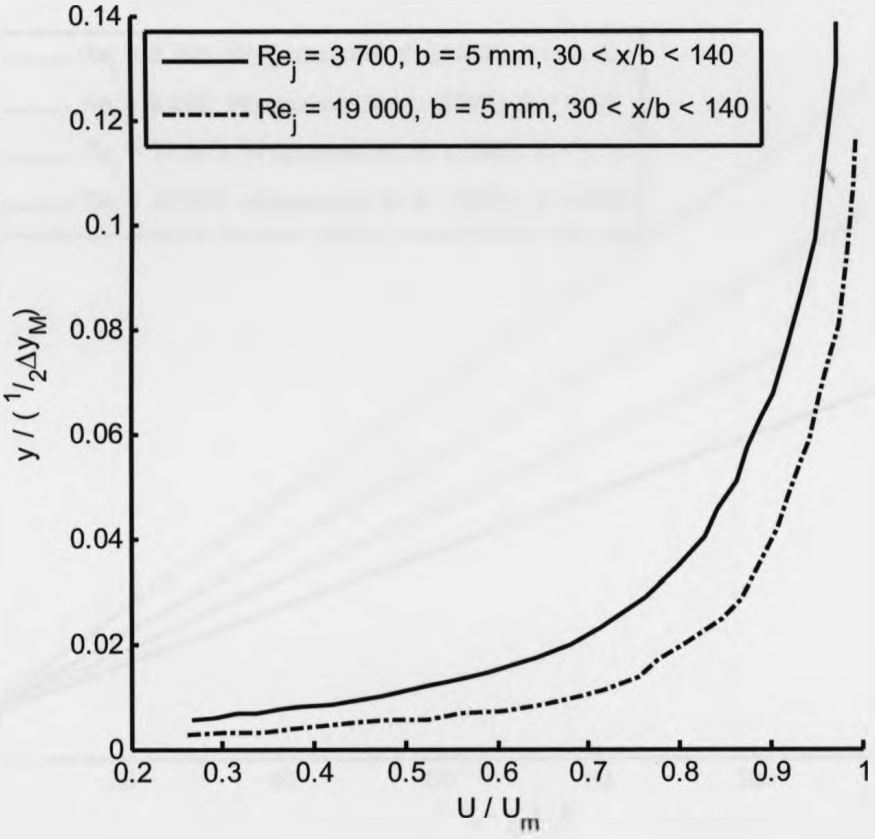

Figure 18: Demonstration of poor scaling in inner region (Wygnanski et al. (1992))

Wygnanski et al. (1992) supported Narasimha et al.'s (1973) work on using M_j for scaling wall jets, **Equations 9 & 10**. Using Narasimha et al. (1973) method, Wygnanski et al. (1992) scaled $\frac{1}{2}\Delta y_M$ and U_m for two Re_j = 5 000 test cases that have different M_j, specified by b = 2.5 mm and 5 mm and U_j = 15 m/s and 30 m/s, respectively, for each case. The two Re_j = 5000 cases scaled to a common curve, using **Equations 9 & 10**, but the curve was offset from a data curve that encompassed Re_j > 10 000. This demonstrates that Narasimha et al.'s (1973) method is dependent on Re_j for low Re_j, but not on M_j.

Wygnanski et al. (1992) modified Narasimha et al.'s (1973) method by using a superficial origin to make the scaling method work for Re_j < 5 000, a superficial origin method not previously mentioned. In this method $\left(\frac{U_m}{U_j}\right)^2 = A\left(\frac{x-x_o}{b}\right)$ is plotted, the requirement being that x_o must shift the curves such that $\left(\frac{U_m}{U_j}\right)^2 = 1$ at $x = x_o$, this can be seen in **Figure 19**.

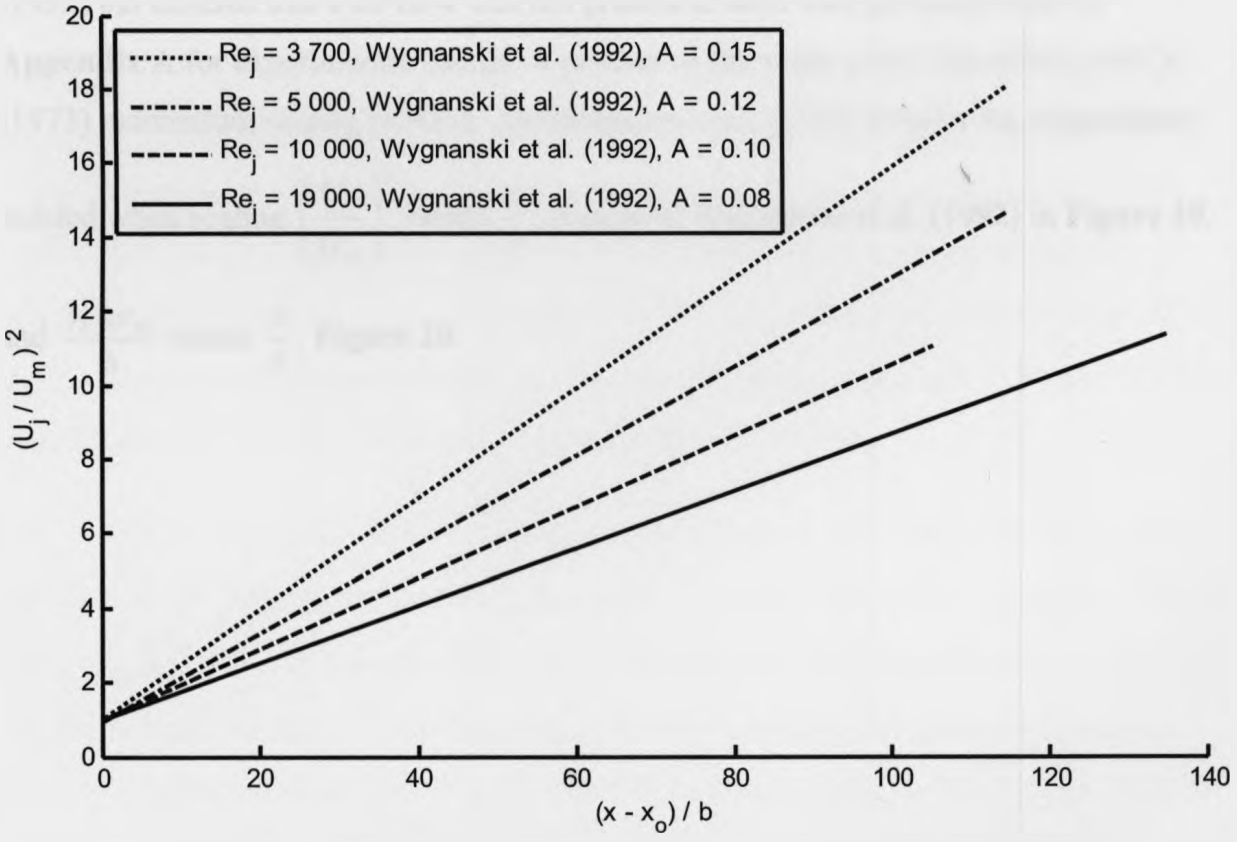

Figure 19: Superficial origin method (Wygnanski et al. (1992))

The value of x_o can then be used as $(x - x_o)$ in place of x in **Equations 9 & 10**, the new relations being **Equations 17 & 18**, which draws the data to common curves for $Re_j > 3$ 700 regardless of the M_j value.

Equation 17: Half-height scaled with momentum and superficial origin (Wygnansk et al. (1992))

$$\frac{(x-x_o)M_j}{\nu^2} \text{ versus } \frac{\frac{1}{2}\Delta y_M M_j}{\nu^2}$$

Equation 18: Maximum velocity scaled with momentum and superficial origin (Wygnansk et al. (1992))

$$\frac{(x-x_o)M_j}{\nu^2} \text{ versus } \frac{U_m \nu}{M_j}$$

Abrahamsson et al. (1994) performed similar experiments to Wygnanski et al. (1992) but ensured that a co-flow was not present in their wall jet study; refer to **Appendix A** for experimental details. A portion of the study tested Narasimha et al.'s (1973) momentum scaling method. Abrahamsson et al. (1994) found a Re_j dependence existed when scaling $\left(\frac{U_j}{U_m}\right)^2$ versus $\frac{x}{b}$, similar to Wygnanski et al. (1992) in **Figure 19**, and $\frac{\frac{1}{2}\Delta y_M}{b}$ versus $\frac{x}{b}$, **Figure 20**.

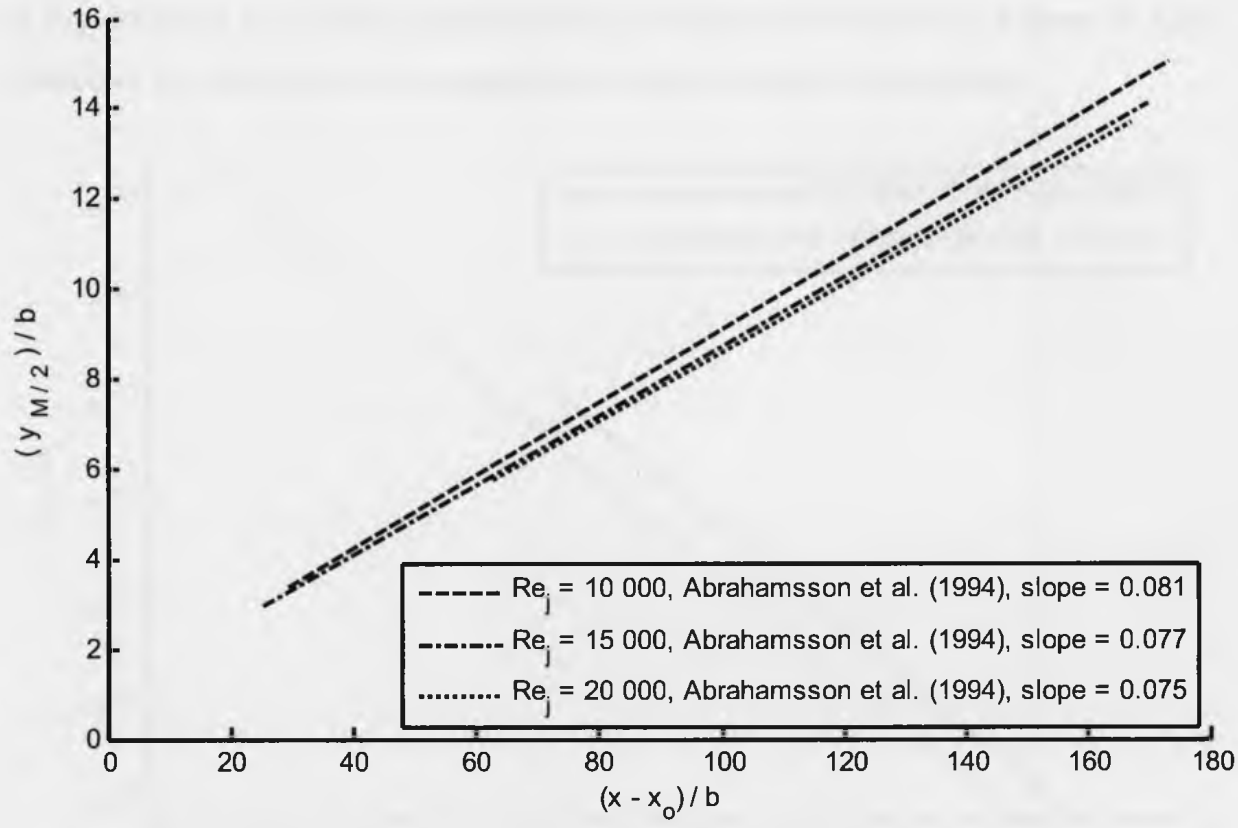

Figure 20: Development of $\frac{1}{2}\Delta y_M$ downstream (Abrahamsson et al. (1994))

Abrahamsson et al. (1994) scaled maximum velocity using **Equation 18**, and the data collapsed for Re_j = 10 000, 15 000 & 20 000; Wygnanski et al.'s (1992) universal curve for maximum velocity was plotted with these results, **Figure 21**. The plots were parallel, but an offset existed between Wygnanski et al.'s (1992) data and Abrahamsson et al.'s (1994) data. Abrahamsson et al. (1994) cited this as being due to the entrained air allowed in Wygnanski et al.'s (1992) case. When $\frac{1}{2}\Delta y_M$ was scaled without a superficial origin, **Equation 10**, a good collapse of data occurred without any offset, **Figure 22**, for both Wygnanski's et al. (1992) and Abrahamsson et al. (1994).

The jet Reynolds number evidently has an effect on the velocity profiles of wall jets. Due to the velocity profiles being modified, the length scale, $\frac{1}{2}\Delta y_M$, and the velocity scale, U_m, are affected. By using M_j it is possible to scale the development of $\frac{1}{2}\Delta y_M$ and U_m downstream for $Re_j > 3\,700$. No attempt has been made in the literature to scale velocity profiles using M_j. Possibly, M_j could be as successful at scaling velocity profiles as scaling downstream development. Abrahamsson et al. (1994) cited the co-flow present

in Wygnanski et al.'s (1992) experiments as the reason for the offset in **Figure 21**. This reinforces the importance of comparing data from the same investigations.

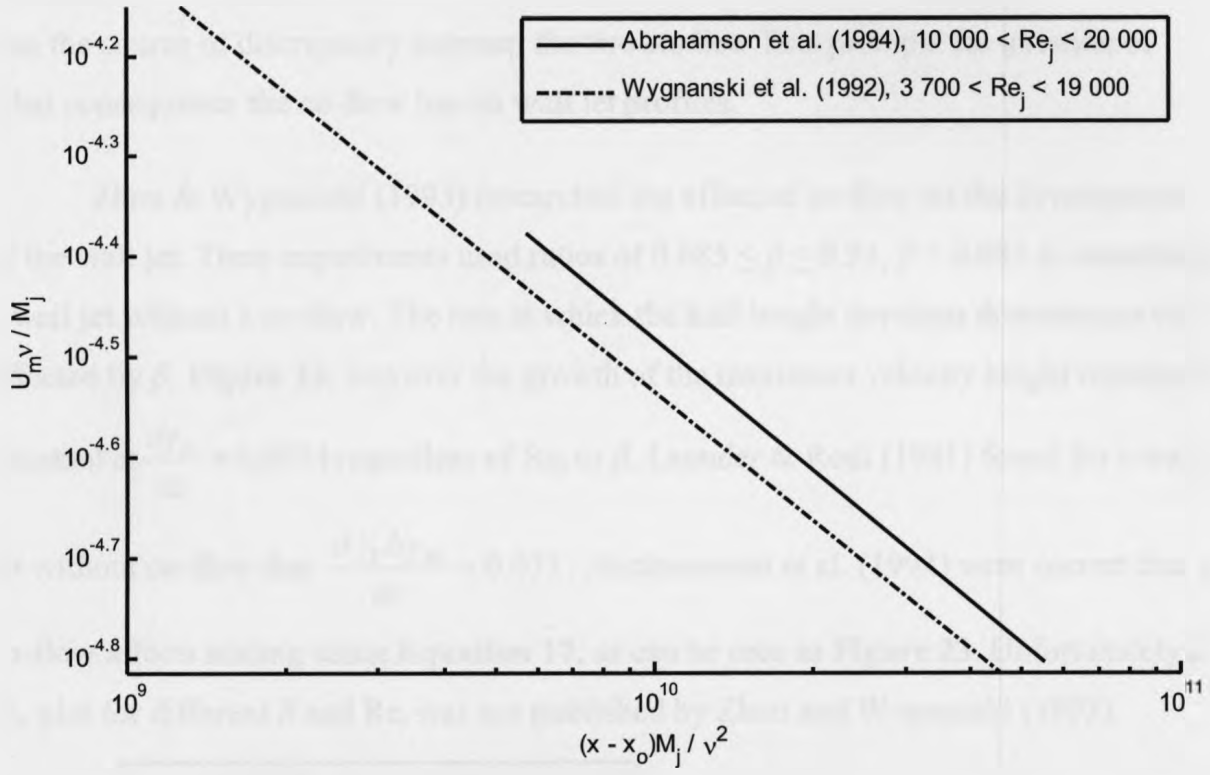

Figure 21: Development of U_m scaled by Equation 17 (Abrahamsson et al. (1994))

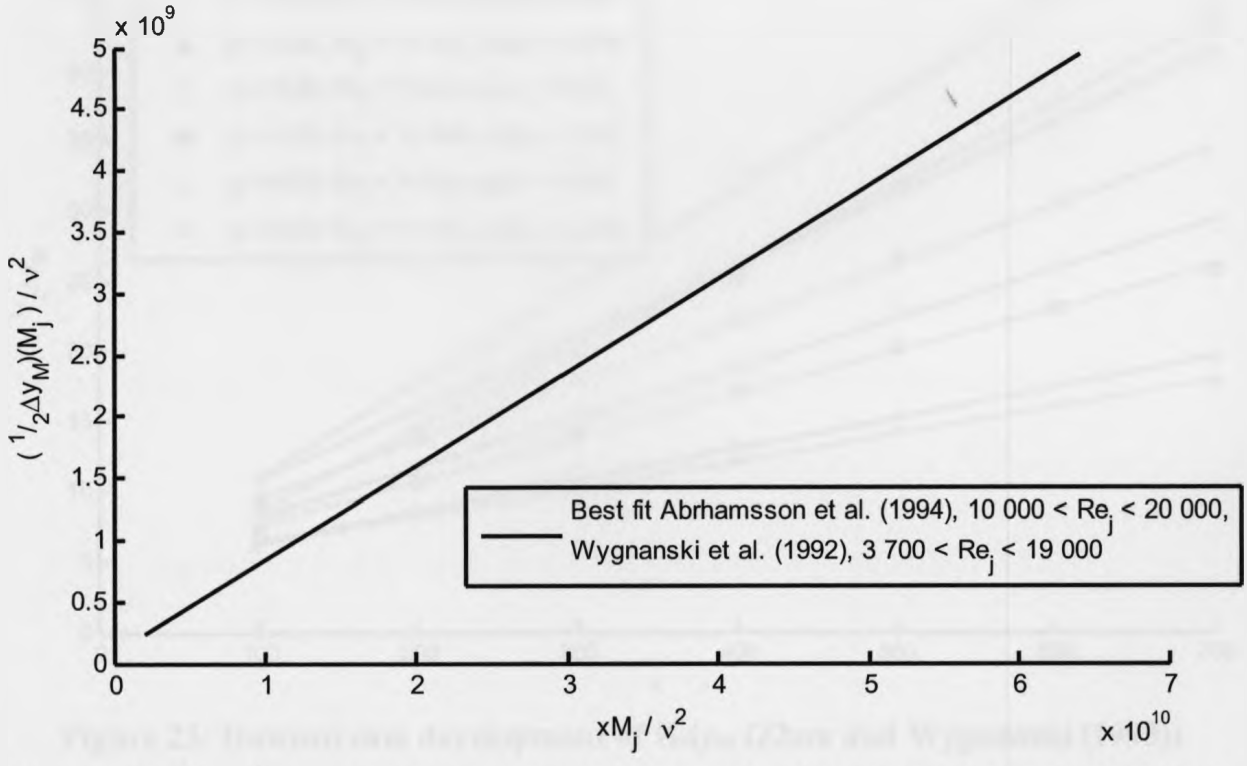

Figure 22: Development of $\frac{1}{2}\Delta y_M$ scaled by Equation 16 (Abrhamsson et al. (1994))

1.6 Effect of velocity ratio

In **Section 1.5**, Abrahamsson et al. (1994) claimed the co-flow in Wygnanski et al. (1992) was the source of discrepancy between the two studies. This prompts the question of what consequence the co-flow has on wall jet profiles.

Zhou & Wygnanski (1993) researched the effect of co-flow on the development of the wall jet. Their experiments used ratios of $0.085 \leq \beta \leq 0.93$; $\beta = 0.085$ is essentially a wall jet without a co-flow. The rate at which the half-height develops downstream was affected by β, **Figure 23**, however the growth of the maximum velocity height remained constant at $\frac{dy_m}{dx} \approx 0.0114$ regardless of Re_j or β. Launder & Rodi (1981) found for a wall jet without co-flow that $\frac{d\,½\Delta y_M}{dx} \approx 0.073$. Abrahamsson et al. (1994) were correct that a co-flow affects scaling using **Equation 17**, as can be seen in **Figure 23**. Unfortunately a U_m plot for different β and Re_j was not published by Zhou and Wygnanski (1993).

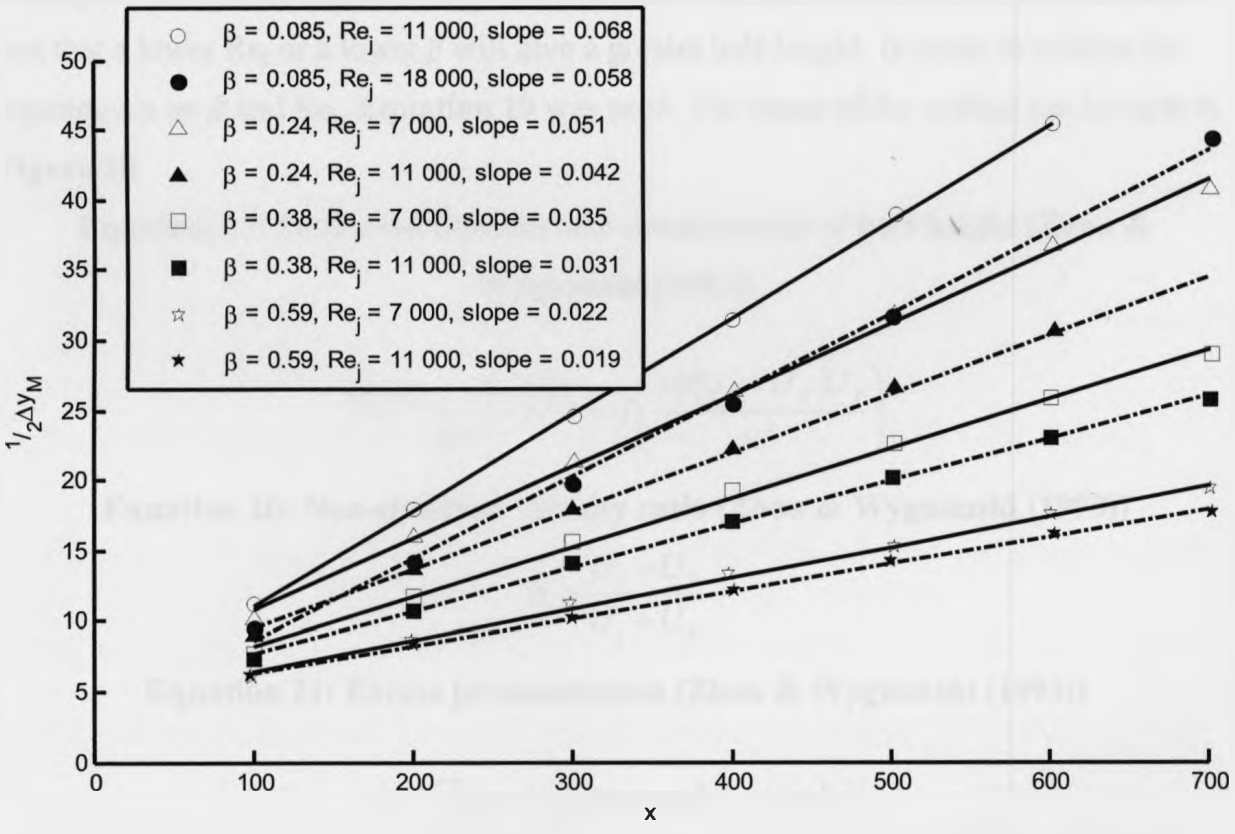

Figure 23: Downstream development of $½\Delta y_M$ (Zhou and Wygnanski (1993))

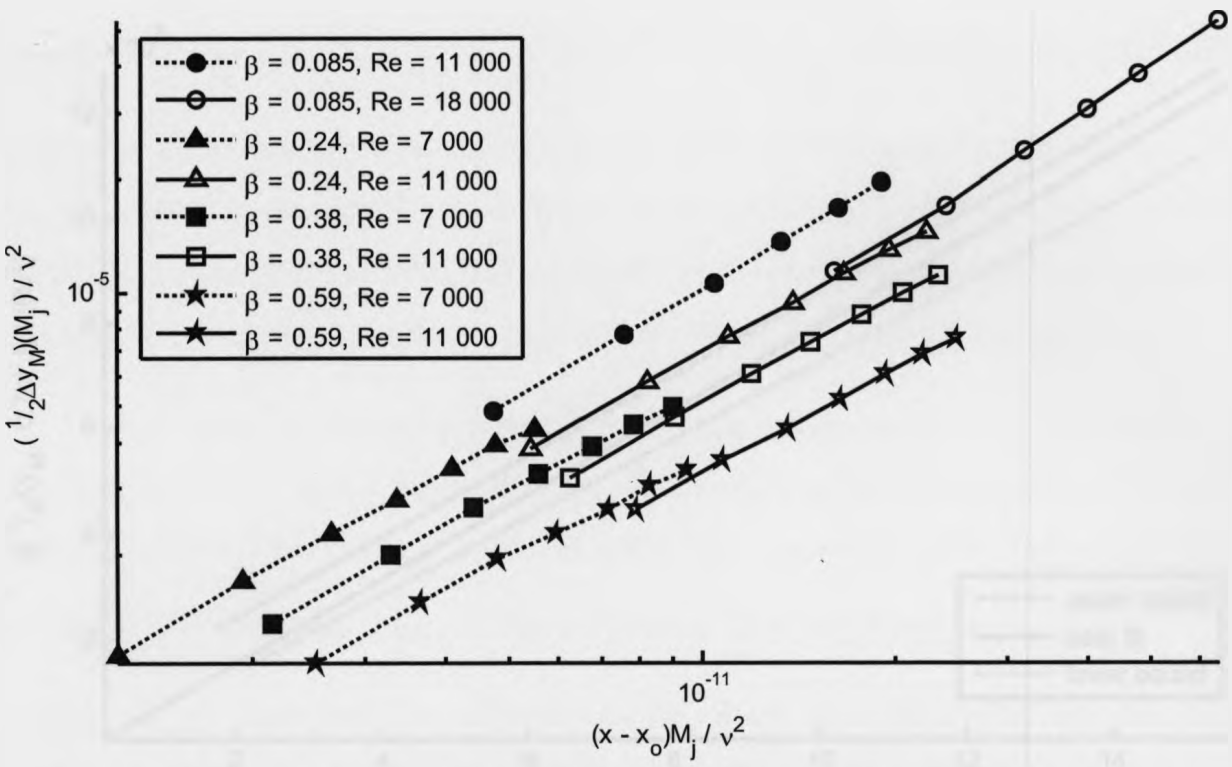

Figure 24: Downstream development of $½\Delta y_M$ (Zhou and Wygnanski (1993))

In, **Figure 23**, it is demonstrated that β manipulates the growth of $½\Delta y_M$ more than Re_j and that a lower Re_j or a lower β will give a greater half-height. In order to remove the dependence on β and Re_j, **Equation 19** was used. The result of the scaling can be seen in **Figure 25**.

Equation 19: Improved downstream development of half-height (Zhou & Wygnanski (1993))

$$\frac{(½\Delta y_M - 0.7b)J}{R\nu^2} = f\left(\frac{xb(U_j - U_E)U_j}{\nu^2}\right)$$

Equation 20: Non-standard velocity ratio (Zhou & Wygnanski (1993))

$$R = \frac{U_j - U_E}{U_j + U_E}$$

Equation 21: Excess jet momentum (Zhou & Wygnanski (1993))

$$J = \int_0^\infty (U - U_E)Udy = b(U_j - U_E)U_j$$

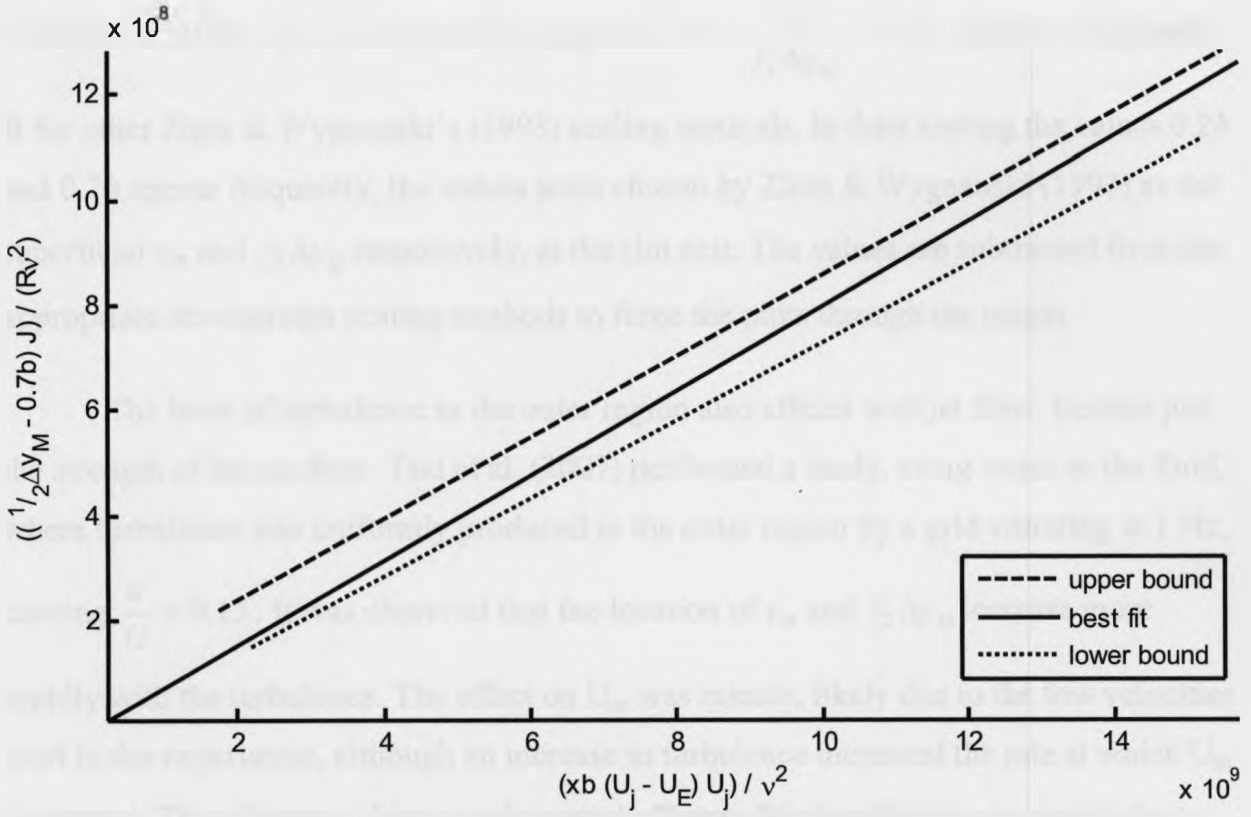

Figure 25: Downstream development of $\frac{1}{2}\Delta y_M$ (Zhou and Wygnanski (1993))

In **Figures 17 & 18** a discrepancy existed in the vertical velocity profiles and was considered to be due to variations in β and Re_j. In order to remove this variation in the profiles, Zhou & Wygnanski (1993) scaled the velocity profile through $\frac{U-U_E}{U_m-U_E}$ versus $\frac{y-y_m}{\frac{1}{2}\Delta y_M - y_m}$ for the outer region and for the inner region, $\frac{U}{U_m}$ versus $\frac{y-y_m}{y_m}$. The inner region method scaled well for $\frac{y}{\frac{1}{2}\Delta y_M} > 0.032$ and for $\frac{y}{\frac{1}{2}\Delta y_M} < 0.032$ the different profiles diverged. At $\frac{y}{\frac{1}{2}\Delta y_M} = 0.032$, y = 0.32 mm and it is possible that the divergence is due to inherent errors in using hot-wire anemometry that close to a surface, Bruun (1995). The collapse of data using this scaling method was best for $\frac{U_E}{U_m} \leq 0.5$. As well, the relation of $\frac{y_m}{\frac{1}{2}\Delta y_M} \approx 0.15$ discussed in **Section 1.4** did not hold under varying β; a

variation of $0.085 < \beta < 0.59$ caused a range of $0.16 < \frac{y_m}{\frac{1}{2}\Delta y_M} < 0.31$. Refer to **Appendix B** for other Zhou & Wygnanski's (1993) scaling methods. In their scaling the values $0.2b$ and $0.7b$ appear frequently, the values were chosen by Zhou & Wygnanski (1993) as the superficial y_m and $\frac{1}{2}\Delta y_M$ respectively, at the slot exit. The values are subtracted from the appropriate downstream scaling methods to force the plots through the origin.

The level of turbulence in the outer region also affects wall jet flow, besides just the strength of the co-flow. Tsai et al. (2007) performed a study, using water as the fluid, where turbulence was uniformly produced in the outer region by a grid vibrating at 1 Hz, causing $\frac{u'}{U} = 0.15$. It was observed that the location of y_m and $\frac{1}{2}\Delta y_M$ increase more rapidly with the turbulence. The effect on U_m was minute, likely due to the low velocities used in the experiment, although an increase in turbulence increased the rate at which U_m decreased. The effect on $\frac{1}{2}\Delta y_M$ can be seen in **Figure 26**, the effect on y_m was far less pronounced.

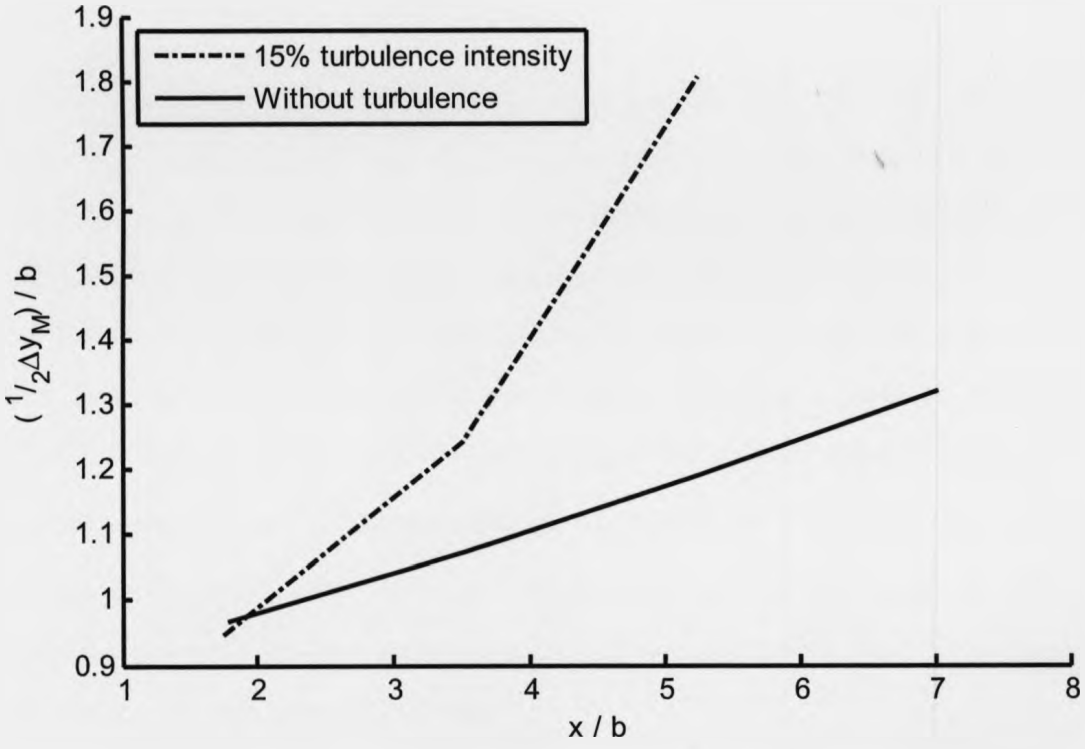

Figure 26: Effect of co-flow turbulence on $\frac{1}{2}\Delta y_M$ (Tsai et al. (2007))

The co-flow has a large effect on the $\frac{1}{2}\Delta y_M$ length scale in the outer region of the flow, as well as the turbulence present in the outer region. The inner region length scale y_m would appear to be impervious to the co-flow. Unfortunately, with the available data, the effect on the maximum velocity is unknown. Zhou & Wygnanski (1993) suggested subtracting the co-flow velocity from the downstream velocity profiles, which may prove to be useful if a co-flow exists in an analysis and difficulty arises in scaling the flow.

1.7 Effect of lip thickness

The jet height, b, is the most common length used to scale t and Y. How the geometry of the wall jet domain impacts the wall jet has been studied for t/b, but not for Y/b. The effect of different b sizes is encompassed in comparisons of Re_j and M_j which was discussed in **Section 1.5**. A better understanding of the t/b ratio will enable ratios to be used that have minimal impact on the wall jet flow, or possibly use the ratio to aid in controlling the flow.

Kacker & Whitelaw (1971) were the only researchers to study the effect of lip thickness with a co-flow, $\beta = 0.43$ & 1.33, and here the focus will be on the former. The lip thicknesses tested were $t = 0.126b$ & $1.14b$. For $t = 1.14b$, the velocity profile in **Figure 27** has a blunter profile than for $t = 0.126b$. Kacker & Whitelaw (1971) view this as being due to greater mixing downstream in the $t = 1.14b$ case. In examining the vertical profiles of the turbulence intensities, **Figure 28**, it can be seen that the turbulence intensity was higher for $t = 1.14b$ than $t = 0.126b$ at the same location, which also indicates greater mixing for $t = 1.14b$.

In the decay downstream of U_m, at $x = 30b$, U_m was 10% lower than for $t = 1.14b$ than for $t = 0.126b$, but by $150b$ U_m is equal in the two cases. The thicker lip was observed to have an effect close to the jet exit, but far downstream (~$100b$) the influence of the lip on turbulence intensity was dominated by β, similarly for turbulent kinetic energy (k). However as only $\beta = 0.43$ and 1.33 were tested this is not conclusive due to wake like flow of $\beta = 1.33$. In turbulent kinetic energy (k) plots, **Figure 29**, $t = 1.14b$ causes k values than $t = 0.126b$ at $10b$ and less than t = $0.126b$ at $150b$. The maxima of the $\overline{uv}$ shear stress profiles follow a similar trend, **Figure 30**. The thicker lip clearly increases the mixing close to the jet exit. Perhaps the reason for the higher $\overline{uv}$ stress and k values of the thin lip downstream is that the inner regions retains more momentum and mixes over a greater distance downstream.

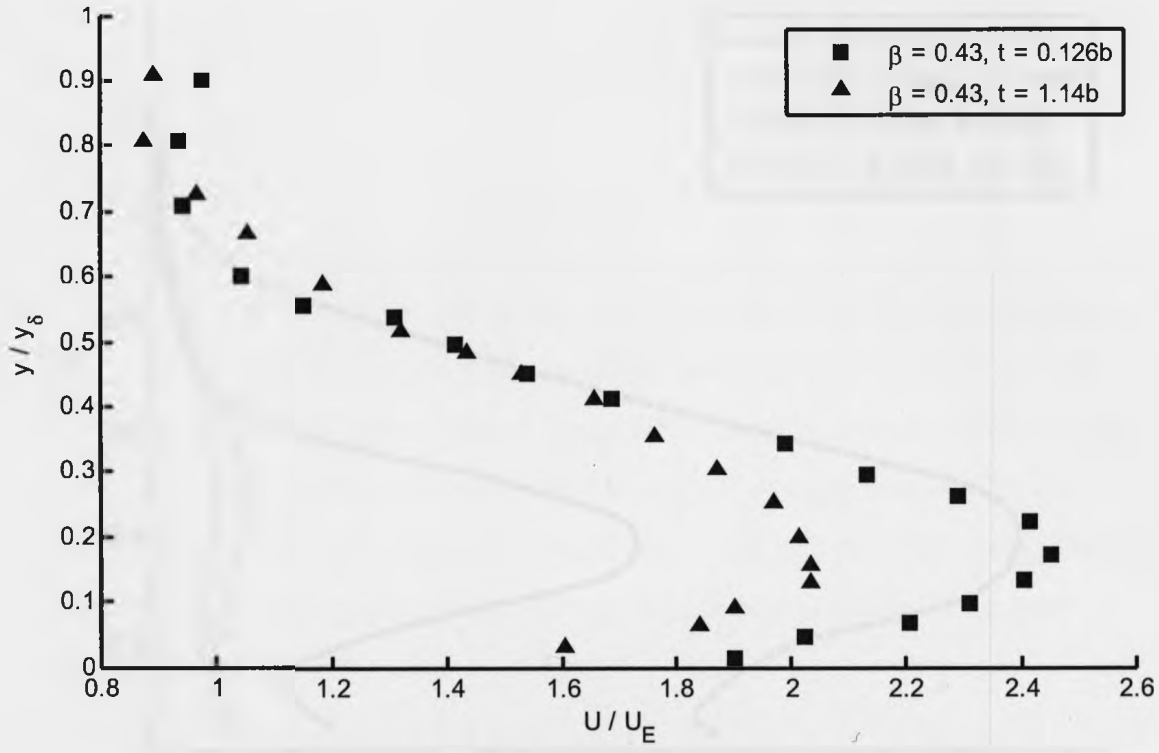

Figure 27: Velocity profiles at $x = 10b$ (Kacker & Whitelaw (1971))

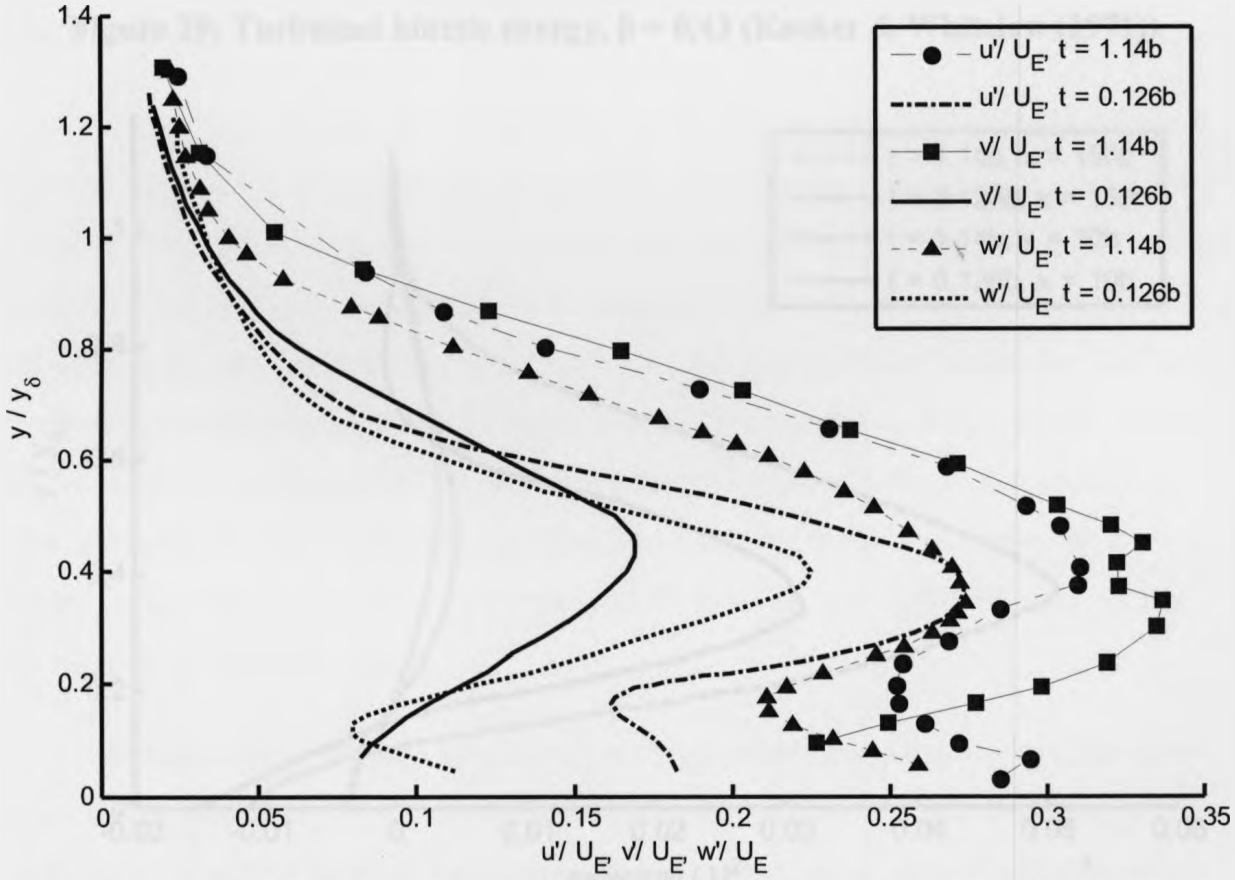

Figure 28: Turbulence profiles at $x = 10b$, $\beta = 0.43$ (Kacker & Whitelaw (1971))

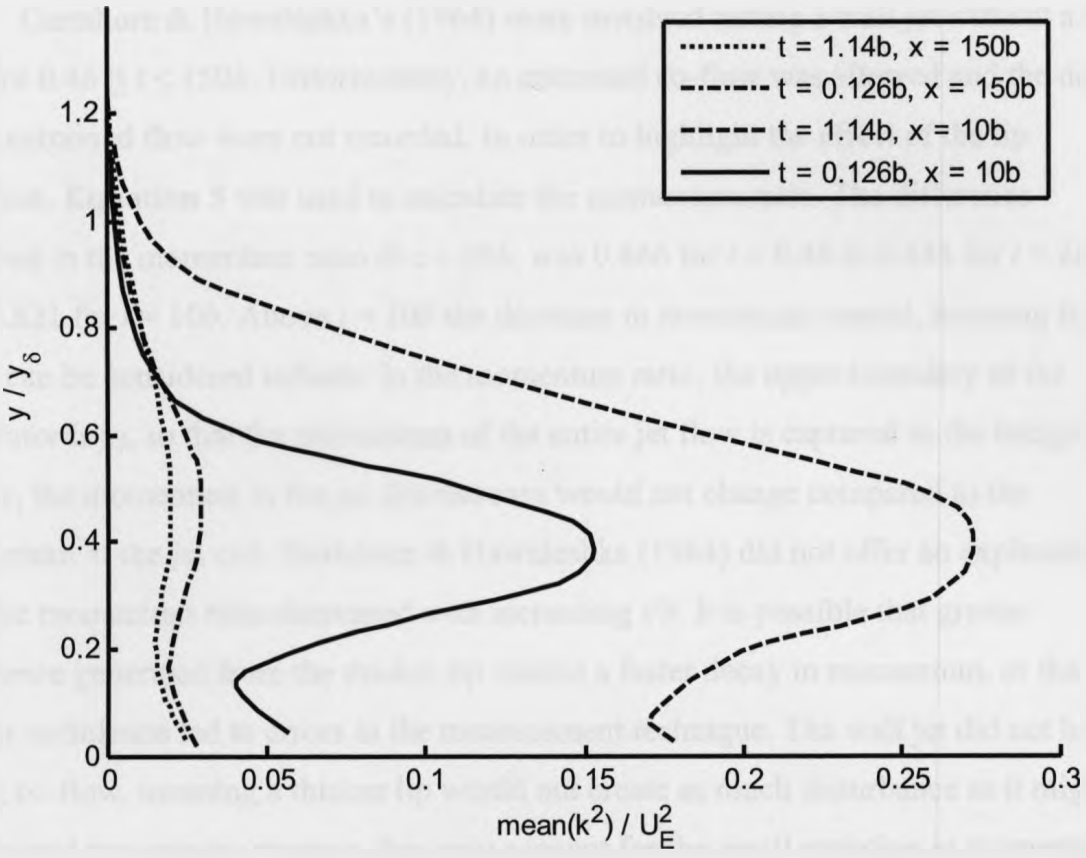

Figure 29: Turbulent kinetic energy, β = 0.43 (Kacker & Whitelaw (1971))

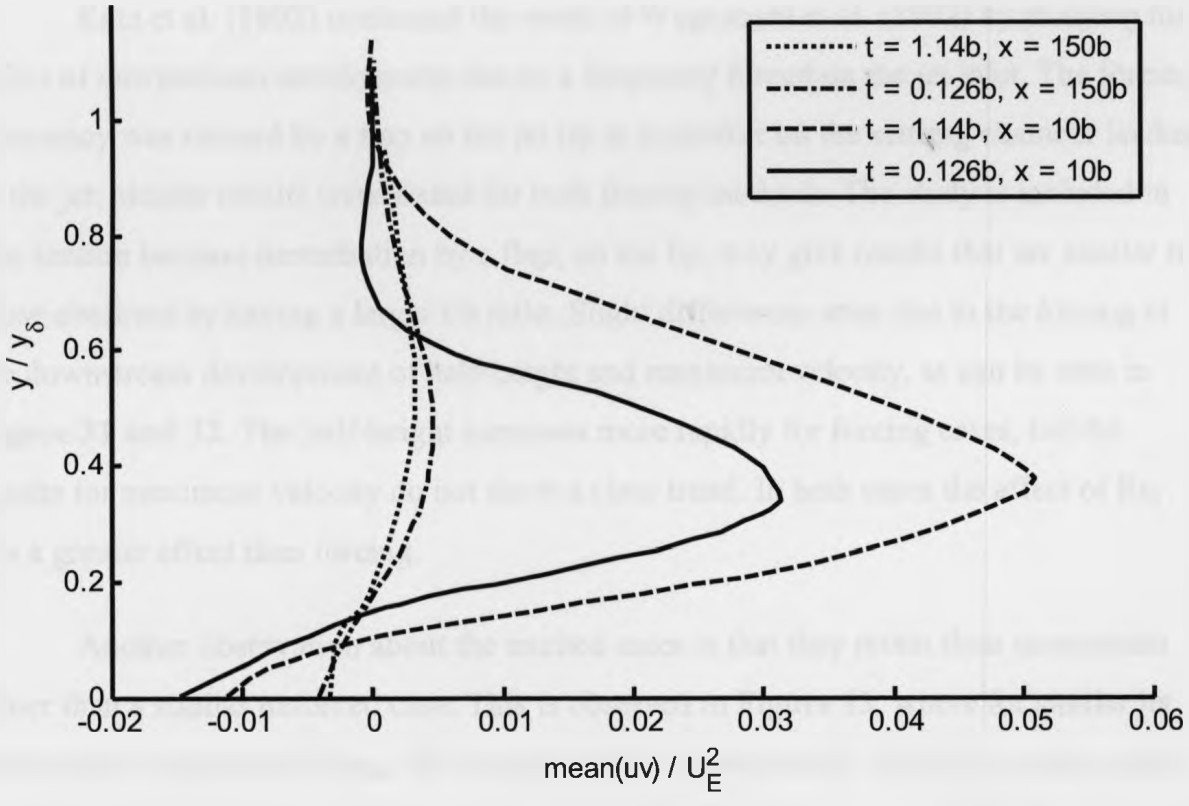

Figure 30: Shear stress profiles, β = 0.43 (Adapted from Kacker & Whitelaw (1971))

Gartshore & Hawaleshka's (1964) work involved testing a wall jet without a co-flow for $0.4b \leq t \leq 150b$. Unfortunately, an entrained co-flow was allowed and the details of the entrained flow were not recorded. In order to highlight the effect of the lip thickness, **Equation 5** was used to calculate the momentum ratio. The difference observed in the momentum ratio at $x = 55b$, was 0.866 for $t = 0.4b$ to 0.844 for $t = 2b$ and then 0.821 for $t = 10b$. Above $t = 10b$ the decrease in momentum ceased, meaning for $t > 10b$, t can be considered infinite. In the momentum ratio, the upper boundary of the numerator is y_δ, so that the momentum of the entire jet flow is captured in the integral. Ideally, the momentum in the jet downstream would not change compared to the momentum at the jet exit. Gartshore & Hawaleshka (1964) did not offer an explanation of why the momentum ratio decreased with increasing *t/b*. It is possible that greater turbulence generated from the thicker lip caused a faster decay in momentum, or that greater turbulence led to errors in the measurement technique. The wall jet did not have a strong co-flow, meaning a thicker lip would not create as much disturbance as it might if it separated two mixing streams, this may account for the small variation in momentum ratio with changes in t/b.

Katz et al. (1992) continued the work of Wygnanski et al. (1992) by studying the effect of downstream development due to a frequency forced on the jet inlet. The forcing frequency was created by a flap on the jet lip or a speaker on the settling chamber leading to the jet; similar results were found for both forcing methods. The study is included in this section because perturbation by a flap, on the lip, may give results that are similar to those obtained by having a larger t/b ratio. Slight differences arise due to the forcing in the downstream development of half-height and maximum velocity, as can be seen in **Figure 31 and 32**. The half-height increases more rapidly for forcing cases, but the results for maximum velocity do not show a clear trend. In both cases the affect of Re_j has a greater effect than forcing.

Another observation about the excited cases is that they retain their momentum better than a similar unforced case. This is observed in **Figure 33**, where for similar jet conditions, other than forcing, the forced case has preserved its' velocity over the whole profile better than the unforced case. Katz et al. (1992) cite the reason for the better

retention of momentum is due to a reduction in wall shear stress due to forcing, reductions in stress being largely 10%, but up to 40% for very large forcing amplitudes.

Katz et al. (1992) studied the production of turbulence, **Equation 22**, in the inner region of the wall jet. The production of turbulence, at $y^+ = 10$, reduced to one-half of the unforced case at $x = 50b$, for $Re_j = 3\ 400$ and a forcing frequency of 34 (Hz).

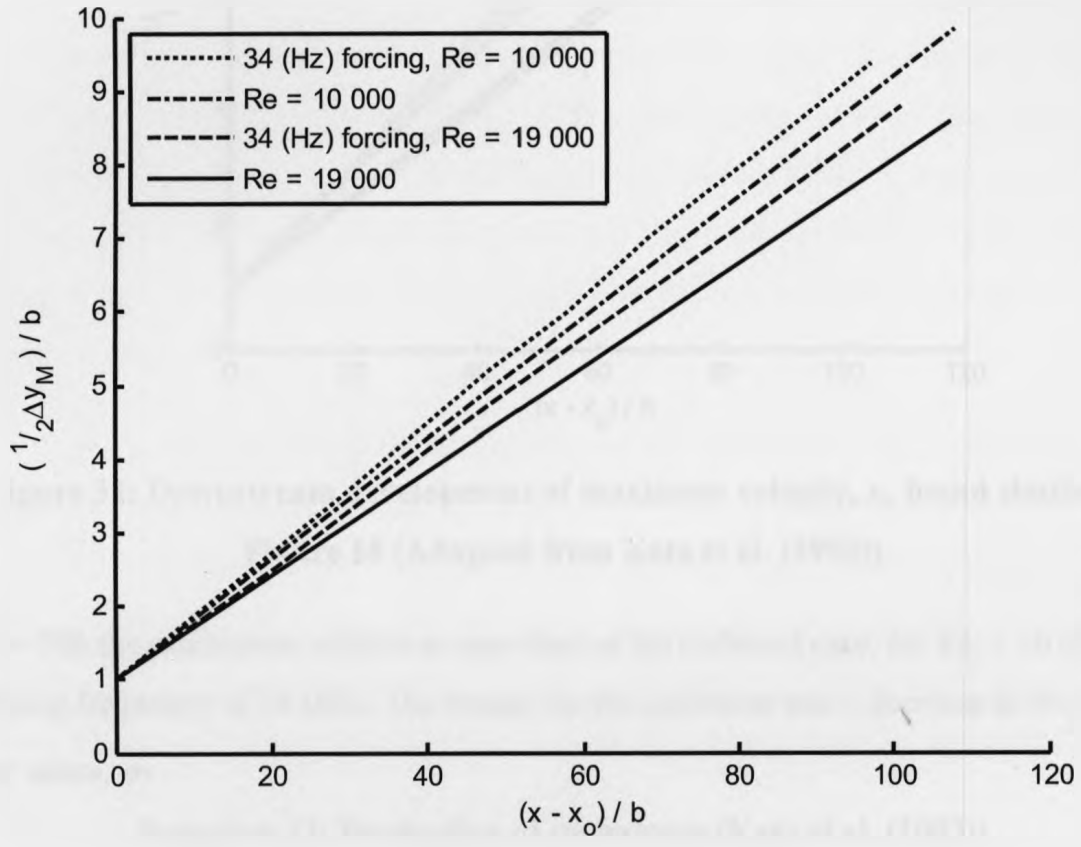

Figure 31: Downstream development of $\frac{1}{2}\Delta y_M$, x_o found similar to Figure 18 (Adapted from Katz et al. (1992))

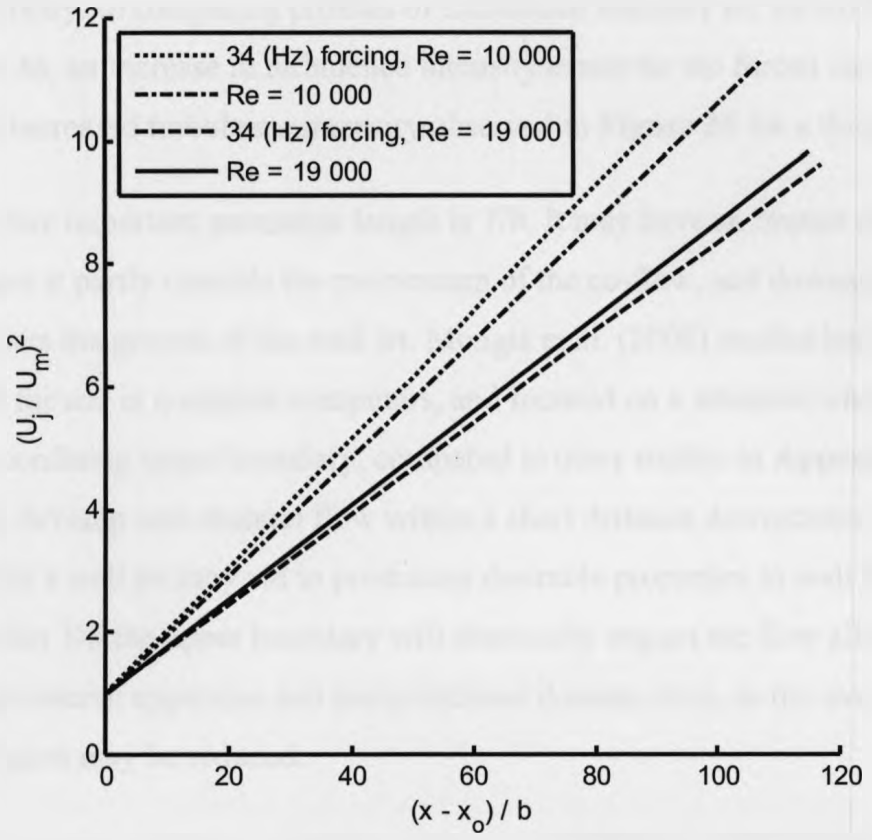

Figure 32: Downstream development of maximum velocity, x_o found similar to Figure 18 (Adapted from Katz et al. (1992))

At $x = 70b$ the production reduces to one-third of the unforced case, for $Re_j = 10\,000$ and a forcing frequency of 34 (Hz). The reason for the reduction was a decrease in Reynolds shear stress, $\overline{uv}$.

Equation 22: Production of turbulence (Katz et al. (1992))

$$\text{Production} \equiv \frac{1}{U_m^3}\int_0^{y_m} -\overline{uv}\frac{\partial U}{\partial y}\,dy\,.$$

Katz et al. (1992) believed the reduction of the production integral altered the turbulent energy balance and the scale of the large coherent eddies. The power spectral densities were measured between $30b \le x \le 100b$. The height at which measurements were taken was y_m and $\frac{y}{y_m} = 1.8$ (where $\frac{U}{U_m} = 0.1$ in the outer region). They observed that the dominant frequency decreases with downstream distance as the jet broadens and

reduces in velocity. In comparing profiles of turbulence intensity for forced and unforced cases, **Figure 34**, an increase in turbulence intensity exists for the forced case. This is similar to the increased turbulence intensity observed in **Figure 28** for a thicker lip.

The other important geometric length is *Y/b*. It may have an impact at the co-flow entrance, where it partly controls the momentum of the co-flow, and downstream where it possibly restricts the growth of the wall jet. Mongia et al. (2008) studied heat transfer with wall jets for use in notebook computers, and focused on a situation where *Y/b* = 2.25. Such a confining upper boundary, compared to other studies in **Appendix B**, forces the wall jet to develop into channel flow within a short distance downstream. Knowing how *Y/b* affects a wall jet may aid in producing desirable properties in wall jets. As well, knowing at what *Y/b* the upper boundary will drastically impact the flow allows for more efficient experimental apparatus and computational domain sizes, as the overall height of the wall jet region may be reduced.

The t/b ratio has effects on the flow. Kacker & Whitelaw (1971) found differences in turbulence quantities close to the lip, but far downstream the differences were minimal. Katz et al. (1992) found that a disturbance at the lip tip causes a greater increase in half-height, as well as slight variations in maximum velocity. The most notable effect was in the wall region where wall shear stress and the Reynolds shear stress were drastically reduced. There has yet to be a study investigating the overall height of the wall jet upper boundary and this may prove to be worthwhile.

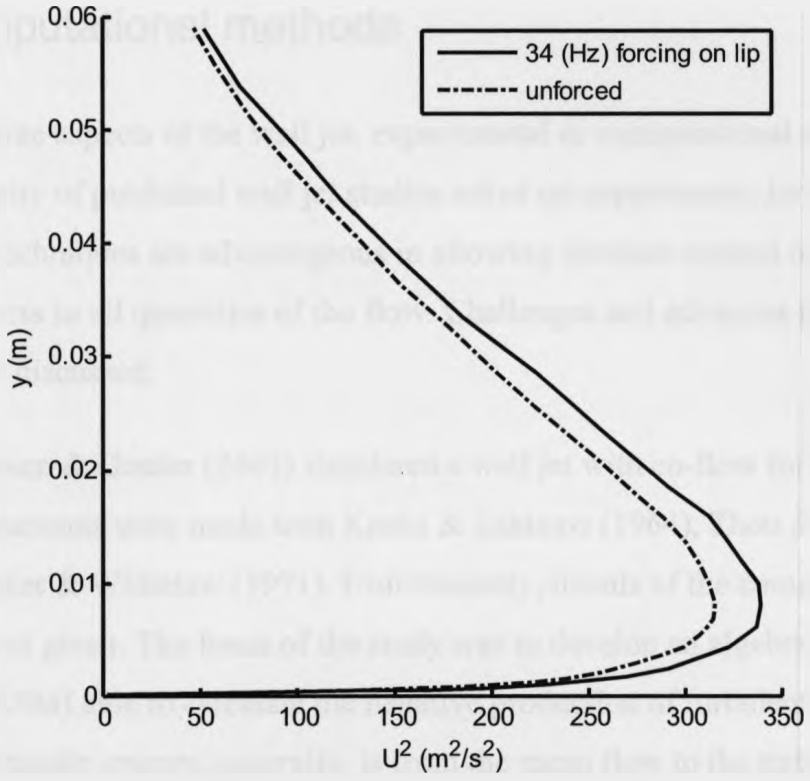

Figure 33: Comparing similar forced and unforced cases of velocity profiles at the same x (Katz et al. (1992))

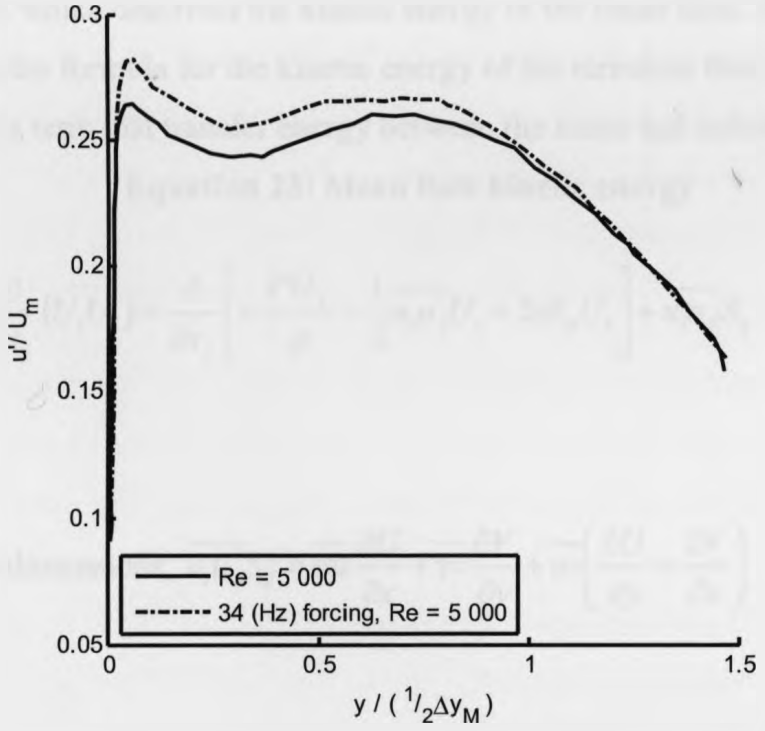

Figure 34: Turbulence intensity compared for comparing similar forced and unforced cases at x = 30b (Katz et al. (1992))

1.8 Computational methods

In order to analyze aspects of the wall jet, experimental or computational methods can be used. The majority of published wall jet studies relied on experiments; however computational techniques are advantageous in allowing absolute control over the wall jet domain and access to all quantities of the flow. Challenges and advances in modeling wall jets will be discussed.

Tangemann & Gretler (2001) simulated a wall jet with co-flow for $\beta = 0.59$, 0.43 and 0.26. Comparisons were made with Kruka & Eskinazi (1964), Zhou & Wygnanski (1993) and Kacker & Whitelaw (1971). Unfortunately, details of the computational domains were not given. The focus of the study was to develop an algebraic Reynolds Stress Model (RSM) able to calculate the negative production of turbulent kinetic energy. The transfer of kinetic energy, generally, is from the mean flow to the turbulent flow, and the negative production of turbulent kinetic energy means that energy is being transferred from the turbulent flow to the mean flow. The turbulent production term, $\overline{u_i u_j} S_{ij}$, appears in **Equation 23,** which describes the kinetic energy of the mean flow. The production term appears in the formula for the kinetic energy of the turbulent flow, but with opposite sign and it is this term that transfer energy between the mean and turbulent flows.

Equation 23: Mean flow kinetic energy

$$\frac{U_j}{2}\frac{\partial}{\partial x_j}\left(U_i U_i\right) = \frac{\partial}{\partial x_j}\left[-\frac{PU_j}{\rho} - \frac{1}{2}\overline{u_i u_j} U_i + 2\nu S_{ij} U_i\right] + \overline{u_i u_j} S_{ij} - 2\nu S_{ij} S_{ij}$$

Where, for two dimensions, $\overline{u_i u_j} S_{ij} = \overline{uu}\frac{\partial U}{\partial x} + \overline{vv}\frac{\partial V}{\partial y} + \overline{uv}\left(\frac{\partial U}{\partial y} + \frac{\partial V}{\partial x}\right)$

Kacker &Whitelaw (1971) considered only $\overline{-uv}\frac{\partial U}{\partial y}$, of the production term, as significant because for x > 10b, $\frac{\partial V}{\partial x} < 0.05\overline{-uv}\frac{\partial U}{\partial y}$ and in order for $\left(\overline{-uu}\frac{\partial U}{\partial x} + \overline{-vv}\frac{\partial V}{\partial y}\right) > 0.05\overline{-uv}\frac{\partial U}{\partial y}$, $\overline{-uv}\frac{\partial U}{\partial y}$ itself must be "very small" and both terms would be inconsequential.

The reason for the specialized model used by Tangemann & Gretler (2001) is that wall jets contain a region where $\frac{dU}{dy}$ is of the opposite sign to $\overline{-uv}$, causing $\overline{-uv}\frac{\partial U}{\partial y}$ to be negative and indicating that energy is being transferred from the turbulent flow to the mean. This flow characteristic cannot be simulated by a Reynolds Averaged Navier-Stokes (RANS) model, for example the standard k-ε model, but can be simulated with a RSM. In making a dedicated algebraic RSM the flow can be simulated with less computational effort and better accuracy. Standard k-ε models, and also standard RSM, predict the location where $\overline{-uv} = 0$ to be too far from away from the wall, which is not the case for the algebraic RSM. A comparison is shown in **Figure 35**, comparing the algebraic RSM to Zhou & Wygnanski's (1993) experimental data. For $x = 20b$ the location of maximum velocity does not line up well, whereas downstream the profile does not match well below the maximum velocity. This may be because the vertical location is not scaled, but as the model is designed to match the experiment, one would have expected the unscaled vertical locations to align better.

Gerodimos & So (1997) tested a range of RANS models in the near wall region and compared them to experimental results. The wall jets were with a co-flow. The modeling of the near wall region is important, as similar to Launder & Rodi (1983) in **Section 1.4**, the log-law does not grow as in a conventional boundary layer meaning a wall function cannot be used and the near wall region must be fully modeled. The best model reviewed was that by Sarker & So (1997), the model simulated the near wall region well, but as can be seen in **Figure 37**, the half-height was not modeled well, through a varying slope of the two plots. In **Section 1.5** it was established in **Figure 22**, that the scaling used in **Figure 37** is robust and will collapse to a common curve, despite

an entrained co-flow. As well in **Figure 24**, it can be seen that if a co-flow does exist the plots of half-height will still be parallel. In **Figure 36** an offset exists for maximum velocity between the experimental data and Sarker & So's (1997) model, this difference could be accounted for by the entrained flow in the Wygnanski et al. (1992) case, similar to **Figure 21**. The difference in curves in **Figure 36** demonstrates that despite modeling the near wall region well the Sarker & So (1997) model, which was the best of several reviewed by Gerodimos & So (1997), was not able to simulate the whole wall jet. This is likely due to the inability of RANS models to correctly simulate the negative production of turbulence.

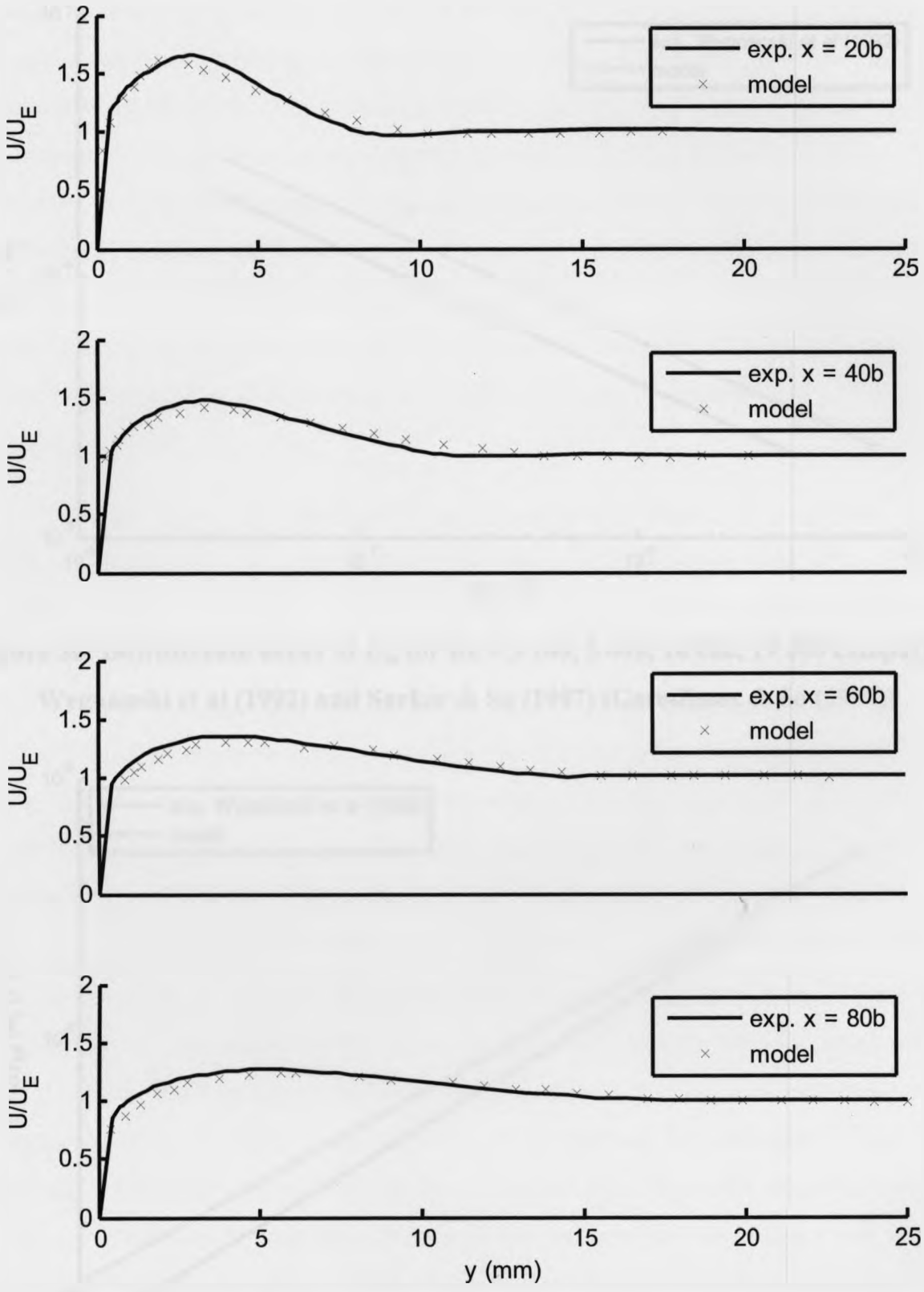

Figure 35: Comparison of U velocity profiles, of $U_E/U_j = 0.59$, for Tangemann & Gretler (2001) Algebraic RSM and Zhou & Wygnanski (1993) experiment (Tangemann & Gretler (2001))

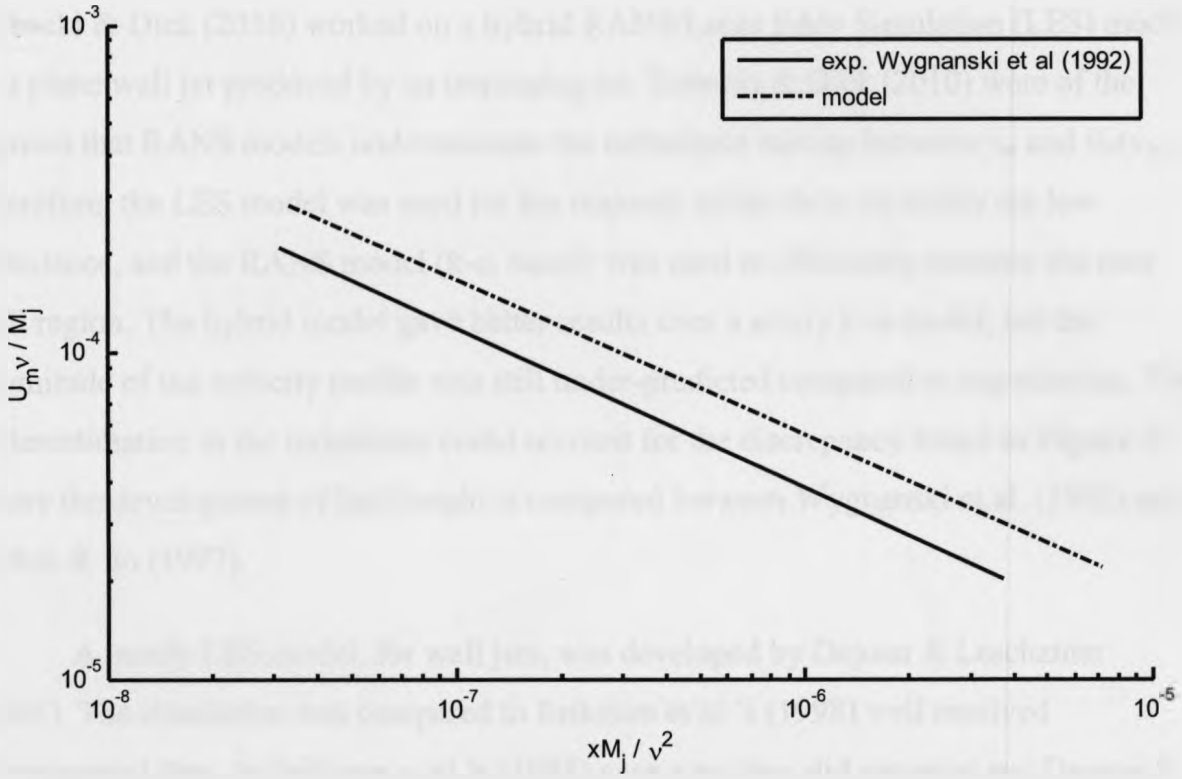

Figure 36: Downstream decay of U_m for Re = 3 700, 5 000, 10 000, 19 000 comparing Wygnanski et al (1992) and Sarker & So (1997) (Gerodimos & So (1997))

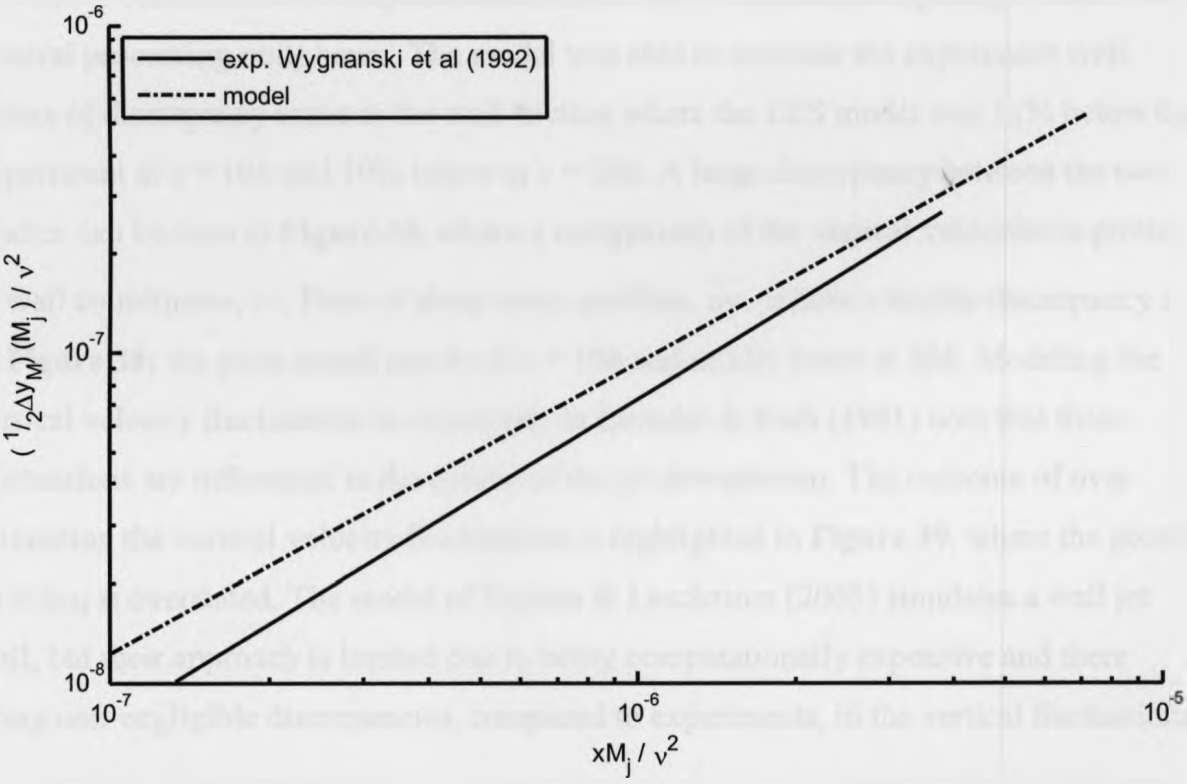

Figure 37: Downstream growth of $\frac{1}{2}\Delta y_M$ for Re = 3 700, 5 000, 10 000, 19 000 comparing Wygnanski et al (1992) and Sarker & So (1997) (Gerodimos & So (1997))

Kubacki & Dick (2010) worked on a hybrid RANS/Large Eddy Simulation (LES) model of a plane wall jet produced by an impinging jet. Kubacki & Dick (2010) were of the opinion that RANS models underestimate the turbulence mixing between y_m and $½\Delta y_M$. Therefore, the LES model was used for the majority of the flow, to rectify the low turbulence, and the RANS model (k-ω based) was used to efficiently estimate the near wall region. The hybrid model gave better results over a solely k-ω model, but the magnitude of the velocity profile was still under-predicted compared to experiments. The underestimation in the turbulence could account for the discrepancy found in **Figure 37**, where the development of half-height is compared between Wygnanski et al. (1992) and Sarker & So (1997).

A purely LES model, for wall jets, was developed by Dejoan & Leschziner (2005). The simulation was compared to Eriksson et al.'s (1998) well resolved experimental data. In Eriksson et al.'s (1998) case a co-flow did not exist and Dejoan & Leschziner (2005) used $\beta = 0.05$. The $Re_j = 9\ 600$ of the experiment was matched in the simulation. The computational domain set $Y = 10b$ and the downstream boundary to $x = 22b$ due to restrictions of computational resources, the simulation requiring 22 000 CPU (central processing unit) hours. The model was able to simulate the experiment well. Points of discrepancy arose in the wall friction where the LES model was 11% below the experiment at $x = 10b$ and 10% below at $x = 20b$. A large discrepancy between the two studies can be seen in **Figure 38**, where a comparison of the vertical velocities is plotted in wall coordinates, v^+. Plots of shear stress profiles, $\overline{uv}$, follow a similar discrepancy as in **Figure 38;** the plots match poorly at $x = 10b$ and mildly better at $20b$. Modeling the vertical velocity fluctuations is important, as Launder & Rodi (1981) note that these fluctuations are influential in the spread of the jet downstream. The outcome of over estimating the vertical velocity fluctuations is highlighted in **Figure 39**, where the growth of $½\Delta y_M$ is overstated. The model of Dejoan & Leschziner (2005) simulates a wall jet well, but their approach is limited due to being computationally expensive and there being non-negligible discrepancies, compared to experiments, in the vertical fluctuations.

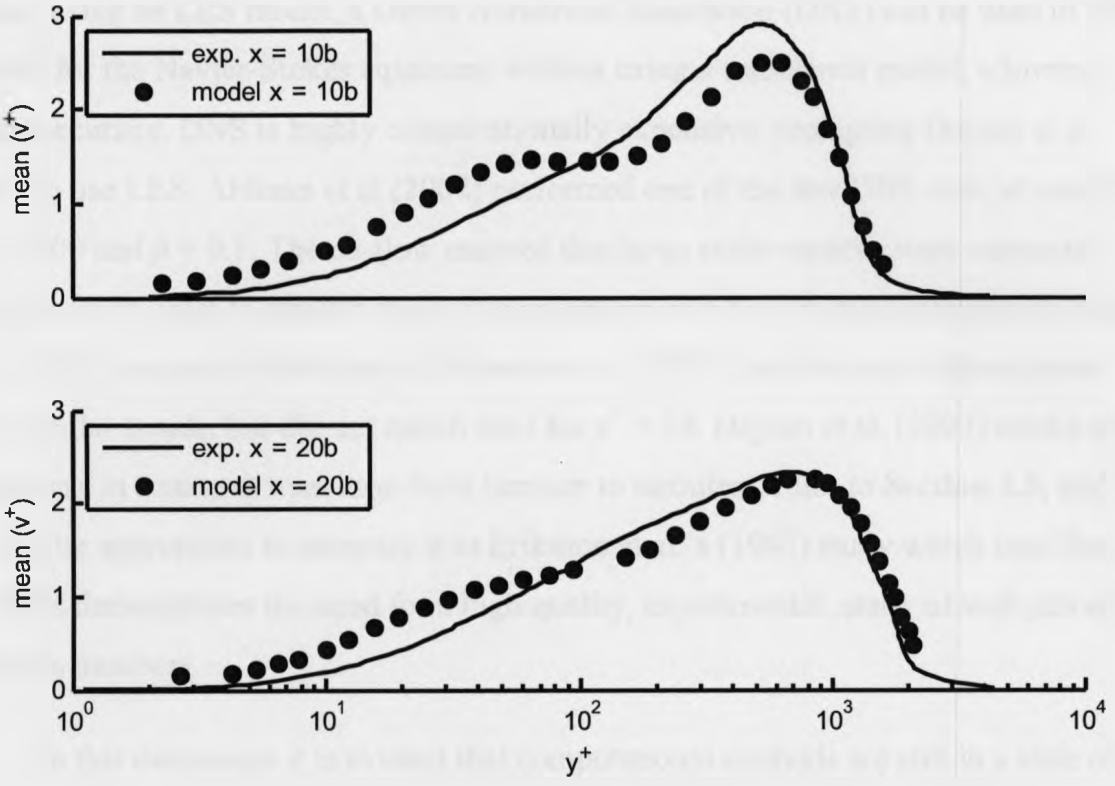

Figure 38: Comparison of vertical velocity of Dejoan & Leschziner (2005) and Eriksson et al.'s (1998) (Dejoan & Leschziner (2005))

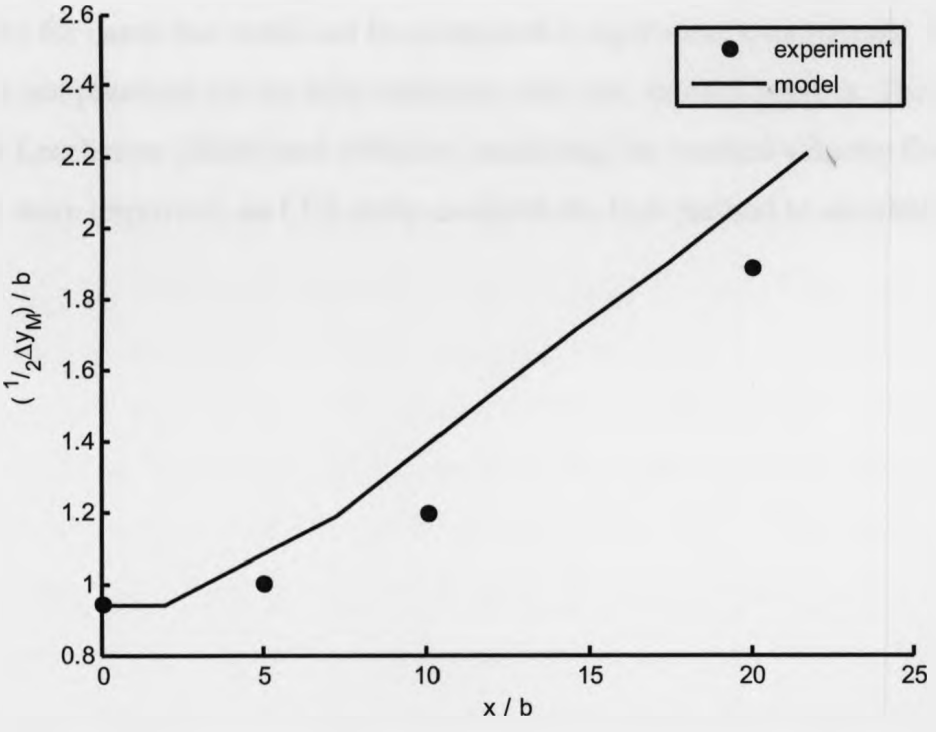

Figure 39: Comparison of ½Δy_M downstream of Dejoan & Leschziner (2005) and Eriksson et al.'s (1998) (Dejoan & Leschziner (2005))

Beyond using an LES model, a Direct Numerical Simulation (DNS) can be used to find a solution for the Navier-Stokes equations without using a turbulence model, allowing greater accuracy. DNS is highly computationally expensive, prompting Dejoan et al. (2007) to use LES. Ahlman et al (2007) performed one of the few DNS wall jet studies, $Re_j = 2000$ and $\beta = 0.1$. The co-flow ensured that large scale vortices were convected downstream in order to remove areas of constant reverse flow in the outer region. Dejoan et al. (2007) compared their data to Eriksson et al. (1998), and the sets of data shared many similar trends, but did not match well for $y^+ > 10$. Dejoan et al. (2007) used a wall jet that was in a state of transition from laminar to turbulent, refer to **Section 1.5**, and it may not be appropriate to compare it to Eriksson et al.'s (1998) study which uses $Re_j = 9$ 600. This demonstrates the need for a high quality, experimental, study of wall jets at low Reynolds numbers.

In this discussion it is evident that computational methods are still in a state of development. The model of Tangemann & Gretler (2001) would appear to be the most efficient method. But doubt would appear from using the algebraic RSM as to whether it was predicting the location of the production of negative turbulent energy correctly, particularly for cases that could not be compared to equivalent experiments. While a DNS solution is not practical yet for fully turbulent wall jets, an LES study is. The model of Dejoan & Leschziner (2005) had difficulty predicting the vertical velocity fluctuations, but if this were improved, an LES study could be the best method to simulate turbulent wall jets.

1.9 Experimental approaches

The two most common methods of measuring wall jet flows are Laser Doppler Velocimetry (LDV) and Cross Hot-wire Anemometry (HWA). There is a concern about HWA being unable to measure reverse flows, which is most prevalent when the turbulence intensity is greater than 30% (Tutu & Chevray (1975)). LDV on the other hand is able to capture reverse flows. A comparison of the two methods is presented below using wall jet data.

Schneider & Goldstein (1994) and Rodman et al. (1986) both performed measurements with LDV and HWA. In each study they used a common wall jet facility to make comparisons of the measurement methods. In both studies LDV was considered more accurate than HWA, and the comparison was made as a validation of using HWA in wall jet flows. It was found by Schneider and Goldstein (1994) that measureable flow reversal began at $\frac{y}{\frac{1}{2}\Delta y_m} = 1.1$. In **Figure 40**, it is evident that the flow reversal caused an underestimation of the Reynolds stress, $\overline{uv}$, when measuring with HWA, seen by how the HWA studies fall off quickly above $\frac{y}{\frac{1}{2}\Delta y_m} \approx 1$.

In **Figure 40**, a range of maximum shear stresses, $\overline{uv}$, can be seen. The variation can be partly explained by the scaling method not being 'universal' with downstream distance, and the profiles being at different downstream locations. Variations can also be explained by how well the measurement method captures the vertical velocity component. Not all of the reviewed studies gave all normal and shear stress profiles, but a comparison between a LDV study, Eriksson et al. (1998), and a HWA study, Abrahamsson et al. (1994), showed variations in the vertical velocities, **Figures 41, 42 & 43**. The normal stress, $\overline{uu}$, can be seen to match well between the two studies, but the normal stress, $\overline{vv}$, does not. Due to the poor vertical velocity measurements the shear stress, $\overline{uv}$, subsequently suffers as can be seen in **Figure 42**.

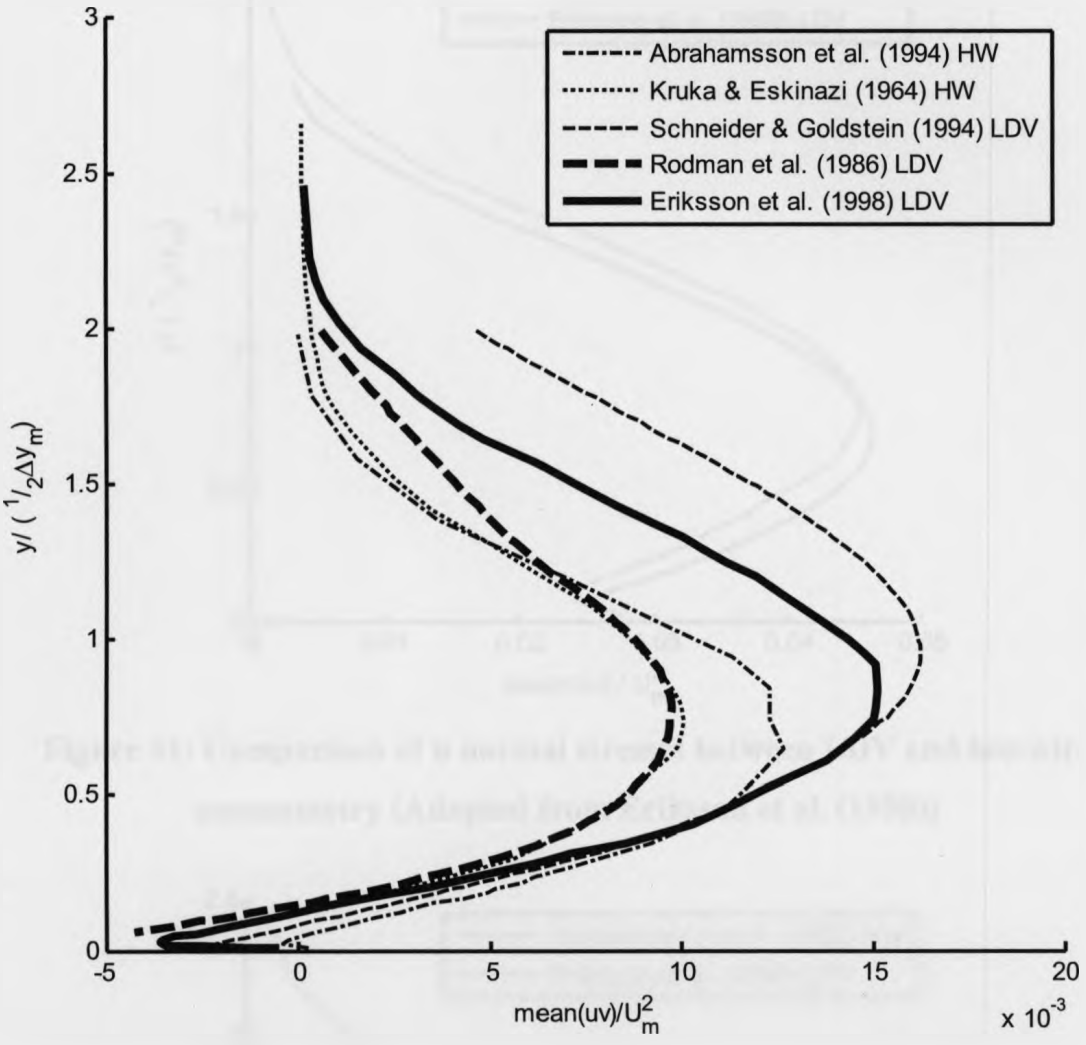

Figure 40: Comparison of uv shear stress profiles between various LDV and hot-wire anemometry studies

In **Figure 44**, velocity profiles are compared for different studies using LDV and HWA. The scaling method in this case is known to work well, although a discrepancy exists in **Figure 44** for the co-flow region of the different wall jet studies, which is caused by the strength of the co-flow present in the experiment, Abrahamsson et al. (1994). The Kruka and Eskinazi (1964) study does not match up well near U_m, due to their data being extensively scaled and errors resulting from rescaling the data to this form. What can be taken from **Figure 44** is that the velocity profile, U, matches well above the half-height regardless of being an LDV or HWA experiment.

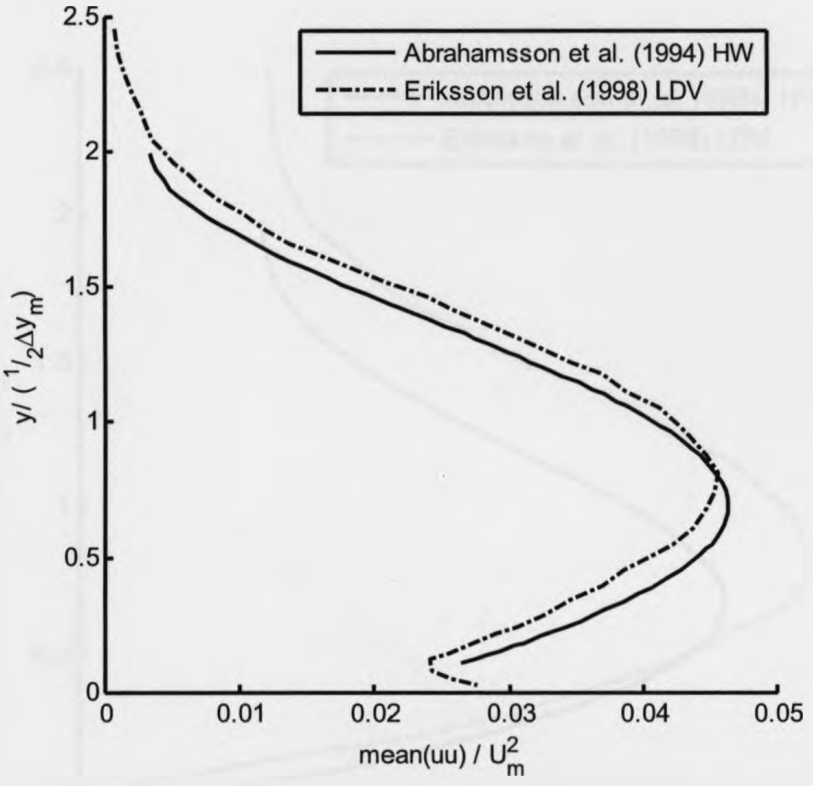

Figure 41: Comparison of u normal stresses between LDV and hot-wire anemometry (Adapted from Eriksson et al. (1998))

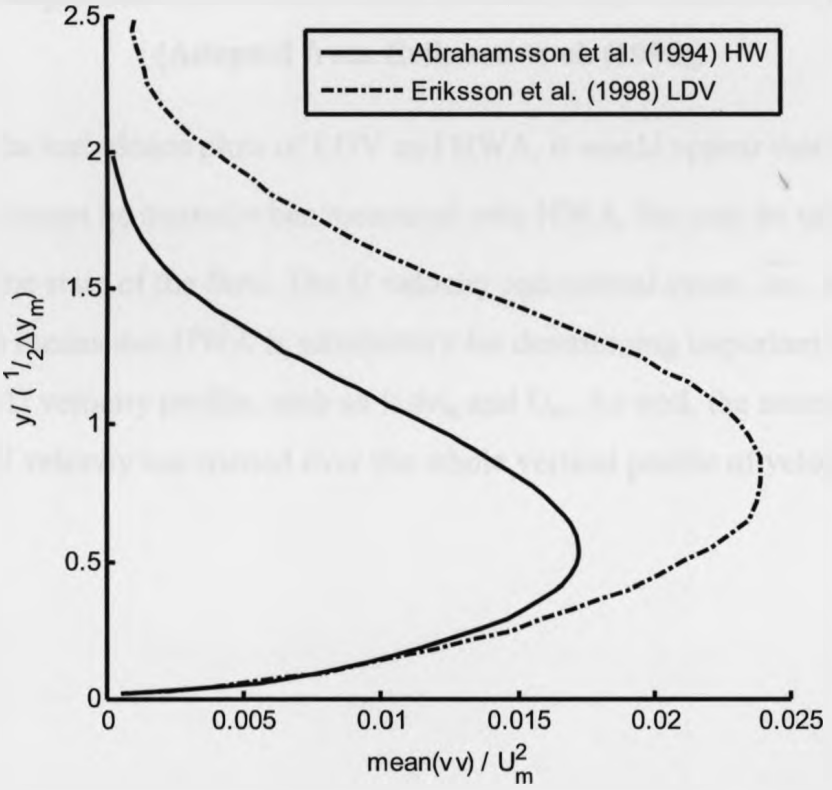

Figure 42: Comparison of v normal stresses between LDV and hot-wire anemometry (Adapted from Eriksson et al. (1998))

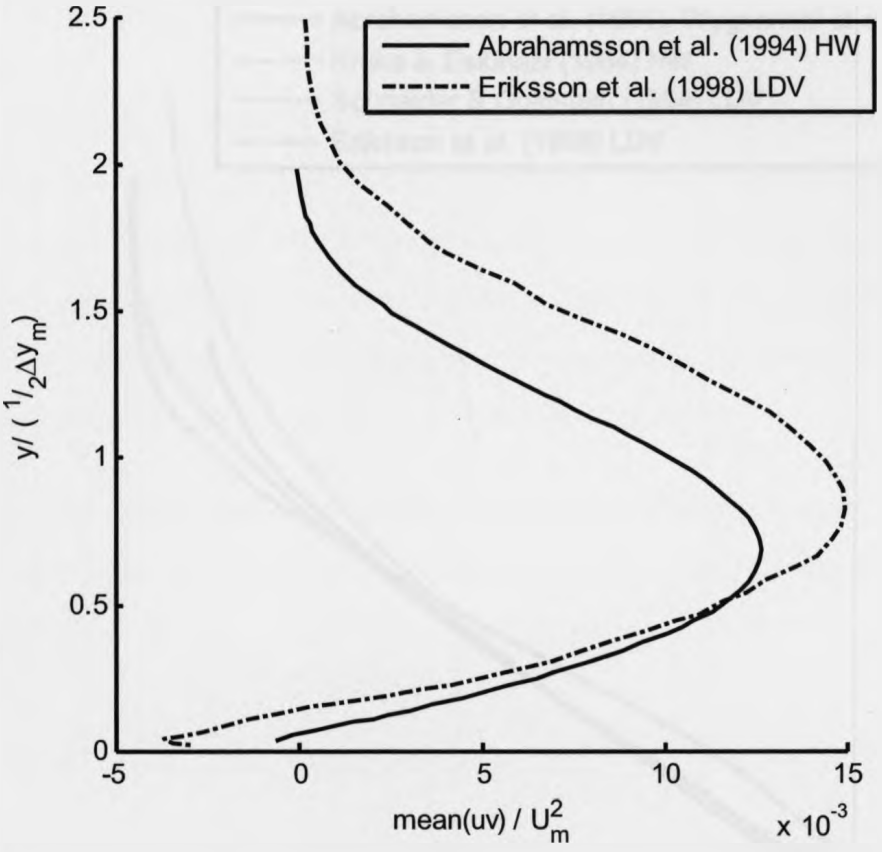

Figure 43: Comparison of uv shear stresses between LDV and hot-wire anemometry (Adapted from Eriksson et al. (1998))

In reviewing the turbulence plots of LDV and HWA, it would appear that the magnitude of $\overline{vv}$ and $\overline{uv}$ cannot be trusted when measured with HWA, but may be used as an indication of the state of the flow. The U velocity and normal stress, $\overline{uu}$, are trustworthy however. This means that HWA is satisfactory for determining important comparison metrics in the U velocity profile, such as $½\Delta y_M$ and U_m. As well, the momentum and mass flux of U velocity can trusted over the whole vertical profile of velocity.

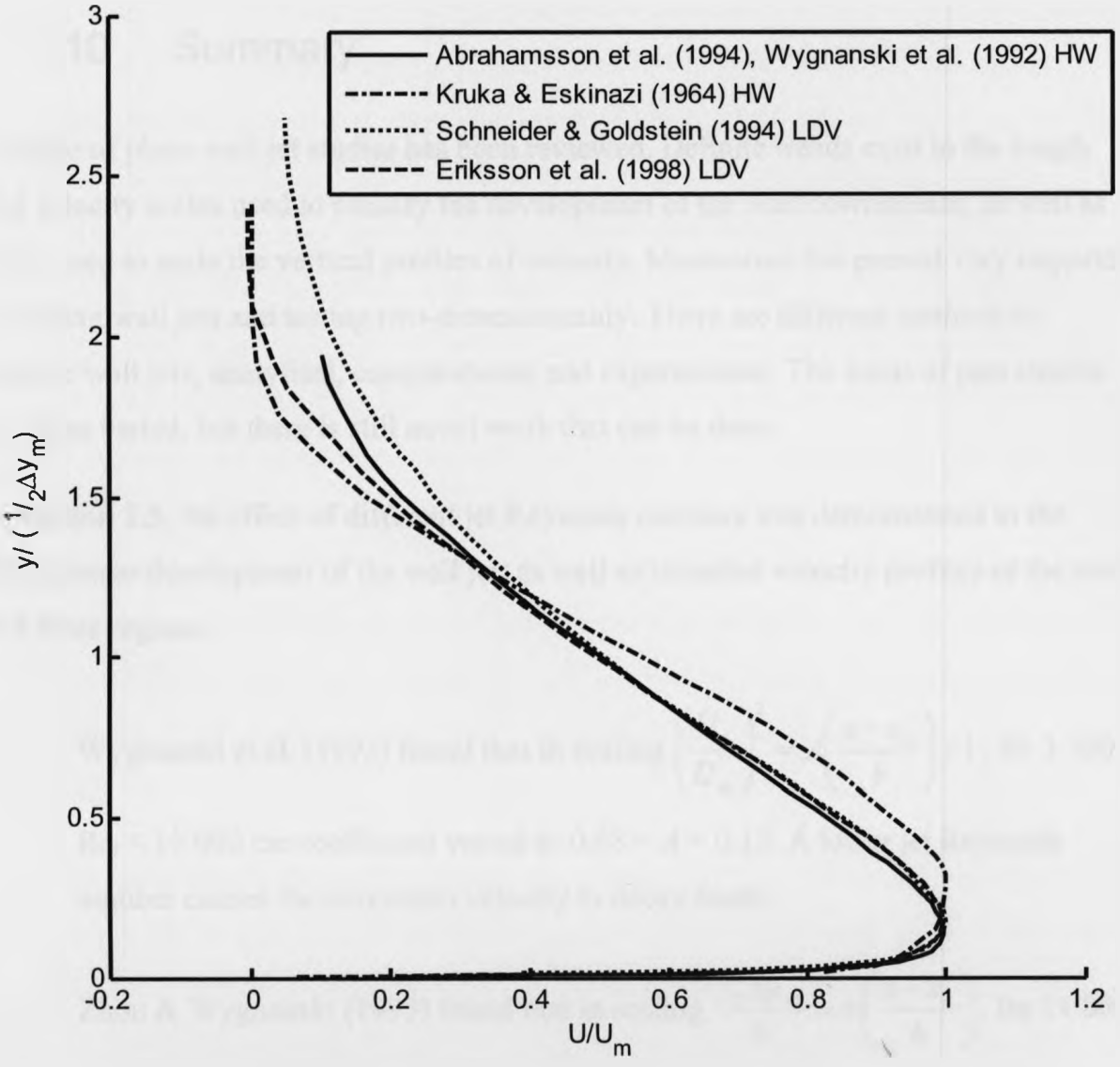

Figure 44: Comparison of U velocity profiles between various LDV and hot-wire anemometry studies

1.10 Summary

A range of plane wall jet studies has been reviewed. Definite trends exist in the length and velocity scales used to classify the development of the wall downstream, as well as those used to scale the vertical profiles of velocity. Momentum has proved very important in scaling wall jets and testing two-dimensionality. There are different methods to explore wall jets; analytical, computational and experimental. The focus of past studies has been varied, but there is still novel work that can be done.

In **Section 1.5**, the effect of different jet Reynolds numbers was demonstrated in the downstream development of the wall jet, as well as in scaled velocity profiles of the outer and inner regions.

- Wygnanski et al. (1992) found that in scaling $\left(\frac{U_j}{U_m}\right)^2 = A\left(\frac{x-x_o}{b}\right)+1$, for 3 700 < Re_j < 19 000 the coefficient varied as $0.08 < A < 0.15$. A lower jet Reynolds number causes the maximum velocity to decay faster.

- Zhou & Wygnanski (1993) found that in scaling $\frac{\frac{1}{2}\Delta y_M}{b} = m\left(\frac{x-x_o}{b}\right)$, for 11 000 < Re_j < 18 000, the slope (m) varies as $0.058 < m < 0.068$. A lower jet Reynolds number causes the flow to spread faster.

- Zhou & Wygnanski (1993) found that in scaling $\frac{\frac{1}{2}\Delta y_M}{b} = m\left(\frac{x-x_o}{b}\right)$, for Re_j = 11 000, $0.085 < \beta < 0.59$, the slope (m) varies as $0.068 > m > 0.019$. A higher velocity ratio causes the flow to spread faster.

In order to remove the jet Reynolds number dependence, jet momentum was used to scale the downstream development of the wall jet. In **Section 1.5**, Wygnanski et al.'s (1992) work was discussed in which the jet Reynolds number was held constant and the jet momentum was changed. A more thorough study comparing jet Reynolds number and jet momentum would be valuable.

In **Section 1.7**, lip thickness was shown to increase the values of normal and shear stress by 20% at $x = 10b$. The conclusions from the studies on lip thickness do not appear definitive, due to a lack of test cases (Kacker & Whitelaw (1971)) and limited resources (Gartshore & Hawaleshka (1964)). Very likely the lip thickness will prove to have minimal impact on the wall jet for $x > 30b$, as even with forcing initiated at the jet exit, Katz et al. (1992), the differences in downstream development were subtle. Possibly a co-flow is required in order to observe effects from lip thickness, as differences were very apparent with Kacker & Whitelaw's (1971) work, which used a velocity ratio of 0.43. The lip thickness is a geometric length that should be tested, as different lip thicknesses are used in each different study. Disparity from the lip thickness could arise in comparing studies, but unknowingly be attributed to other parameters. Likely with increasing the t/b ratio the rate the half-height grows will increase, similar to Katz. et al.'s (1992) forcing case. The effect on maximum velocity was not so definite in Katz et al. case, but Kacker and Whitelaw (1971) found a decrease in maximum velocity with increasing lip thickness.

Another important geometric length that has not been studied is the overall height of the downstream region that the wall jet develops in. The studies reviewed in **Section 1.8** use $Y < 20b$ in the computational studies, whereas most experimental studies use $Y > 40b$. Whether this height restricts the growth of the wall jet downstream is unknown and should be tested. This will lead to more efficiently sized computational domains for wall jets. Knowing how the Y/b ratio effects the development of the wall jet may lead to better choices in jet height, b, for confined regions such as in Mongia et al.'s (2008) work for notebook computers, where $Y = 2.25b$. The height Y also determines the co-flow height above the jet lip. Different co-flow heights dictate, for a constant velocity, the momentum in the co-flow and this is another parameter that has not been previously tested. By reducing the overall height that the wall jet has to develop in will likely reduce the growth rate of the half-height and cause the wall jet flow to turn into channel flow closer to the jet exit. As the wall jet is expanding less the maximum velocity of the wall jet will likely increase with a lower Y/b ratio due to momentum being conserved.

In order to investigate the ratios, *t/b* and *Y/b*, there are different ways to approach them. In **Section 1.1**, it was discussed how a solution had been found for the laminar wall jet and that one had still not been found for the turbulent case. As a solution has yet to be found for the turbulent case, it would not be a realistic method to discover variations due to *t* and *Y*.

Several promising CFD studies were reviewed in **Section 1.8**. The simpler methods had difficulty in replicating wall jets, whereas the more accurate LES study of Dejoan & Leschziner (2005) was computationally expensive for a small domain, particularly since several different cases would have to be simulated for the various *t* and *Y*. As the effects of *t* and *Y* are unknown, it would be better to do an experimental study in order to remove doubt from a computational study.

In **Section 1.9**, LDV and HWA were compared. There are clear advantages in using LDV as reverse flows are captured. However the LDV probe would require a large traverse in order to capture the entire vertical profile of the flow and seeding would be required as air would be used as the fluid medium. The main disadvantage to using HWA in wall jet flows is capturing the vertical fluctuations of velocity, although the streamwise fluctuations are captured well, allowing the principal velocity and length scales to be captured. Due to ease of use in HWA, it will be more efficient than LDV in taking the number of measurements involved in the several case studies for various *t* and *Y*.

In past studies, the inlet conditions were poorly stated. This experimental study will have well defined conditions in order for comparison with possible future computational studies. Many different scaling methods have been discussed and more are listed in **Appendix B** and using the different methods the variation due to *t* and *Y* will hopefully be distinguished.

The next section of this manuscript will discuss how lip thickness and tunnel height were varied in a wall jet wind tunnel and how the flow was measured through cross hot-wire anemometry.

2 Experimental method

In order to take measurements, a wind tunnel facility built by Lin & Savory (2006) was used. The lip thickness and overall height of the tunnel were deemed the important parameters of wall jet flow to test and modifications to the tunnel were required before experimental measurements could commence. Discussed in this section will be the novel inlet cone that was built for the tunnel, which allowed for variations in tunnel height, and the validation of the tunnel for two-dimensionality. The measurement apparatus used will be discussed, as well as validation of the measurement samples.

2.1 Existing facility

The experimental work will be performed in a wind tunnel built specifically to produce plane wall jets. The tunnel as pictured in **Figure 45** was designed and built by Lin & Savory (2006). The jet flow originates under the tunnel and travels through a 180° turn and a contraction before exiting the jet. A New York Blower Compact G1106 fan produces the flow with a 1.5 horsepower motor; additional details can be found in Lin & Savory (2006). The co-flow region was found to be non-uniform, as discussed in the following **Section 2.3**. As the facility required modifications in order to investigate the parameters discussed in **Section 1.10**, the flow quality of the co-flow was also addressed.

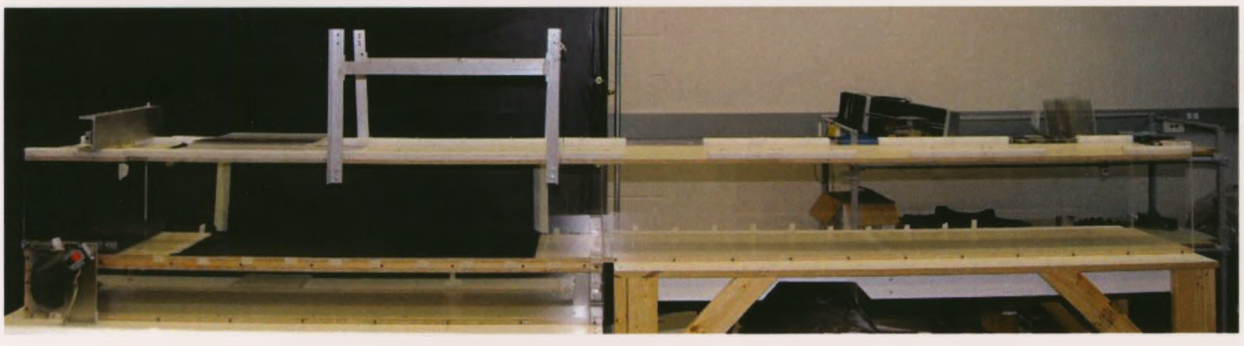

Figure 45: Wall jet facility Lin & Savory (2006)

In **Figure 46** the size of the jet outlet and lip area can be seen, as well as the coordinate axes that will be used.

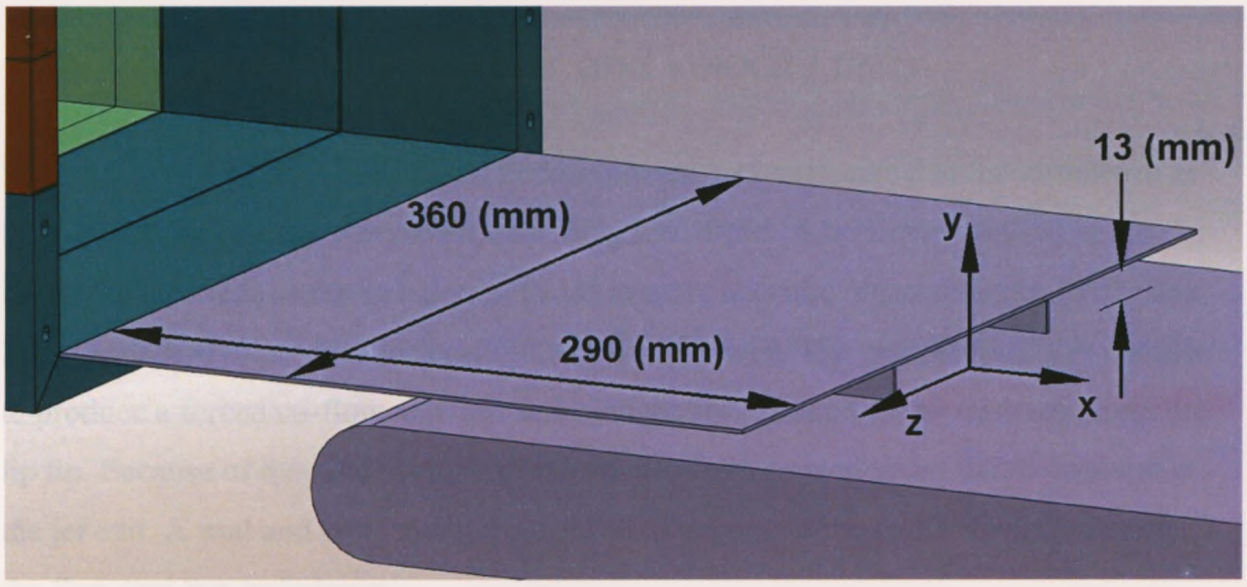

Figure 46: Geometry of jet outlet and coordinate axes, image was captured after modification to lip thickness (*t*)

2.2 Jet Reynolds number and velocity ratio

Wygnanski & Fiedler (1969) found in their plane jet experiments that the turbulence at the edge of the jet flow was reduced by using a co-flow. A co-flow was used in the current to also reduce the turbulence, to aid in more accurate measurements. In **Section 2.3**, the method to produce the co-flow will be discussed. The current facility is not able to produce a forced co-flow and thus relies on the jet entraining flow upstream from the lip tip. Because of this, the strength of the co-flow was dependent on the momentum at the jet exit. A trial and error method was used to maximize the co-flow while ensuring the flow had low turbulence.

The facility uses an adjustable speed drive to control the blower motor. The controller is a 3 phase 230 V Toshiba VFS9-2015PM-WN. The controller is operated by specifying a frequency from 0 – 60 (Hz). The controller will operate above 60 (Hz) but this is not recommended, Toshiba (2000). At 60 (Hz) the facility is capable of producing approximately $U_j = 47$ (m/s). The facility was chosen to be operated at 40 (m/s) as this was able to produce a co-flow of approximately 4 (m/s), $\beta = 0.1$ and $Re_j = 30\ 700$. By not operating at 47 (m/s) the hot-wire probes could calibrated, within the jet flow, above the operating velocity. This ensured that the velocity span within which the hot-wire probes were calibrated encompassed all possible velocities that the probe could be subjected to.

The jet Reynolds number was higher than most studies tabulated in **Appendix A**. However comparisons with other studies was still possible as Narasimha's method of scaling, refer to **Section 1.5**, was not dependent on jet Reynolds number for $Re_j > 5\ 000$.

2.3 Flow conditioning

Before the current study could be carried out the uniformity of the co-flow had to be improved. Patel (1978) found the mixing of free streams was affected by the free stream turbulence, so an effort was made to reduce the turbulence in the co-flow. In order to do this an inlet cone was designed and built for the existing facility. The velocity at the outlet of the jet was also measured and checked for uniformity and whether it was suitable to use in calibrating hot-wire probes.

The vertical profiles of *U* and u', above the jet lip, are plotted in **Figures 47 & 48**. A large boundary layer exists in both the upper and lower portions of the velocity profile. As there is no smooth contraction at the co-flow inlet the flow likely impacts the edges of the inlet, creating large amounts of turbulence, as in **Figure 48**. The hot-wire probe would have difficulty resolving the U velocity in the turbulent region and the result is the large velocity gradients in **Figure 47**.

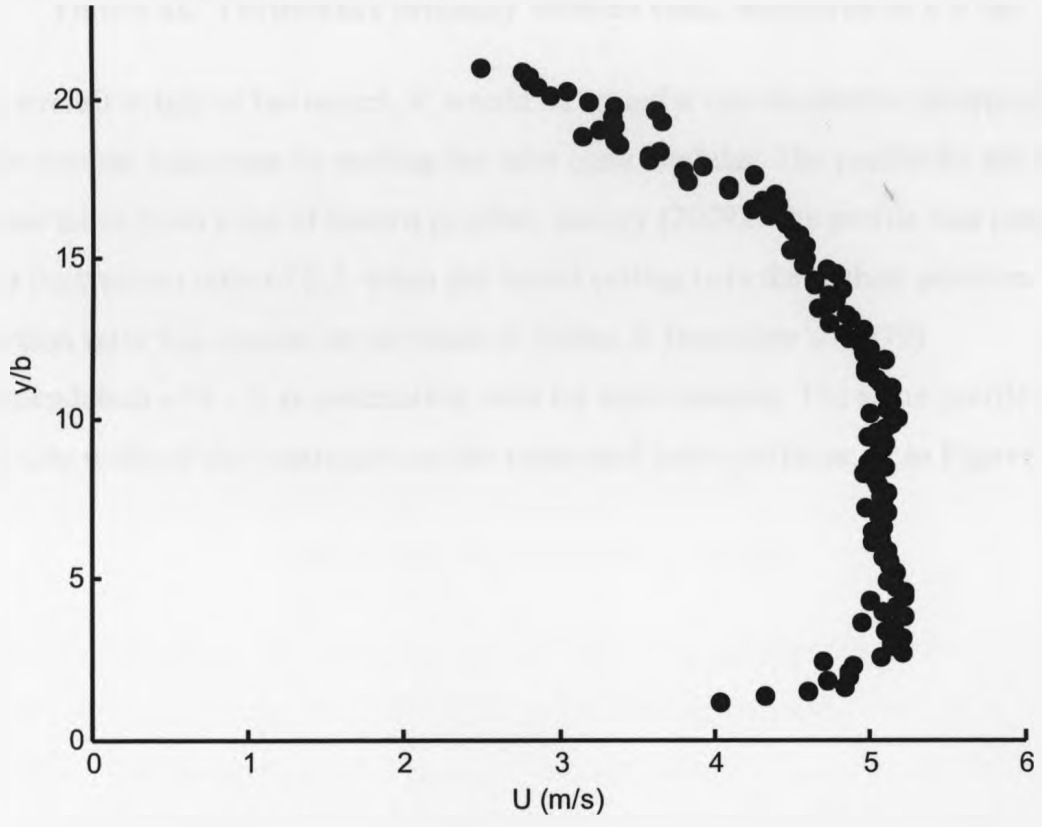

Figure 47: U co-flow velocity without cone, measured at x = -4b

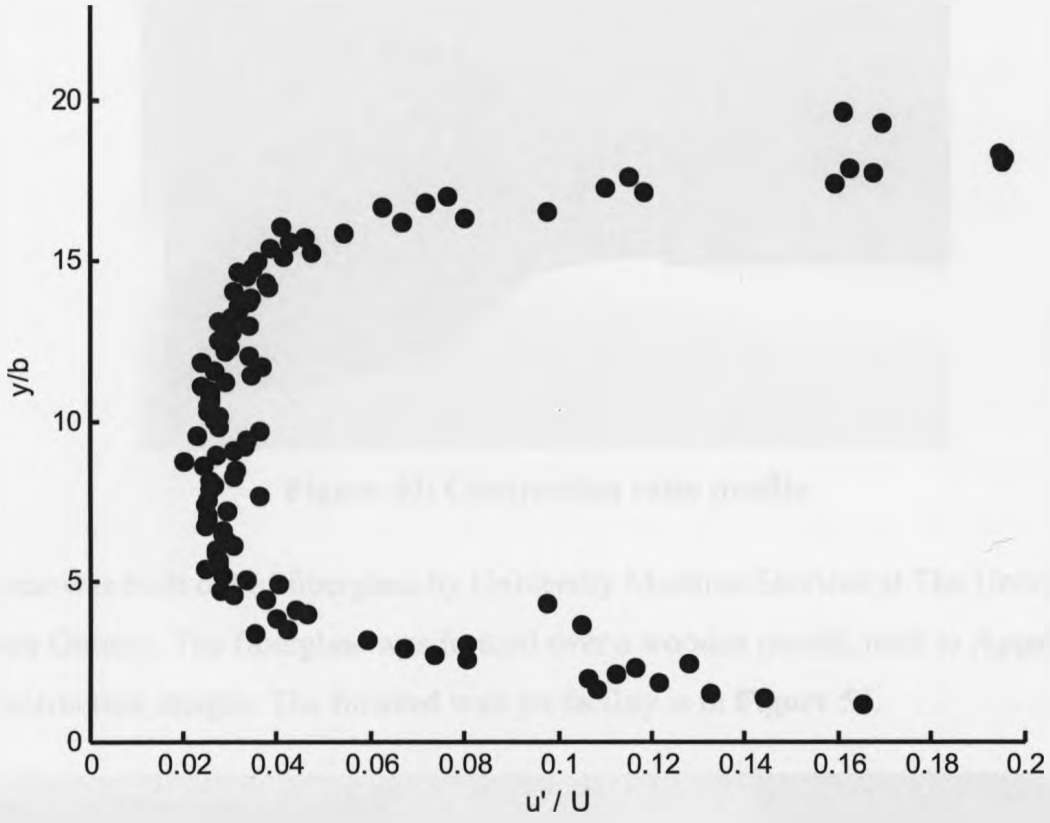

Figure 48: Turbulence intensity without cone, measured at x = -4b

As the overall height of the tunnel, *Y*, would be varied it was decided to incorporate this concept into the inlet cone by making the inlet cone modular. The profile for the inlet cone was taken from a list of known profiles, Savory (2009). The profile was chosen to allow a contraction ratio of 8.2, when the tunnel ceiling is in the highest position. The contraction ratio was chosen on the basis of Metha & Bradshaw's (1979) recommendation of 6 – 9 as contraction ratio for small tunnels. The same profile is used for the side walls of the contraction as the upper and lower surfaces, as in **Figure 49**.

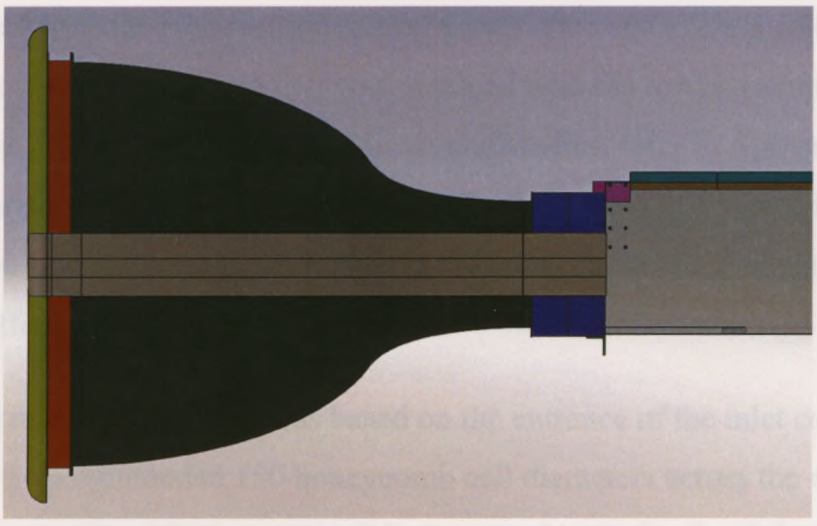

Figure 49: Contraction ratio profile

The cone was built out of fiberglass by University Machine Services at The University of Western Ontario. The fiberglass was formed over a wooden mould; refer to **Appendix E** for construction images. The finished wall jet facility is in **Figure 50**.

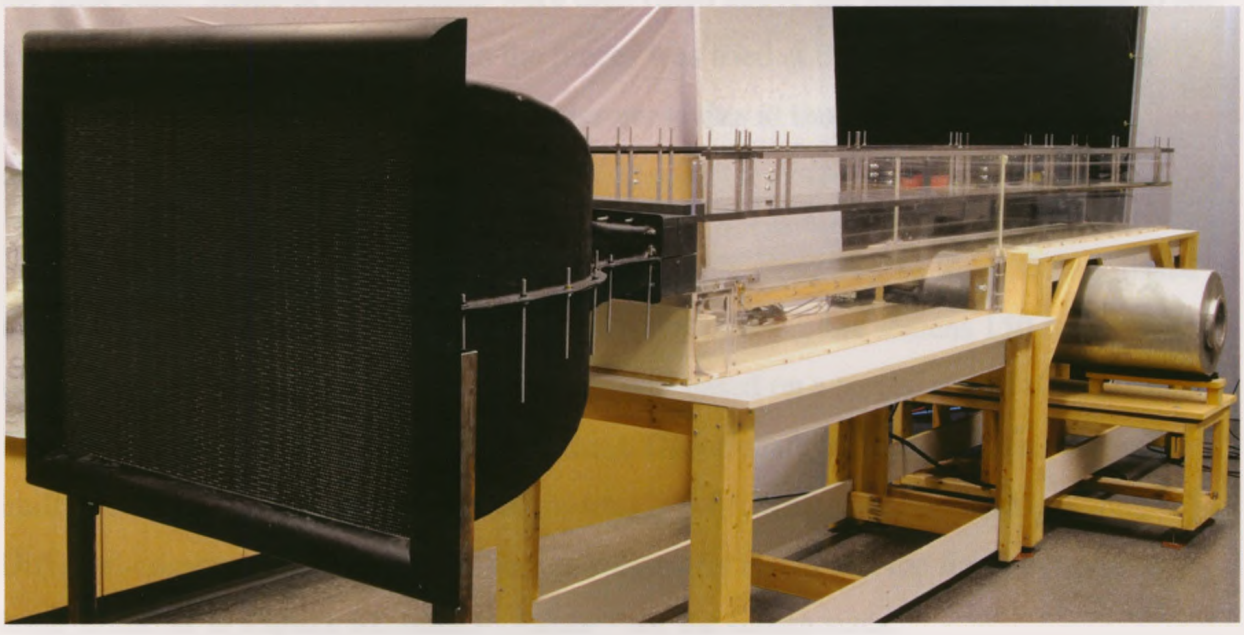

Figure 50: Finished wall jet facility

Different combinations of screens and aluminum honeycomb were used in conjunction with the inlet cone in order to minimize the turbulence at the co-flow entrance. The honeycomb was installed at the entrance to the inlet cone and a small settling chamber was incorporated at the exit of the inlet cone. The settling chamber used three screens. As the flow was not forced through the inlet cone but entrained, a minimal number of

screens were used to reduce the restriction of the inlet cone and allow a co-flow. The maximum co-flow to velocity ratio that was obtained with the lowest turbulence intensity was $\beta = 0.1$. This β was close to that used in several studies, refer to **Appendix A**, allowing comparisons with other investigations. The low value of β would mean the wall jet would behave similar to a wall jet without a co-flow. The co-flow might also emphasize lip effects downstream.

The size of the honeycomb was based on the entrance of the inlet cone. Mehta & Bradshaw (1979) recommended 150 honeycomb cell diameters across the width it is used. As well the length of the honeycomb is suggested to be 6 – 8 cell diameters. This resulted in honeycomb 1 ½" in length and ¼" in diameter. A 48" by 48" sheet of aluminium honeycomb was obtained from Plascore (part number PCGA-XR1 3003) and the required honeycomb was cut out of that. As the entrance of the inlet cone changes size with varying Y, the main piece of honeycomb was cut shorter than that required for the inlet cone. Strips of honeycomb were then fitted above the main piece in order to fill the inlet entrance. The join between the pieces was tried at the top and bottom of the entrance in order to test if any discrepancies arose due to the join. There were no discrepancies noted in vertical profiles of U or u' in the co-flow due to the join.

In the settling chamber the three screens had a separation each of 75 mm, based on Hancock & Johnson (1997) recommendation of spacing the screens 150 screen wire diameters, or 50 mesh diameters, apart. This was based on a screen with a wire diameter of 0.5 (mm) and mesh diameter of 1.64 (mm). Unfortunately, once the inlet cone was built and tested the u' was found to be uniformly 0.05, which was deemed too high. Different combinations of screens were subsequently tested and the final set up used honeycomb as in **Figure 51**, refer to **Table 1** for the screen sizes.

Table 1: Honeycomb and mesh specifications

	Wire/Wall thickness (mm)	Opening widths (mm)
Honeycomb	0.1	6.35
Mesh 1	0.5	1.64
Mesh 2	0.16	1.48

The final vertical profiles of U and turbulence intensity are in **Figures 52 & 53**. Spanwise measurements were taken in the co-flow in order to test the two-dimensionality. The velocity spread was $3.637 \leq U \leq 4.1687$ (m/s) and the spread of turbulence intensity was $0.0162 \leq u' \leq 0.0221$, which was a vast improvement over **Figures 47 & 48**. A lower overall turbulence would have been desirable but the co-flow dropped to $\beta \approx 0.05$ with very fine screens and this ratio was deemed too low, based on the available data for comparison. Possibly in future use of the wind tunnel a forced flow with additional screens in the settling chamber could be used.

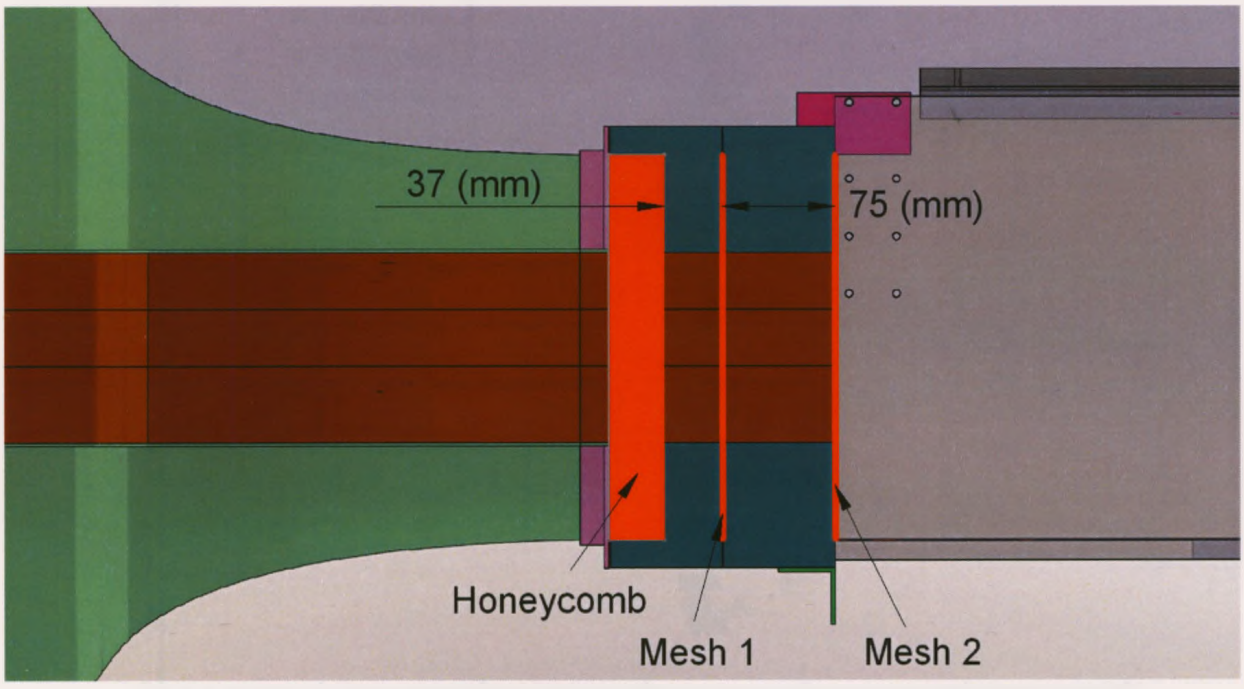

Figure 51: Close-up of settling chamber, red areas denote honeycomb and screen locations within the settling chamber

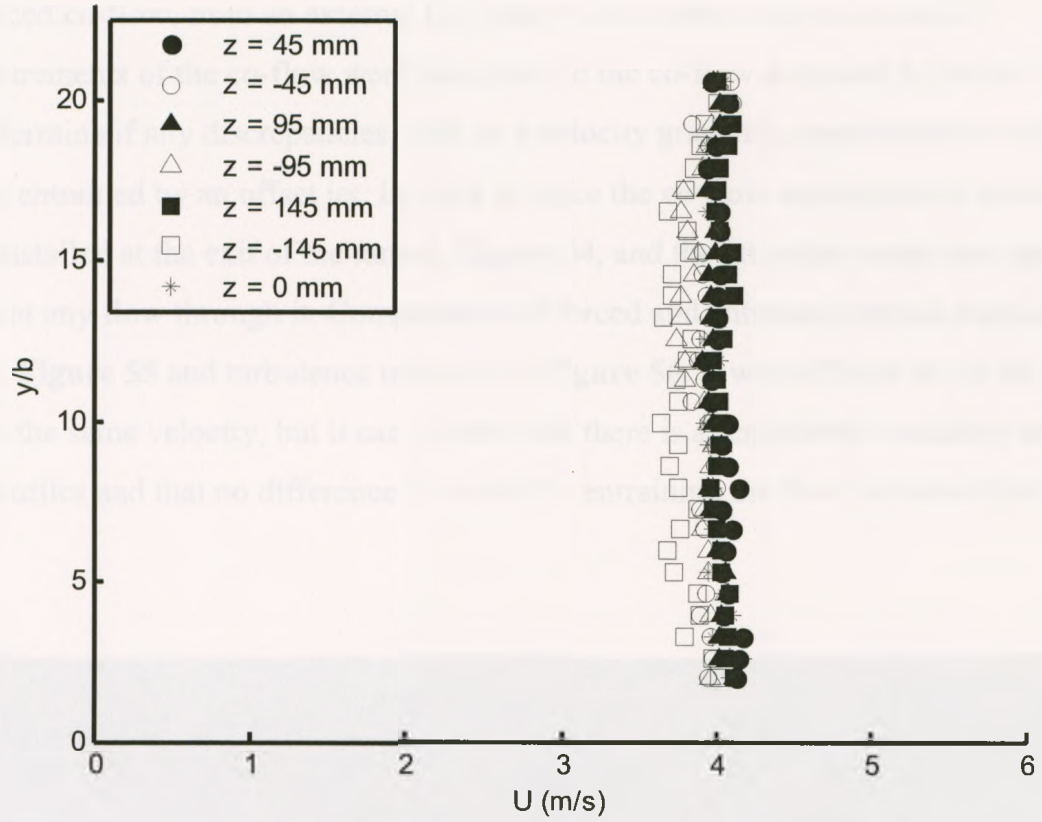

Figure 52: U velocity in co-flow with flow conditioning

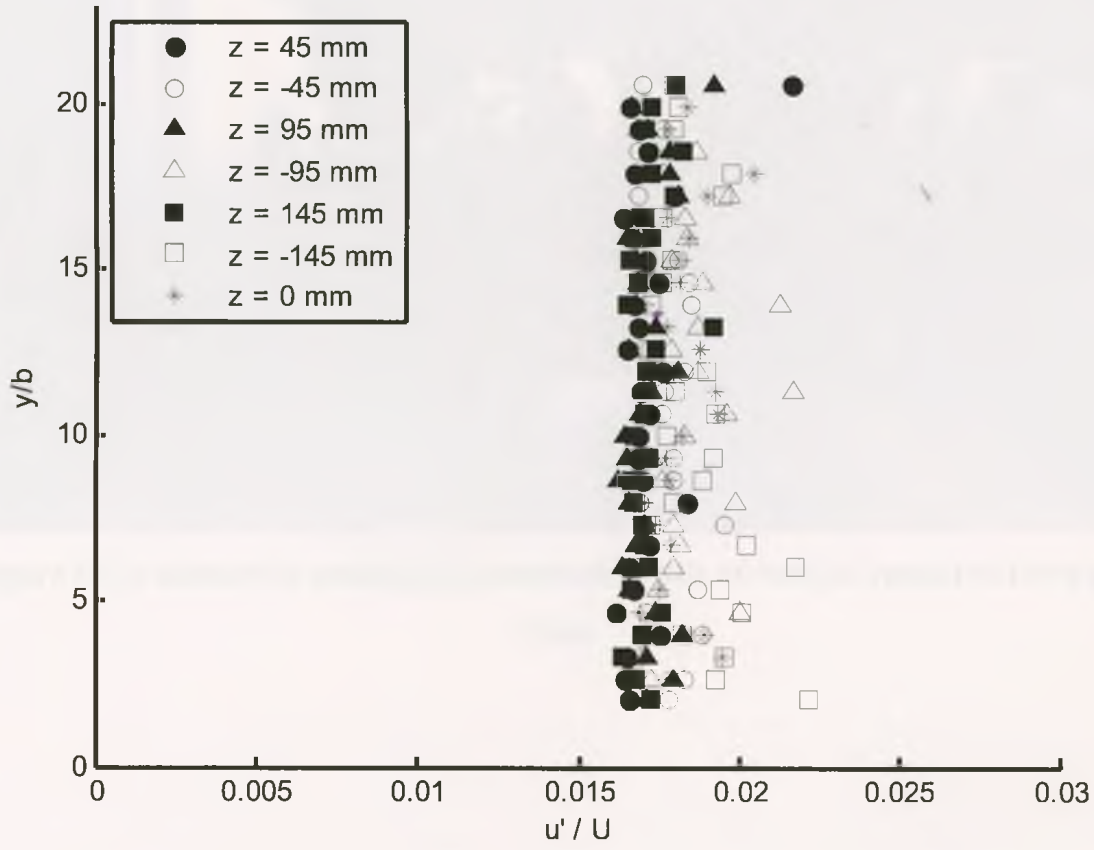

Figure 53: Turbulence intensity in co-flow with flow conditioning

A forced co-flow, from an external fan, was trialed in the wind tunnel and U measurements of the co-flow were compared to the co-flow entrained by the jet. This was to determine if any discrepancies, such as a velocity gradient, arose from the co-flow being entrained by an offset jet. In order to force the co-flow an automotive cooling fan was installed at the exit of the tunnel, **Figure 54**, and the jet in the tunnel was taped off to prevent any flow through it. Comparisons of forced and entrained vertical profiles of U are in **Figure 55** and turbulence intensity in **Figure 56**. It was difficult to get the two flows the same velocity, but it can be seen that there is a remarkable similarity between the profiles and that no difference is caused by entraining the flow with an offset jet.

Figure 54: Automotive cooling fan mounted at exit of wall jet tunnel to force a co-flow

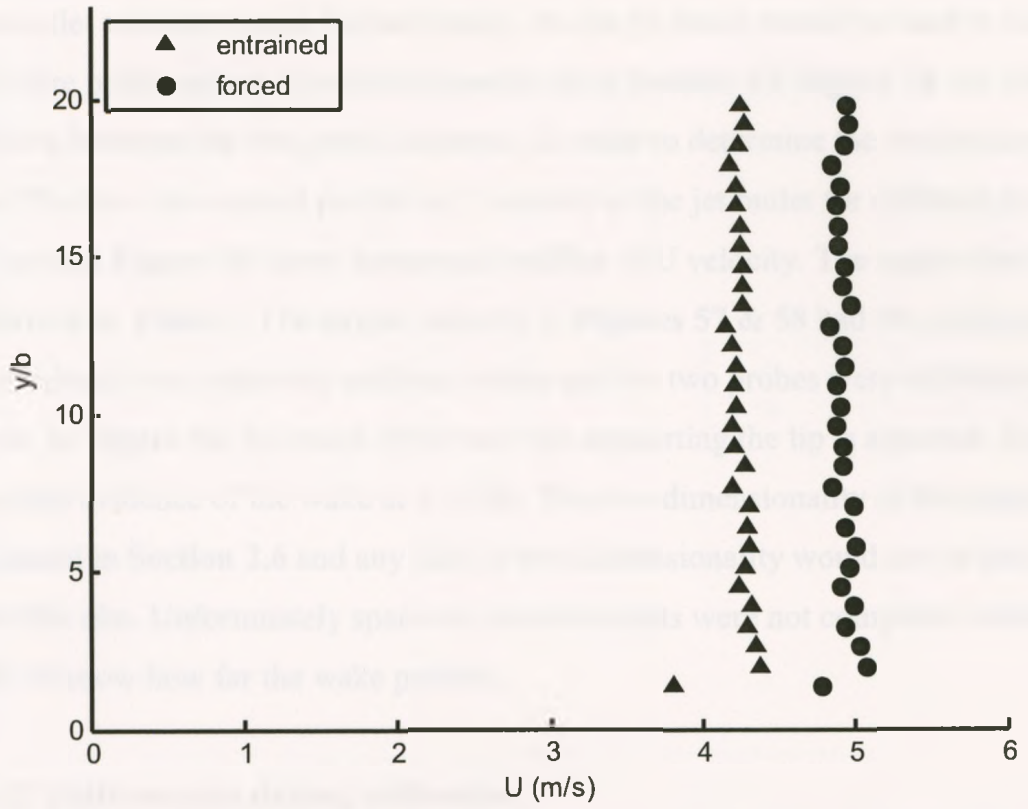

Figure 55: Comparison of U velocity in co-flow for entrained and forced co-flows

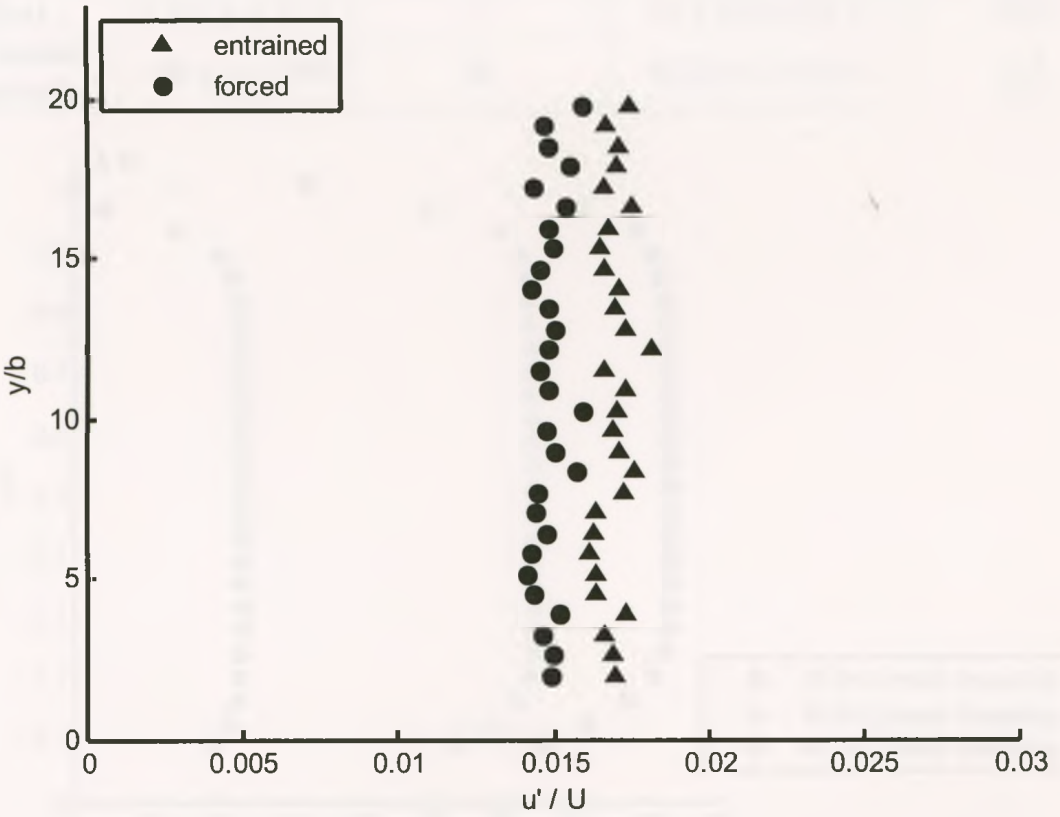

Figure 56: Comparison of turbulence intensity in co-flow for entrained and forced co-flows

The jet outlet was also tested for uniformity. As the jet outlet would be used to calibrate the hot-wire probe against a pitot-static probe, as in **Section 2.7 Figure 74**, the flow must be uniform between the two probe locations. In order to determine the vertical location, **Figure 57** shows the vertical profile of *U* velocity at the jet outlet for different jet velocities and **Figure 58** shows horizontal profiles of U velocity. The region that the flow is uniform is in **Table 2**. The largest velocity in **Figures 57 & 58** had the smallest area that the velocity was relatively uniform within and the two probes were calibrated within that area. In **Figure 58**, the wake of the two ribs supporting the lip is apparent. Lin (2006) did not find evidence of the wake at x = 50b. The two-dimensionality of the tunnel will be discussed in **Section 2.6** and any lack of two-dimensionality would not be due to the wake of the ribs. Unfortunately spanwise measurements were not completed within 10b < x < 50b to know how far the wake persists.

Table 2: Uniform area during calibration

	Distance (mm)	Distance range (mm)	Spread in velocity (m/s)	Velocity range (m/s)
Vertical	$4.1 \leq y \leq 11.1$	7	$41.1 \leq U \leq 41.7$	0.6
Horizontal (centered)	$-40 \leq z \leq +40$	81	$42.0 \leq U \leq 41.6$	0.6

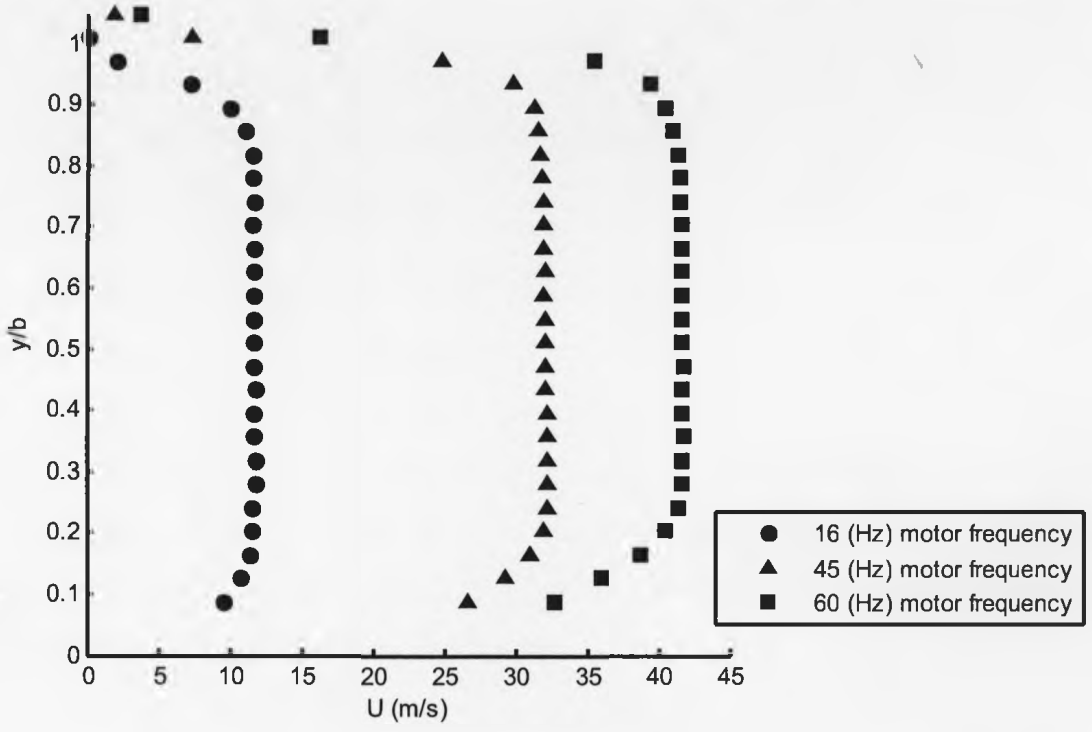

Figure 57: Jet outlet U velocity at x = 0b

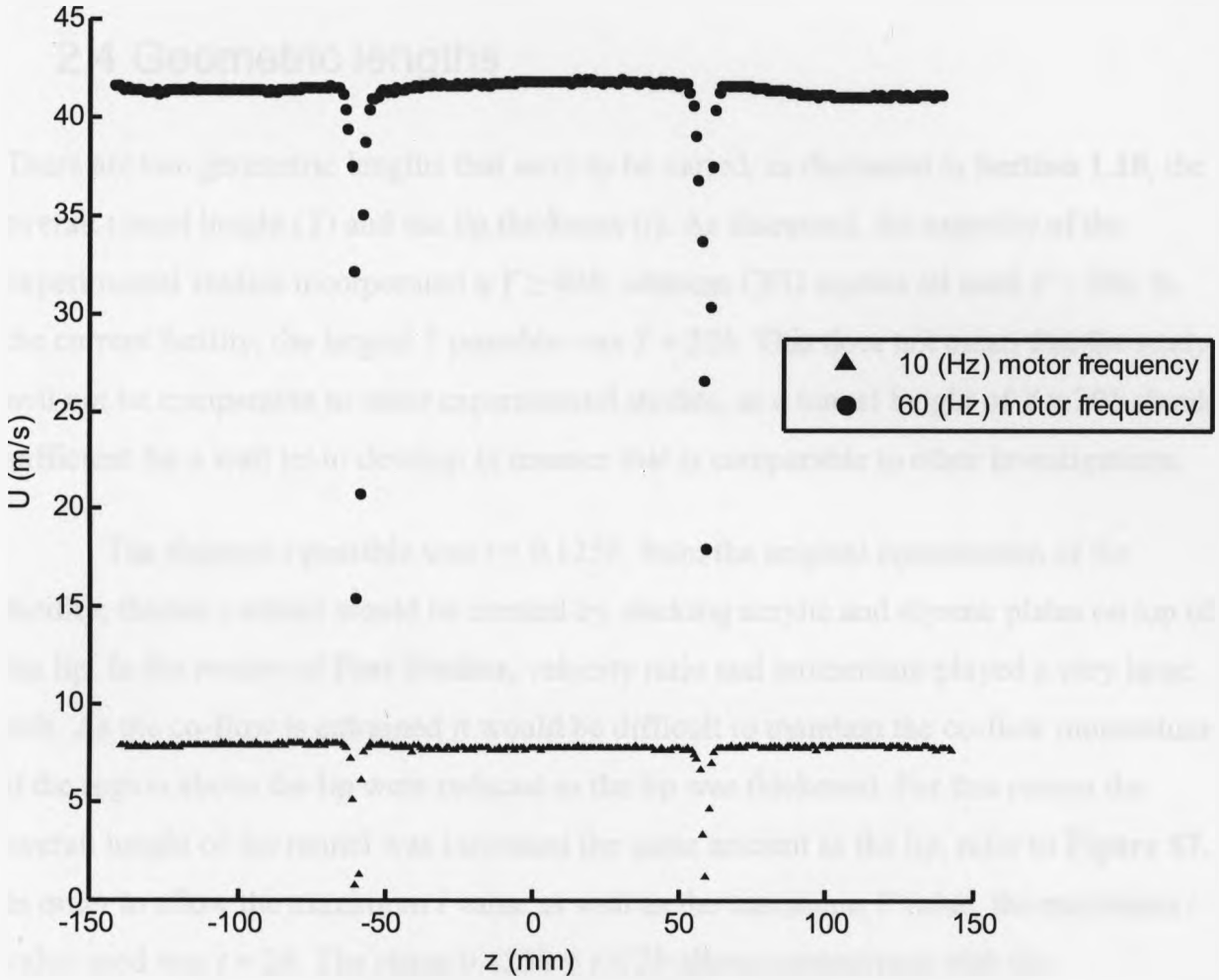

Figure 58: Jet outlet U velocity at x = 0b

2.4 Geometric lengths

There are two geometric lengths that were to be varied, as discussed in **Section 1.10**, the overall tunnel height (Y) and the lip thickness (t). As discussed, the majority of the experimental studies incorporated a $Y \geq 40b$, whereas CFD studies all used $Y < 20b$. In the current facility, the largest Y possible was $Y = 22b$. This does not mean that the study will not be comparable to other experimental studies, as a tunnel height of $Y \approx 20b$ should sufficient for a wall jet to develop in manner that is comparable to other investigations.

The thinnest t possible was $t = 0.125b$, from the original construction of the facility; thicker t values would be created by stacking acrylic and styrene plates on top of the lip. In the review of **Past Studies**, velocity ratio and momentum played a very large role. As the co-flow is entrained it would be difficult to maintain the co-flow momentum if the region above the lip were reduced as the lip was thickened. For this reason the overall height of the tunnel was increased the same amount as the lip, refer to **Figure 57**. In order to allow the maximum t value as well as the maximum Y value, the maximum t value used was $t = 2b$. The range $0.125b \leq t \leq 2b$ allows comparison with the experimental studies of Kacker and Whitelaw (1971) and Gartshore & Hawaleshka (1964), who both investigated lip thickness effects. Refer to **Table 3** for specific values. It is possible that changing the height of the tunnel with the lip will create effects not just from the lip. But the investigation of overall tunnel height may help to differentiate between lip and tunnel height effects.

The variation of the tunnel height will be $10b \leq Y - (t + b) \leq 20$b, refer to **Table 3** for specific values. The co-flow height of $Y - (t + b)$ will be referred to instead as simply B. This range will encompass Dejoan & Leschziner's (2005) CFD model height of $B = 9b$ and Ahlman et al.'s (2007) CFD model height of $B = 17b$. The maximum value of $B = 20b$ allows the lip to be thickened, up to $t = 2b$, for an overall height of $Y = 22b$. Each B value was tested with the range of $0.125b \leq t \leq 2b$. This parametric approach resulted in a total of 16 different cases, refer to **Figure 59**.

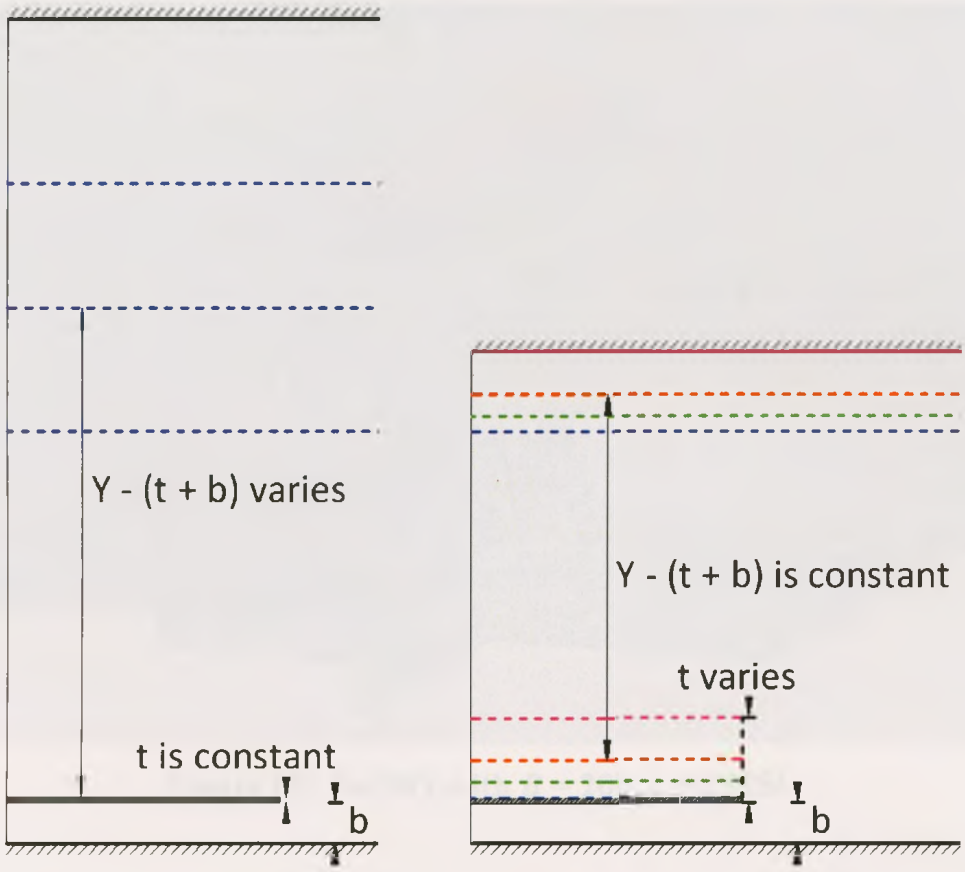

Figure 59: (Left) Tunnel height variation, (Right) Lip thickness variation

- Table 3

Table 3: Geometric lengths

t	*B*
0.125b	10b
0.5b	13b
1b	16b
2b	20b

In **Figures 60 – 62**, the facility (modeled in Solidworks) can be seen for different combinations of geometric lengths, note the lower boundary of the facility is not shown in the figures for clarity. In order for the ceiling of the tunnel to vary, spacers are used with threaded rods, as in **Figure 63**. The ceiling simply rests on top of the side walls of the tunnel.

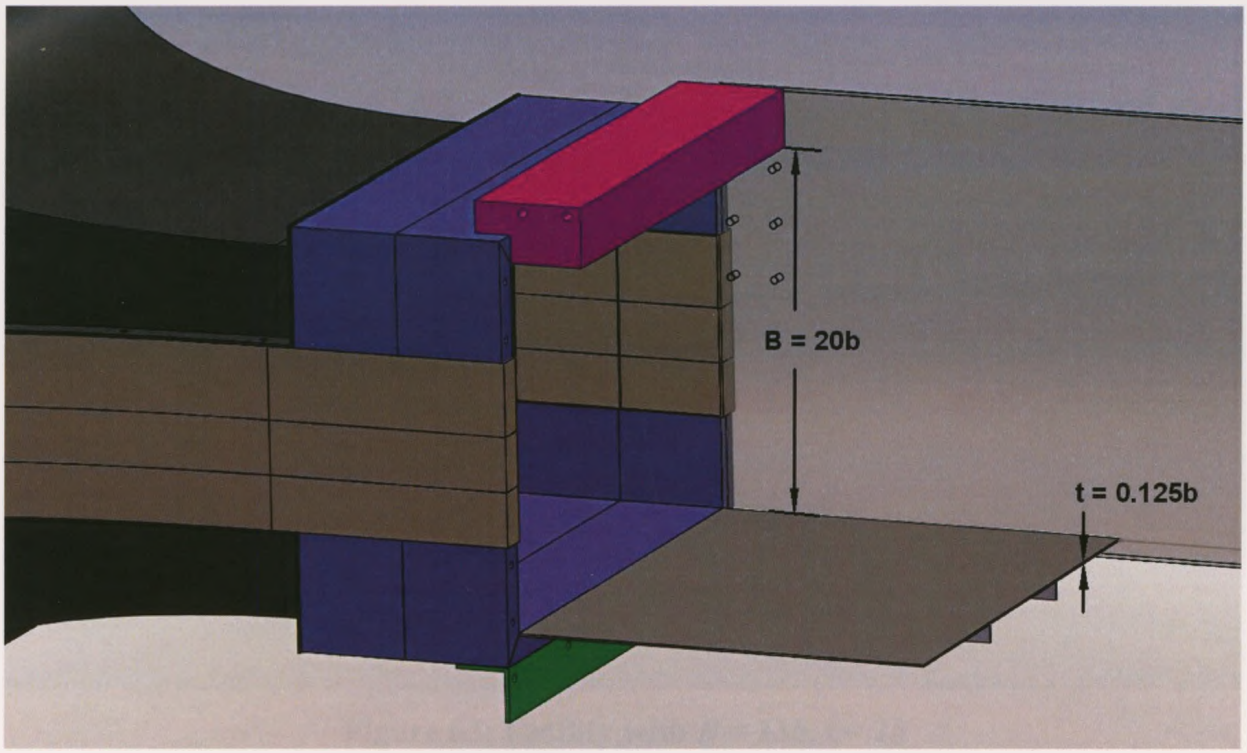

Figure 60: Facility with B = 20b, t = 0.125b

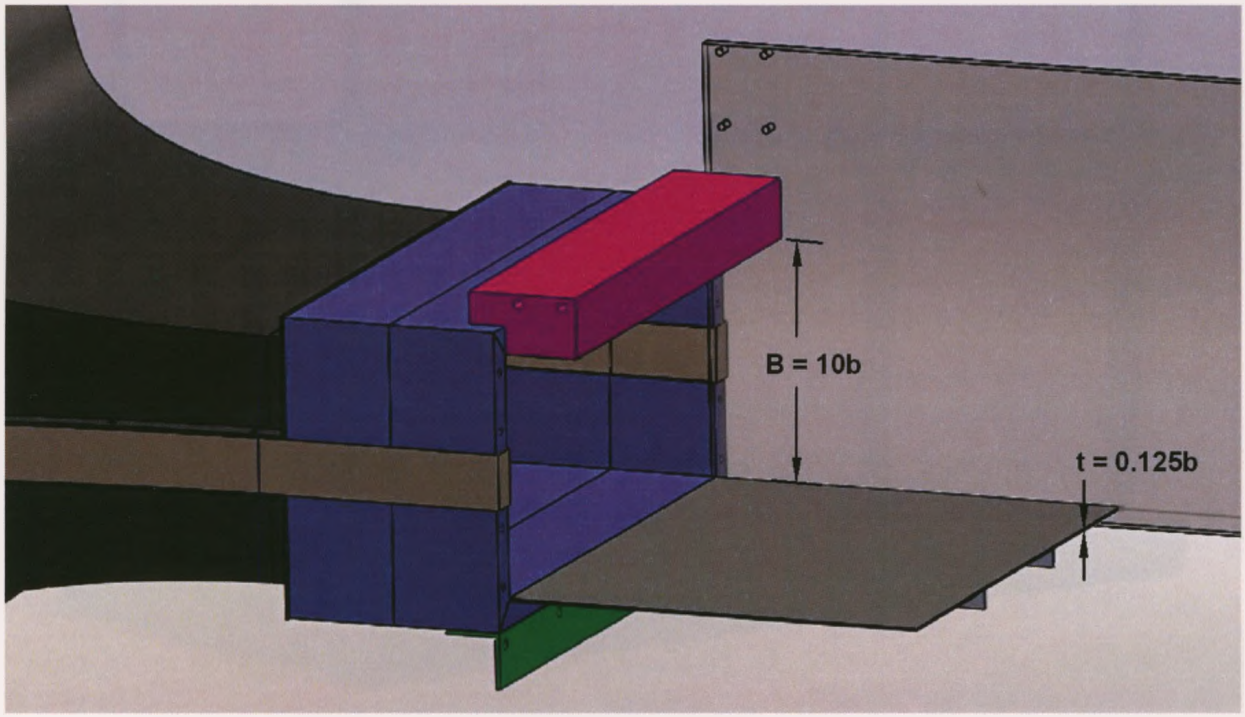

Figure 61: Facility with B = 13b, t = 0.125b

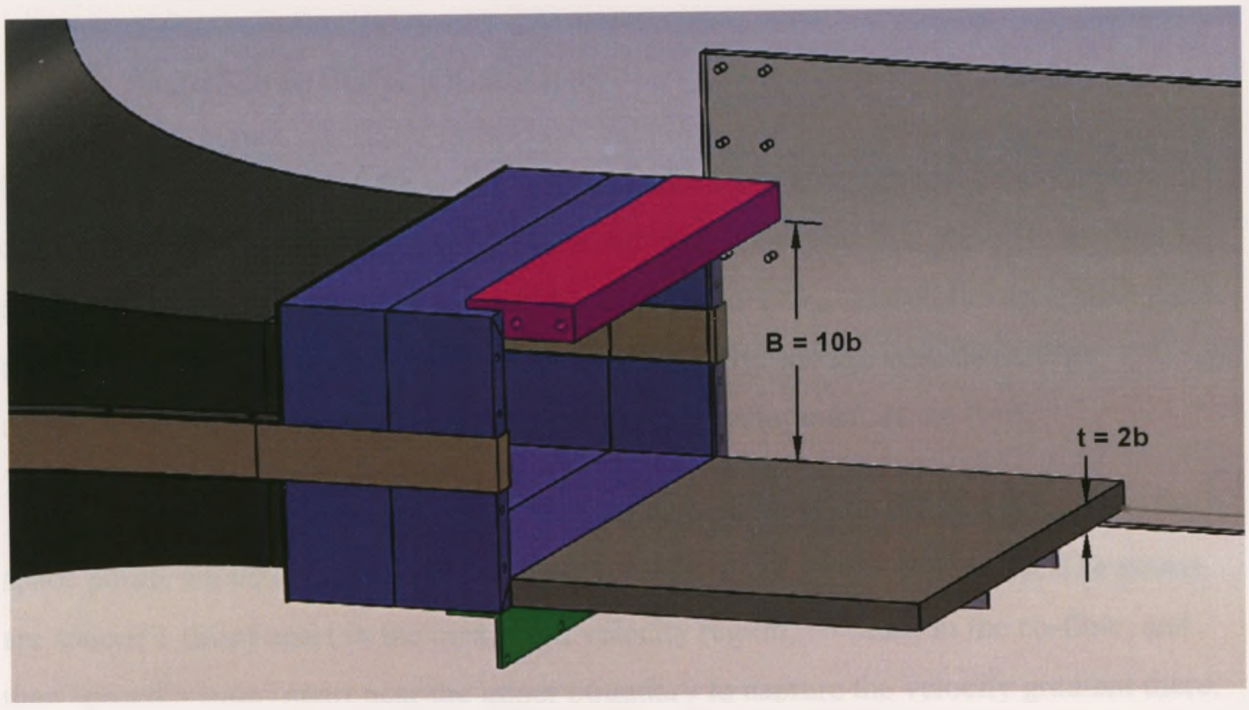

Figure 62: Facility with $B = 13b$, $t = 2b$

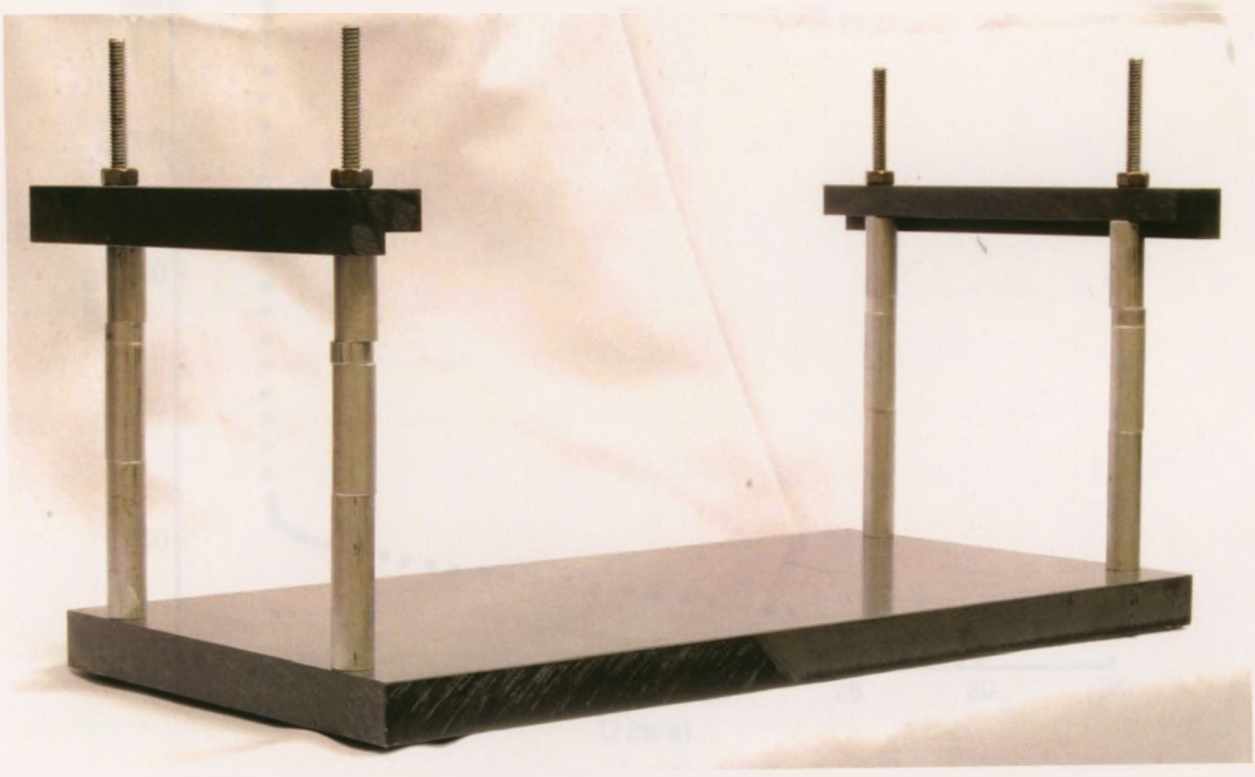

Figure 63: Ceiling section with spacers to determine ceiling height

2.5 Measurement locations

In taking measurements of the wall jet flow, the location spacing must be close enough in order to capture the flow but spaced far enough to be efficient. The principle metrics for classifying the development of the wall jet are U_m and $\frac{1}{2}\Delta y_m$. In order to determine these metrics a curve must be fitted to the data points. Lastly, enough vertical profiles downstream must be taken in order to capture the development of the flow.

In determining the required spacing of vertical points an effort was made to finely space points where large gradients in velocity existed, as seen in **Figure 62**. The points are spaced 1 (mm) apart in the maximum velocity region, 10 (mm) in the co-flow, and then spaced 5 (mm) apart near the upper boundary to capture the velocity gradient there.

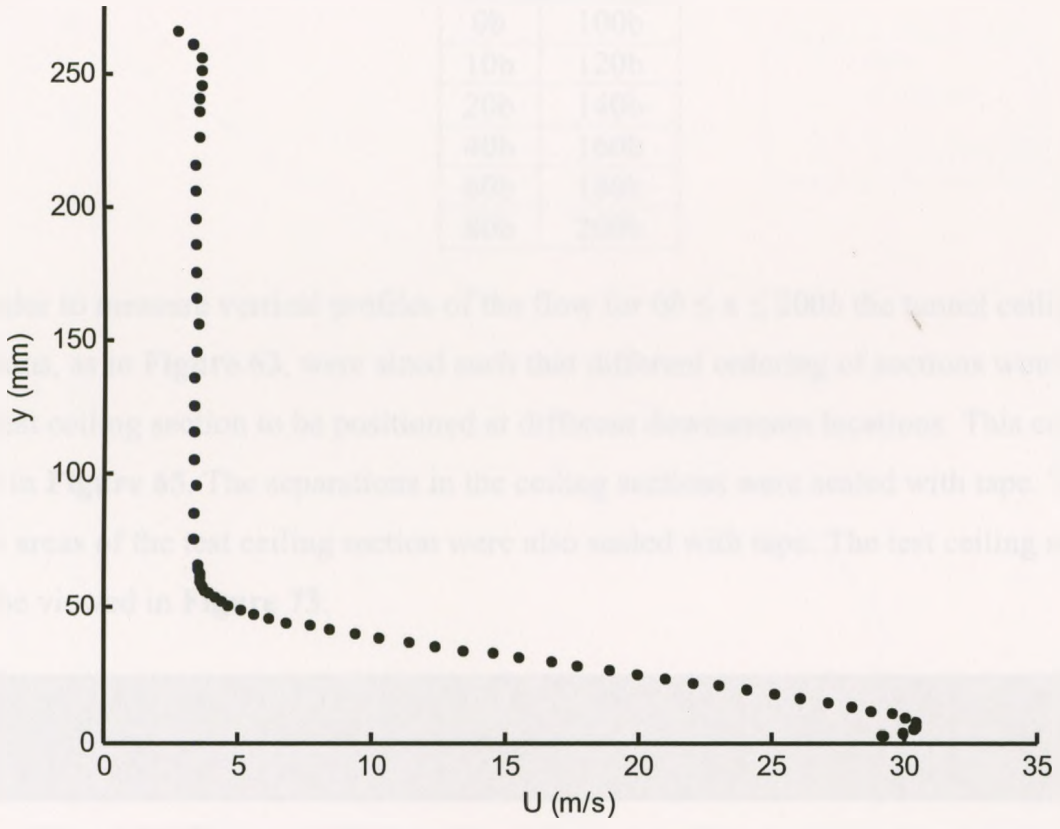

Figure 64: Vertical U profile for $t = 0.125$, $B = 20b$ at $x = 20b$

The downstream locations chosen for the investigation can be viewed in **Table 4**. By taking a vertical profile of velocity at $x = 0b$, the details of the co-flow and jet flow will be known. Narasimha et al. (1979) determined that the flow was still developing for $x < 30b$, by taking measurements at $x = 10b$ & $20b$ this development can be gauged. Two very particular experimental studies were Eriksson et al. (1998) who acquired measurements at $0b$, $5b$, $10b$, $20b$, $40b$, $70b$, $100b$, $150b$ & $200b$ and Wygnanski et al. (1992) who acquired measurements at $20b$, $30b$, $40b$, $50b$, $60b$, $70b$, $80b$, $90b$, $100b$, $110b$ & $120b$. As Lin & Savory (2006) studied downstream up to $x = 208b$, it was decided that measurements up to $x = 200b$ would be performed. Basing the spacing of profiles on those of Eriksson et al. (1998) and Wygnanski et al. (1992), the final locations of **Table 4** were decided.

Table 4: Downstream vertical profile locations

Locations (x)	
0b	100b
10b	120b
20b	140b
40b	160b
60b	180b
80b	200b

In order to measure vertical profiles of the flow for $0b \leq x \leq 200b$ the tunnel ceiling sections, as in **Figure 63**, were sized such that different ordering of sections would allow the test ceiling section to be positioned at different downstream locations. This can be seen in **Figure 65**. The separations in the ceiling sections were sealed with tape. The open areas of the test ceiling section were also sealed with tape. The test ceiling section can be viewed in **Figure 73**.

Figure 65: Tunnel ceiling sections, the test section contains cross pattern

Two different methods were used to fit a curve to the vertical velocity profiles. The method used in many studies was Verhoff's (1970), **Equation 24**, where a least squares fit is used to find the constants *A, B & C*. In contrast, Wilson (1970) used a high order polynomial.

Equation 24: Non-dimensionalized form of Verhoff's (1970) curve fit

$$U = Ay^{D}\left[1.0 - erf(Cy)\right]$$

A comparison was made between the two fit methods. In order to implement the polynomial method an eighth-order polynomial was fitted to maximum velocity region and a sixth-order polynomial was fitted to the half-height region. The result can be seen in **Figure 66**, for $t = 0.125$b, $B = 20b$ and $x = 20b$. A curve fit of the same data can be seen in **Figure 67**, but with Verhoff's (1970) curve fit overlaid.

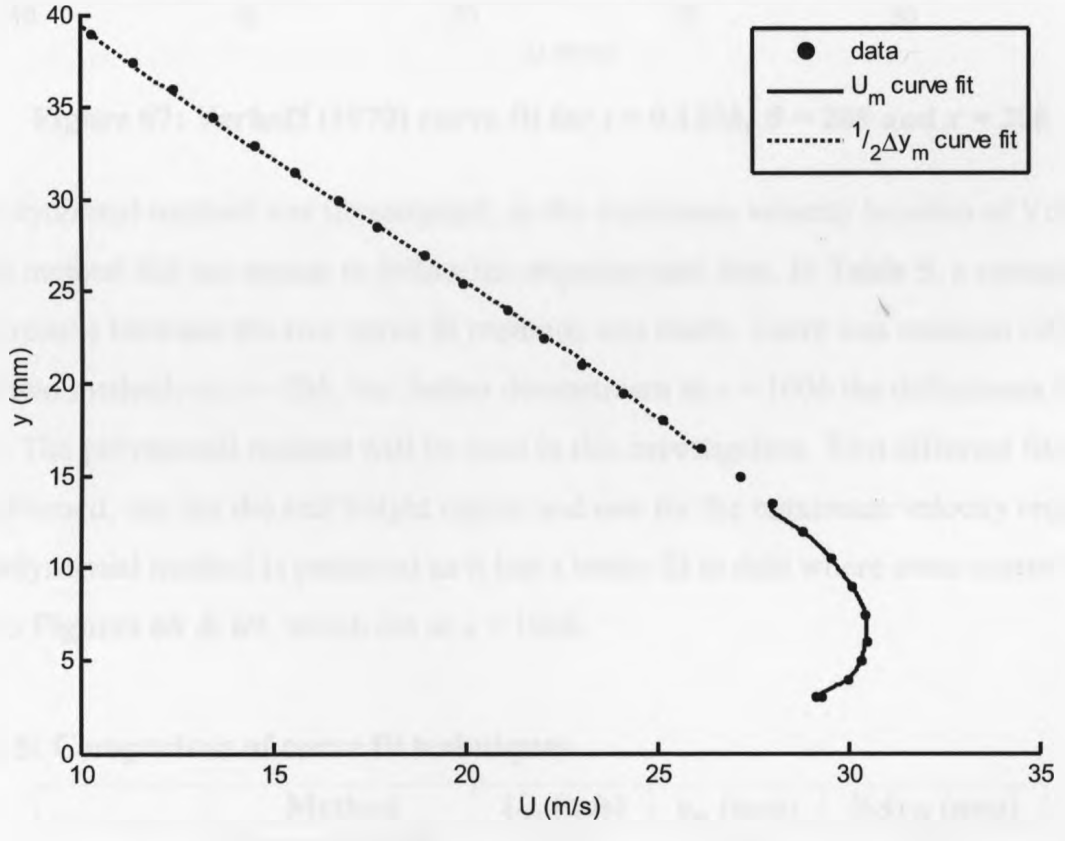

Figure 66: Polynomial curve fit for $t = 0.125b$, $B = 20b$ and $x = 20b$

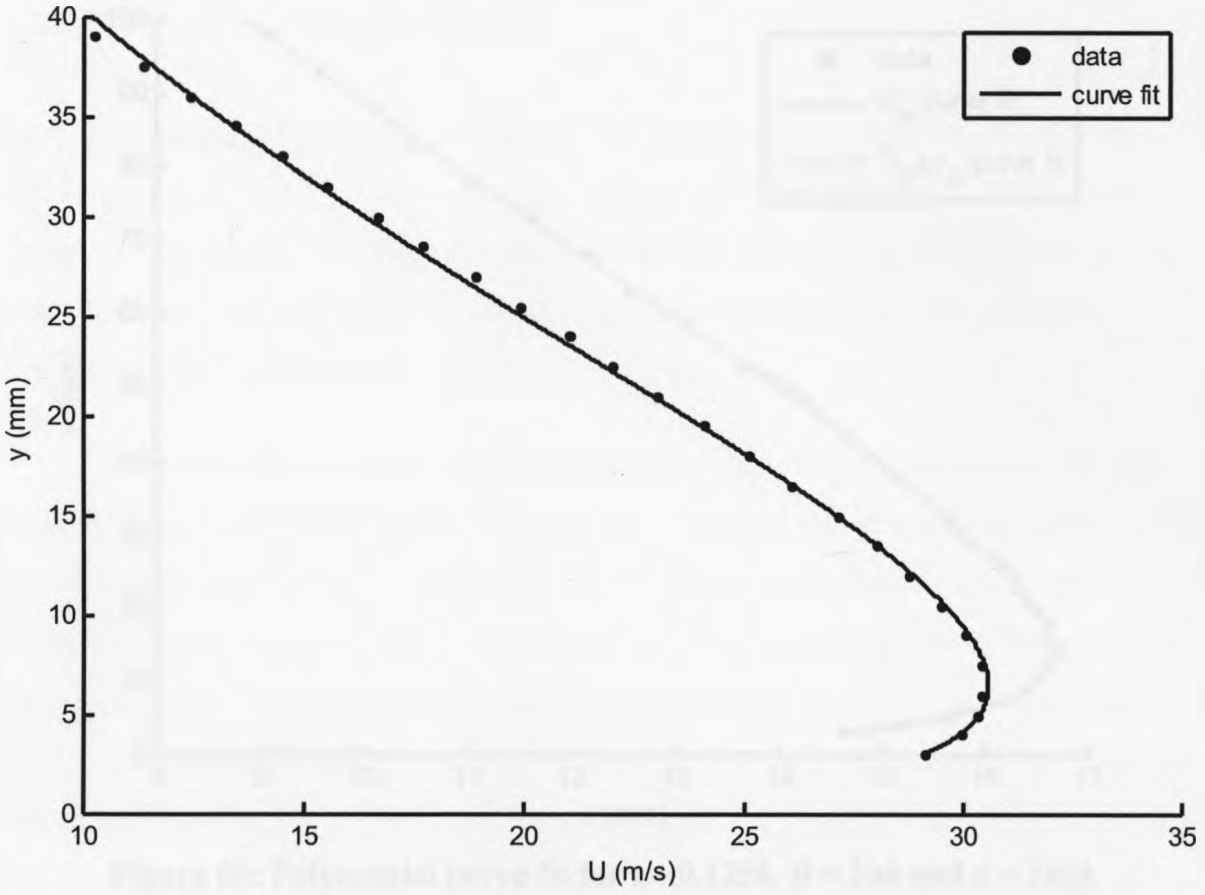

Figure 67: Verhoff (1970) curve fit for $t = 0.125b$, $B = 20b$ and $x = 20b$

The polynomial method was investigated, as the maximum velocity location of Verhoff's (1970) method did not appear to follow the experimental data. In **Table 5**, a comparison of the results between the two curve fit methods was made. There was minimal difference in the two methods at $x = 20b$, but farther downstream at $x = 100b$ the differences were larger. The polynomial method will be used in this investigation. Two different fits will be performed, one for the half height region and one for the maximum velocity region. The polynomial method is preferred as it has a better fit to data where some scatter exists, refer to **Figures 68 & 69**, which are at $x = 100b$.

Table 5: Comparison of curve fit techniques

	Method	U_m (m/s)	y_m (mm)	$\frac{1}{2}\Delta y_M$ (mm)
x = 20b	**Verhoff (1970)**	30.6	6.69	35.1
	Polynomial	30.5	6.78	35.0
x = 100b	**Verhoff (1970)**	16.5	15.5	70.0
	Polynomial	16.7	14.5	68.6

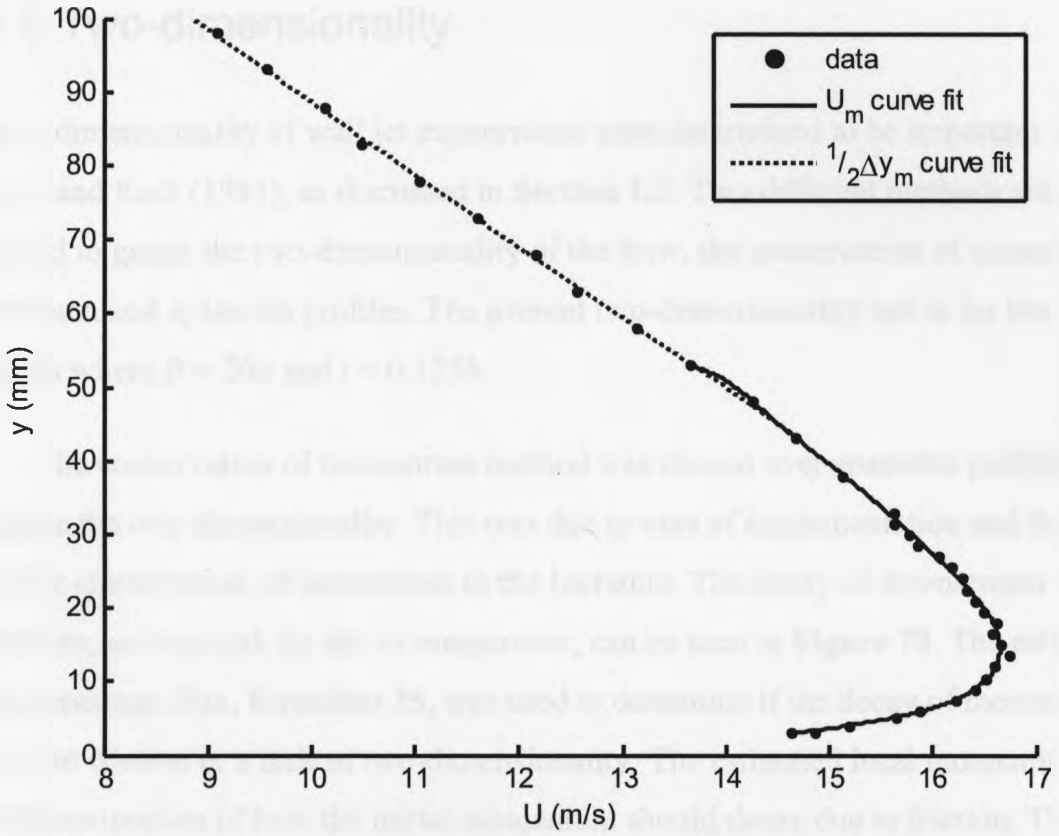

Figure 68: Polynomial curve fit for $t = 0.125b$, $B = 20b$ and $x = 100b$

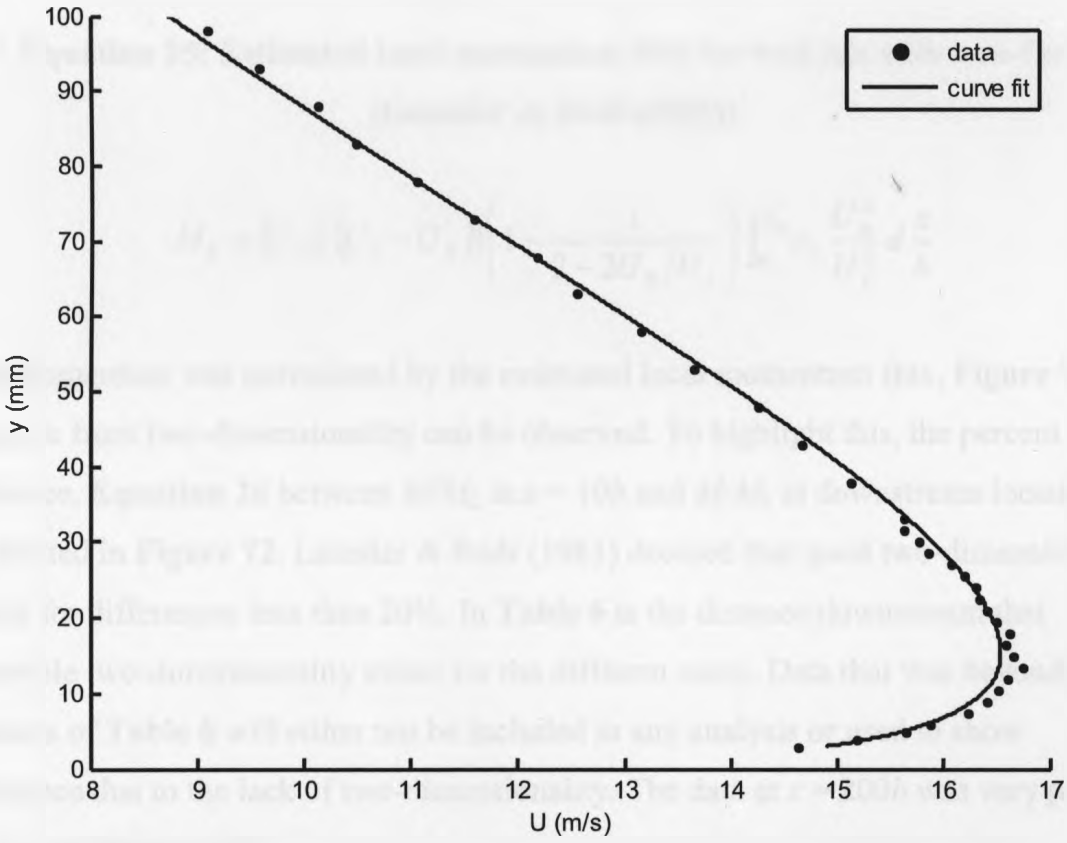

Figure 69: Verhoff (1970) curve fit for $t = 0.125b$, $B = 20b$ and $x = 100b$

2.6 Two-dimensionality

The two dimensionality of wall jet experiments were determined to be important by Launder and Rodi (1981), as discussed in **Section 1.3**. Two different methods were suggested to gauge the two-dimensionality of the flow, the conservation of momentum downstream and spanwise profiles. The present two-dimensionality test is for the condition where $B = 20b$ and $t = 0.125b$.

The conservation of momentum method was chosen over spanwise profiles to determine the two-dimensionality. This was due to ease of implementation and the wide use of the conservation of momentum in the literature. The decay of downstream momentum, normalized, by the jet momentum, can be seen in **Figure 70**. The estimated local momentum flux, **Equation 25**, was used to determine if the decay of momentum was due to friction or a lack of two-dimensionality. The estimated local momentum flux is an approximation of how the initial momentum should decay due to friction. The local wall friction, c_f, was determined from Bradshaw & Gee's (1964) estimation, **Equation 16**.

Equation 25: Estimated local momentum flux for wall jets with a co-flow (Launder & Rodi (1981))

$$M_L = \left(U_J b \left(U_j - U_E\right)\right)\left(1 - \frac{1}{2 - 2U_E/U_j}\right)\int_0^{x/b} c_f \frac{U_m^2}{U_j^2} d\frac{x}{b}$$

Once momentum was normalized by the estimated local momentum flux, **Figure 71**, the departure from two-dimensionality can be observed. To highlight this, the percent difference, **Equation 26** between M/M_L at $x = 10b$ and M/M_L at downstream locations was plotted in **Figure 72**. Launder & Rodi (1981) decided that good two-dimensionality existed for differences less than 20%. In **Table 6** is the distance downstream that acceptable two-dimensionality exists for the different cases. Data that was beyond the distances of **Table 6** will either not be included in any analysis or used to show divergence due to the lack of two-dimensionality. The data at $x = 200b$ was very poor and will not be shown at all.

Equation 26: Percent difference

$$Percent\ difference = \left| \frac{a-b}{(a+b)/2} \right| \times 100\%$$

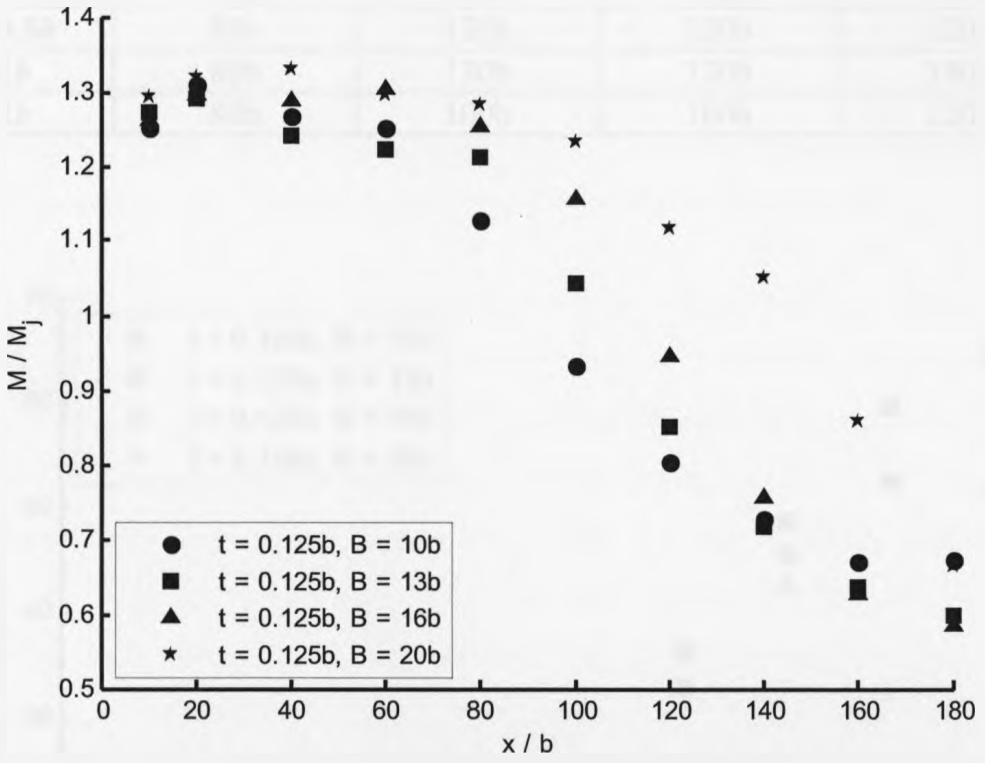

Figure 70: Decay of downstream momentum normalized by the jet momentum flux.

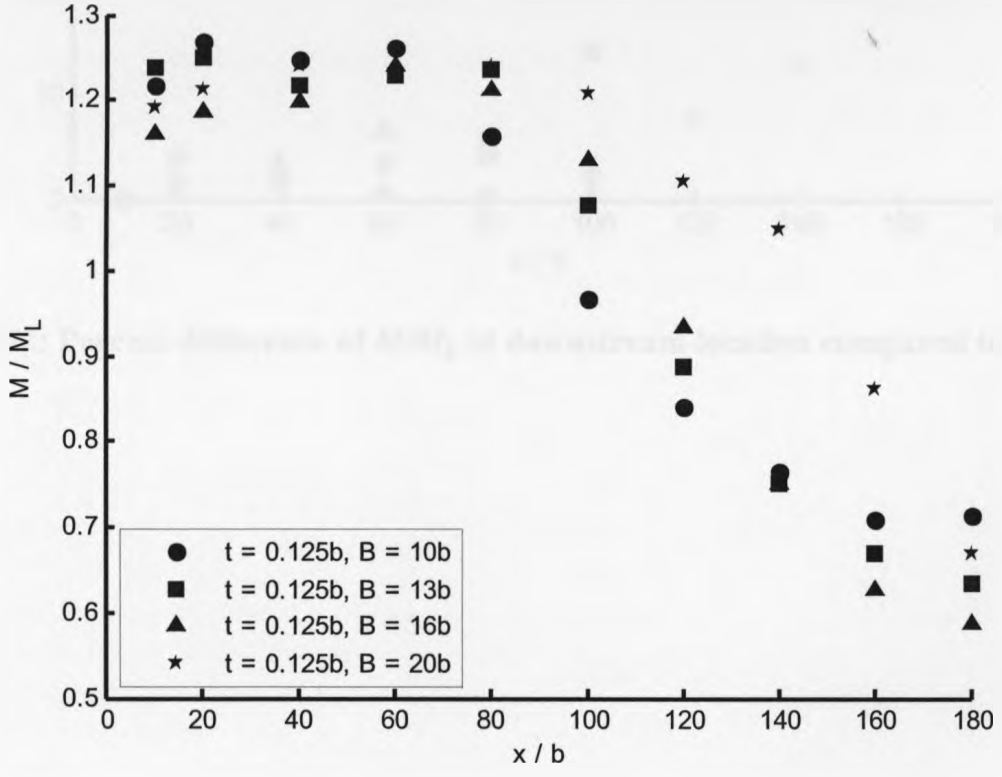

Figure 71: Decay of downstream momentum normalized by the estimated local momentum flux.

Table 6: Maximum downstream distance that acceptable momentum exists

	$B = 10b$	$B = 13b$	$B = 16b$	$B = 20b$
$t = 0.125b$	80b	100b	100b	140b
$t = 0.5b$	80b	120b	120b	120b
$t = 1b$	80b	120b	120b	140b
$t = 2b$	80b	100b	100b	120b

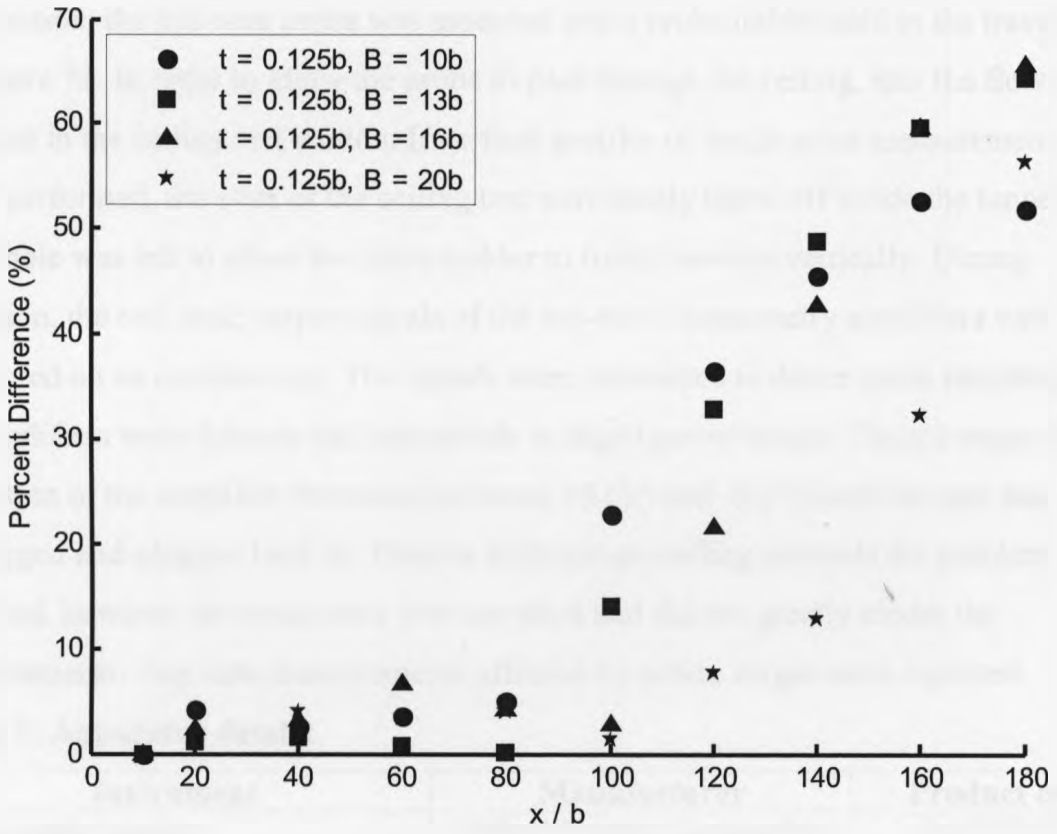

Figure 72: Percent difference of M/M_L at downstream location compared to $x = 10b$.

2.7 Measurement apparatus

As discussed in **Section 1.9**, cross hot-wire anemometry was used for all measurements in the flow. A pitot-static tube was used for velocity calibrations of the hot-wire probe and a specialized unit was used for yaw calibrations. In order to locate the hot-wire probe a screw operated traverse was used. Refer to **Table 7** for a list of the equipment manufacturers and product codes. Discussions of the formulas used and the uncertainty for the measurements are in **Appendix C** and **Appendix D** respectively.

In operation, the hot-wire probe was mounted into a probe holder held in the traverse, as in **Figure 73**. In order to allow the probe to pass through the ceiling, into the flow, slots were cut in the ceiling test section. If vertical profiles or single point measurements were being performed, the slots of the ceiling test were neatly taped off inside the tunnel and a small hole was left to allow the probe holder to freely traverse vertically. During operation, the real-time output signals of the hot-wire anemometry amplifiers were monitored on an oscilloscope. The signals were monitored to detect noise interference, as the amplifiers were delicate and susceptible to slight power surges. Once a surge occurred the output of the amplifier fluctuated between +5 (V) and -5 (V) until the unit was unplugged and plugged back in. Despite different grounding methods the problem persisted, however the occurrence was not often and did not greatly hinder the measurements. Any data measurements affected by power surges were repeated.

Table 7: Apparatus details

Instrument	Manufacturer	Product code
Pitot-static probe	United Sensor Corporation	PAE-18-KL
Cross hot-wire probe	Dantec Dynamics	55P0611
Constant temperature hot-wire anemometry amplifier	Dantec Dynamics	54T30
Yaw calibrator	Dantec Dynamics	90H02 Flow Unit
Rule for U-tube manometer	Starret	C330-300
Micro-manometer	Dwyer Instruments, Inc.	M1430
Vertical traverse slide	Velmex	MA2518B-S2.5-0
Horizontal traverse slide	Velmex	MB2524W1J-S2.5
Vertical & horizontal traverse stepper motors	Vexta	PK264-03A-P1
Traverse controller	Velmex	VXM-2

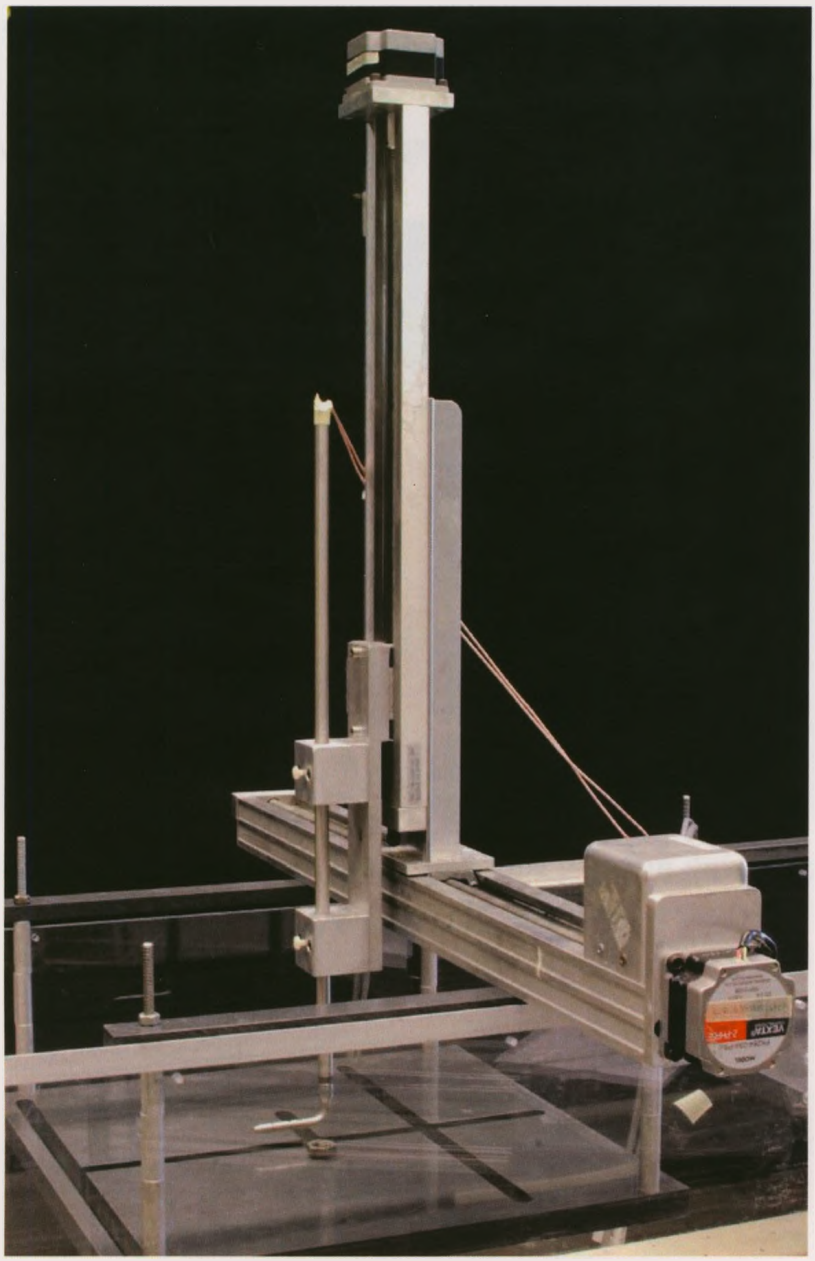

Figure 73: Hot-wire probe mounted in the traverse, the unit is above the test ceiling section

Labview NI was used to coordinate data collection and the traverse location. A simplified version of Lin & Savory's (2006) Control & Acquisition Microburst Simulator program was used. Within Lin & Savory's (2006) program, Labview accesses Velmex's software COSMOS in order to send the correct data train to the traverse controller.

For the velocity calibration, a pitot-static tube was used to determine the total and static pressure of the flow at the jet exit. During this process the pitot-static tube and hot-wire probe were located at the jet exit, as in **Figure 74**. In order to determine the

differential pressure of the pitot-static two different fluid manometers were used; a micro-manometer for $U_j \leq 28$ (m/s) and a ruled manometer for $U_j > 28$ (m/s), **Figure 75**. The ruled manometer was built in-house using a precision steel metric rule, refer to **Table 7**.

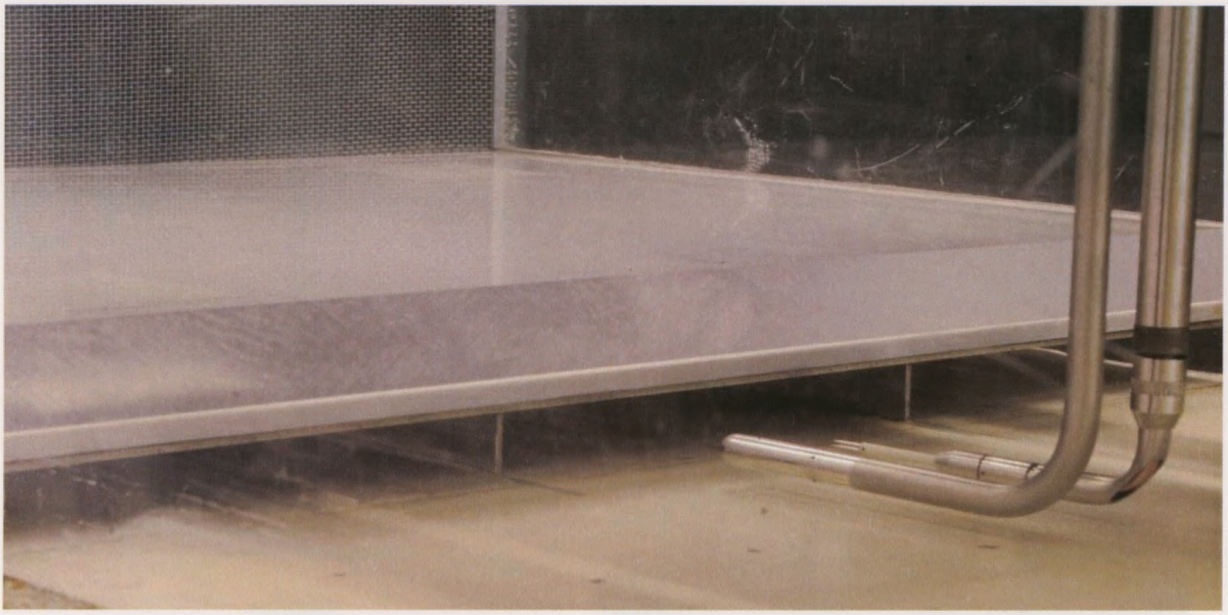

Figure 74: Pitot-static tube and hot-wire probe location during the velocity calibration (note t = 2)

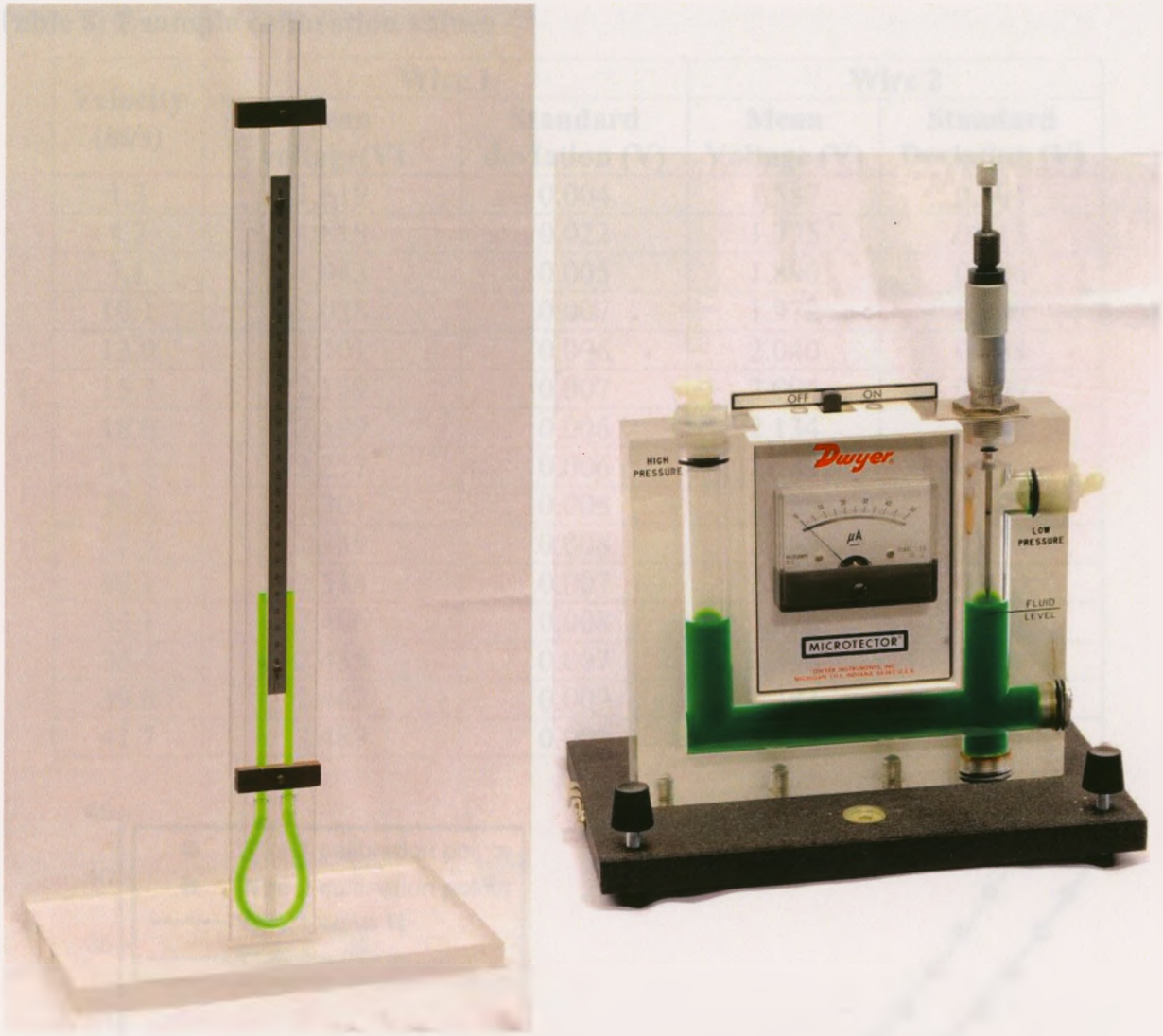

Figure 75: (Left) Large ruled U-tube manometer. (Right) Mirco-manometer

During the velocity calibration, the velocity of the jet was varied for ~1< U_j < ~45 (m/s). A 15 (s) sample at 10 (kHz) was taken for each calibration point, for a total of 15 calibration locations, an example is in **Table 8**. A curve fit of the calibration velocities and voltages can be seen in **Figure 76**. Refer to **Appendix C** for information regarding the curve fit method and determining U and V from the probe signal.

Table 8: Example calibration values

Velocity (m/s)	Wire 1		Wire 2	
	Mean voltage(V)	Standard deviation (V)	Mean Voltage (V)	Standard Deviation (V)
1.3	1.619	0.004	1.587	0.004
4.2	1.818	0.022	1.775	0.013
7.1	1.943	0.005	1.890	0.006
10.1	2.028	0.007	1.972	0.008
13.0	2.101	0.006	2.040	0.008
15.7	2.159	0.007	2.094	0.009
18.0	2.199	0.006	2.134	0.007
21.5	2.257	0.006	2.189	0.008
24.6	2.301	0.006	2.230	0.008
27.5	2.339	0.008	2.265	0.010
30.1	2.374	0.007	2.298	0.010
33.1	2.406	0.008	2.328	0.011
36.1	2.435	0.007	2.356	0.009
39.0	2.462	0.009	2.383	0.011
41.7	2.489	0.009	2.409	0.011

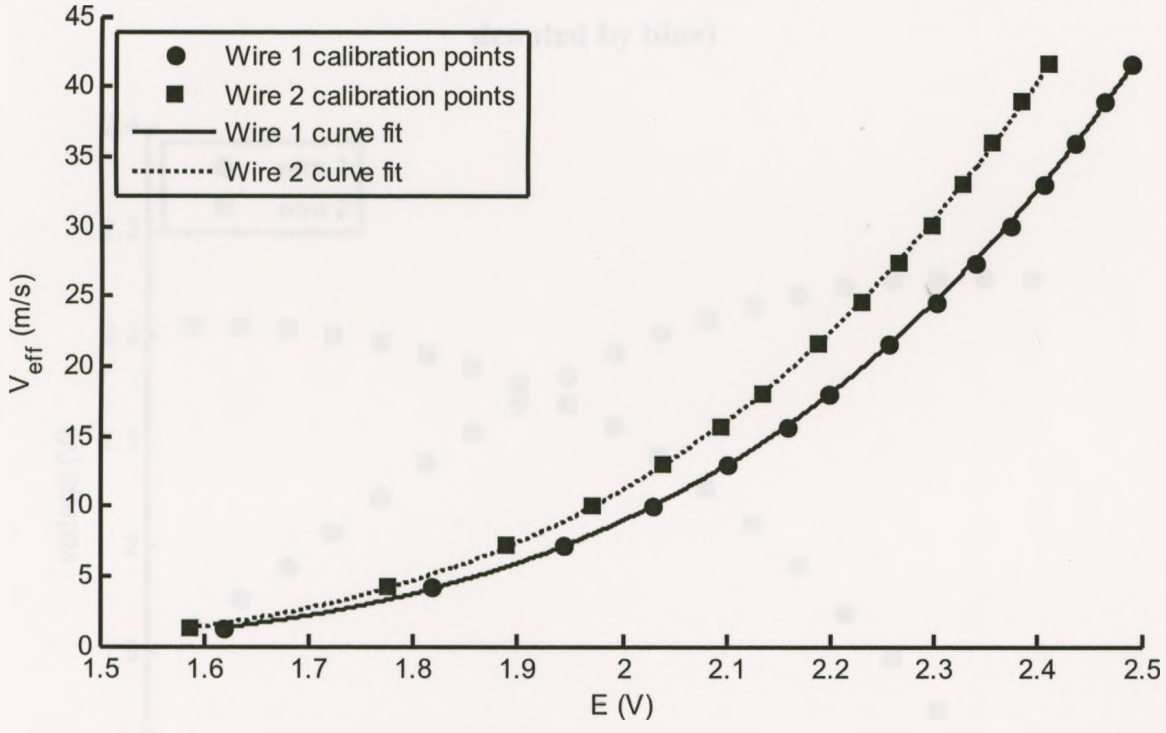

Figure 76: Example calibration curves for wires 1& 2

The yaw calibration was performed in a Dantec Streamline 90H02 Flow Unit, **Figure 75**. The hot-wire probe was held in a chuck with the plane of the wires oriented normal to the yaw control axis. A jet issued from the unit along the probe axis with the yaw control at

0°; in that position a velocity calibration was performed. Samples were then taken at known velocities and angles to produce **Figure 77** and **Table 9**. This data was used in **Appendix C** to determine the yaw coefficients, $\mathbf{k^2}$.

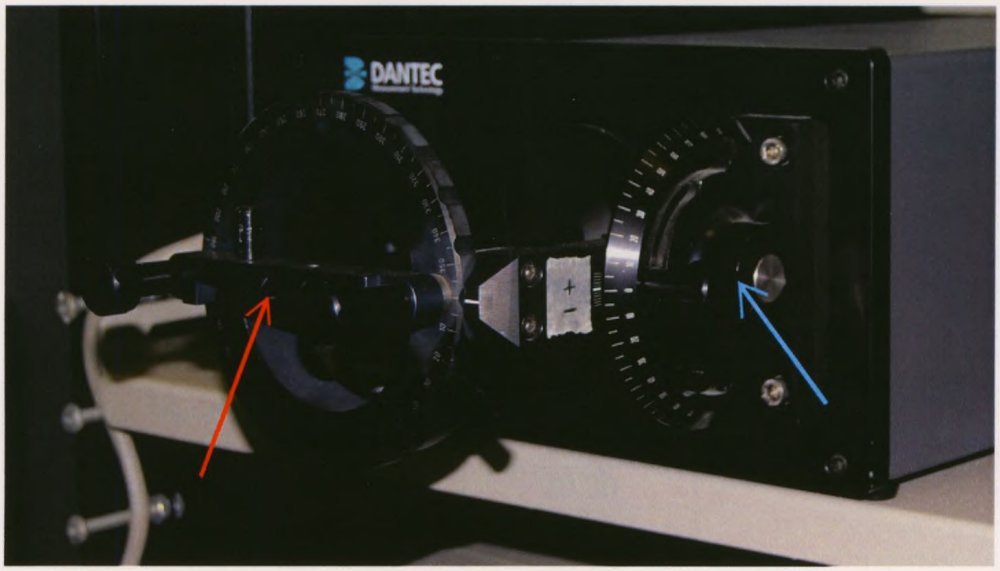

Figure 77: Dantec Streamline 90H02 Flow Unit (chuck denoted by red, yaw control denoted by blue)

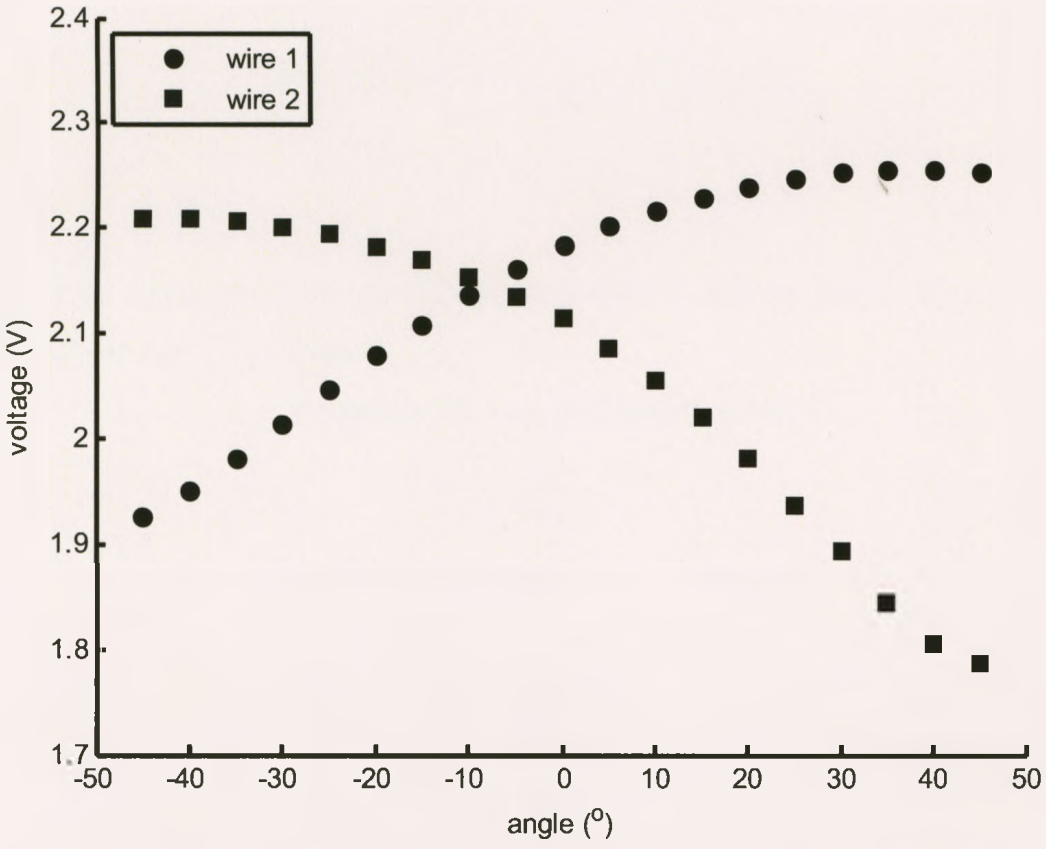

Figure 78: Sample voltages for wires1 & 2 from a yaw calibration

Table 9: Sample yaw calibration velocities

Angle (°)	Velocity (m/s)
-45	20.29
-40	20.30
-35	20.29
-30	20.33
-25	20.31
-20	20.32
-15	20.29
-10	20.29
-5	20.32
0	20.29
5	20.31
10	20.29
15	20.31
20	20.30
25	20.31
30	20.30
35	20.31
40	20.29
45	20.30

2.8 Sampling

The length of a sample, and the rate that the data is collected, are important in order to have a statistically independent sample. In order to determine whether the samples were statically independent the integral time and length scale of the flow for the sample were calculated, along with the velocity and Taylor micro time scale. Samples were also tested for dominant frequencies from the tunnel's blower motor or obstructions in the flow.

The integral time scale was determined from **Equation 27**. However the integral of **Equation 27** was estimated by the area under the curve $R(\tau)$, from $R(0)$ up to the first occasion that $R(\tau) = 0$.

Equation 27: Integral time scale

$$T_E = \int_0^\infty R(\tau) d\tau$$

Where

$$R(\tau) = R(r\Delta t) = \frac{1}{u^2} \frac{1}{(N-r)} \sum_{n=1}^{n=N-r} u_n \cdot u_{n+r}$$

for $r = 0, 1, 2, \ldots, m$

Integral length scale was determined from **Equation 28**, and the Taylor micro time scale was determined from **Equation 29**.

Equation 28: Integral length scale

$$L = T_E U$$

Equation 29: Taylor micro time scale

$$\tau_E = \frac{\sqrt{2}\sqrt{\overline{u^2}}}{\sqrt{\left(\frac{\partial u}{\partial t}\right)^2}}$$

The test cases were sampled for a maximum of 25 (s) at 1 000, 5 000, 8 000 & 10 000 (Hz). Different downstream locations were tested, as well as in flow close to the jet flow and in the co-flow, refer to **Table 10**. Lin & Savory (2006) performed measurements in the facility for 30 (s) at 1 000 (Hz). Due to the large number of measurements that had to be completed, measurement lengths of 25 (s) were desired. The saving of 5 (s) resulted in a reduction of testing by ~ 20 (hrs). In **Tables 10 & 11**, separate samples were taken at the specified location with the different frequencies. Separate samples were taken for each frequency rather than simulating the lower frequencies from the 10 000 (Hz) data. This was due to difficulty in simulating between 5 000 and 10 000 (Hz). Minor differences may have arisen in the data from using separate samples. The percent difference between a value and the value taken at the next lowest frequency is shown in **Tables 10 & 11**. Between 8 000 and 10 000 (Hz) the lowest percent differences occurred for most cases, at $x = 180b$ the high turbulence of the flow made no clear distinction in the required sampling frequency. A sample frequency of 10 000 (Hz) was chosen for all measurements, although 8 000 would have been sufficient. The higher sampling frequency was chosen to allow any high frequencies in the flow to be captured.

Table 10: Determination of sampling frequency for a 25 (s) sample

Location	Frequency (Hz)	Integral time scale (s)	Integral time scale percent difference (%)	Integral length scale (m)	Integral length scale percent difference (%)
$x = 20b$ $y = 4.6b$	1000	0.0013		0.0044	
	5000	0.0013	0	0.0044	0
	8000	0.0014	7	0.0046	4
	10000	0.0014	0	0.0046	0
$x = 20b$ $y = 16.2b$	1000	0.013		0.041	
	5000	0.012	8	0.039	5
	8000	0.021	55	0.069	56
	10000	0.021	0	0.070	1
$x = 100b$ $y = 4.6b$	1000	0.0044		0.054	
	5000	0.0045	2	0.055	2
	8000	0.0048	6	0.059	7
	10000	0.0048	0	0.060	2
$x = 100b$ $y = 16.2b$	1000	0.022		0.037	
	5000	0.025	13	0.043	15
	8000	0.023	8	0.039	10
	10000	0.022	4	0.040	3
$x = 180b$ $y = 4.6b$	1000	0.013		0.11	
	5000	0.013	0	0.11	0
	8000	0.015	14	0.13	17
	10000	0.012	22	0.10	26
$x = 180b$ $y = 16.2b$	1000	0.017		0.063	
	5000	0.020	16	0.072	13
	8000	0.024	18	0.090	22
	10000	0.023	4	0.081	11

Table 11: Determination of sampling frequency for a 25 (s) sample

Location	Frequency (Hz)	U (m/s)	U percent difference (%)	Taylor micro time scale (s)	Taylor micro time scale percent difference (%)
$x = 20b$ $y = 4.6b$	1000	3.34		0.0023	
	5000	3.35	0	0.0013	56
	8000	3.37	1	0.0011	17
	10000	3.38	0	0.0011	0
$x = 20b$ $y = 16.2b$	1000	3.3		0.00255	
	5000	3.31	0	0.00055	129
	8000	3.34	1	0.00035	44
	10000	3.35	0	0.00027	26
$x = 100b$ $y = 4.6b$	1000	12.31		0.0032	
	5000	12.25	0	0.0011	98
	8000	12.32	1	0.0009	20
	10000	12.71	3	0.0008	12
$x = 100b$ $y = 16.2b$	1000	1.7		0.0048	
	5000	1.77	4	0.0023	70
	8000	1.7	4	0.002	14
	10000	1.82	7	0.0019	5
$x = 180b$ $y = 4.6b$	1000	8.79		0.0043	
	5000	8.62	2	0.0016	92
	8000	8.62	0	0.0013	21
	10000	8.74	1	0.0012	8
$x = 180b$ $y = 16.2b$	1000	3.69		0.0047	
	5000	3.54	4	0.0021	76
	8000	3.8	7	0.0018	15
	10000	3.6	5	0.0017	6

In **Tables 12 & 13**, the samples were acquired at 10 000 (Hz) for 25 (s) and then truncated to give different sample lengths. In this case the differences in the Taylor micro time scale were minimal, whereas the integral scales displayed poor convergence in the sample length. The percent differences in the integral scale were greatest for locations where $Y = 16.2b$. This is in the co-flow region where the turbulence may be such that the hot-wire anemometry is not able to discern reverse flows, as discussed in **Experimental approaches**. This may contribute to the poor convergence in the integral scales. The location $Y = 16.2b$ is above where the half-height of the flow would be measured and is therefore less critical. In other locations the percent differences are minimal for a 25 (s) sample length and that length was used for all subsequent sampling.

Table 12: Determination of sample length at 10 000 (Hz)

Location	Sample time (s)	Integral time scale (s)	Integral time scale percent difference (%)	Integral length scale (m)	Integral length scale percent difference (%)
$x = 20b$ $y = 4.6b$	5	0.0014		0.0047	
	10	0.0014	0	0.0046	2
	15	0.0014	0	0.0046	0
	20	0.0013	7	0.0045	2
	25	0.0014	7	0.0046	2
$x = 20b$ $y = 16.2b$	5	0.014		0.045	
	10	0.017	19	0.056	22
	15	0.019	11	0.065	15
	20	0.017	11	0.056	15
	25	0.021	21	0.070	22
$x = 100b$ $y = 4.6b$	5	0.0042		0.054	
	10	0.0044	5	0.056	4
	15	0.0045	2	0.058	4
	20	0.0047	4	0.060	3
	25	0.0048	2	0.060	0
$x = 100b$ $y = 16.2b$	5	0.024		0.040	
	10	0.023	4	0.040	0
	15	0.023	0	0.042	5
	20	0.021	9	0.038	10
	25	0.022	5	0.040	5
$x = 180b$ $y = 4.6b$	5	0.009		0.081	
	10	0.010	11	0.090	11
	15	0.012	18	0.107	17
	20	0.012	0	0.108	1
	25	0.012	0	0.104	4
$x = 180b$ $y = 16.2b$	5	0.032		0.122	
	10	0.025	25	0.093	27
	15	0.020	22	0.075	21
	20	0.018	11	0.067	11
	25	0.023	24	0.081	19

Table 13: Determination of sample length at 10 000 (Hz)

Location	Sample time (s)	U (m/s)	U percent difference (%)	Taylor micro time scale (s)	Taylor micro time scale percent difference (%)
$x = 20b$ $y = 4.6b$	5	3.38		0.0010	
	10	3.38	0	0.0010	0
	15	3.38	0	0.0010	0
	20	3.38	0	0.0010	0
	25	3.38	0	0.0010	0
$x = 20b$ $y = 16.2b$	5	3.36		0.00027	
	10	3.36	0	0.00027	0
	15	3.35	0	0.00027	0
	20	3.35	0	0.00027	0
	25	3.35	0	0.00027	0
$x = 100b$ $y = 4.6b$	5	12.79		0.00077	
	10	12.7	1	0.00078	1
	15	12.73	0	0.00077	1
	20	12.73	0	0.00078	1
	25	12.71	0	0.00079	1
$x = 100b$ $y = 16.2b$	5	1.65		0.0018	
	10	1.74	5	0.0019	5
	15	1.82	4	0.0019	0
	20	1.81	1	0.0019	0
	25	1.82	1	0.0019	0
$x = 180b$ $y = 4.6b$	5	8.59		0.0011	
	10	8.76	2	0.0011	0
	15	8.8	0	0.0012	9
	20	8.81	0	0.0012	0
	25	8.74	1	0.0012	0
$x = 180b$ $y = 16.2b$	5	3.81		0.0018	
	10	3.72	2	0.0018	0
	15	3.66	2	0.0017	6
	20	3.65	0	0.0017	0
	25	3.6	1	0.0017	0

The u frequency spectrum of the flow at $x = 20b$, $100b$ & $180b$ for $Y = 4.6b$ is shown in **Figures 79 - 81**. If a dominate frequency existed at a flow location it would be highlighted by a spike in the plot, but none existed. Kolmogorov's -5/3 decay line was overlaid in the plots to confirm that the decay of the turbulence was correct. The decay of the turbulence was as expected for **Figure 80 & 81**. The decay of turbulence in **Figure 79** does not follow the decay line as the location, $x = 20b$, $Y = 4.6b$, is not in the jet flow but still in the co-flow.

The hot-wire probe signal was also sampled, at $f = 10\ 000$ (Hz) for 25 (s), while shielded from any flow with the wall jet facility running at operating velocity. The root mean squares of the u signals were $rms_{wire\ 1} = 0.0027$ and $rms_{wire\ 2} = 0.0030$. The frequency spectrum for this condition is in **Figure 82**, no dominant frequencies emerged which demonstrates the facility does not cause interference with the hot-wire probe signal.

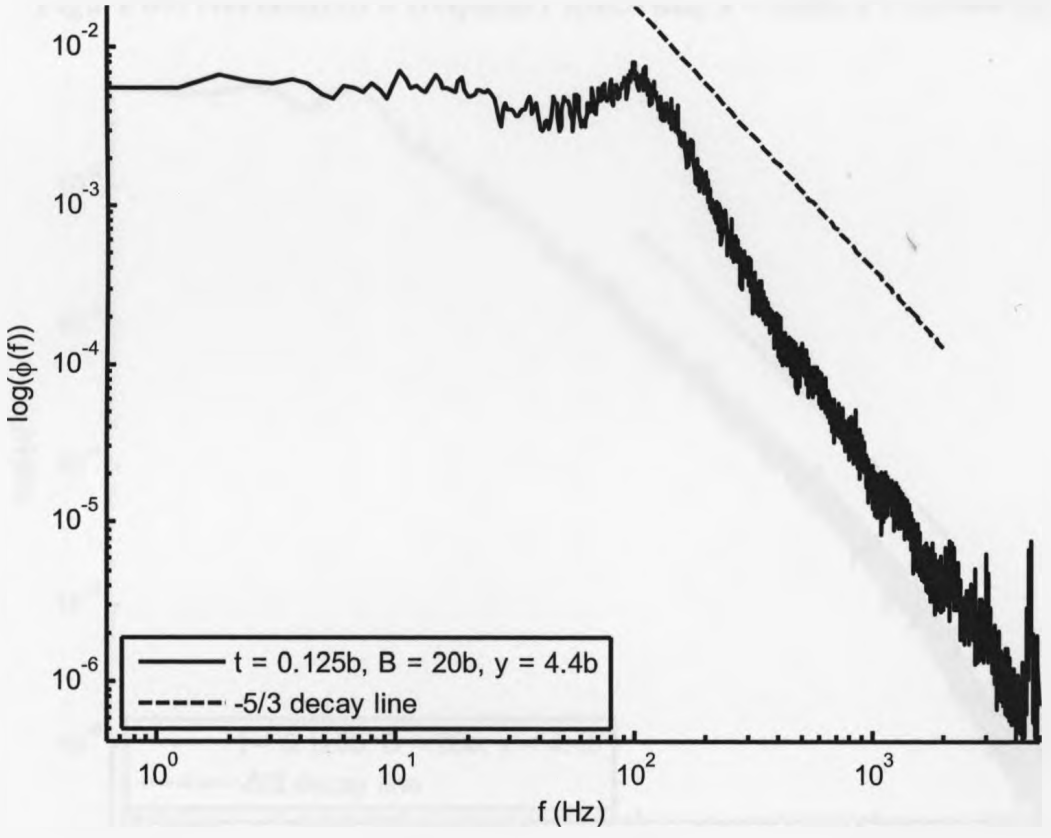

Figure 79: Normalized u frequency spectrum, x = 20b, f = 10 000 (Hz)

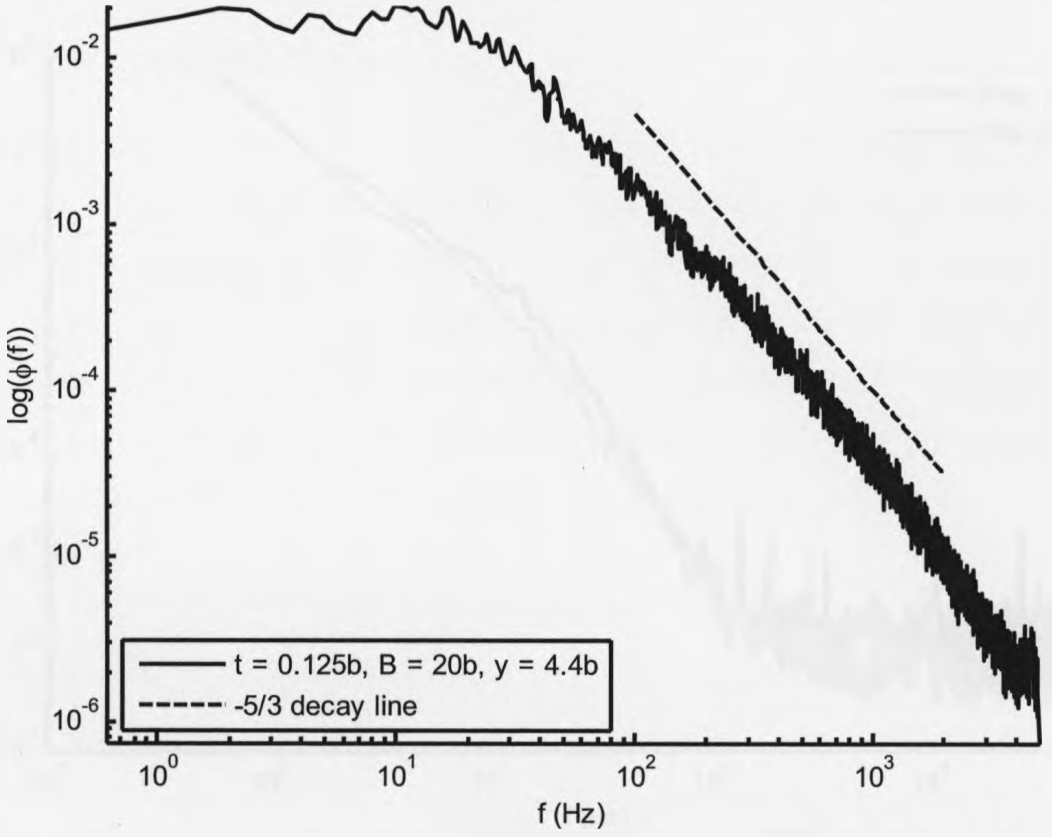

Figure 80: Normalized u frequency spectrum, x = 100b, f = 10 000 (Hz)

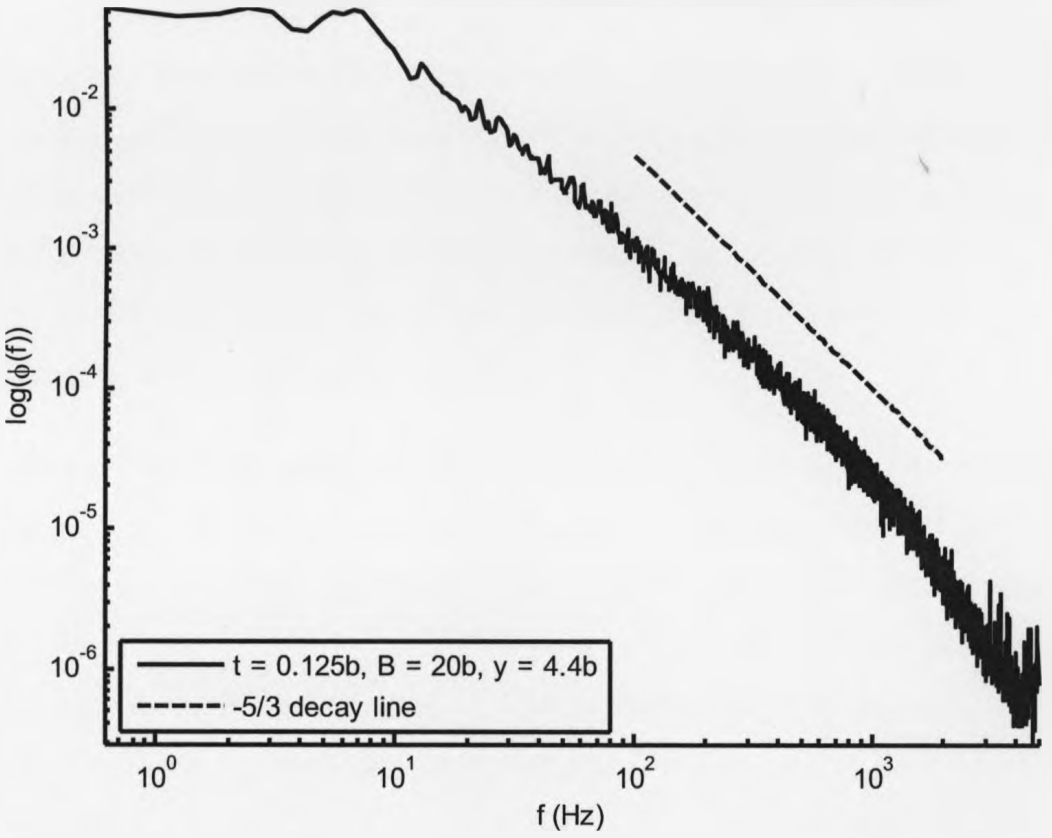

Figure 81: Normalized u frequency spectrum, x = 180b, f = 10 000 (Hz)

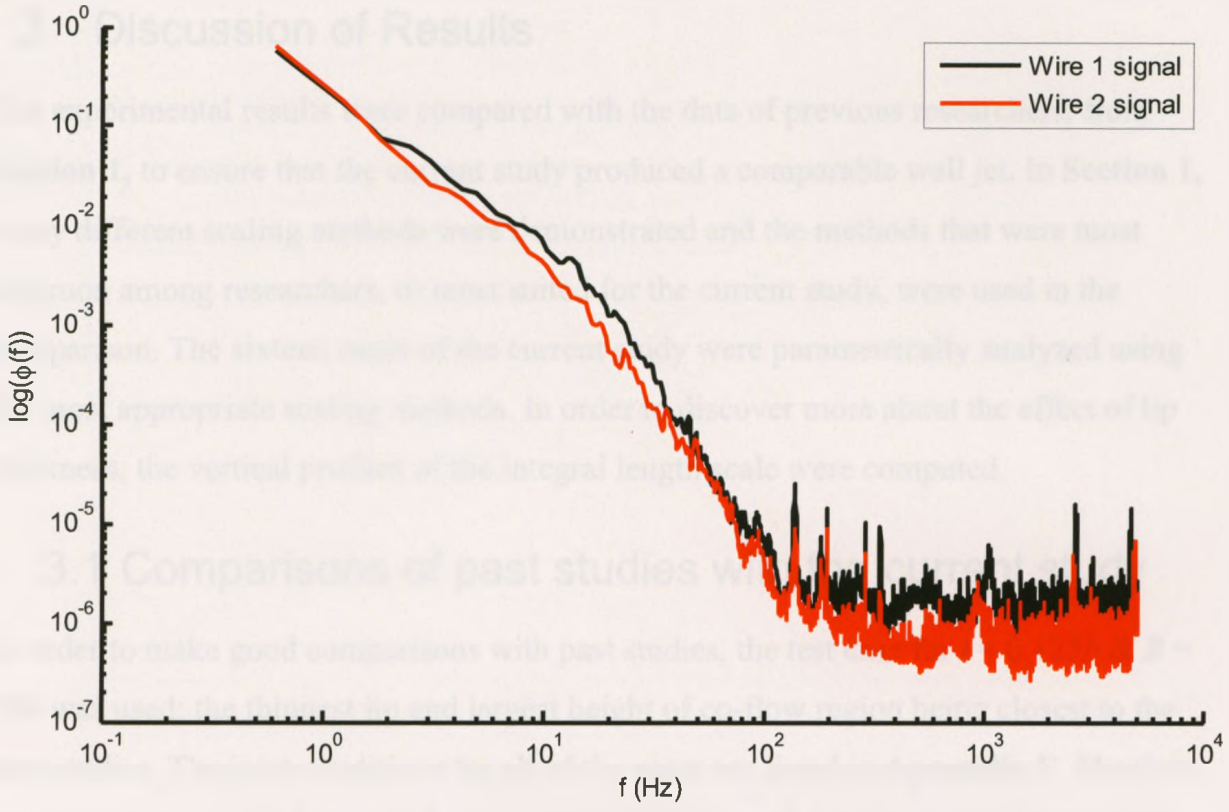

Figure 82: Wire 1 and 2 normalized voltage frequency spectrum, probe shielded from flow, but wall jet facility at operating conditions

3 Discussion of Results

The experimental results were compared with the data of previous researchers, from **Section 1,** to ensure that the current study produced a comparable wall jet. In **Section 1**, many different scaling methods were demonstrated and the methods that were most common among researchers, or most suited for the current study, were used in the comparison. The sixteen cases of the current study were parametrically analyzed using the most appropriate scaling methods. In order to discover more about the effect of lip thickness, the vertical profiles of the integral length scale were computed.

3.1 Comparisons of past studies with the current study

In order to make good comparisons with past studies, the test case for $t = 0.125b$ & $B = 20b$ was used; the thinnest lip and largest height of co-flow region being closest to the past studies. The inlet conditions for all of the cases are listed in **Appendix F**. The first comparison was with Kruka & Eskinazi (1964), **Figure 83**, which allowed comparison with a flow of a similar velocity ratio. The length scale, $½\Delta y_M - y_m$, was scaled with x_t, refer to **Equation 3**. The superficial origin method, x_t, takes account of the velocity ratio, and the current study falls within the bounds set by Kruka & Eskinazi (1964). This method was used in a parametric comparison of the current data, as it takes into account the initial conditions of the flow as well as the maximum excess velocity at each downstream location. As can be seen in **Appendix F**, the initial conditions vary from case to case. Notably, the co-flow increases in velocity as B is reduced, so it was good to have a method of eliminating that variation.

The jet momentum scaling method of Narasimha et al. (1973) was used for a comparison of y_m, **Figure 84**, as it was the only study to propose a scaling method for the development of y_m. The jet momentum of the current study is at the upper limit of that used by Narasimha et al. (1973), but it can be seen that the current data falls within the bounds of the study. Narasimha et al. (1973) recommended jet momentum scaling for $x > 30b$, and this was borne out in the current results, as can be seen by the poor scaling for $10b < x < 20b$.

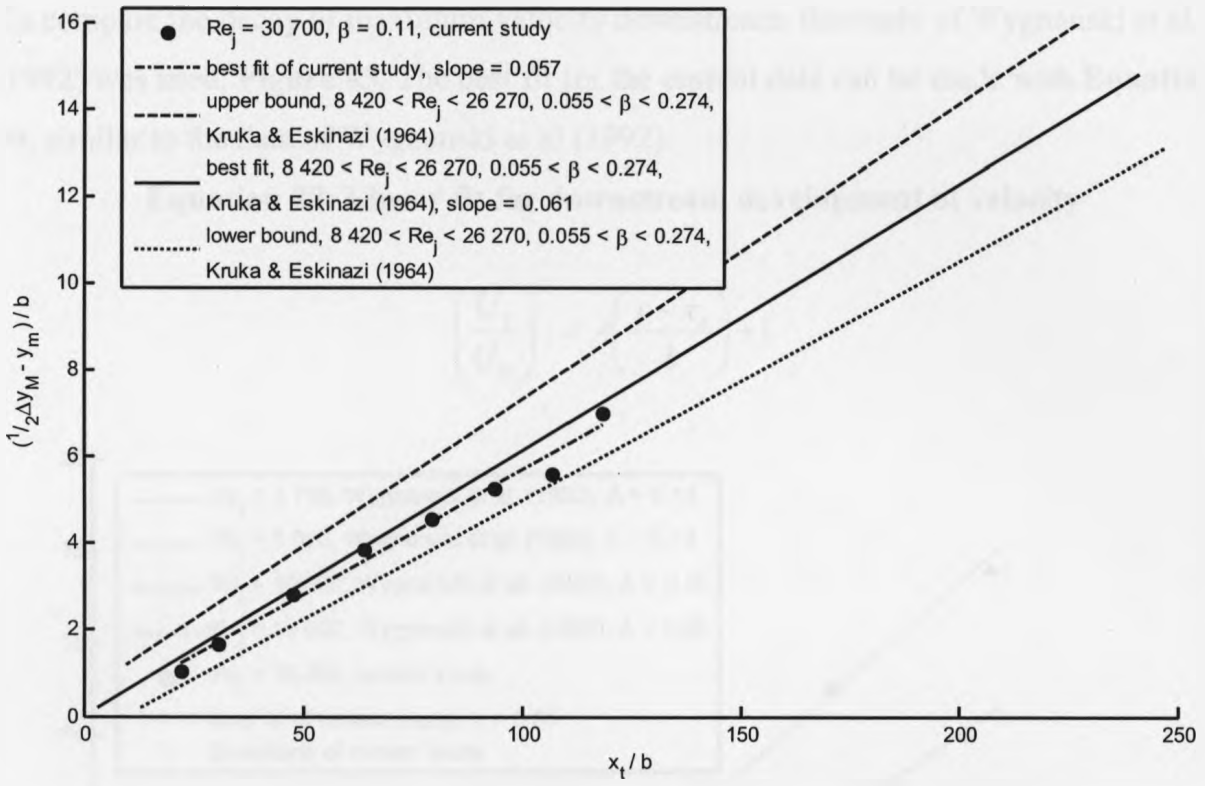

Figure 83: Case $t = 0.125b$ & $B = 20b$ superimposed on Figure 4 (Kruka & Eskinazi (1964))

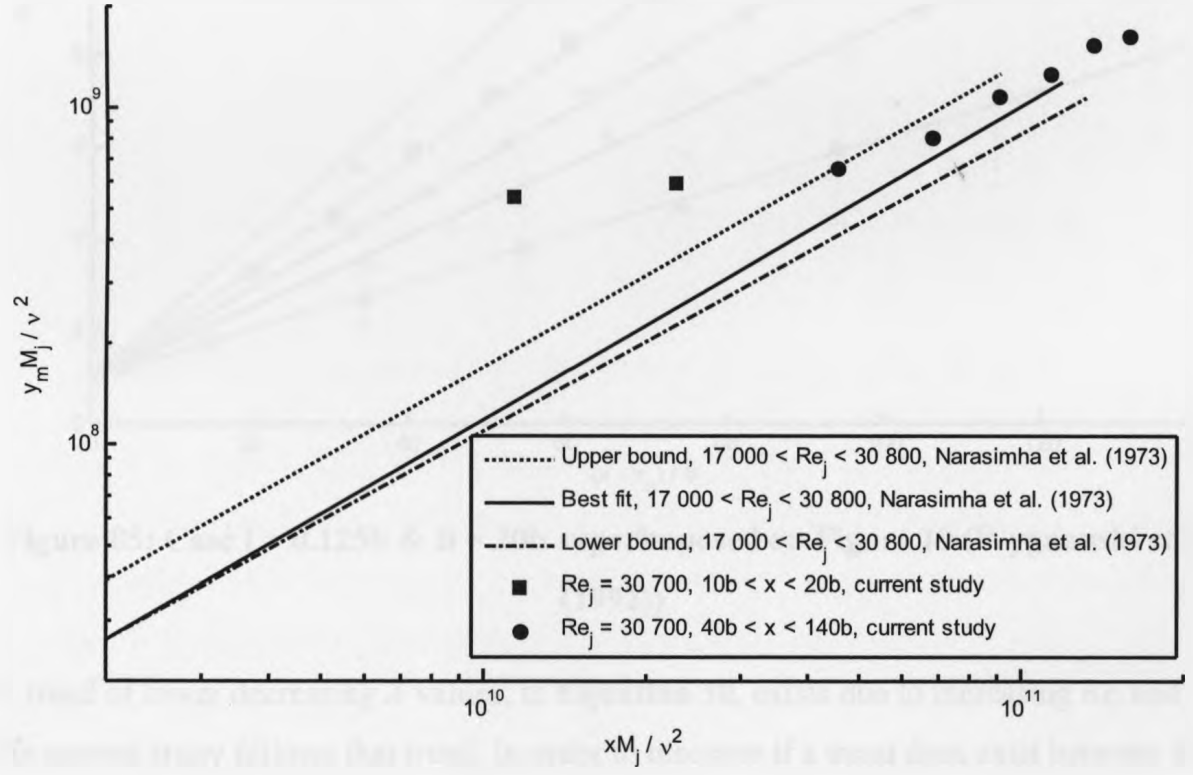

Figure 84: Case t = 0.125b & B = 20b superimposed on Figure 15 (Narasimha et al. (1973))

To compare the decay of maximum velocity downstream, the study of Wygnanski et al (1992) was used, **Figure 85**. The best fit for the current data can be made with **Equation 30**, similar to the data of Wygnanski et al (1992).

Equation 30: Linear fit for downstream development of velocity

$$\left(\frac{U_j}{U_m}\right)^2 = A\left(\frac{x-x_o}{b}\right)+1$$

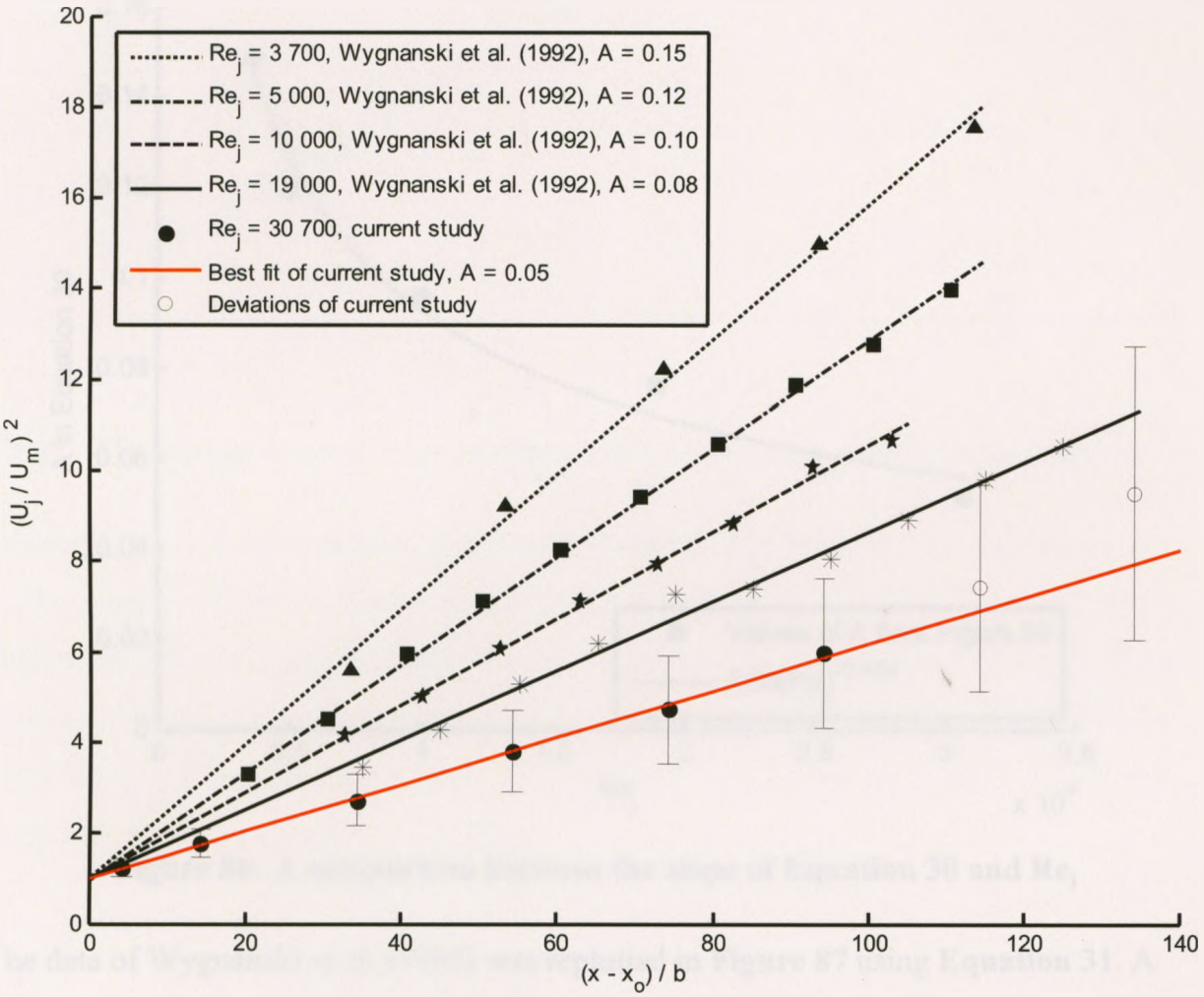

Figure 85: Case t = 0.125b & B = 20b superimposed on Figure 19 (Wygnanski et al. (1992))

A trend of lower decreasing A values, in **Equation 30**, exists due to increasing Re_j and the current study follows that trend. In order to discover if a trend does exist between Re_j and A, the data was plotted in **Figure 86** and a curve fitted to the data. An exponential curve was the best fit and a suggested development downstream of maximum velocity is

in **Equation 31**. A similar approach to predicting downstream development with Re_j was not observed during the literature review.

Equation 31: Expected maximum velocity development for different Re_j

$$\left(\frac{U_j}{U_m}\right)^2 = 6.08\,\mathrm{Re}_j^{-0.454}\left(\frac{x-x_o}{b}\right)+1$$

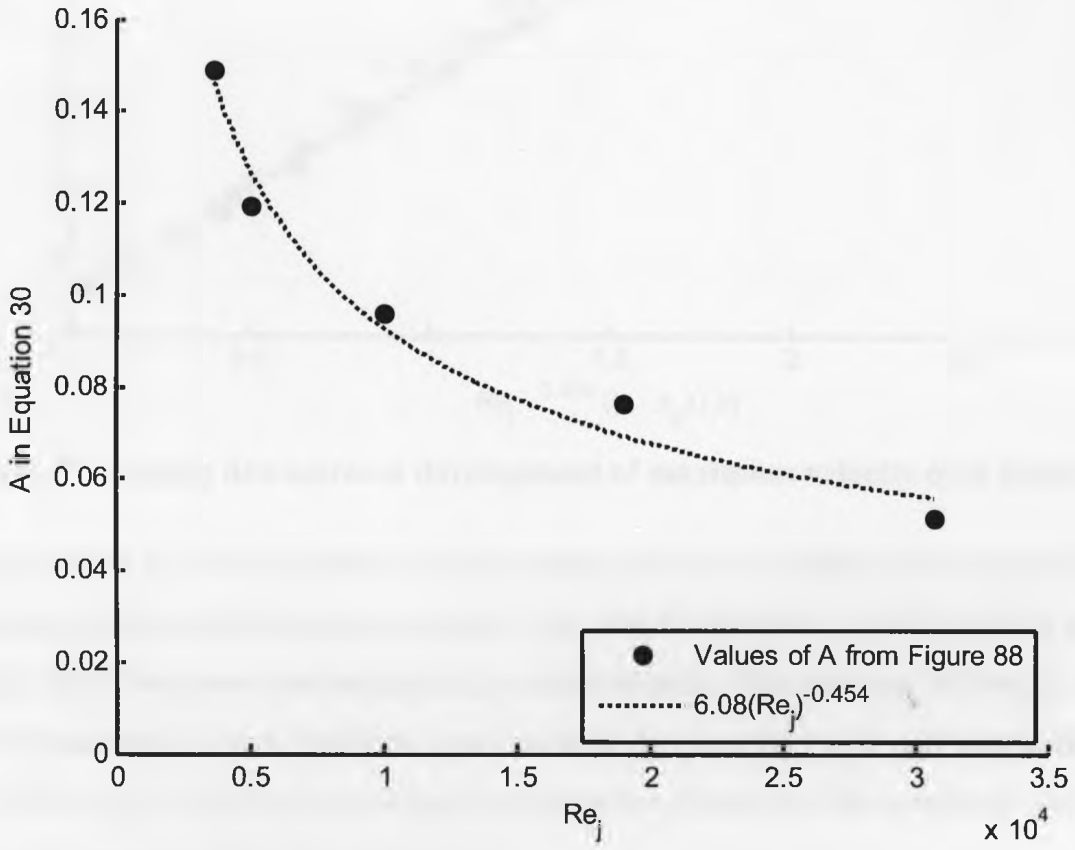

Figure 86: A comparison between the slope of Equation 30 and Re_j

The data of Wygnanski et al. (1992) was replotted in **Figure 87** using **Equation 31**. A new coefficient was used for the linear curve fit of **Equation 31**. The data can be seen to collapse well onto this single curve. This scaling method will be useful in future studies to gauge the decay of maximum velocity downstream for varying Re_j.

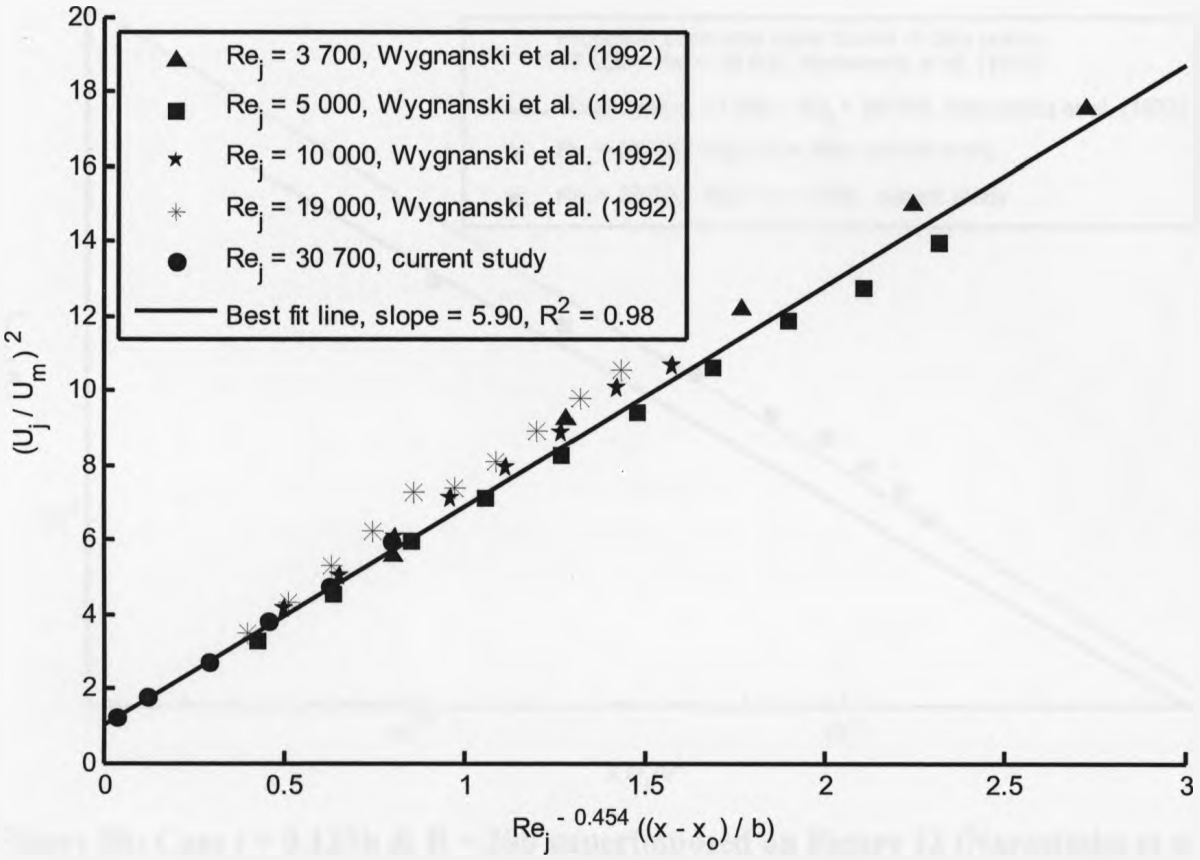

Figure 87: Scaling downstream development of maximum velocity on a single curve.

Wygnanski et al (1992) decided that the variation of slope in **Figure 85** was due to jet momentum; therefore the data was scaled with Narasimha et al.'s (1973) method in **Figure 88**. The current data appears at the upper bound of the plot and follows the decay downstream well. Again, the data is only suitable to be scaled by jet momentum for $x >$ 40b. Thus, by jet momentum scaling the maximum velocity and the maximum velocity height are comparable with past studies.

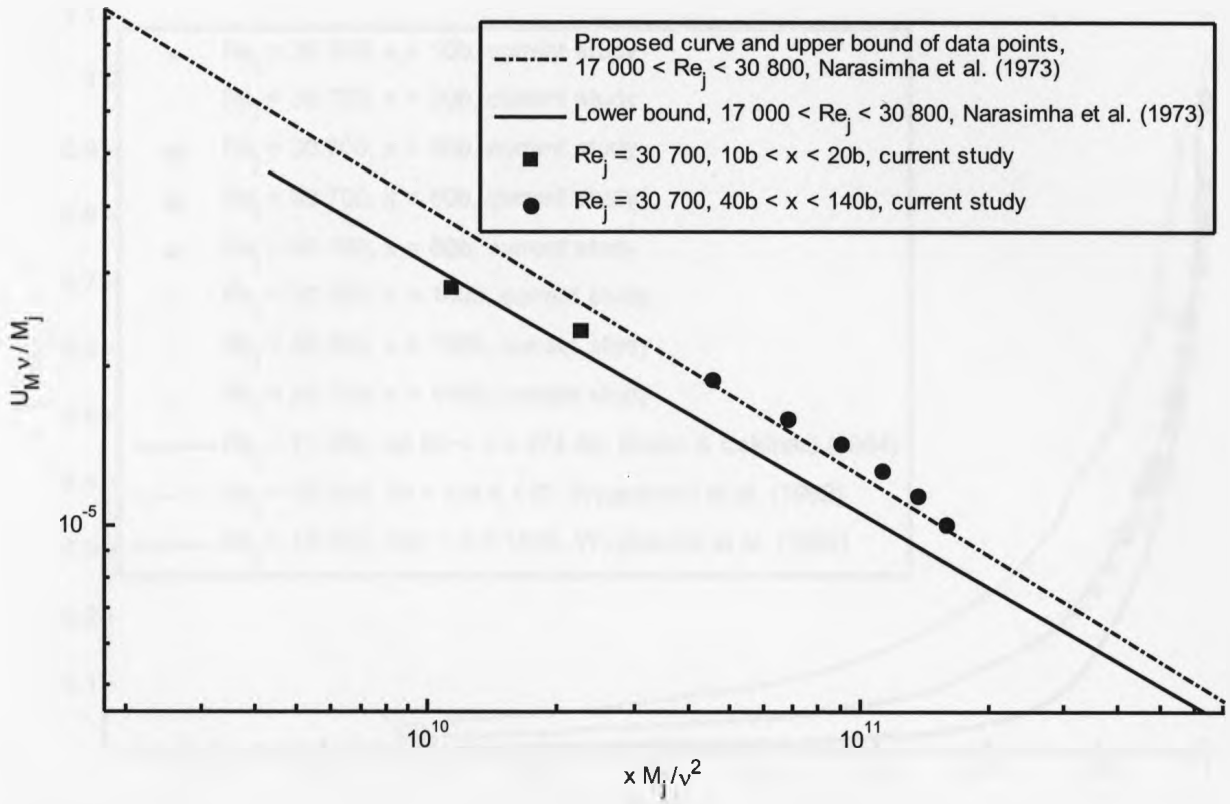

Figure 88: Case t = 0.125b & B = 20b superimposed on Figure 13 (Narasimha et al. (1973))

The maximum velocity and the maximum velocity height were used by Kruka & Eskinazi (1964) to scale the vertical velocity profile for $y/y_m < 1$. This scaling is demonstrated in **Figure 89** for the current data, the best fit line of Kruka & Eskinazi's (1964) and the data of Wygnanski et al. (1992). For 20b < v < 140b, the current data was similar to Wygnanski et al.'s (1992) data for Re_j = 19 000. Variations exist in the boundary layer of the flow. In **Section 1.4** it was discussed how a Re_j dependence exists within the inner region. However between the different studies there may be variations due to the surface conditions for the individual studies. The deviation in the current data for $x = 10b$, may be due to the jet not being fully developed.

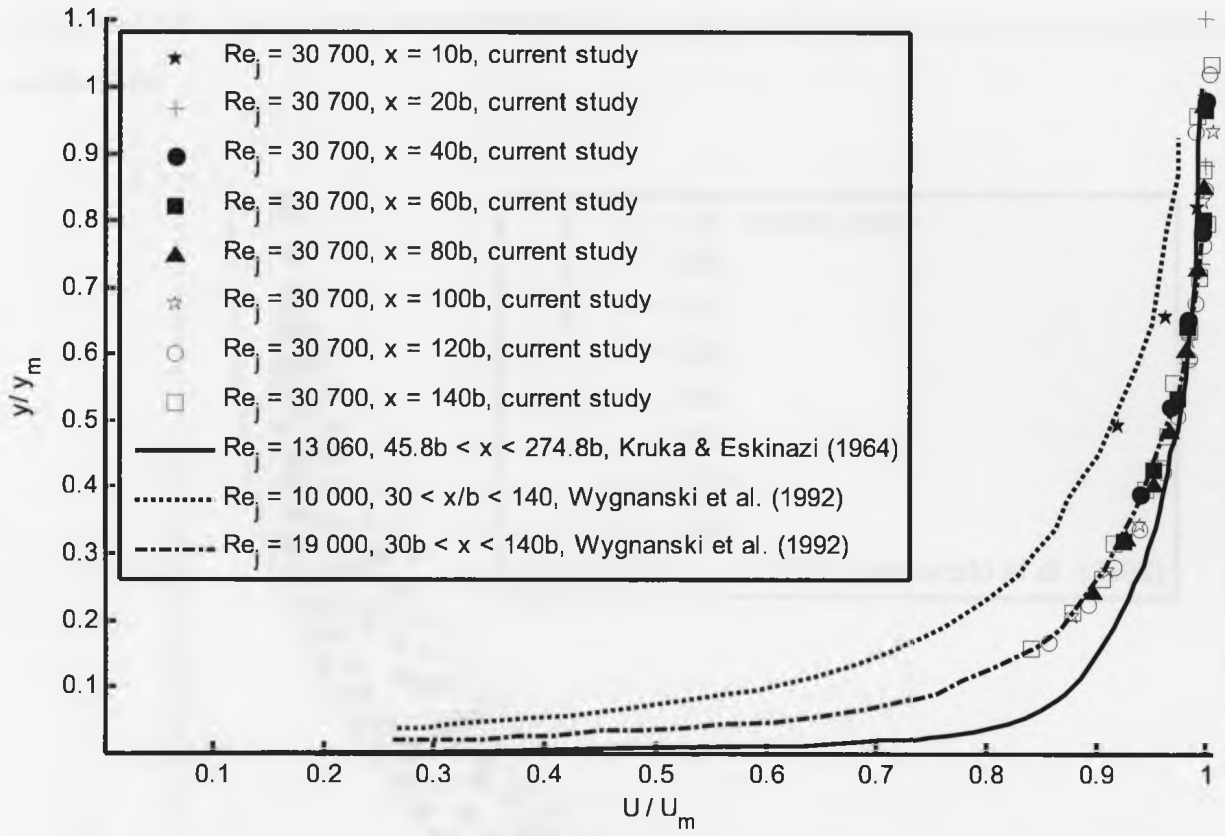

Figure 89: Case t = 0.125b & B = 20b superimposed on Figure 16 (Kruka & Eskinazi (1964))

The vertical profiles of velocity of the current study are compared to that of Wygnanski et al. (1992) in **Figures 90 & 91**. Two different half-heights are used in the scaling of the plots, $\frac{1}{2}\Delta y_M$ and $y_{M/2}$ respectively. The former method is that which has been used up to now and recommended for studies involving a co-flow, as the co-flow value is subtracted from the maximum velocity. The latter method does not account for a co-flow; in fact $\frac{1}{2}\Delta y_M$ simplifies to $y_{M/2}$ if a co-flow is not present, which was the case for the Wygnanski et al. (1992) data. In **Figure 90**, the current study appears above the best fit line of Wygnanski et al. (1992) when scaled with $\frac{1}{2}\Delta y_M$. In **Figure 91**, the profiles can be seen to align well with the best fit line when scaled with $y_{M/2}$. The better alignment when using $y_{M/2}$ indicates that the current study may be compared to studies that do not have a co-flow. This agrees with the findings of Patel that for $\beta < 0.167$, a wall jet behaves as though a co-flow does not exist, as discussed in **Section 1.3**. The half-height ($y_{M/2}$) was scaled in **Figure 92**, and compared with Abrahamsson et al.'s (1994) data. Abrahamsson et al. (1994) took care to not have a co-flow and a good match can be seen between that

study and the current data, demonstrating the growth of the wall jet in the current study is acceptable.

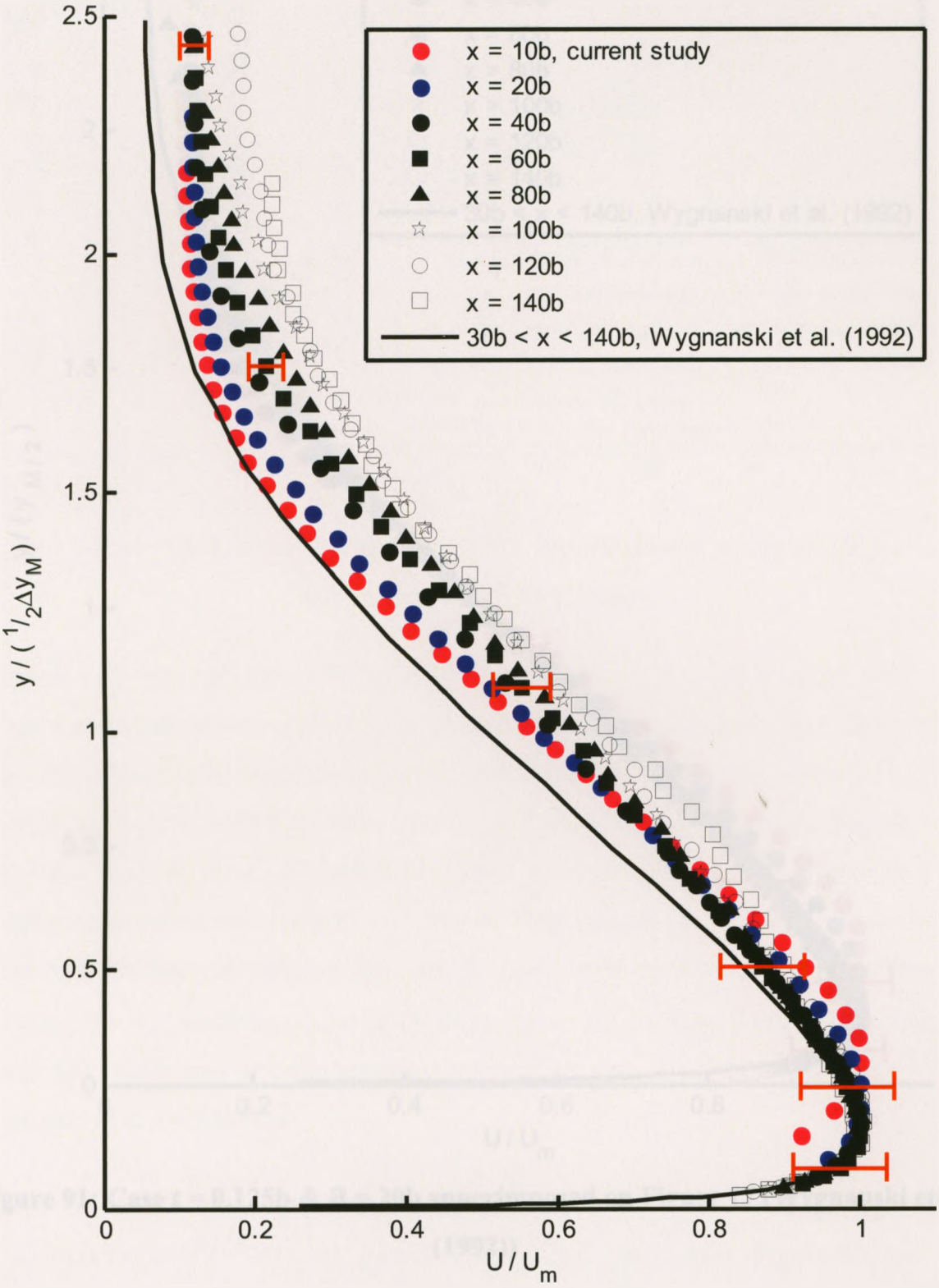

Figure 90: Case t = 0.125b & B = 20b superimposed on Figure 17 (Wygnanski et al. (1992))

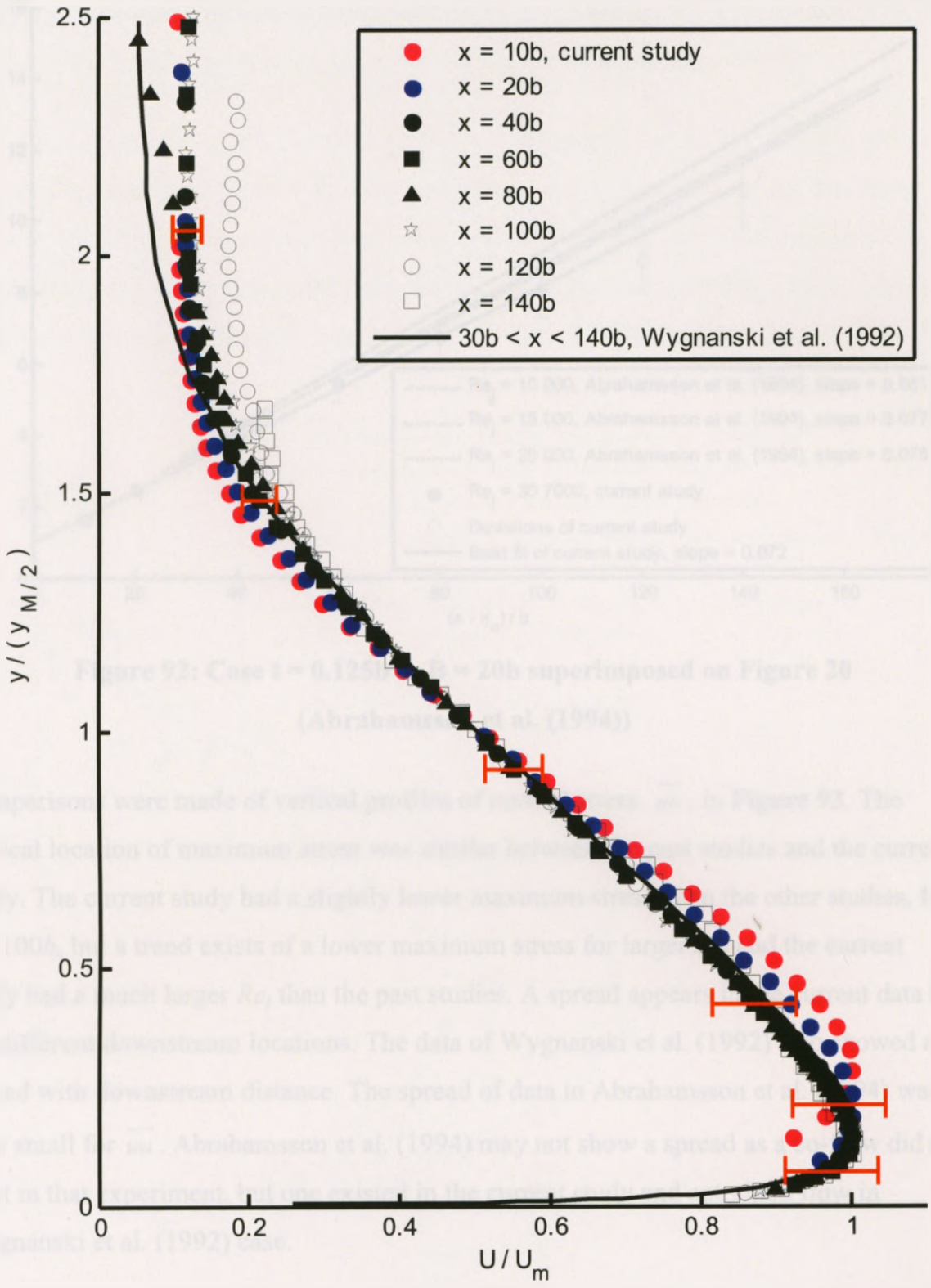

Figure 91: Case t = 0.125b & B = 20b superimposed on Figure 17 (Wygnanski et al. (1992))

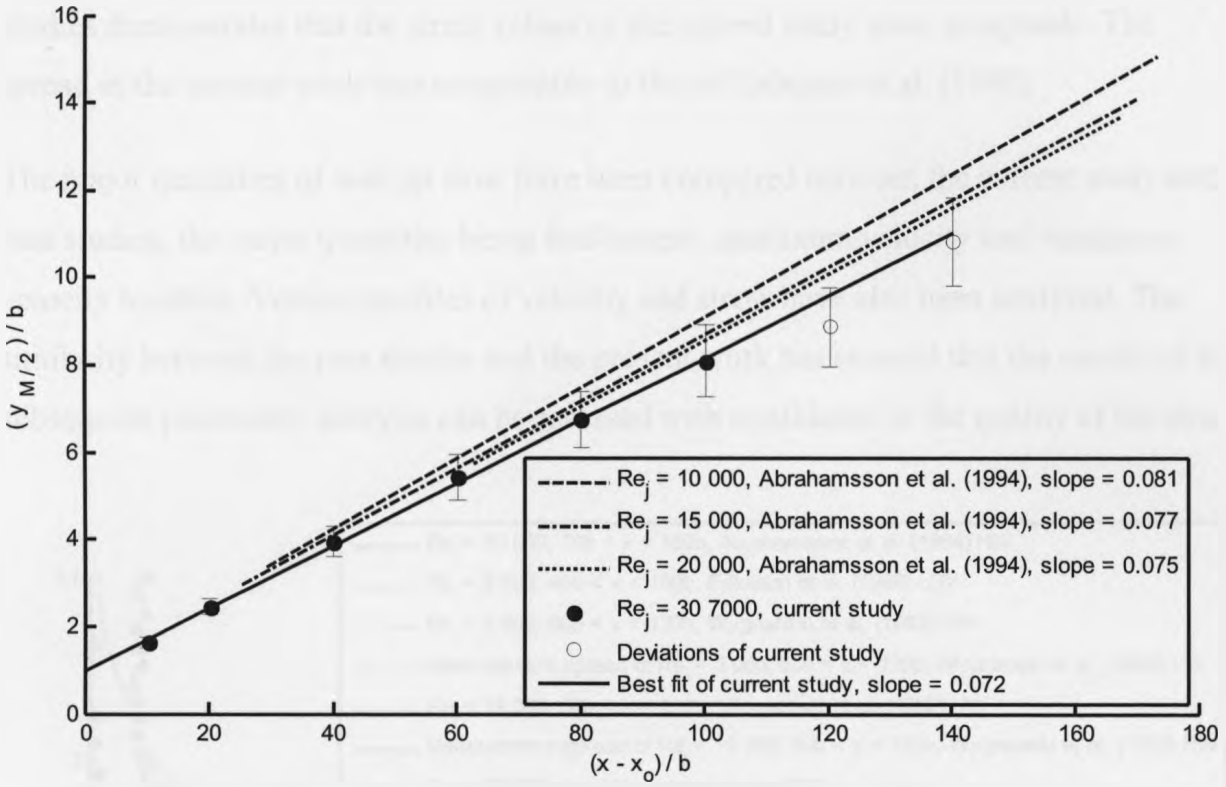

Figure 92: Case t = 0.125b & B = 20b superimposed on Figure 20 (Abrahamsson et al. (1994))

Comparisons were made of vertical profiles of normal stress, $\overline{uu}$, in **Figure 93**. The vertical location of maximum stress was similar between the past studies and the current study. The current study had a slightly lower maximum stress, than the other studies, for $x < 100b$, but a trend exists of a lower maximum stress for larger Re_j and the current study had a much larger Re_j than the past studies. A spread appears in the current data for the different downstream locations. The data of Wygnanski et al. (1992) also showed a spread with downstream distance. The spread of data in Abrahamsson et al. (1994) was very small for $\overline{uu}$. Abrahamsson et al. (1994) may not show a spread as a co-flow did not exist in that experiment, but one existed in the current study and entrained flow in Wygnanski et al. (1992) case.

The comparison of the $\overline{vv}$ normal stress, **Figure 94**, showed remarkable similarity to Abrahamsson et al.'s (1994) work, as well as the $\overline{uv}$ Reynolds stress, **Figure 95**. As discussed in **Section 1.9**, the hot-wire studies understandably have lower values of $\overline{vv}$ & $\overline{uv}$ stress than that of an LDV study. However the good agreement with past hot-wire

studies demonstrates that the stress values of the current study were acceptable. The spread in the current work was comparable to that of Eriksson et al. (1998).

The major quantities of wall jet flow have been compared between the current study and past studies, the major quantities being half-height, maximum velocity and maximum velocity location. Vertical profiles of velocity and stress have also been analyzed. The similarity between the past studies and the present work has ensured that the results of the subsequent parametric analysis can be assessed with confidence in the quality of the data.

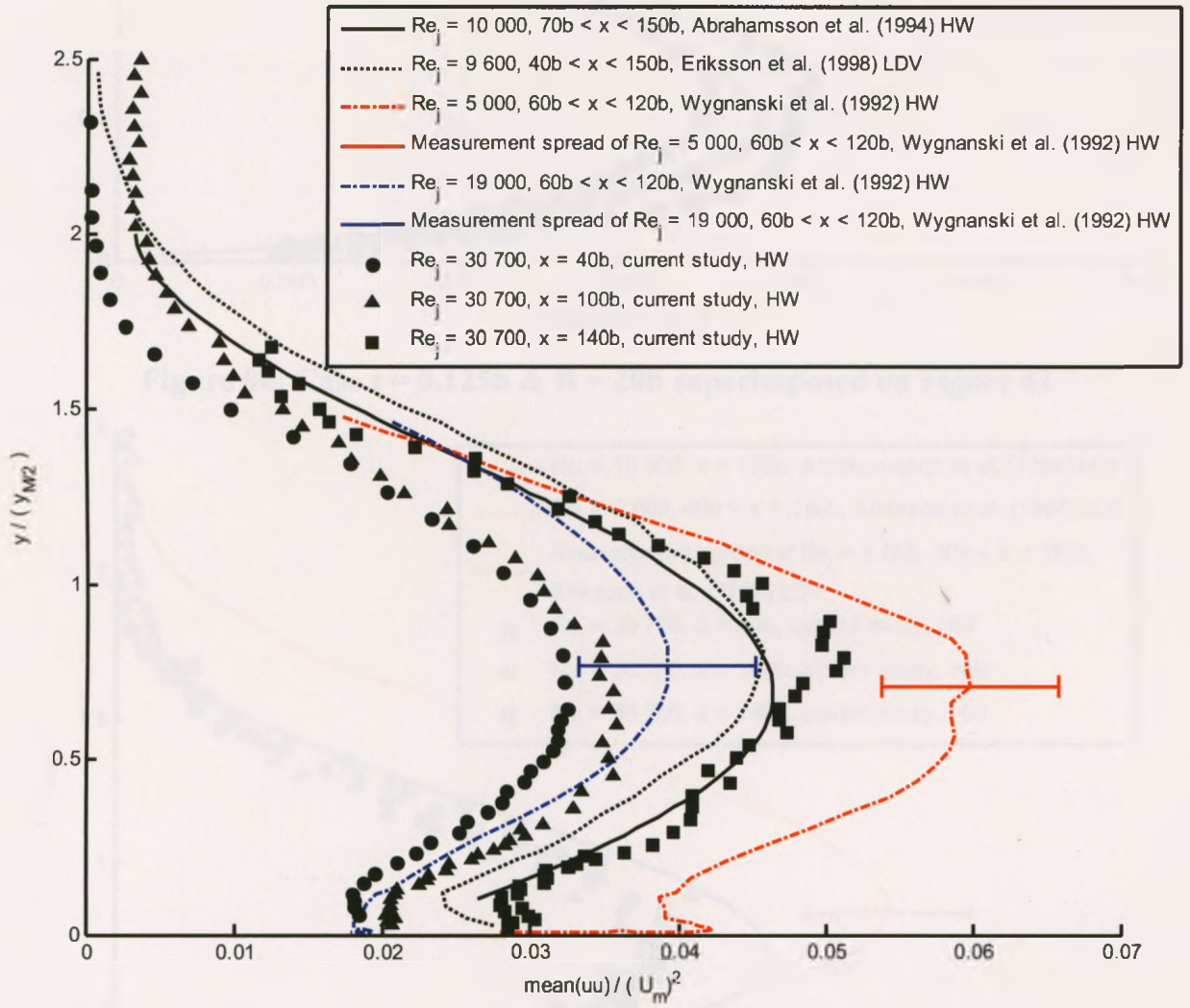

Figure 93: Case t = 0.125b & B = 20b superimposed on Figure 41.

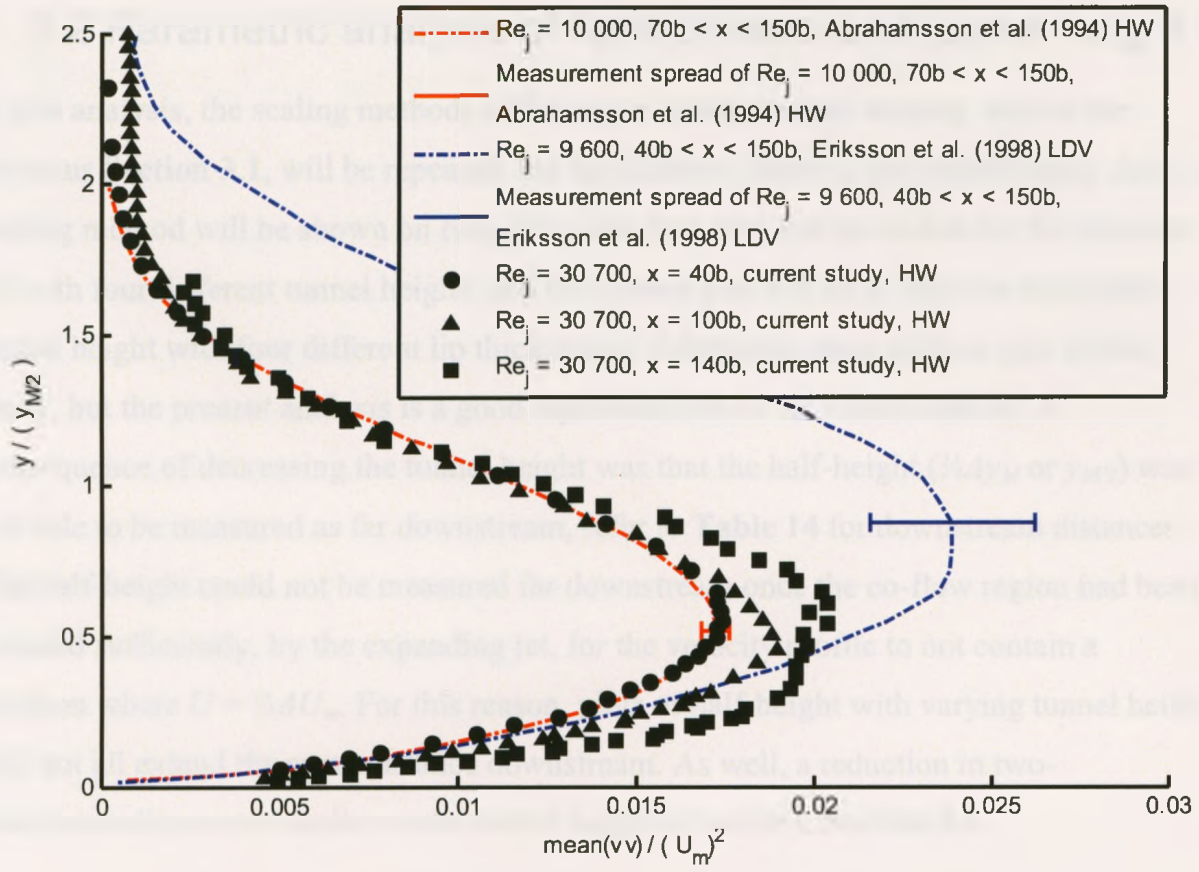

Figure 94: Case t = 0.125b & B = 20b superimposed on Figure 42

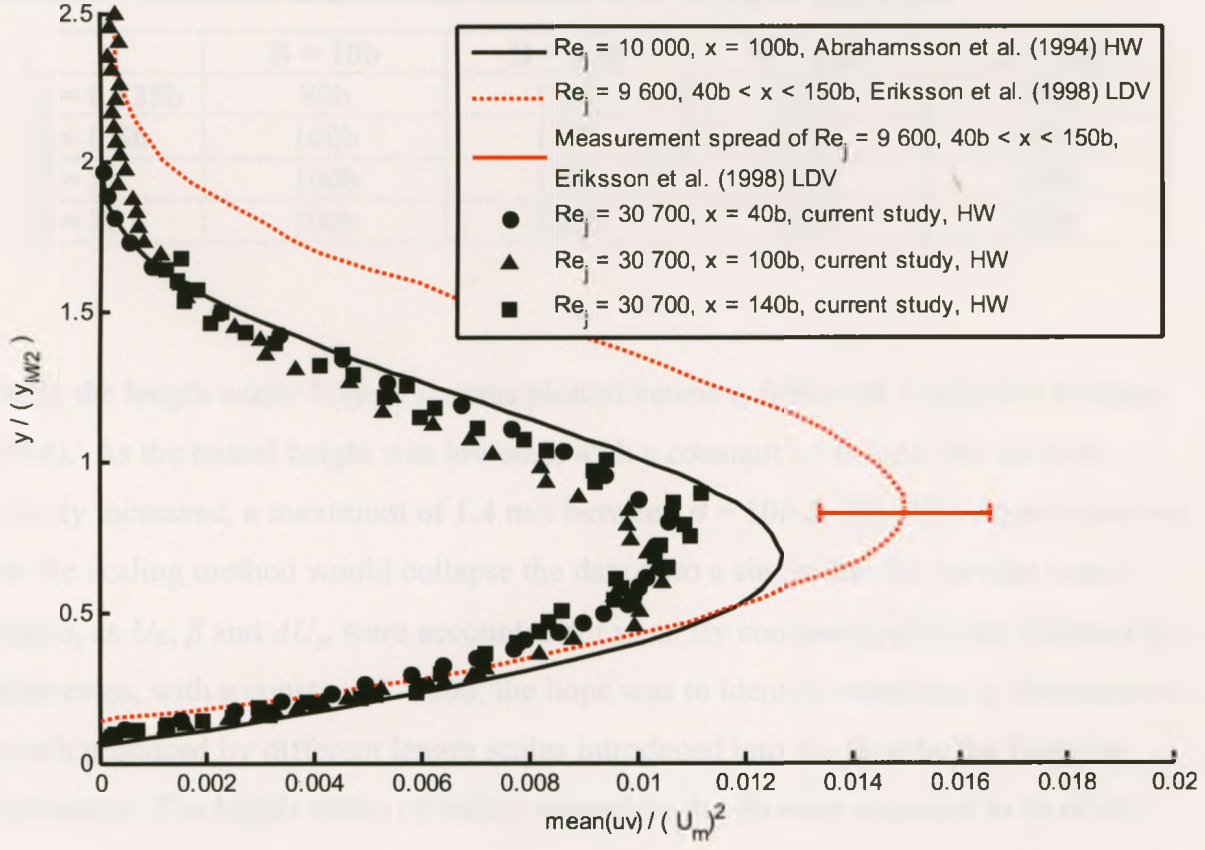

Figure 95: Case t = 0.125b & B = 20b superimposed on Figure 43

3.2 Parametric analysis of lip thickness and tunnel height

In this analysis, the scaling methods of the major quantities and stresses, used in the previous **Section 3.1**, will be repeated, but for different cases of the current study. Each scaling method will be shown on two plots. The first plot will be of data for the thinnest lip with four different tunnel heights and the second plot will be of data for the highest tunnel height with four different lip thicknesses. Additional cases exist as part of this study, but the present analysis is a good representation of the whole data set. A consequence of decreasing the tunnel height was that the half-height ($½\Delta y_M$ or $y_{M/2}$) was not able to be measured as far downstream, refer to **Table 14** for downstream distances. The half-height could not be measured far downstream once the co-flow region had been reduced sufficiently, by the expanding jet, for the velocity profile to not contain a location where $U = ½\Delta U_m$. For this reason, plots of half-height with varying tunnel height will not all extend the same distance downstream. As well, a reduction in two-dimensionality occurs earlier as the tunnel height is lowered, **Section 2.6**.

Table 14: Maximum downstream distance that $½\Delta y_M$ or $y_{M/2}$ exists

	B = 10b	**B = 13b**	**B = 16b**	**B = 20b**
t = 0.125b	80b	120b	140b	160b
t = 0.5b	100b	120b	140b	160b
t = 1b	100b	120b	140b	140b
t = 2b	100b	120b	140b	160b

Firstly the length scale, $½\Delta y_M - y_m$, was plotted versus x_t following Kruka and Eskinazi (1964). As the tunnel height was lowered, with a constant t = 0.125b, the co-flow velocity increased, a maximum of 1.4 m/s between $B = 10b$ & $20b$. The expectation was that the scaling method would collapse the data onto a single line for varying tunnel heights, as U_E, β and ΔU_m were accounted for in x_t. By comparing plots for different lip thicknesses, with a constant $B = 20b$, the hope was to identify variations in downstream growth produced by different length scales introduced into the flow by the finite lip thicknesses. The length scales of eddies created by the lip were expected to be of the same order of magnitude as the lip thickness. With larger eddies introduced into the flow,

the exchange of momentum between the co-flow and jet was expected to increase and cause the jet to thicken at a greater rate.

The result was that data collapsed well for varying both t and B, the case for different B is in **Figure 96**. In **Appendix G, Figure 122** the scaling was repeated for varying t and a good collapse of data occurred. The scaling method proved to take into account the variations in co-flow velocity. No trend was observed from the variations in t and B, and this could be due to the robust scaling method. In **Appendix D.iii** an estimation of error was made for half-height and the error was found to be small. In **Figure 96**, the error was on the order of the data markers size, but was not included for clarity in the figure. Evidently, with this particular scaling, differences caused by lip thickness were not evident, as the data collapses onto itself well.

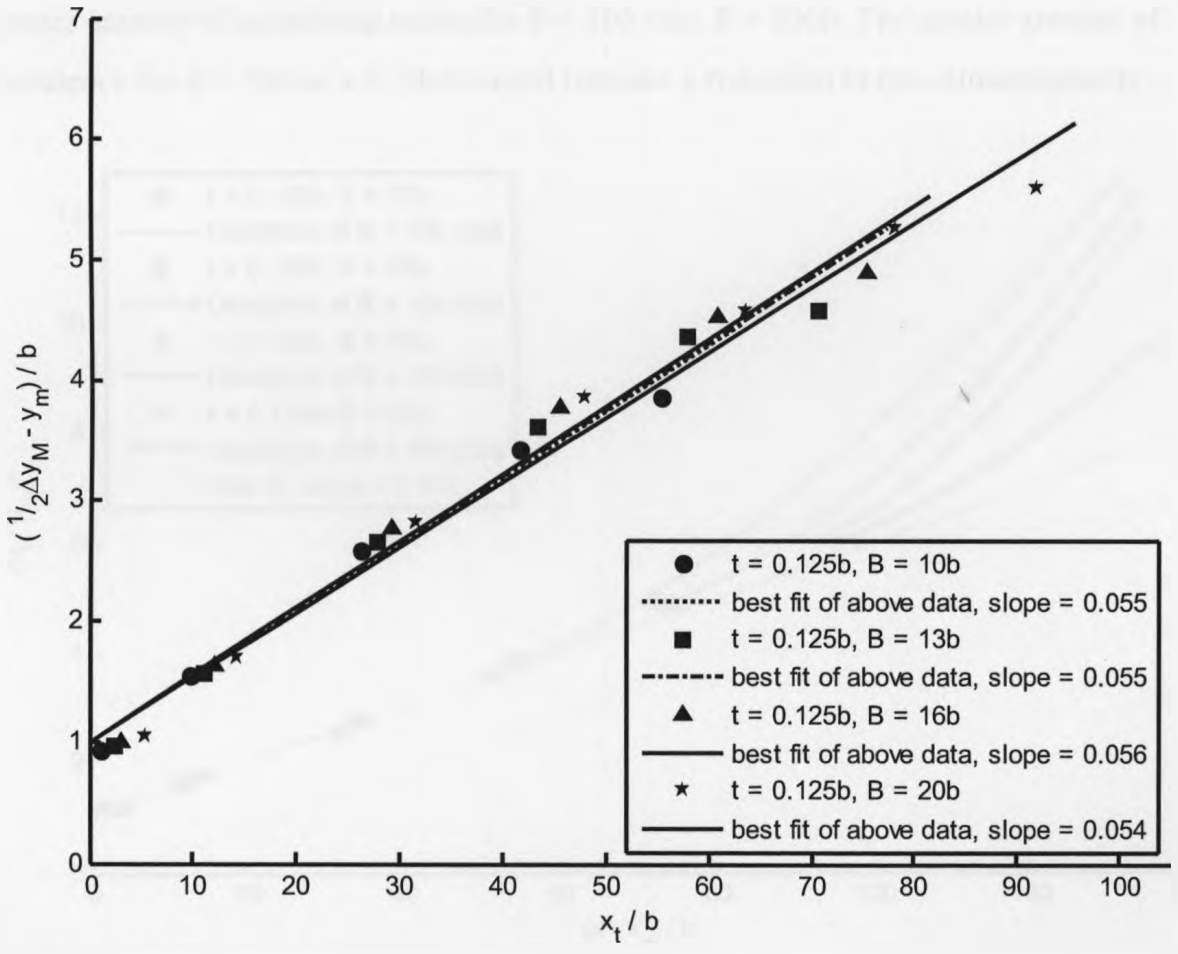

Figure 96: Scaling method for $\frac{1}{2}\Delta y_M - y_m$ of Kruka & Eskinazi (1964) for constant lip thickness

Using Wygnanski et al.'s (1992) scaling method, $\left(\frac{U_j}{U_m}\right)^2$ from **Section 1.5**, the effect of B and t on maximum velocity was examined, **Figures 97 & 98**. In **Figure 97**, as the tunnel height is reduced, it can be seen to have an effect on U_m at $x = 60b$, $80b$ & $100b$. The different plots diverge in order of tunnel height. Not all of the plots should have extended up to $x = 140b$, on the basis of poor two-dimensionality, but the data was included to demonstrate the divergence of the data more plainly. An exponential fit was made of the divergent data to find if the deviation could be predicted, but a good fit could not be made. The decrease in U_m with lower tunnel height was most likely due to the breakdown in two-dimensionality, which is enforced by comparing plots of turbulence intensity. In **Appendix G, Figures 123 & 124** are plots of turbulence intensity and demonstrate that at x = 60b, similar levels of turbulence occur for $B = 10b$ and $B = 100b$, but at $x = 100b$ a greater amount of turbulence exists for $B = 10b$ than $B = 100b$. The greater amount of turbulence for $B = 10b$ at x = $100b$ would indicate a reduction in two-dimensionality.

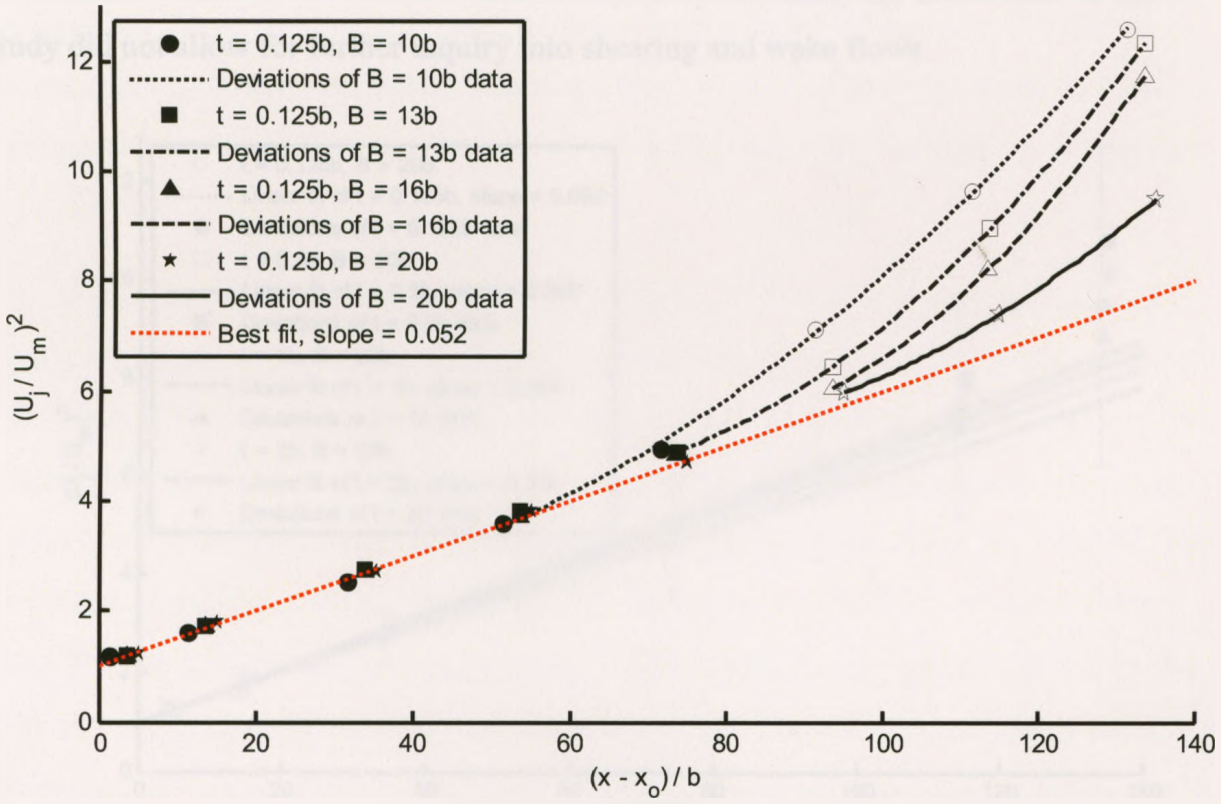

Figure 97: Maximum velocity scaling method of Wygnanski et al. (1992) for constant lip thickness

In **Figure 98**, the lip thickness was varied and a spread in $\left(\frac{U_j}{U_m}\right)^2$ appeared, although the spread was not larger than the error bounds of the plots, making the spread insignificant. Kacker and Whitelaw (1971) found that a thicker lip ($t = 1.14b$ versus $0.126b$) caused the flow to spread more rapidly (a 24% increase in $y_{M/2}$) and in turn U_m was reduced (19% decrease in U_m) due to a finite amount of momentum in the flow, refer to **Section 1.7 Figure 27**. This result enforces the concept of larger eddies produced by the lip causing an increase in mixing between the jet and co-flow. The current results only show a divergence in the decay of U_m, not a trend with increasing lip thickness. Possibly, a different flow situation is created by the thicker lip. A possible scenario is that $t = 0.125b$ and $0.5b$ are thin enough to produce a shearing flow, whereas $t = 1b$ & $2b$ produce a wake flow. An example of the different flow patterns are in **Figure 99**. Only the wake flow case was anticipated, with the scale of eddies the same order as the lip thickness. The different flow patterns between shearing and wake flow may give rise to different rates of momentum transfer between the co-flow and jet. Unfortunately the time frame of this study did not allow for further inquiry into shearing and wake flows.

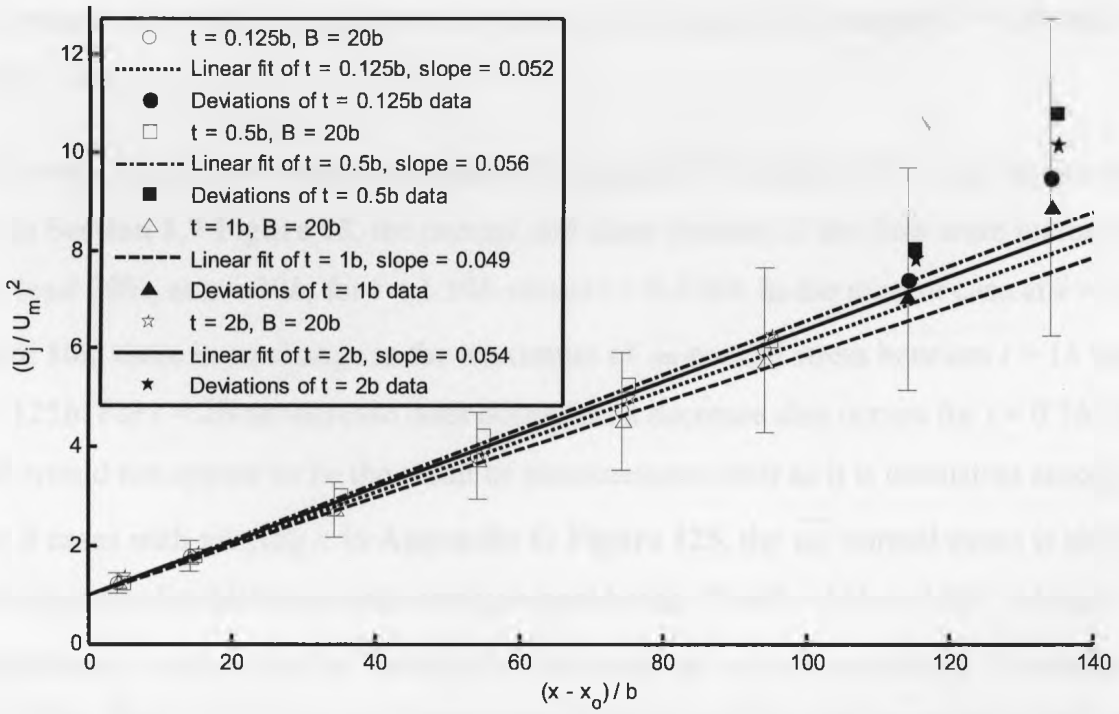

Figure 98: Maximum velocity scaling method of Wygnanski et al. (1992) for constant tunnel height. Error bounds for $t = 0.125b$ are included in the plot.

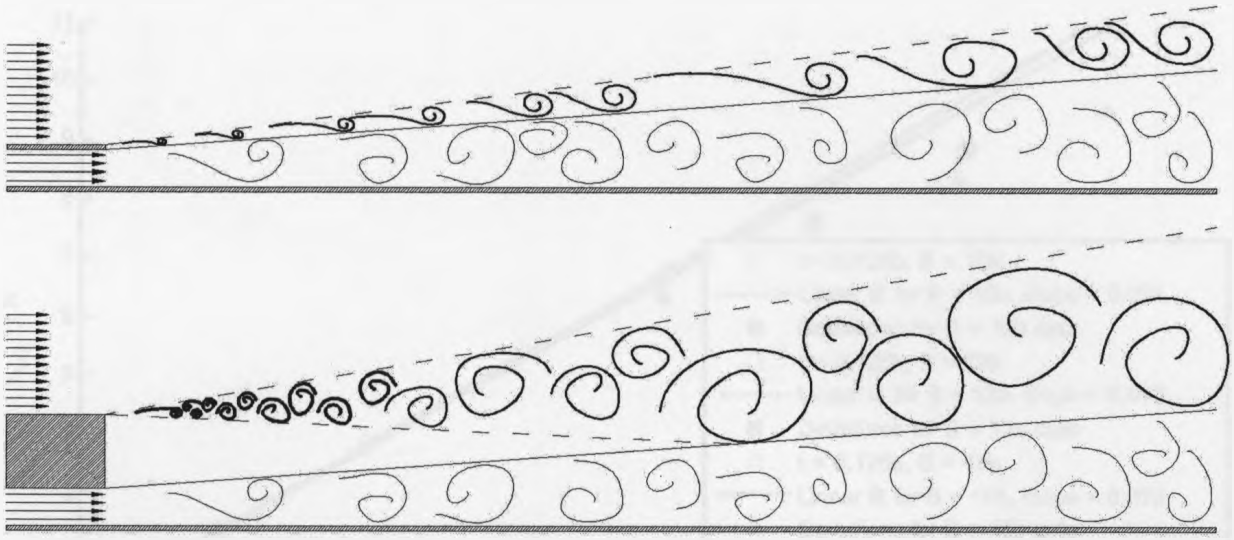

Figure 99: (top) Structure of mixing shear layers, based on the flow visualization of Slessor et al. (1998). (bottom) Structure of wake flow, based on the flow visualization of Taneda (1958). Note that the current flow does not contain periodicity.

The half-height ($y_{M/2}$) was scaled in **Figures 100 & 101** following Abrahamsson's et al (1994) study. The growth of $y_{M/2}$ did not vary for different tunnel heights or different lip thicknesses. There was no clear trend, as found by Kacker & Whitelaw (1971), of an increase in $y_{M/2}$ with lip thickness. The lack of a trend was consistent among the other combinations of t and B cases that were tested in this study (for example $B = 16b$ and $t = 0.125b$ - $2b$).

The stresses in the flow were measured by Kacker and Whitelaw (1971), and as can be seen in **Section 1.7 Figure 28**, the normal and shear stresses of the flow were increased by at least 20%, at $x = 10b$, for $t = 1.14b$ versus $t = 0.126b$. In the present case at $x = 10b$, **Figure 102**, there is no change in the maximum of $\overline{uu}$ normal stress between $t = 1b$ versus $t = 0.125b$. For $t = 2$b an increase does occur, but a decrease also occurs for $t = 0.5b$. The result would not appear to be the result of measurement error as it is consistent among other B cases with varying t. In **Appendix G Figure 125**, the $\overline{uu}$ normal stress is shown with a constant lip thickness and varying tunnel height. For $B = 16b$ and $20b$, a larger maximum $\overline{uu}$ exists, which is likely due to the increase in co-flow velocity for smaller B. At x = 10b, for y < 3.5b, changes due to tunnel height would not be expected as the upper boundary is far away from the flow.

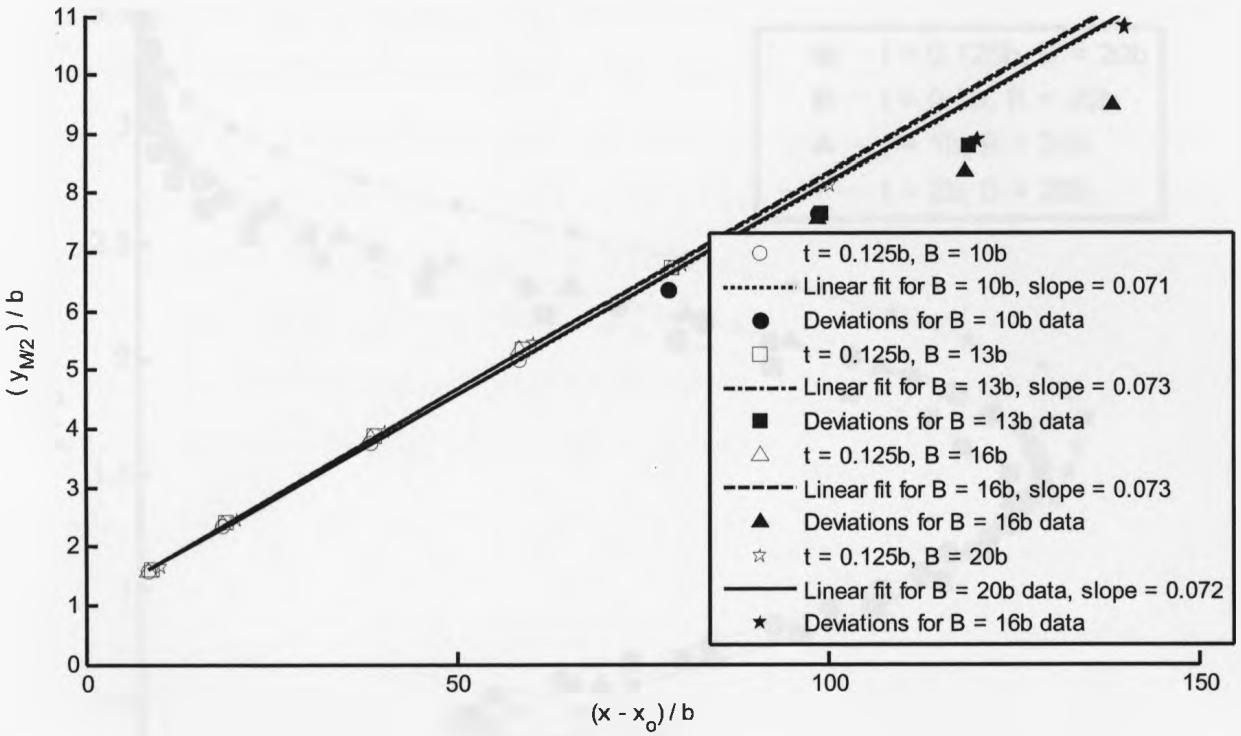

Figure 100: Scaling method for half-height of Abrahamsson et al. (1994) for constant lip thickness

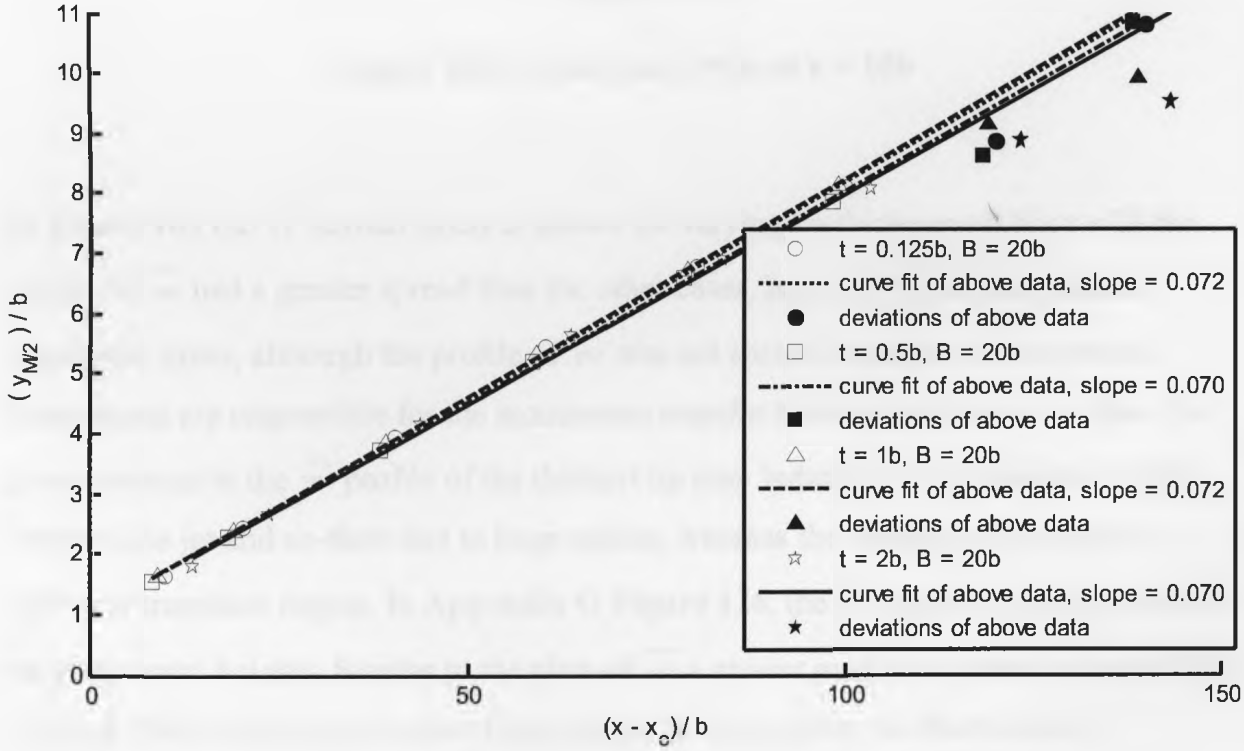

Figure 101: Scaling method for half-height of Abrahamsson et al. (1994) for constant tunnel height

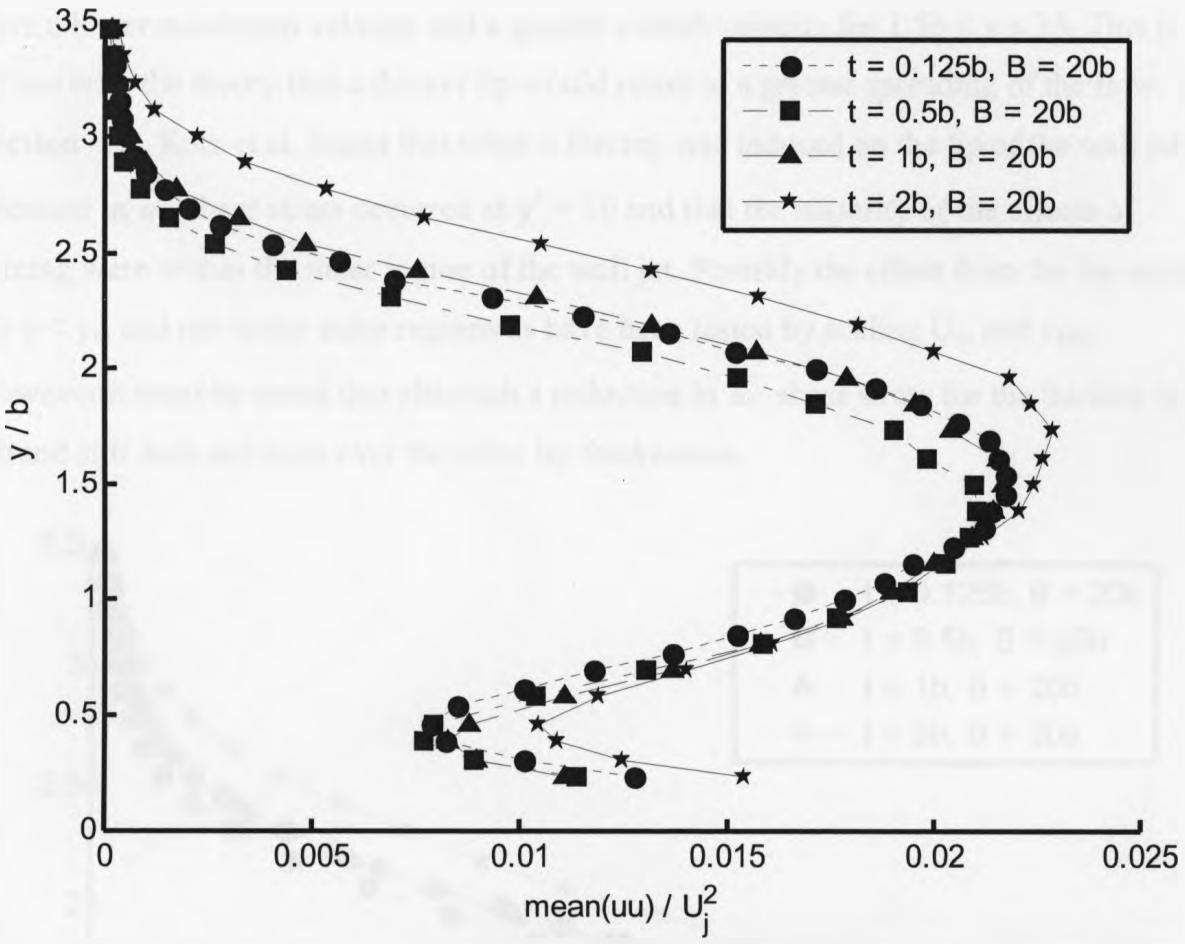

Figure 102: uu normal stress at x = 10b

In **Figure 103** the $\overline{vv}$ normal stress is shown for varying lip thicknesses. For $t = 2b$ the profile of $\overline{vv}$ had a greater spread than the other cases, but $t = 0.125$b had a similar maximum stress, although the profile of $\overline{vv}$ was not spread as much. As the vertical fluctuations are responsible for the momentum transfer between the jet and co-flow, the greater spread in the $\overline{vv}$ profile of the thickest lip may indicate a large transition region between the jet and co-flow due to large eddies, whereas the thinnest lip may have a narrower transition region. In **Appendix G Figure 126**, the $\overline{vv}$ normal stress is shown for varying tunnel heights. Similar to the plots of $\overline{uu}$ a greater maximum stress occurred for $B = 16b$ & $20b$, which again is most likely due to the increase in co-flow velocity.

In **Figure 104** the $\overline{uv}$ shear stress is compared for plots of varying lip thickness, alongside corresponding velocity profiles. For $t = 2b$ the velocity profile can be seen to

have a lower maximum velocity and a greater overall velocity for $1.5b < y < 3b$. This is in line with the theory that a thicker lip would result in a greater spreading of the flow. In **Section 1.7**, Katz et al. found that when a forcing was induced on the lip of the wall jet a decrease in $\overline{uv}$ shear stress occurred at $y^+ = 10$ and that the majority of the effects of forcing were within the inner region of the wall jet. Possibly the effect from the lip occurs for $y < y_m$ and not in the outer regions as have been tested by scaling U_m and $y_{M/2}$. However it must be noted that although a reduction in $\overline{uv}$ shear stress for the thickest lip a trend still does not exist over the other lip thicknesses.

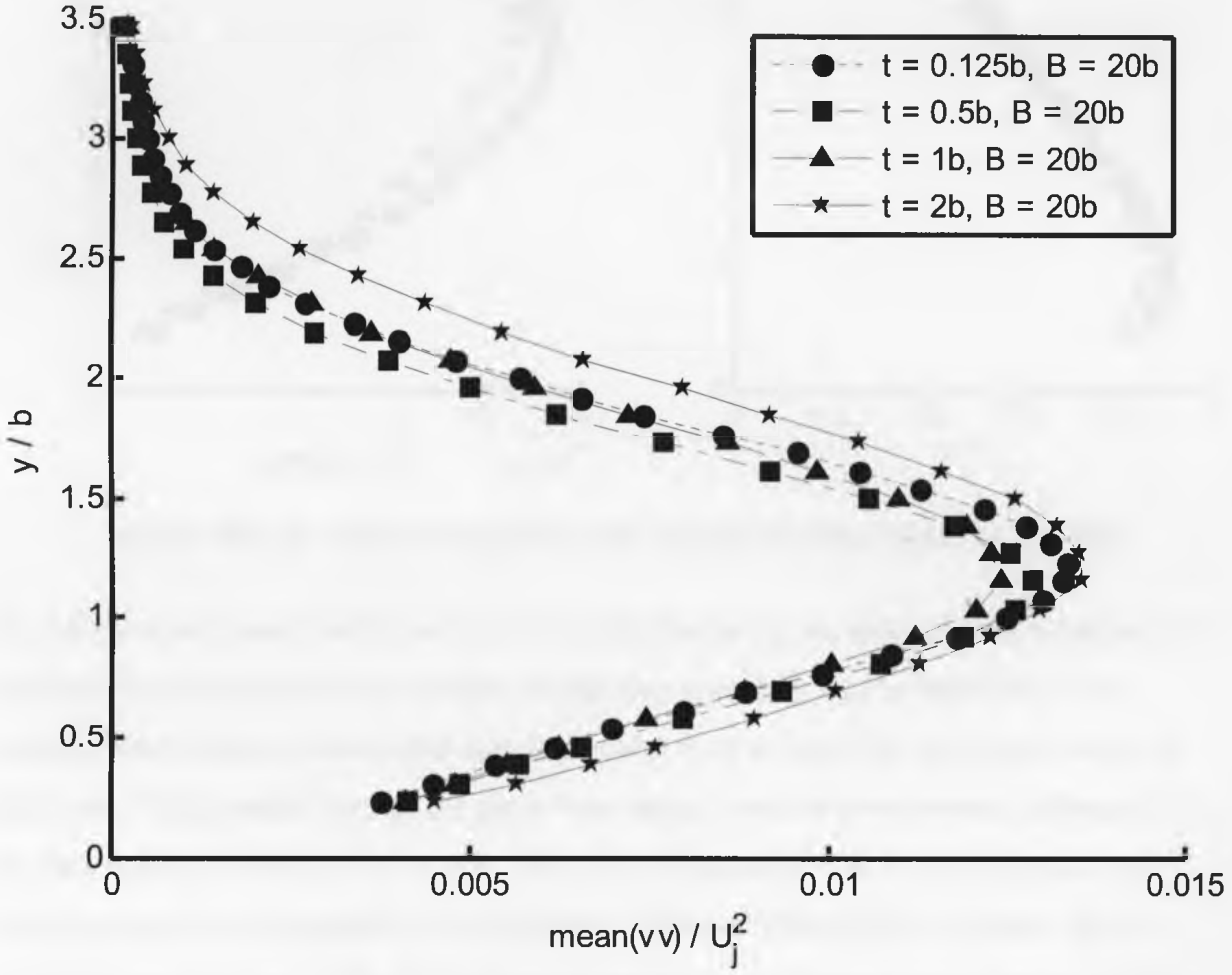

Figure 103: vv normal stress at x = 10b

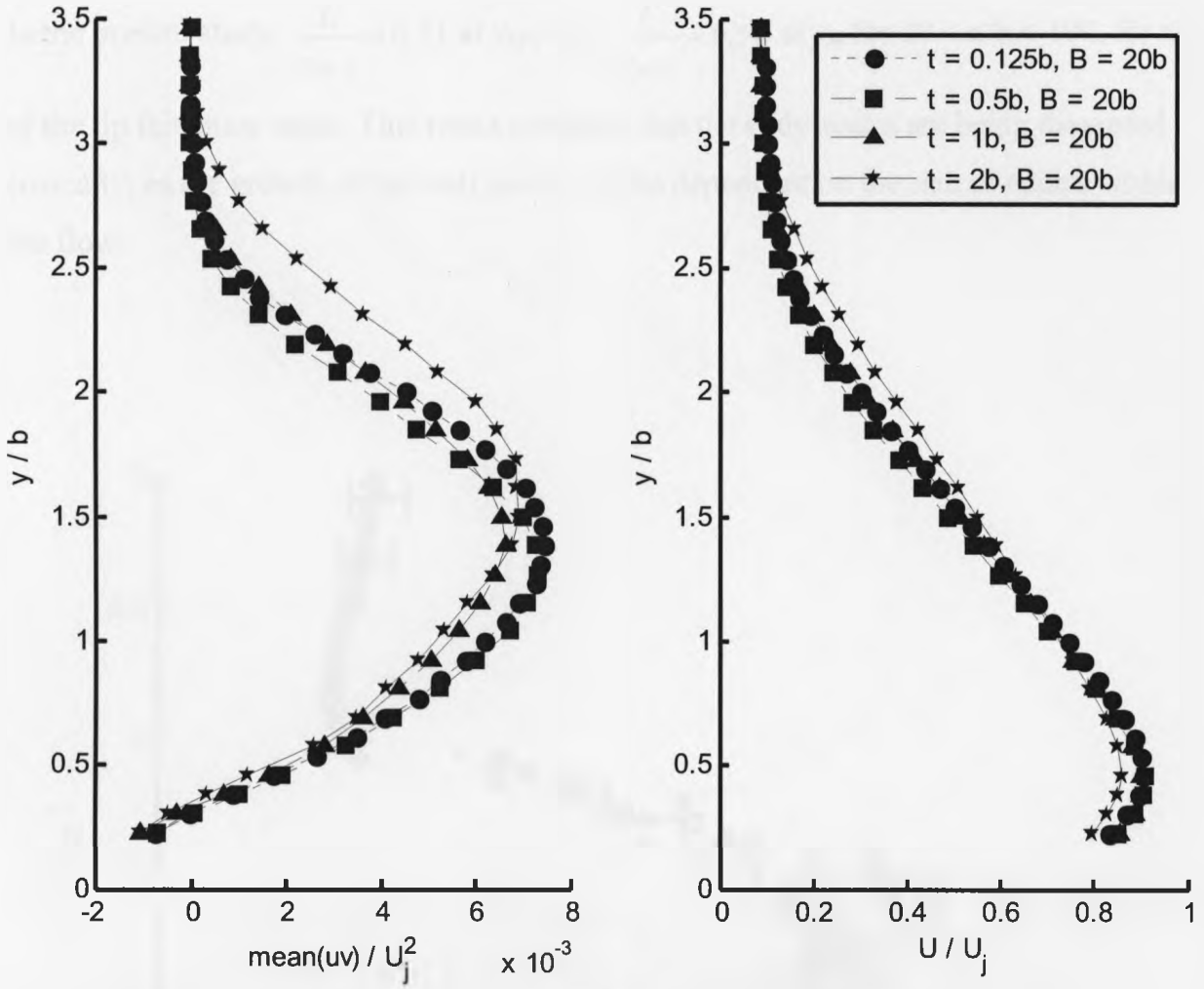

Figure 104: uv shear stress (left) and velocity profile (right) at x = 10b

In order to understand further the role of the lip thickness, the integral length scales (L) of the flow were calculated. The integral length was scaled by $y_{M/2}$ to determine if the profiles were similar downstream and also scaled by b to highlight differences from lip thickness. When scaled by $y_{M/2}$ the plots were largely similar downstream, although the profiles differed within the jet at $x = 10b$ & $20b$, **Figures 105 & 106**. Additional plots downstream are in **Appendix G** for reference, **Figures 128 & 129**. In **Figure 105**, $x = 10b$, the cases for $t = 0.125b$ & $0.5b$ can be seen to have a larger integral length scale just above the half height, this is also present at $x = 20b$, **Figure 106**. This longer length scale may show a variation the turbulence at the edge of the jet compared to cases $t = 1b$ & $2b$. Further downstream this longer length scale was not apparent. Gutmark & Wygnanski (1976) found that in a plane free jet, along the centreline, $\frac{L}{y_{M/2}} = 0.47$ for $30 < x/b < 90$.

In the present study, $\frac{L}{y_{M/2}} \approx 0.53$ at $y_{M/2}$ and $\frac{L}{y_{M/2}} \approx 0.54$ at y_m for 20 < x/b < 100, for all of the lip thickness cases. This result confirms that the eddy scales are being measured correctly, as the growth of the wall jets would be dependent on the size of eddies within the flow.

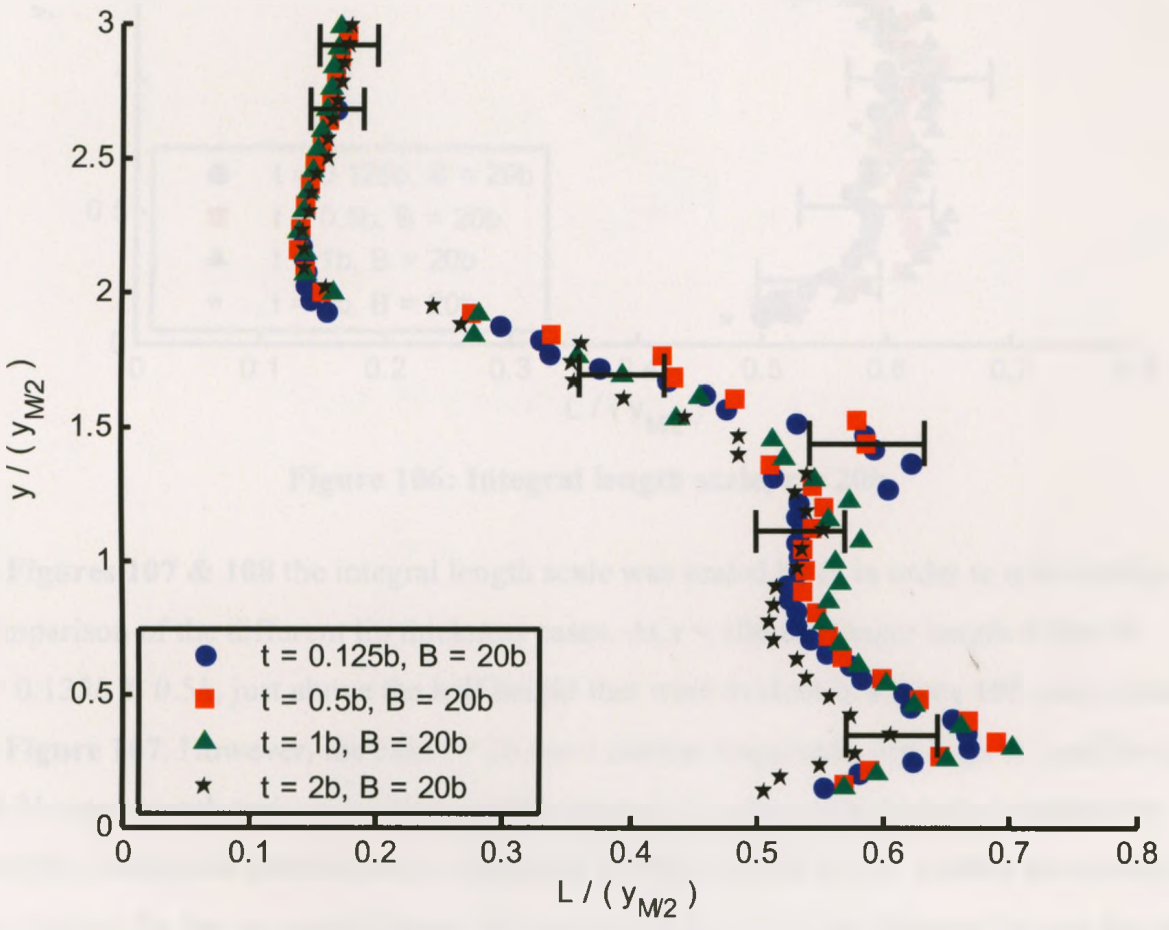

Figure 105: Integral length scale, x = 10b

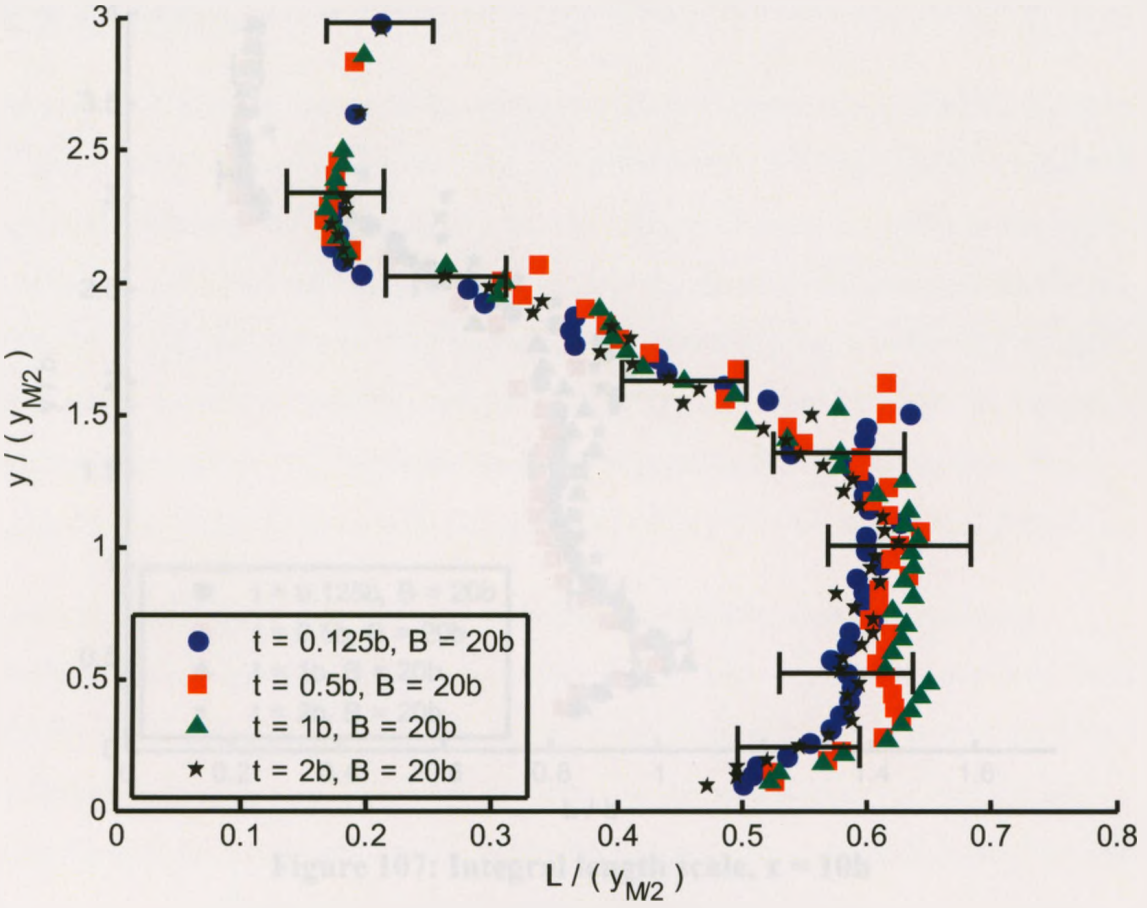

Figure 106: Integral length scale, x = 20b

In **Figures 107 & 108** the integral length scale was scaled by b, in order to make a direct comparison of the different lip thickness cases. At $x = 10b$ the longer length scales of $t = 0.125b$ & $0.5b$, just above the half height that were evident in **Figure 105**, are evident in **Figure 107**. However, the case $t = 2b$ has a similar magnitude, although the profile of $t = 2b$ was smooth and $t = 0.125b$ and $0.5b$ appears as a deviation from their respective profiles. Additional profiles are in **Appendix G Figures 130 & 131**. Farther downstream, the thickest lip has an overall longer integral length scale, but the thinnest lip case has the second longest integral length scale. The thin and thick lip must create different mechanisms in the flow to produce integral length scales of similar size, which are produced by lips that are an order of magnitude different in size. As the integral length scales are different in size between the different lip thickness cases, the fact that the integral length scale collapses well when scaled by $y_{M/2}$ enforces the fact that the development of the flow downstream was dependent on the size of the eddies within the respective flows.

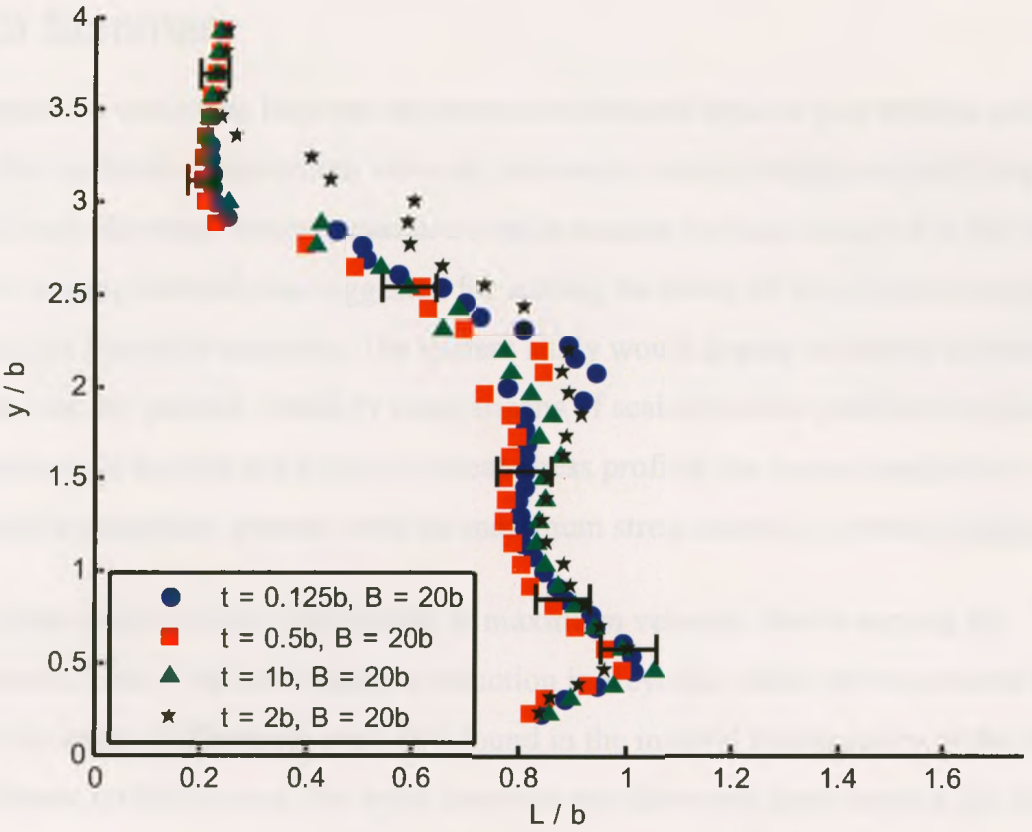

Figure 107: Integral length scale, x = 10b

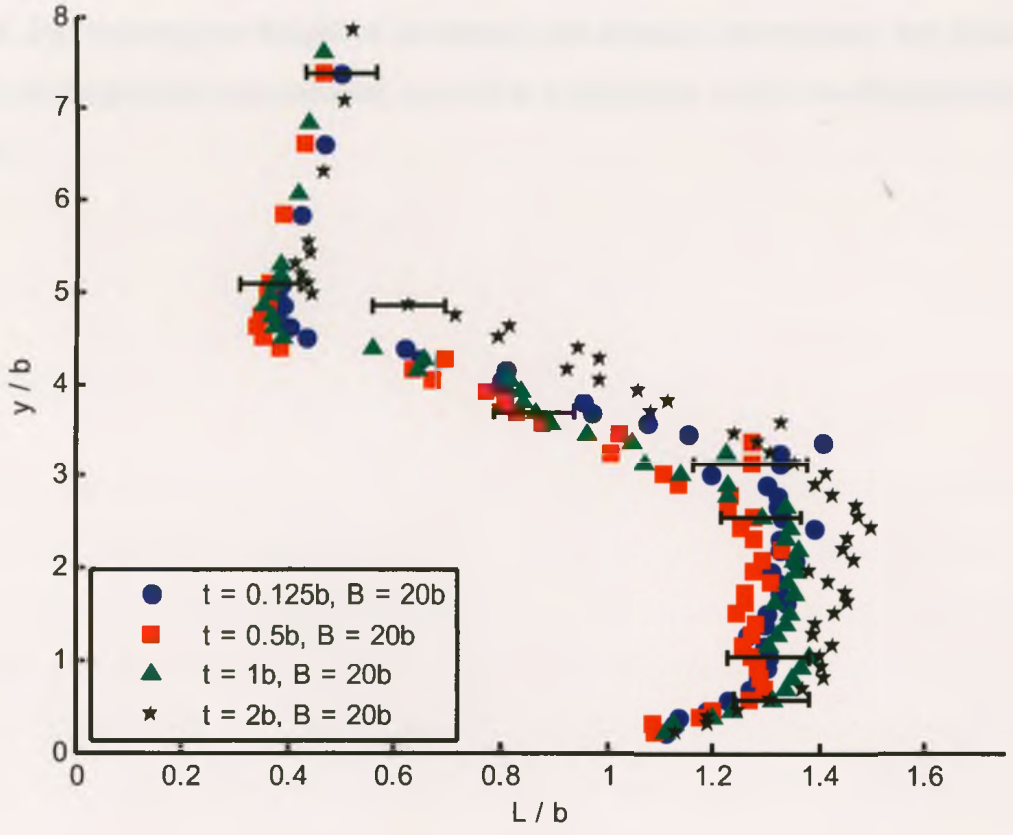

Figure 108: Integral length scale, x = 20b

3.3 Summary

A comparison was made between the current results and those of past studies, and it was found that in terms of maximum velocity, maximum velocity height and half-height the current study develops downstream in a similar manner to those accepted in the literature. A novel scaling method was suggested for scaling the decay of maximum velocity for different jet Reynolds numbers. The current study would appear to behave as though a co-flow was not present, found by comparisons of scaled vertical profiles of velocity. In comparisons of normal and Reynolds shear stress profiles the current results have comparable maximum stresses with the maximum stress located at similar heights.

The current results display differences in maximum velocity, due to varying lip thicknesses. Below the half-height, a reduction in Reynolds shear stress occurred for the thicker lip cases. Differences were also found in the integral length scales of the flow for the different lip thicknesses. No trend however was discerned from varying the lip thickness and it was proposed that the flow may convert from a shear flow case to a wake flow case as the lip thickness increases. Further investigation of this phenomenon is required. By lowering the height of the tunnel, the distance downstream that a half-height could be distinguished was reduced, as well as a reduction in the two-dimensionality of the flow.

Conclusions and Recommendations

In this manuscript, the focus of many wall jet related studies has been discussed as well as the different methods for scaling wall jets. In the literature review, it was identified that the effect of lip thickness on wall jet flow had not been rigorously tested. The external stream height of the wall jet had not been investigated at all and it was decided that a parametric study of lip thickness and external stream height would be carried out.

In order to complete the investigation experimental methods were chosen over computational methods, as the computational methods were deemed to not give results consistent with those of experiments. Cross hot-wire anemometry was used for data acquisition. Before the experiment could begin a novel inlet cone had to be constructed to improve the flow quality of the wall jet wind tunnel facility.

The results of the study were compared with those of the literature review. Good agreement was found in the development of the flow in the current study with that in the literature. A novel scaling method was suggested for the decay of maximum velocity downstream with different jet Reynolds numbers. The parametric analysis of the different cases of overall tunnel height identified that the role of the upper boundary far downstream was to reduce the two-dimensionality of the flow and remove the upper portion of the wall jet velocity profile from the flow. The lip thickness affected the maximum velocity of the flow downstream, although no clear trend was observed. Differences also occurred in profiles of Reynolds shear and normal stress as well as integral length scale, although no trends were identified.

During this study, a large amount of experimental data was produced. In the literature review, many different methods for analyzing wall jets were identified and not all of the methods were used in this study. Future work, with the current data set, should begin with determining the mass flow entrainment into the jet from the external stream, as per Gartshore and Hawaleshka (1964). Greater turbulence from the lip would increase the mass flow across the turbulent transition region between the jet and co-flow. In order to

do this, the boundary between the jet and external stream must be identified and be consistent among all of the different experimental cases.

A thorough knowledge of shear and wake flows would be necessary before trends in the profiles of velocity, Reynolds shear and normal stress and integral length scale could be identified. Further experiments that could be completed with the current facility are additional measurements close to the jet outlet, to aid in identifying lip thickness effects. As well measurements in the near wall region of the flow may indicate differences in wall shear stress with varying lip thickness as Katz et al. (1992) found wall shear stress to be reduced with forcing at the lip of the wall jet.

An extensive error analysis was included in the Appendix of this manuscript. A noteworthy portion of the analysis is the estimation of error produced in the calibration of the hot-wire probe with a pitot-static anemometer. Error bounds of the calibration curve are determined. The error is not often considered in this manner and will prove useful in future experimental studies.

References

Abramovich, G. N. *The theory of turbulent jets*. Trans. by L. H. Schindel. Cambridge, Massachusetts: M. I. T. Press (1963).

Abrahamsson, H., Johansson, B., & Lofdahl, L. (1994). A turbulent plane two-dimensional wall-jet in a quiescent surrounding. *European Journal of Mechanics, B/Fluids*, 13(5), 533-556.

Ahlman, D., Brethouwer, G. & Johannsson, A. V. (2007). Direct numerical simulation of a plane turbulent wall-jet including scalar mixing. *Physics of Fluids*, 6(19),

Bakke, P. (1957). Experimental investigation of wall jet. *Journal of Fluid Mechanics*, 2, 467-472.

Beguier, C., Giralt, F., Fulachier, L., & Keffer, J. F. (1978). Negative production in turbulent shear flows. Paper presented at the *Structure and Mechanisms of Turbulence II*, 22-35.

Bradshaw, P. and Gee, M. T. (1960). *Turbulent wall jets with and without an external stream*, Report and Memoranda No. 3252, England: Aeronautical Research Council.

Bruun, H. H., Nabhani, N., Fardad A. A. & Al-Kayiem H. H. (1990). Velocity component measurements by X hot-wire anemometry. *Measurement Science and Technology*, 1(12), 1314-1321.

Bruun, H. H. (1995). *Hot-wire anemometry principles and signal analysis*. New York, New York: Oxford University Press Inc.

Cheun, B. S. (1981). *Separated shear layers behind two-dimensional square-edged bodies*. PhD thesis, University of Surrey, Guildford, Surrey.

Coleman, H. W. & Steele, W. G. (2009). *Experimentation, validation and uncertainty analysis for engineers*. Hoboken, New Jersey: John Wiley & Sons.

Dantec Measurement Technology (1996). *Streamline installation and user's guide*. Skovlunde, Denmark: Dantec Measurement Technology.

Dejoan, A., & Leschziner, M. A. (2005). Large eddy simulation of a plane turbulent wall jet. *Physics of Fluids*, 17, 025102 (16 pages).

Eriksson, J. G., Karlsson, R. I. & Persson, J. (1998). An experimental study of a two-dimensional plane turbulent wall jet. *Experiments in Fluids*, 25(1), 50-60.

Gartshore, I., & Hawaleshka, O. (1964). *The design of a two-dimensional blowing slot and its application to a turbulent wall jet in still air.* Technical Note 64–5. Montreal: McGill University.

George, A. R. (1959). *An Investigation of a wall jet in a free stream*. Princeton University Report No. 479, Princeton, New Jersey: Princeton University.

George, W. K., Abrahamsson, H., Eriksson, J., Karlsson, R. I., Löfdahl, L & Wosnik, M. (2000). A similarity theory for the turbulent plane wall jet without an external stream. *Journal of Fluid Mechanics*. 425, 367–411.

Gerodimos, G. & So, R. M. C. (2000). Near-Wall Modeling of Plane Turbulent Wall Jets. *Journal of Fluids Engineering*. 119, 304–313.

Glauert, M. B. (1956). The wall jet. *Journal of Fluid Mechanics*. Cambridge: Cambridge University Press.

Gogineni, S. & Shih, C. (1997). Experimental investigation of the unsteady structure of a transitional plane wall jet. *Experiments in Fluids*, 23(2), 121-129.

Jørgensen, F. E. (1971). Directional sensitivity of wire and fiber film probes. DISA INFO, 11, 31-37

Kacker, S. C., & Whitelaw, J. H. (1971). Turbulence characteristics of two-dimensional wall-jet and wall-wake flows. *Journal of Applied Mechanics*, 38(1), 239-252.

Katz, Y., Horev, E., & Wygnanski, I. (1992). The forced turbulent wall jet. *Journal of Fluid Mechanics*, 242, 577-609.

Kobayashi, R. & Fujisawa (1983). Curvature effects on two-dimensional turbulent wall jet. *Ingenieur-Archiv*, 53(6), 409-417.

Kruka, V., & Eskinazi, S. (1964). The wall-jet in moving stream. *Journal of Fluid Mechanics*, 20, 555-579.

Kubacki, S., & Dick, E. (2010). Simulation of plane impinging jets with k-ω based hybrid RANS/LES models. *International Journal of Heat and Fluid Flow*, 31, 862-878.

Launder, B. E., & Rodi, W. (1981). The turbulent wall jet. *Progress in Aerospace Sciences*, 19, 81-128.

Launder, B. E., & Rodi, W. (1983). The turbulent wall jet - measurements and modeling. *Annual Review of Fluid Mechanics*, 15, 429-459. Palo Alto, California: Annual Reviews.

Lin, W. E. & Savory (2006). *Large-scale quasi-steady modeling of a downburst outflow using a slot jet*. Wind and Structures, 9, 419-440.

Metha, R. D. & Bradshaw, P. (1979). Design rules for small low speed wind tunnels. *Aeronautical Journal*, 73, 443-449.

Mongia, R., Bhattacharya, A. & Pokharna, H. (2008). Skin cooling and other challenges in future mobile form factor computing devices. *Microelectronics Journal*, 39(7), 992–1000.

Narasimha, R., Yegna Narayan, K., & Parthasarathy, S. P. (1973). Parametric analysis of turbulent wall jets. *Aeronautical Quarterly*, 24, 207-18.

National Instruments Corporation (1999). PCI E series user manual: Multifunction I/O boards for PCI bus computers. Manual part number 320945D-01.

Rodman, L. C., Jarrah, M. A., Wood, N. J., & Roberts, L. (1986). Turbulence measurements in a plane wall jet. Paper presented at the *AIAA 24th Aerospace Sciences Meeting.* AIAA, New York, NY, USA.

Patel, R. P. (1970). *A study of two-dimensional symmetric and asymmetric turbulent shear flows*, PhD thesis. Montreal, Quebec: Department of Mechanical Engineering, McGill University.

Patel, R. P. (1971). Turbulent jets and wall jets in uniform streaming flow. *Aeronautical Quarterly*, 22, 311-26.

Sarker, A. & So, R. M. C. (1997). A critical evaluation of near-wall two-equation models against direct numerical simulation data. *International Journal of Heat and Fluid Flow*, 18(2), 197-208.

Savory, E. (2009). Personal communication.

Schlichting, H. & Gersten, K. (2003). *Boundary layer theory*. Heidelberg, Berlin: Springer-Verlag.

Schneider, M. E., & Goldstein, R. J. (1994). Laser Doppler measurement of turbulence parameters in a two-dimensional plane wall jet. *Physics of Fluids*, 6(9), 3116-3129.

Schwarz, W. H. & Cosart, W. P. (1961). Two-dimensional turbulent wall-jet. *Journal of Fluid Mechanics*, 10, 481-495.

Slessor, M. C., Bond, C. L. & Domotakis, P. E. (1998). Turbulent shear-layer mixing at high Reynolds numbers: effects of inflow conditions. *Journal of Fluid Mechanics*, 376, 115-138.

Taneda, S. (1958). Oscillation of the wake behind a flat plate parallel to the flow. *Journal of the Physical Society of Japan*, 13, 418.

Tangemann, R. & Gretler, W. (2001). The computation of a two-dimensional wall jet in an external stream. *Journal of Fluids Engineering*, 123, 154-160.

Toshiba (2000). Instruction manual: The new generation compact inverter Tosvert VF-S9. Manual part number E6580757.

Tsai, Y. S., Hunt, J.C.R. & Nieuwstadt, F.T.M. (2007). Effect of strong external turbulence ona wall jet boundary layer. *Flow, Turbulence and Combustion*, 79, 155-174.

Tutu, N. K. & Chevray, R. (1975). Cross-wire anemometry in high intensity turbulence. *Journal of Fluids Mechanics*, 71(4), 785-800.

Velmex Inc. (2008, September). *Velmex motor driven assemblies price list M08*. Retrieved July 18, 2009, from the World Wide Web: http://www.velmex.com/pdf/m-cat-pdf/motorized-price-list.pdf

Verhoff A. (1970). *Steady and pulsating two-dimensional turbulent wall jets in a uniform stream.* Princeton University Report No. 723, Princeton, New Jersey: Princeton University.

Wheeler, A. J. & Ganji, A. R. (2004). *Introduction to Engineering Experimentation: Second Edition*. Upper Saddle River, New Jersey: Pearson Education, Inc.

Wilson, D. J. (1970). *An experimental investigation of the mean velocity, temperature, and turbulence fields in plane and curved two-dimensional wall jets: Coanda effect*, PhD thesis. Minneapolis, Minnesota: Mechanical Engineering Department, University of Minnesota.

Wygnanski. I. & Fiedler, H. (1969). Some measurements in the self-preserving jet. *Journal of Fluid Mechanics*, 38(3), 577-612.

Wygnanski, I., Katz, Y., & Horev, E. (1992). On the applicability of various scaling laws to the turbulent wall jet. *Journal of Fluid Mechanics*, 234, 669-90.

Zhou, M. D., & Wygnanski, I. (1993). Parameters governing the turbulent wall jet in an external stream. *AIAA Journal*, 31(5), 848-853.

Appendix A Facility sizes and initial conditions of past studies

Study	Re	U_j [m/s]	t/b	Y/b	b [mm]	x/b	U_E/U_j
George (1959)	3 810	46.0	1.25	>200	1.30	0 – 411.8	0.338
	7 500	90.5	1.25	>200	1.40	0 – 381.8	0.333
	7 600	91.6	1.25	>200	1.33	0 – 400	0.17
Bradshaw & Gee (1960)	6 000	198	2.78	>200	0.46	0 - > 500	0.17
Schwarz & Cosart (1961)	13 510	8.2	unknown	Open top	25.4	29 - 85	0
	20 100	12.2			25.4	29 - 85	0
	30 000	18.3			25.4	29 - 85	0
	41 600	25.3			25.4	29 - 85	0
Kruka & Eskinanzi (1964)	10 740	66.1	Sharp lip	69.7	3.33	45.8 – 274.8	0.263
	13 060	66.1		69.7	3.33	45.8 – 274.8	0.100
	26 270	126.2		69.7	3.33	45.8 – 274.8	0.055
	5 790	35.7		69.7	3.33	13.7 – 91.6	0.263
	11 420	68.3		77.3	3.0	25.6 – 408.5	0.100
Gartshore & Hawaleshka (1964)	31 000	~53	0.4, 2, 3.7, 10, 150	Open top	7.72	18 - 124	0
Kacker & Whitelaw (1971)	20 600	44.2	0.126	49.126	6.27	10 - 150	0.43
	20 600	44.2	1.14	50.14	6.27	10 - 150	0.43
	11 800	25.5	0.126	49.126	6.27	10 - 150	0.75
	11 800	25.5	1.14	50.14	6.27	10 - 150	0.75
Wygnanski et al. (1992)	19 000	57	Sharp lip	62	5	20 - 140	~0
	15 000	30		42	7.5	20 - 140	~0
	10 000	30		62	5	20 - 140	~0
	7 500	15		42	7.5	20 - 140	~0
	5 000	15		62	5	20 - 140	~0
	5 000	30		123	2.5	20 - 140	~0
	3 700	10		62	5	20 - 140	~0
Zhou & Wygnanski (1993)	11 000	33.0	Sharp lip	62	5	20 - 200	0.085
	11 000	32.7		62	5	20 - 200	0.24
	11 000	33.0		62	5	20 - 200	0.38
	11 000	32.8		62	5	20 - 200	0.59
	7 000	20.5		62	5	20 - 200	0.24
	7 000	20.8		62	5	20 - 200	0.38
	7 000	20.9		62	5	20 - 200	0.59
	7 000	21.0		62	5	20 - 200	0.93
	7 000	33.0		96.3	3.2	20 - 200	0.24
	18 000	55.0		62	5	20 - 200	0.09
	11 000	33.0		62	5	20 - 200	0.24
	11 000	33.0		62	5	20 - 200	0.38
Study	**Re**	**U_j [m/s]**	**t/b**	**Y/b**	**b [mm]**	**x/b**	**U_E/U_j**
Abrahamsson et al (1994)	10 000	~ 15	infinite	240	10	70 - 150	0
	15 000	~23				70 - 150	0
	20 000	~31				70 - 150	0

Schneider & Goldstein (1994)	14 000	44	1.06	Open top	5.4	43 - 110	~0
Tsai et al. (2007)	2 200	0.11	infinite	~5	40	2 - 7	0
Katz et al. (1992)	19 000	57	Sharp lip	62	5	30 – 120	~0
	5 000	15		62	5	30 – 120	~0
	3 400	10		62	5	30 – 120	~0
	5 000	15		62	5	30 – 120	~0
	7 500	15		41.67	7.5	30 – 120	~0
	10 000	30		62	5	30 – 120	~0
Mongia et al. (2008)	205	1.55	Sharp lip	2.25	2	0 – 25	~0.3
Gerodimos & So (1997)	3 700	unknown	infinite	unknown	unknown	30 – 150	~0
	5 000					30 – 150	~0
	10 000					30 – 150	~0
	19 000					30 – 150	~0
Dejoan & Leschziner (2005)	9 600	unknown	0	10	unknown	0 - 20	0.05
Ahlman et al (2007)	2 000	unknown	0	18	unknown	0 - 40	0.1

Appendix B Scaling methods

Scaling is not necessarily unique to the study that is credited, but that study contains an example of the method.

Focus of Scaling	Horizontal Axis	Vertical Axis	Applicable study
Vertical profile of velocity scaled by local variables			
General velocity profile	$\frac{U}{U_m}$	$\frac{y}{y_a}$ where $U(y_a)=\frac{U_m+U_E}{2}$	George (1959)
	$\frac{U}{U_m}$	$\frac{y}{\frac{1}{2}\Delta y_M - y_m}$	Bradshaw & Gee (1960)
	$\frac{\Delta U}{\Delta U_M}$	$\frac{y-y_m}{\frac{1}{2}\Delta y_M}$	Kruka & Eskinanzi (1964)
	$\frac{U}{U_m}$	$\frac{y}{\frac{1}{2}\Delta y_M}$	Launder & Rodi (1981)
	$\frac{V/U}{(u_\tau/U_m)^2}$	$\frac{y}{\frac{1}{2}\Delta y_M}$	George et al. (2000)
Comparison of local velocity	U^2	y	Katz et al. (1992)
Outer region	$\left(\frac{U}{U_m}\right)^2$	$\frac{y-y_m}{\frac{1}{2}\Delta y_M - y_m}$	Gartshore and Hawaleshka (1964)
Inner region	$\frac{U}{U_m}$	$\frac{y}{y_m}$	Kruka & Eskinanzi (1964)
	$\frac{U-U_m}{U_\tau}$	$\frac{y}{\frac{1}{2}\Delta y_M}$	Wygnanski et al. (1992)
	$\frac{U}{U_m}$	$\frac{y-y_m}{y_m}$	Zhou & Wygnanski (1993)
Vertical profile of velocity scaled by initial variables			
General velocity profile	$\frac{U}{U_E}$	y	George (1959)
	$\frac{U}{U_E}$	$\frac{y}{y_a}$ where $U(y_a)=\frac{U_m+U_E}{2}$	George (1959)
General velocity profile	$\frac{U}{U_j}$	y	Gartshore & Hawaleshka (1964)

Outer region	$\frac{U-U_E}{U_m-U_E}$	$\frac{y-y_m}{\frac{1}{2}\Delta y_M - y_m}$	Zhou & Wygnanski (1993)
Length scale growth downstream			
Growth of half-height	$\frac{xM_j}{\nu^2}$	$\frac{\frac{1}{2}\Delta y_M M_j}{\nu^2}$	Narasimha et al. (1973)
	Ax_s	$\frac{1}{2}\Delta y_m$	Schwarz and Cosart (1961)
	$\frac{x}{b}$	$\frac{\frac{1}{2}\Delta y_M}{b}$	Launder & Rodi (1981)
	$\frac{x-x_o}{\frac{\int_0^\infty U^2 dy}{U_E^2}}$	$\frac{\frac{1}{2}\Delta y_M}{\frac{\int_0^\infty U^2 dy}{U_E^2}}$	Launder & Rodi (1981)
	$\frac{(x-x_o)M_j}{\nu^2}$	$\frac{\frac{1}{2}\Delta y_M M_j}{\nu^2}$	Wygnanski et al. (1992)
	$\frac{xb(U_j-U_E)U_j}{\nu^2}$	$\frac{(\frac{1}{2}\Delta y_M - 0.7b)J}{R\nu^2}$ where $R=\frac{U_j-U_E}{U_j+U_E}$	Zhou & Wygnanski (1993)
	$\frac{xb(U_j-U_E)U_j}{\nu^2}$	$\frac{(\frac{1}{2}\Delta y_M - 0.7b)J}{\nu^2}$	Zhou & Wygnanski (1993)
Growth of jet	$\frac{x}{b}$	$\frac{y_a}{b}$ where $U(y_a)=\frac{U_m+U_e}{2}$	George (1959)
	$\log\frac{x}{b}$	$\log\frac{\frac{1}{2}\Delta y_M - y_m}{b}$	Bradshaw & Gee (1960)
Outer region length scale	$\frac{xb(U_j-U_E)U_j}{\nu^2}$	$\frac{(\frac{1}{2}\Delta y_M - y_m - 0.5b)J}{R\nu^2}$ where $R=\frac{U_j-U_E}{U_j+U_E}$	Zhou & Wygnanski (1993)
Change in length scale with change in velocity scale	$\left(\frac{U_E}{\Delta U_M}\right)^2 \times \frac{1}{0.724+\frac{U_E}{U_m-U_E}}$	$\frac{\frac{1}{2}\Delta y_M}{\int_0^\infty \left(\frac{U}{U_E}\right)\cdot\left(1-\left(\frac{U}{U_E}\right)\right)dy}$	Patel (1971)
Growth of width in free mixing region	$\frac{x_t}{b}$	$\frac{\frac{1}{2}\Delta y_M - y_m}{b}$	Kruka & Eskinanzi (1964)
Maximum velocity height			
Growth of maximum	$x_t b$	$\frac{y_m}{b}$	Kruka & Eskinanzi (1964)

velocity height	$\frac{xM_j}{\nu^2}$	$\frac{y_m M_j}{\nu^2}$	Narasimha et al. (1973)
Maximum velocity height	$\frac{xb(U_j - U_E)U_j}{\nu^2}$	$\frac{(y_m - 0.2b)J}{\nu^2}$	Zhou & Wygnanski (1993)
Velocity decay downstream			
Decay of maximum velocity	x	U_m	Kruka & Eskinanzi (1964)
	$\log\frac{x}{b}$	$\log\frac{U_m}{U_j}$	Bradshaw & Gee (1960)
	Bx_s^a	U_m	Schwarz and Cosart (1961)
	$\frac{x}{b}$	$\frac{U_m}{U_j}$	Gartshore & Hawaleshka (1964)
	$\frac{xM_j}{\nu^2}$	$\frac{U_m \nu}{M_j}$	Narasimha et al. (1973)
	$\frac{x}{b}$	$\left(\frac{U_j}{U_m}\right)^2$	Launder & Rodi (1981)
	$\frac{x - x_o}{b}$	$\frac{U_m}{U_j}$	Wygnanski et al. (1992)
	$\frac{(x - x_o)M_j}{\nu^2}$	$\frac{U_m \nu}{M_j}$	Wygnanski et al. (1992)
	$\frac{xb(U_j - U_E)U_j}{\nu^2}$	$\frac{U_m \nu R}{J}$ where $R = \frac{U_j - U_E}{U_j + U_E}$	Zhou & Wygnanski (1993)
	$\frac{\frac{1}{2}\Delta y_M u_\tau}{\nu}$	$\frac{u_\tau}{U_m}$	George et al. (2000)
	$\frac{x}{b}$	$\frac{U_m}{U_E}$	George (1959)
	x	$\frac{U_m}{U_E}$	Bradshaw & Gee (1960)
Decay of maximum excess velocity	x_t	ΔU_M	Kruka & Eskinanzi (1964)
	$\frac{x}{b}$	$\frac{U_E}{\Delta U_M}$	Patel (1971)
Decay of maximum excess velocity	$\frac{x - x_o}{\frac{\int_0^\infty U^2 dy}{U_E^2}}$	$\frac{U_E}{\Delta U_M}$	Launder & Rodi (1981)

Decay of Maximum excess velocity accounting for β	bx_t^a where $a=\frac{1.06}{(1-\beta)}-0.50$	$\frac{\Delta U_M}{U_0}$	Kruka & Eskinanzi (1964)
Outer Region velocity scale	$\frac{xb(U_j-U_E)U_j}{\nu^2}$	$\frac{\Delta U_M \nu}{J}$	Zhou & Wygnanski (1993)
Maximum velocity and half-height relation			
Maximum velocity and half-height relation	$\frac{\frac{1}{2}\Delta y_M}{b}$	$\frac{U_m}{U_j}$	George et al. (2000)
	$\frac{\frac{1}{2}\Delta y_M M_j}{\nu^2}$	$\frac{U_m \nu}{M_j}$	George et al. (2000)
Momentum Ratios			
Mass flow entrainment	$\frac{x}{b}$	$\frac{b}{\int_0^{\delta_{av}} \rho U_{jet} dy}\frac{\partial}{\partial x}\int_0^{\infty}\rho(\Delta U)dy$	George (1959)
Momentum ratio	$\frac{t}{b}$	$\frac{\int_0^{y_\delta}\rho U^2 dy}{\int_0^b \rho U_j^2 dy}$	Gartshore & Hawaleshka (1964)
Shear Stress			
Shear profile	$\frac{y}{y_\delta}$	$\frac{\overline{uv}}{U_E^2}$	Kacker & Whitelaw (1971)
	$\frac{y}{\frac{1}{2}\Delta y_M}$	$\frac{\overline{uv}}{U_m^2}$	Launder & Rodi (1981)
Wall region shear profile	y^+	$\frac{\overline{uv}}{u_\tau^2}$	George et al. (2000)
Outer shear profile	$\frac{y}{\frac{1}{2}\Delta y_m}$	$\frac{\overline{uv}}{u_\tau^2}$	George et al. (2000)
	$\frac{y-y_{uv=0}}{b-y_{uv=0}}$	$\frac{\overline{uv}}{\overline{uv}_{\max}}$	Kruka & Eskinanzi (1964)
Excess velocity at maximum shear	ΔU_M	$\sqrt{\overline{uv}_{\max}}$	Kruka & Eskinanzi (1964)
Decay of maximum shear	x_t [m]	$\overline{uv}_{\max}$ [m²/s²]	Kruka & Eskinanzi (1964)
Wall shear stress	$\frac{xb(U_j-U_E)U_j}{\nu^2}$	$\frac{\tau_w R}{\rho}\left(\frac{\nu}{J}\right)^2$ where $R=\frac{U_j-U_E}{U_j+U_E}$	Zhou & Wygnanski (1993)

Normal Stress			
Stress profile, u	$\frac{y-y_{uv=0}}{b-y_{uv=0}}$	$\frac{\sqrt{\overline{u^2}}}{\sqrt{\overline{uv}_{\max}}}$	Kruka & Eskinanzi
Stress profile, u	$\frac{y}{\frac{1}{2}\Delta y_M}$	$\frac{\overline{u^2}}{U_m^2}$	Launder & Rodi (1981)
Stress profile, v	$\frac{y-y_{uv=0}}{b-y_{uv=0}}$	$\frac{\sqrt{\overline{v^2}}}{\sqrt{\overline{uv}_m}}$	Kruka & Eskinazi
	$\frac{y}{\frac{1}{2}\Delta y_M}$	$\frac{\overline{v^2}}{U_m^2}$	Launder & Rodi (1981)
	y^+	$\frac{\overline{v^2}}{u_\tau^2}$	George et al. (2000)
Stress profile, w	$\frac{y}{\frac{1}{2}\Delta y_M}$	$\frac{\overline{w^2}}{U_m^2}$	Abrahamsson (1994)
Turbulence			
Turbulent kinetic energy	$\frac{y}{y_\delta}$	$\frac{\overline{k^2}}{U_E^2}$	Kacker & Whitelaw (1971)
	$\frac{y}{\frac{1}{2}\Delta y_M}$	$\frac{\overline{k^2}}{U_m^2}$	Launder & Rodi (1981)
Turbulence intensity	$\frac{y}{y_m}$	$\frac{u'}{U_m}$	Wygnanski et al. (1992)
	$\frac{y}{y_\delta}$	$\frac{\sqrt{\overline{u^2}}}{U_e}, \frac{\sqrt{\overline{v^2}}}{U_e}, \frac{\sqrt{\overline{w^2}}}{U_e}$	Kacker & Whitelaw (1971)
Production of turbulent kinetic energy	$\frac{y}{y_\delta}$	$\rho\overline{uv}\left(\frac{\partial U}{\partial y}\right)$	Kacker & Whitelaw (1971)
Shear work integral	$\frac{x}{b}$	$\frac{1}{\rho U_e^3}\int_0^\delta \rho\overline{uv}\frac{\partial U}{\partial y}dy$	Kacker & Whitelaw (1971)

Appendix C Decomposition of Probe Signal

There are various methods that can be used to calibrate cross hot-wire probes and decompose the voltage signal for two components of velocity. The following method from Bruun (1995) was found to be the most robust for cross hot-wire probes that do not have accurately aligned wires. An example of such a probe can be seen in **Figure 109**, where the wires are not aligned at 45° to the probe axis; refer to **Figure 111** for a schematic of hot-wire probe variables. The Dantec 55P0611 cross hot-wire probe was used in the experiments.

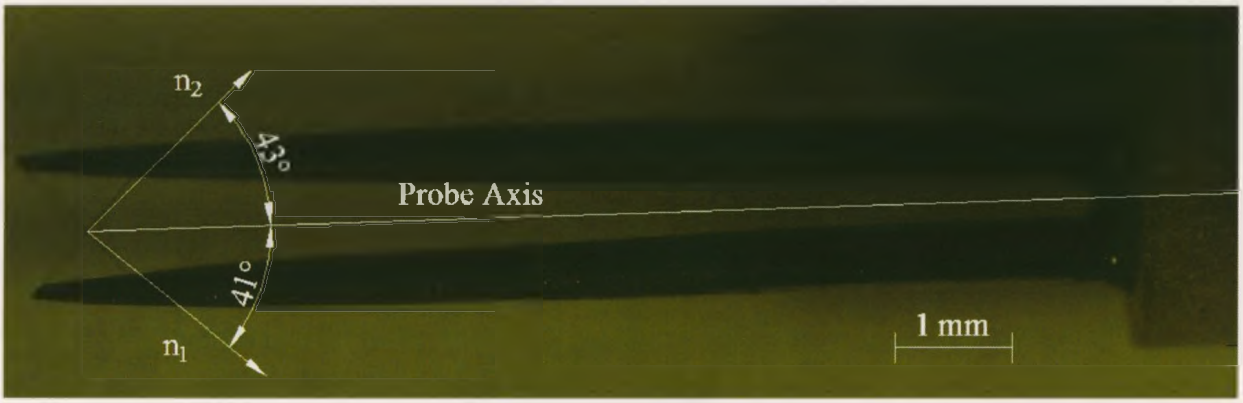

Figure 109: Microscopic image of Dantec 55P0611 cross hot-wire probe, with wire angles overlaid

In developing this method, Bruun et al. (1990) extended the normal and tangential velocities concept of Jørgensen (1971), **Equation 32**. A schematic of the equation is in **Figure 110**. Bruun (1995) outlined several methods to decompose the V_{eff} of wires one and two for the U and V velocity components. The sum and difference method was used in this investigation. The velocity V denotes the lateral velocity, as the probe could be rotated to gather V or W. The calibration constant, k, denotes the yaw coefficient of the hot-wire – the value is particular to individual wires. The direction and magnitude of V_{eff} is somewhat arbitrary due to the k factor, except during the yaw velocity calibration when the calibration jet is parallel with the probe axis. In that case V_{eff} has the magnitude of the calibration jet.

Equation 32: General hot-wire velocity relationship, Jørgensen (1971)

$$V_{eff}^2 = U_N^2 + k^2 U_T^2$$

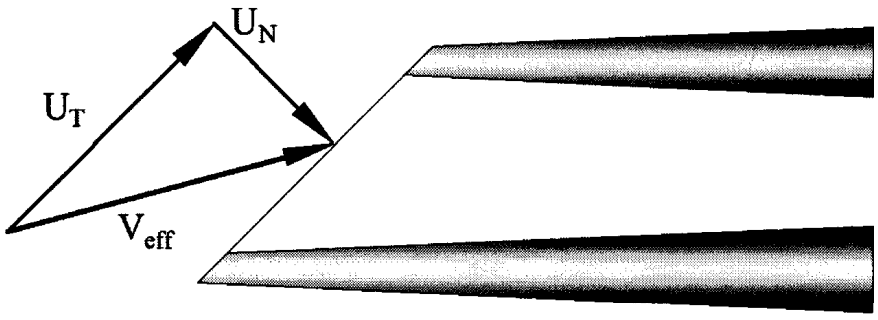

Figure 110: Effective velocity, with normal and tangential components, approaching a hot-wire

In hot-wire anemometry a calibration curve is created that relates known velocities to the voltage output of the anemometer system. The calibration curve consists of 15 sample points and a best fit equation is made of the curve. A 6th order polynomial is popular for the calibration curve, but such a high order polynomial is prone to diverge from the calibration points near the ends of the curve. To eliminate the chance of a divergence, King's law is used, **Equation 33**.

Equation 33: King's Law

$$E^2 = A + BV_{eff}^n$$

In King's Law, E is the voltage output and A, B and n are constants for the curve between E and V_{eff}. All velocity calibrations are done with the calibration jet flow parallel with the axis of the probe. Other than during yaw calibrations, the velocity calibration of the hot-wire was done using the jet in the wall jet wind tunnel facility with a pitot-static tube to determine velocity. Controlled conditions were required to perform a yaw calibration, in determining k, for such calibrations a Dantec Dynamics calibrator (Streamline 90H02 Flow Unit) was used.

Following Bruun (1990), the yaw calibration was as follows. A velocity calibration was first done with King's law, **Equation 33**, with the calibration jet parallel with the hot-wire probe axis ($\theta = 0°$). Wires 1 and 2 of the cross hot-wire were calibrated simultaneously for values of A_1, B_1 & n_1 and A_2, B_2 & n_2, using the voltage signals $E_{\theta_1=0°}$ and $E_{\theta_2=0°}$. A constant velocity was used in the yaw calibration, and following

recommendations in the Dantec Dynamics Streamline Installation and User's Guide (1996), the average of the highest and lowest expected experimental velocities was used. For the current study the calibration velocity was chosen as 20 (m/s). The probe was then rotated in the Dantec Dynamics calibrator through a maximum range of of $45° \leq \theta \leq -45°$ and readings taken every 5° for E_{θ_1} and E_{θ_2}. The angle measurements were manually done to a resolution of ± 0.5°. That data were then used as follows.

In **Equation 32**, $\overline{V}\cos\alpha_1$ and $\overline{V}\sin\alpha_1$ were substituted for U_N and U_T respectively for wire 1, resulting in **Equation 34**. $\overline{V}$ is the magnitude of the flow past the probe at angle θ and in this calibration setting it is the magnitude of the yaw calibration jet, refer to **Figure 111**.

Equation 34: Effective velocity for Wires 1 and 2, Bruun (1990)

a) $V_{1\,eff}^2 = \overline{V}^2\cos^2\alpha_1 + k^2\overline{V}^2\sin^2\alpha_1$ b) $V_{2\,eff}^2 = \overline{V}^2\cos^2\alpha_2 + k^2\overline{V}^2\sin^2\alpha_2$

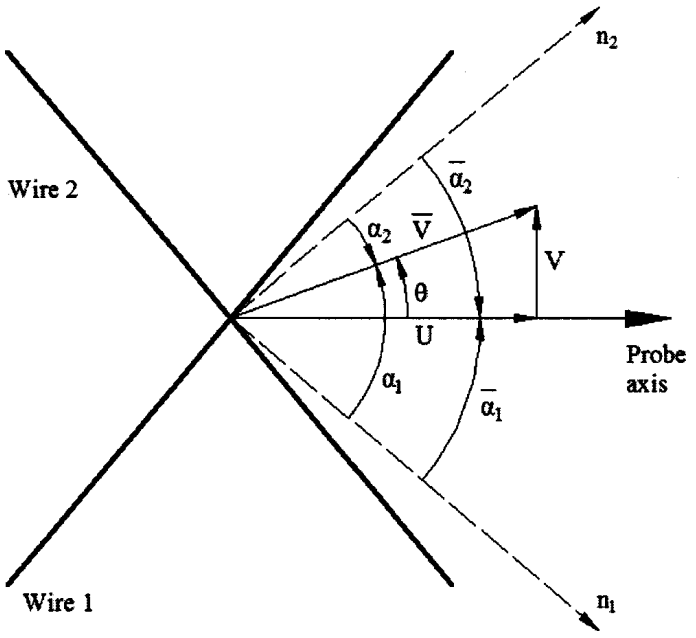

Figure 111: Hot-wire schematic, adapted from Bruun (1990)

In order to be specific, Equation 33 **is written out for wires 1 and 2 in** Equation 35a & 33b. Equation 34 **is then substituted into** Equation 35, **to get** Equation 36.

Equation 35: King's Law for wires 1 and 2

$$\text{a) } E_1^2 = A_1 + B_1 V_{1\,eff}^{n_1} \qquad \text{b) } E_2^2 = A_2 + B_2 V_{2\,eff}^{n_2}$$

Equation 36: Velocity/voltage relationship with yaw coefficient, Bruun (1990)

$$\text{a) } E_1^2 = A_1 + B_1\left(\overline{V}^2 \cos^2 \alpha_1 + k_1^2 \overline{V}^2 \sin^2 \alpha_1\right)^{n_1}$$

$$\text{b) } E_2^2 = A_2 + B_2\left(\overline{V}^2 \cos^2 \alpha_2 + k_2^2 \overline{V}^2 \sin^2 \alpha_2\right)^{n_2}$$

A ratio is made using **Equation 36**, to get **Equation 37**, which uses **k**, α and $\overline{\alpha}$, but importantly not $\overline{V}$. Details of this can be found in Bruun (1990). The assumption is made from the initial velocity calibration that constants B and k will not vary much with θ.

Equation 37: Elimination of $\overline{V}$, Bruun (1990)

$$\text{a) } \left(\frac{E_{\theta_1}^2 - A_1}{E_{\theta_1=0^\circ}^2 - A_1}\right)^{\frac{2}{n_1}} = \frac{\cos^2(\overline{\alpha}_1 + \theta) + k_1^2 \sin^2(\overline{\alpha}_1 + \theta)}{\cos^2 \overline{\alpha}_1 + k_1^2 \sin^2 \overline{\alpha}_1}$$

$$\text{b) } \left(\frac{E_{\theta_2}^2 - A_2}{E_{\theta_2=0^\circ}^2 - A_2}\right)^{\frac{2}{n_2}} = \frac{\cos^2(\overline{\alpha}_2 + \theta) + k_2^2 \sin^2(\overline{\alpha} + \theta)}{\cos^2 \overline{\alpha}_2 + k_2^2 \sin^2 \overline{\alpha}_2}$$

Equation 37 was rearranged to get **Equation 38**, which can be viewed as a 1st order linear equation, where $1 - \boldsymbol{k}^2$ is the slope. A least squares regression was performed, using the data from the different angles, to find the slope and in turn $\mathbf{k}^2$.

Equation 38: Linear relationship to determine $\mathbf{k}^2$, Bruun (1990)

$$\text{a) } \left(\frac{E_{\theta_1}^2 - A_1}{E_{\theta_1=0^\circ}^2 - A_1}\right)^{\frac{2}{n_1}} - 1 = \left(1 - k_1^2\right)\left(\left(\frac{E_{\theta_1}^2 - A_1}{E_{\theta_1=0^\circ}^2 - A_1}\right)^{\frac{2}{n_1}} \sin^2 \overline{\alpha}_1 - \sin^2(\overline{\alpha}_1 + \theta)\right)$$

$$\text{b) } \left(\frac{E_{\theta_2}^2 - A_2}{E_{\theta_2=0^\circ}^2 - A_2}\right)^{\frac{2}{n_2}} - 1 = \left(1 - k_2^2\right)\left(\left(\frac{E_{\theta_2}^2 - A_2}{E_{\theta_2=0^\circ}^2 - A_2}\right)^{\frac{2}{n_2}} \sin^2 \overline{\alpha}_2 - \sin^2(\overline{\alpha}_2 - \theta)\right)$$

A k^2 value is constant for the wire it applies to. To reduce errors, k^2 was determined from data taken within ± 35°. In **Figures 113 & 114** it can be seen that the error in the hot-wire values increased greatly after 35°.

In order to take daily measurements in the laboratory, the hot-wire was calibrated against a pitot-static tube and manometer in the wall jet wind tunnel facility. The calibration would follow **Equation 36**, in the manner of King's Law, with $\overline{V}$ as the jet velocity, k^2 known from the yaw calibration and $\alpha = 45°$. The variables A, B and n would be found from the calibration. Once a data series was recorded in the form of a voltage output, E, a V_{eff} series would then be found from **Equation 39**.

Equation 39: Voltage to velocity signal conversion

$$\textbf{a)}\ V_{1\,eff} = \left(\frac{E_1^2 - A_1}{B_1}\right)^{1/n_1} \qquad \textbf{b)}\ V_{2\,eff} = \left(\frac{E_2^2 - A_2}{B_2}\right)^{1/n_2}$$

V_{eff} is subsequently used in the sum and difference method, **Equation 40**, to determine the velocity series of both the U and V components of velocity. The benefit to the sum and difference method is that it is somewhat insensitive to $\overline{\alpha}$, Bruun (1990), making it appropriate for probes that have poorly aligned wires. The sum and difference method demonstrated is from Bruun (1995), which does not assume, as did Bruun (1990), that the k^2 values for each wire were the same.

Equation 40: Sum and difference method, Bruun (1995)

$$\textbf{a)}\ U = \frac{\frac{V_{1\,eff}}{f_1(\overline{\alpha})} g_2(\overline{\alpha}) + \frac{V_{2\,eff}}{f_2(\overline{\alpha})} g_1(\overline{\alpha})}{g_1(\overline{\alpha}) + g_2(\overline{\alpha})} \qquad \textbf{b)}\ V = \frac{\frac{V_{2\,eff}}{f_2(\overline{\alpha})} - \frac{V_{1\,eff}}{f_1(\overline{\alpha})}}{g_1(\overline{\alpha}) + g_2(\overline{\alpha})}$$

Where

$$\textbf{a)}\ f_i(\overline{\alpha}) = \sqrt{\cos^2\overline{\alpha} + k_i^2 \sin^2\overline{\alpha}} \qquad \textbf{b)}\ g_i(\overline{\alpha}) = \frac{\cos^2\overline{\alpha}\left(1 - k_i^2\right)}{\cos^2\overline{\alpha} + k_i^2 \sin^2\overline{\alpha}}$$

Appendix D Estimation of uncertainty in velocity

The discussion of the uncertainty in velocity measurements will consist of three parts. Firstly the appropriate uncertainty equations will be identified. Secondly the uncertainty equations will be applied to the equations found in **Appendix C**. The bias and random errors of the measurement apparatus will be identified and used in the error equations. Finally the equations will be used to get an estimate of velocity and extended to get an error estimate of half-height and integral length scale.

Appendix D.i Overall uncertainty equations

In order to determine the uncertainty in velocity from cross hot-wire anemometry measurements, there are three main areas that will be tested. Uncertainty exists from the velocity calibration curve, the yaw calibration and turbulence in the flow velocity. Uncertainty exists in the Velmex traverse locating the vertical distances, but this is minimal and will be discussed briefly at the end of this section.

From Coleman & Steele (2009), the form of the uncertainty analysis will follow **Equation 41 & 42**. Coleman & Steele (2009) determined for most scientific and engineering applications that $t_{\%} = 2$ is appropriate for a 95% confidence level.

Equation 41: Total uncertainty

$$W_P^2 = \sum_{i=1}^{J} \left(\frac{\partial P}{\partial X_i} \right)^2 W_{X_i}^2$$

Equation 42: Uncertainty in a variable

$$W_{X_i}^2 = t_{\%}^2 \left(b_{X_i}^2 + r_{X_i}^2 \right)$$

Where the bias error and random error are,

$$b_{X_i}^2 = \sum_{j=1}^{N}\left(\frac{\partial X_i}{\partial Q_j}\right)^2 b_{Q_j}^2 \qquad r_{X_i}^2 = \sum_{j=1}^{J}\left(\frac{\partial X_i}{\partial Q_j}\right)^2 r_{Q_j}^2$$

The random error is not previously known for the velocity of the flow, and for a well resolved sample size the random error in the mean value will be found from the standard deviation of the mean, **Equation 43**.

Equation 43: Standard deviation of the mean

$$r_{\bar{Q}_j}^2 = \frac{\sum_{i=1}^{N}\left(X_{ij} - \bar{X}_j\right)^2}{(N-1)N}$$

Two cases of bias error exist in velocity found by hot-wire anemometry. The bias error is known through experimental measurements and that error will be added to the error found in **Equation 41**, as **Equation 44**.

Equation 44: Total error

$$W_{P\,total}^2 = W_P^2 + \sum_{m=1}^{n} W_{i\,bias}^2$$

The error bounds of the final result would be in the form of **Equation 45**.

Equation 45: Uncertainty interval

$$P - W_{P\,total} \le P_{true} \le P + W_{P\,total}$$

Appendix D.ii Uncertainty in probe signal decomposition

Uncertainty exists in the calibration curve used for hot-wire probes. Following Coleman & Steele's (2009) method a new curve, **Equation 47**, was created which provides the error in V_{eff} for a given E, following the constant names in **Equation 39**. Where possible, formulae will be given; discriminating between wire 1 and wire 2 of the cross hot-wire probe. Several of the formulae are too cumbersome to have that distinction made and if it is not stated the reader must assume the formulae are to be applied separately to both of the wire signals.

From **Appendix D.i, Equation 41** is the starting point for the analysis. **Equation 42** is applied to **Equation 40**, from **Appendix C**, which results in **Equation 46**.

Equation 46: Expanded uncertainty in velocity

$$\text{a) } W_U^2 = \left(\frac{dU}{dV_{1\,eff}}\right)^2 W_{V_{1\,eff}}^2 + \left(\frac{dU}{dV_{2\,eff}}\right)^2 W_{V_{2\,eff}}^2$$

$$\text{b) } W_V^2 = \left(\frac{dV}{dV_{1\,eff}}\right)^2 W_{V_{1\,eff}}^2 + \left(\frac{dV}{dV_{2\,eff}}\right)^2 W_{V_{2\,eff}}^2$$

Where,

$$\frac{dU}{dV_{1\,eff}} = \frac{g_2(\bar{\alpha})}{f_1(\bar{\alpha})(g_1(\bar{\alpha}) + g_2(\bar{\alpha}))} \qquad \frac{dU}{dV_{2\,eff}} = \frac{g_1(\bar{\alpha})}{f_2(\bar{\alpha})(g_1(\bar{\alpha}) + g_2(\bar{\alpha}))}$$

$$\frac{dV}{dV_{1\,eff}} = \frac{-1}{f_1(\bar{\alpha})(g_1(\bar{\alpha}) + g_2(\bar{\alpha}))} \qquad \frac{dV}{dV_{2\,eff}} = \frac{1}{f_2(\bar{\alpha})(g_1(\bar{\alpha}) + g_2(\bar{\alpha}))}$$

The derivatives of **Equation 46** are straightforward to calculate, whereas $W_{V_{eff}}^2$ encompasses several factors beginning with **Equation 47**. In **Equation 47** the notation $V_{eff\,i}$ is used, the i denotes the i^{th} point of the 15 calibration samples.

Equation 47: Uncertainty in effective velocity

$$W_{V_{eff}}^2 = W_{V_{eff}-regress}^2 + t^2\left(\frac{\partial V_{eff}}{\partial E_{New}}\right)^2 s_{\overline{E}_{New}}^2$$

The term $W_{V_{eff}-regress}^2$ creates error bounds curves around the V_{eff} curve as in **Figure 112.** The term $W_{V_{eff}-regress}^2$ is based on known uncertainties in E_i from the calibration equipment. The term $t^2\left(\frac{\partial V_{eff}}{\partial E_{New}}\right)^2 s_{\overline{E}_{New}}^2$ is the error based on the voltage signal collected during the experiment itself, E_{new}, and not the calibration process. The two different sources of error are added together as in **Equation 47** to give the total error of V_{eff}.

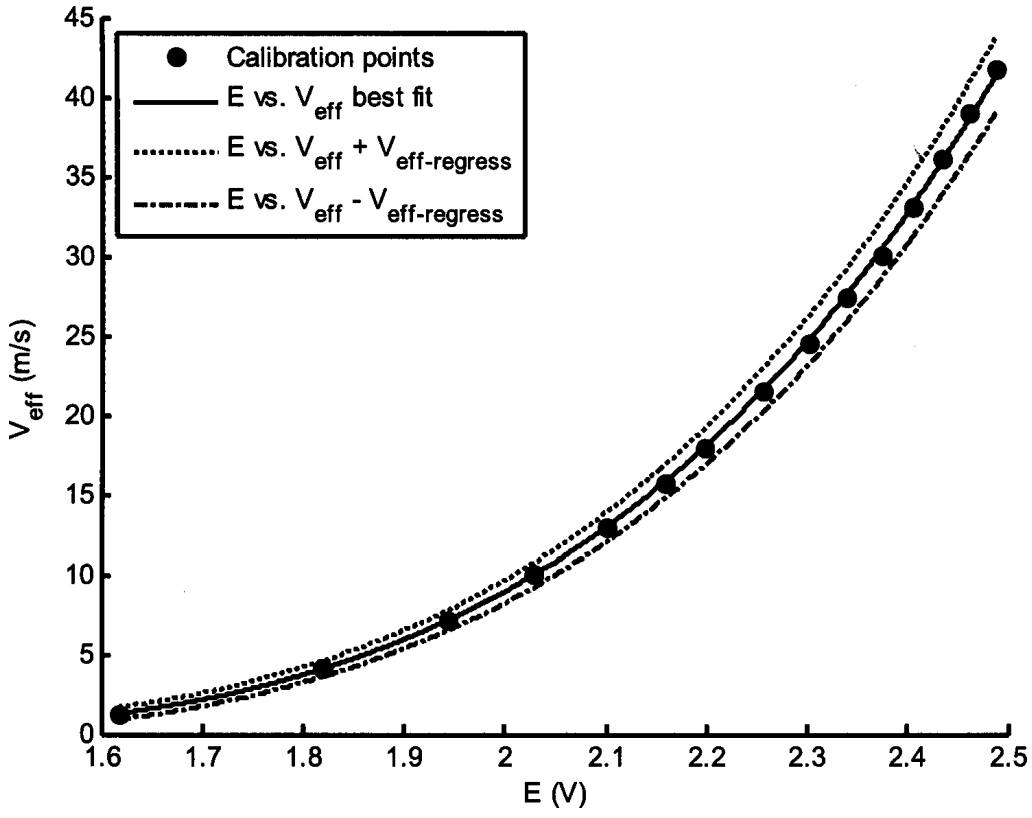

Figure 112: Example of a calibration plot with error

The term $W^2_{V_{eff}-regress}$ is expanded in **Equation 48**. In order to create the error bounds of **Figure 112**, the 15 calibration values of E_i are used in **Equation 46** to generate 15 values for $W^2_{V_{eff}-regress}$. A third order polynomial (one order greater than the calibration curve, as specified by Coleman & Steele's (2009)) was fitted to the 15 values of $W^2_{V_{eff}-regress}$ to provide an uncertainty for E_{new}. The terms of **Equations 48** will now be discussed.

Equation 48: Regression portion of calibration uncertainty

$$W^2_{V_{eff}-regress} = t^2\left[\begin{array}{l}\sum_{i=1}^{N}\left(\frac{\partial U_{V_{eff}}}{\partial E_i}\right)^2 r^2_{E_i} + \sum_{i=1}^{N}\left(\frac{\partial U_{V_{eff}}}{\partial V_{eff\,i}}\right)^2 b^2_{V_{eff\,i}} + 2\sum_{i=1}^{N-1}\sum_{j=i+1}^{N}\left(\frac{\partial V_{eff}}{\partial V_{eff\,i}}\right)\left(\frac{\partial V_{eff}}{\partial V_{eff\,j}}\right) b_{V_{eff\,i}} b_{V_{eff\,j}} \\ + \sum_{i=1}^{N}\left(\frac{\partial V_{eff}}{\partial E_i}\right)^2 b^2_{E_i} + 2\sum_{i=1}^{N-1}\sum_{j=i+1}^{N}\left(\frac{\partial V_{eff}}{\partial E_i}\right)\left(\frac{\partial V_{eff}}{\partial E_j}\right) b_{E_i} b_{E_j} + \left(\frac{\partial V_{eff}}{\partial E_{new}}\right)^2 b^2_{E_{new}} \\ + 2\sum_{i=1}^{N}\left(\frac{\partial V_{eff}}{\partial E_{new}}\right)\left(\frac{\partial V_{eff}}{\partial E_i}\right) b_{E_{new}} b_{E_i}\end{array}\right]$$

The partial derivatives, $\frac{\partial V_{eff}}{\partial V_{eff\,i}}$ and $\frac{\partial V_{eff}}{\partial E_i}$, of **Equation 48** were evaluated by numerical differentiation; **Equations 49 a & b**. The variable V_{eff} is that found by **Equation 39**. The constant ε determines the incremental step in the derivative and was taken to be 0.000 01, as that is when convergence was found as in **Table 15**.

Equation 49: Numerical differentiation

a) $$\frac{\partial V_{eff}}{\partial V_{eff\,i}} = \frac{f\left(V_{eff\,i} + \varepsilon V_{eff\,i}\right) - f\left(V_{eff\,i}\right)}{\varepsilon V_{eff\,i}}$$

b) $$\frac{\partial V_{eff}}{\partial E_i} = \frac{f\left(E_i + \varepsilon E_i\right) - f\left(E_i\right)}{\varepsilon E_i}$$

Table 15: Equation 18a, for i = 2, with various ε

ε	0.01	0.001	0.000 1	0.000 01	0.000 001
Calibration point 1	0.471642	0.442894	0.443028	0.443041	0.443043
Calibration point 2	0.167883	0.168626	0.168701	0.168708	0.168709
Calibration point 3	0.094255	0.097423	0.097483	0.097489	0.09749
Calibration point 4	0.062513	0.064852	0.064905	0.06491	0.064911
Calibration point 5	0.044496	0.046394	0.046443	0.046448	0.046448
Calibration point 6	0.029263	0.032037	0.032083	0.032087	0.032088
Calibration point 7	0.020383	0.021771	0.021813	0.021817	0.021818
Calibration point 8	0.012361	0.013594	0.013633	0.013637	0.013637
Calibration point 9	0.006558	0.007682	0.007719	0.007722	0.007723
Calibration point 10	0.002502	0.002848	0.002882	0.002886	0.002886
Calibration point 11	-0.00166	-0.00134	-0.0013	-0.0013	-0.0013
Calibration point 12	-0.00467	-0.00495	-0.00492	-0.00492	-0.00492
Calibration point 13	-0.00722	-0.00802	-0.00799	-0.00799	-0.00798
Calibration point 14	-0.00944	-0.00586	-0.01068	-0.01068	-0.01068
Calibration point 15	-0.01164	-0.00883	-0.01329	-0.01329	-0.01329

For the numerical differentiation in **Equation 49a**, each (i^{th}) data point in the calibration curve is subsequently shifted by $\varepsilon V_{eff\,i}$, along the V_{eff} axis, (with the remaining data points unaffected). An i^{th} curve fit is performed over the calibration points, with the i^{th} point shifted, to obtain new curve fit constants, n_i, A_i and B_i, and the curve fit is denoted $f\left(V_{eff\,i} + \varepsilon V_{eff\,i}\right)$. The term $f\left(V_{eff\,i}\right)$ is the original curve fit. A similar process is used for **Equation 49b**, but with the shift done along the E axis. The random and bias uncertainty terms in **Equation 48** are listed in **Table 16** and will be discussed next.

Table 16: Random and Bias errors of the calibration curve

Error Term	Error Source
$r_{E_i}^2$	The standard deviation of the mean of the hot-wire signal.
$b_{V_{eff\,i}}^2$	The bias error of the calculated velocity from the manometers.
$b_{V_{eff\,i}} b_{V_{eff\,j}}$	The correlation of bias error in calculated velocity from the manometers.
$b_{E_i}^2$	The bias error of the data acquisition system.
$b_{E_i} b_{E_j}$	The correlation of the bias error of the data acquisition system.
$b_{E_{new}}^2$	The bias error for the data acquisition system of the new voltages. As the data acquisition system does not change, it is the same as $b_{E_i}^2$.
$b_{E_{new}} b_{E_i}$	The correlation of the bias error of the data acquisition system between the calibration and new voltages.

The bias error of the manometers was from determining the pressure differential of the pitot-static tube used to establish velocity in the calibration process. Two different manometers are used because the Microtector manometer has a water column height of 50 cm, requiring the higher velocities to be calibrated with a conventional ruled U-tube manometer. Refer to the **Section 2.7** for additional details. Different formulae are required for velocity due to the different manometer styles, **Equations 50 & 51**. The large manometer measures the difference between the columns of the manometer. The Microtector manometer measures the height in only one column. Meaning the zero height, with no flow, must be subtracted from the measured column height and the result doubled for the final measurement.

Equation 50: Velocity from ruled manometer

$$V_{eff} = \sqrt{\frac{2\rho_{water} g\left(h_{upper} - h_{lower}\right)}{\rho_{air}}}$$

Equation 51: Velocity from Microtector manometer

$$V_{eff} = \sqrt{\frac{2\rho_{water} g\left(2\left(h - h_{zero}\right)\right)}{\rho_{air}}}$$

To determine the uncertainty in velocity from the manometers, the expanded error in **Equations 52 a & b** were used. Values of bias uncertainty are listed in **Table 17**. The random error of the manometers was not taken into account as only a single measurement was made for each point.

Equation 52: Expanded uncertainty of manometer measured velocity

a) $$b^2_{V_{eff\ ruler}} = \left(\frac{\partial V_{eff}}{\partial h_{upper}}\right)^2 b^2_{h_{upper}} + \left(\frac{\partial V_{eff}}{\partial h_{lower}}\right)^2 b^2_{h_{lower}}$$

b) $$b^2_{V_{eff\ Microtector}} = \left(\frac{\partial V_{eff}}{\partial h}\right)^2 b^2_{h} + \left(\frac{\partial V_{eff}}{\partial h_{zero}}\right)^2 b^2_{h_{zero}}$$

Where

$$\frac{\partial V_{eff}}{\partial h_{upper}} = \frac{1}{2}\sqrt{\frac{\rho_{air}}{2\rho_{water}g\left(h_{upper}-h_{lower}\right)}}\left(\frac{2\rho_{water}g}{\rho_{air}}\right)$$

$$\frac{\partial V_{eff}}{\partial h_{lower}} = -\frac{1}{2}\sqrt{\frac{\rho_{air}}{2\rho_{water}g\left(h_{upper}-h_{lower}\right)}}\left(\frac{2\rho_{water}g}{\rho_{air}}\right)$$

$$\frac{\partial V_{eff}}{\partial h} = \frac{1}{2}\sqrt{\frac{\rho_{air}}{2\rho_{water}g\left(2\left(h-h_{zero}\right)\right)}}\left(\frac{4\rho_{water}g}{\rho_{air}}\right)$$

$$\frac{\partial V_{eff}}{\partial h_{zero}} = -\frac{1}{2}\sqrt{\frac{\rho_{air}}{2\rho_{water}g\left(2\left(h-h_{zero}\right)\right)}}\left(\frac{4\rho_{water}g}{\rho_{air}}\right)$$

Table 17: Manometer bias uncertainty and data acquisition system uncertainty

Source	Bias (±)	Random (±)	Resulting Error
Microtector Manometer	0.000 01 [mm]		Varies
Large Manometer	0.000 5 [mm]		Varies
PCI-6071E card Linearity[1]	1 Least Significant Bit		0.000 73 (V)
PCI-6071E card Gain[1]	0.02 % of full scale		0.000 6 (V)
PCI-6071E Quantization[1]		½ Least Significant Bit	0.000 18 (V)
PCI-6071E card Noise[1]		0.5 % of full scale	0.015 (V)

[1]NI Corporation (1999).

Bias uncertainty exists in the data acquisition system because of the analog to digital conversion. The system in this investigation uses a PCI-6071E card which was 12 bit and the voltage range was set to 0 – 3 (V). The uncertainty values can be seen in **Table 17**. The resulting uncertainty followed Wheeler & Ganji (2004) calculations, for $b_{E_i} = 0.015\,(V)$, the noise of the card dominating the error value.

For the uncertainty due to E_{new}, **Equations 53 a & b** were used for the partial differentiation. The value of $b_{E_{new}}$ is equal to b_{E_i}.

Equation 53: Partial differentiation of effective velocity

a) $$\frac{\partial V_{1\,eff}}{\partial E_{1\,new}} = \frac{1}{n_1}\left(\frac{E_{1\,new}^2 - A_1}{B_1}\right)^{1/n_1 - 1}\left(\frac{2E_{1\,new}}{B_1}\right)$$

b) $$\frac{\partial V_{2\,eff}}{\partial E_{2\,new}} = \frac{1}{n_2}\left(\frac{E_{2\,new}^2 - A_2}{B_2}\right)^{1/n_2 - 1}\left(\frac{2E_{2\,new}}{B_2}\right)$$

Appendix D.iii Including yaw and turbulence bias error

Another source of velocity error that was examined was based on inaccuracies of the hot-wire probe in determining yawed velocities. The estimation is based on Bruun et al.'s (1990) work in which **Figures 113 & 114** are reproduced from. The plots are used to assign an error to the measured velocity based on the velocity magnitude and approach angle. **Equation 54 a & b** are what **Figures 113 & 114** are based upon; U and V being calculated from **Equation 40** and $U_{reference}$ and $V_{reference}$ being the components of the calibration jet during a yaw calibration.

Equation 54: Yaw Error, Bruun (1990)

$$\textbf{a)}\ \Delta U = \frac{U - U_{reference}}{U_{reference}} \times 100\% \qquad \textbf{b)}\ \Delta V = \frac{V - V_{reference}}{V_{reference}} \times 100\%$$

Equations 54 a & b were rearranged for $U_{reference}$ & $V_{reference}$ and then the absolute difference was found between those values and the values found by **Equation 40**. This can be seen in **Equation 55**.

Equation 55: Bias error from Figures 88 & 89

$$\textbf{a)}\ W_{U\,1\,bias} = \left| U - \frac{U}{1 + \Delta U/100} \right| \qquad \textbf{b)}\ W_{V\,2\,bias} = \left| V - \frac{V}{1 + \Delta V/100} \right|$$

The measured U and V, from **Equation 40**, were categorized into sections, corresponding to the different curves in **Figures 113 & 114**. Within each curve the angles were separated into 0 – 5 (°), 5 – 15 (°), 15 – 25 (°) and 25 – 35 (°), the error of each angle range was given the largest error of the range. The velocities were also categorized into sections of 0 – 5 (m/s), 5 – 10 (m/s), 10 – 20 (m/s), 30 – 40 (m/s) and 40 – 50 (m/s), the error of each range was also given the largest error of the range. The reason for using the largest error of each range was to ensure that no error was underestimated.

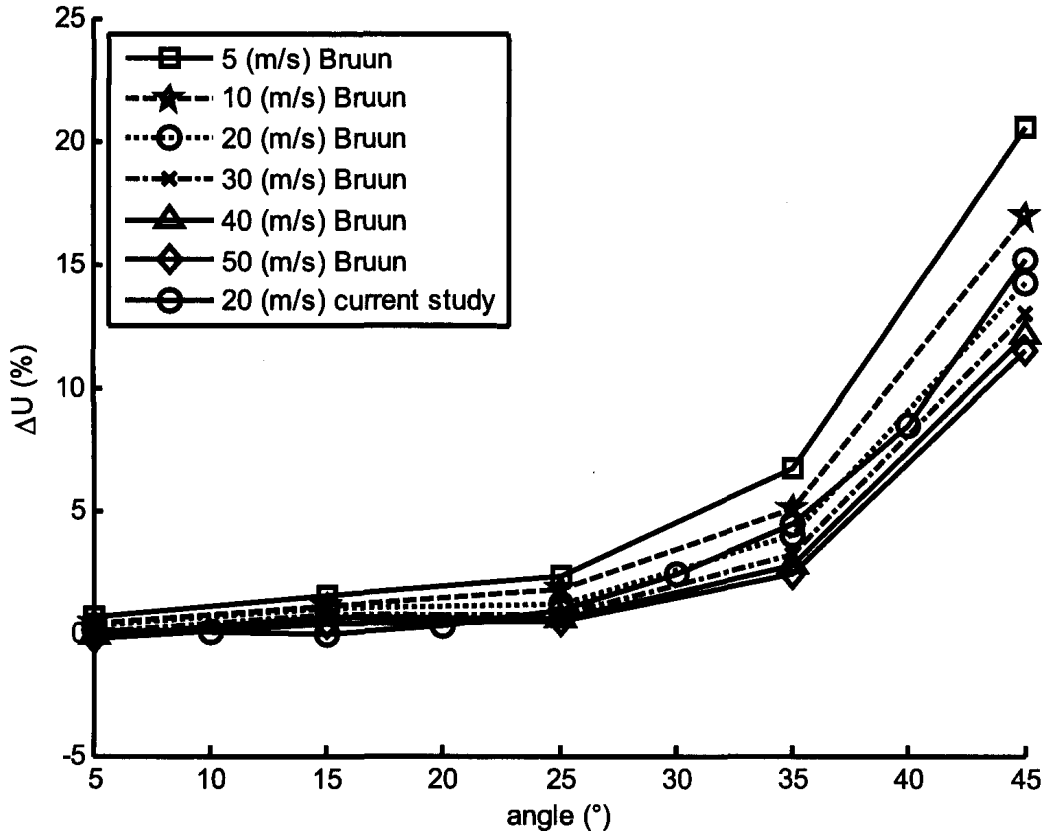

Figure 113: Sum and difference U yaw error, refer to Equation 54 a, Bruun (1990)

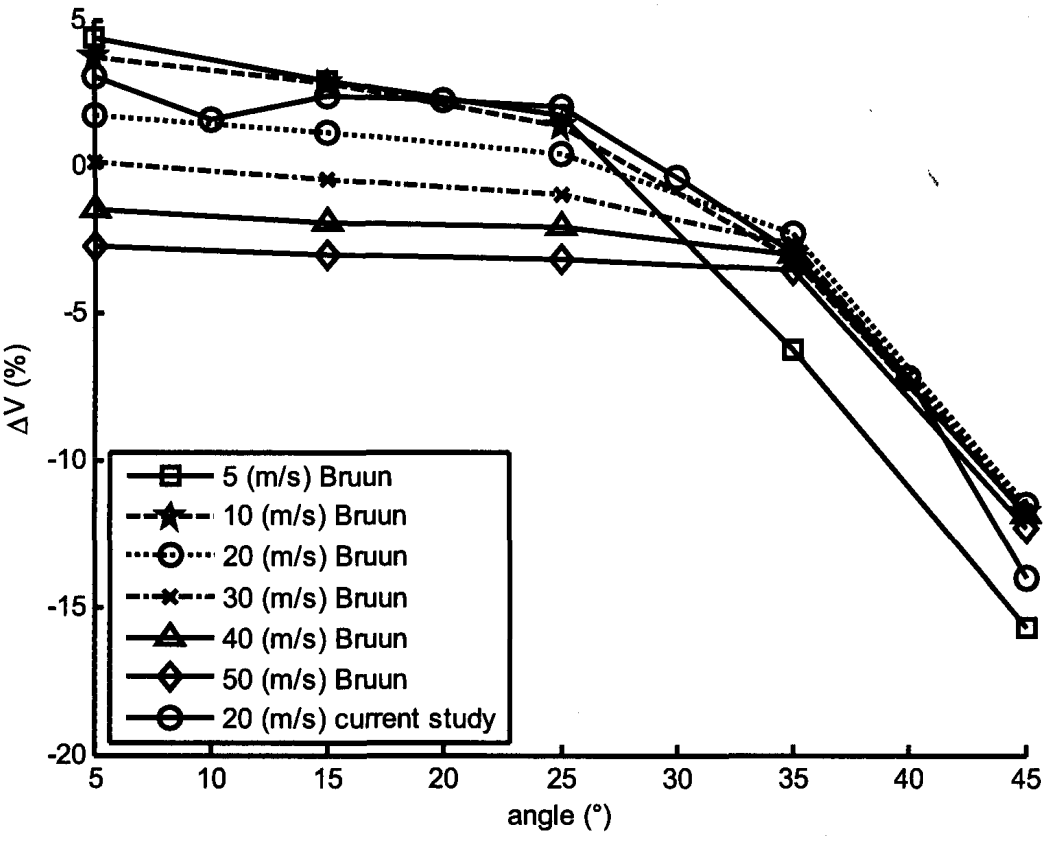

Figure 114: Sum and difference V yaw error, refer to Equation 54 b, Bruun (1990)

The last source of error that will be discussed is the error in U due to turbulence in the flow measured by the hot-wire probe. In **Figure 115** the ratio $\frac{U}{U_{reference}}$ can be used to correct the measured U by level of the turbulence intensity. This figure was adapted to **Equation 56** to give an estimate of the error due to turbulence.

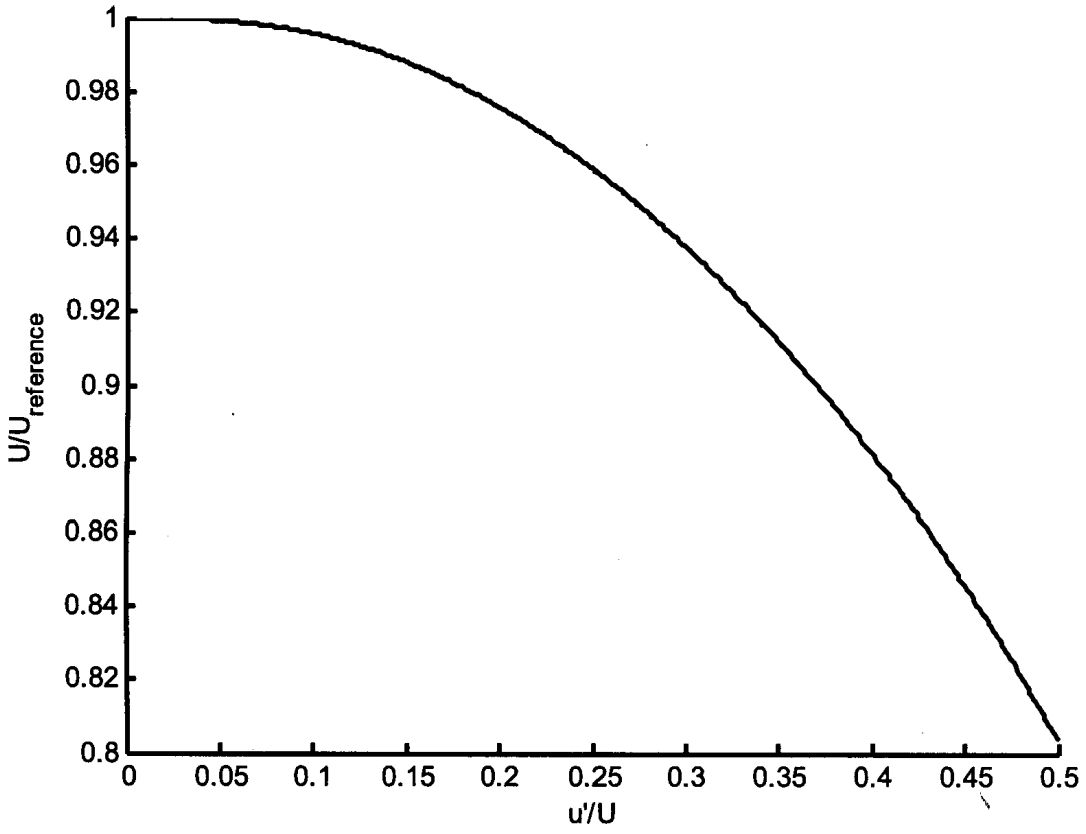

Figure 115: U corrected for turbulence intensity (adapted from Tutu & Chevray (1975) by Cheun (1981))

Equation 56: Bias error from Figure 90

$$W_{U\,2\,bias} = \left| U - \frac{U}{f\left(\sqrt{\overline{uu}}/U\right)} \right|$$

The uncertainty, $W_{U\,2\,bias}$, from **Equation 90** was added to the yaw uncertainty in **Equation 55**, following **Equation 44**, resulting in **Equation 57**.

Equation 57: Total velocity uncertainty

$$\text{a)}\, U_{error} = \sqrt{W_{U_{cal}}^2 + W_{U1\,bia}^2 + W_{U2\,bia}^2} \qquad \text{b)}\, V_{error} = \sqrt{W_{V_{cal}}^2 + W_{V1\,bia}^2}$$

The resulting error from **Equation 57** can be seen in the error bars of the vertical profiles of velocity in **Figure 116**.

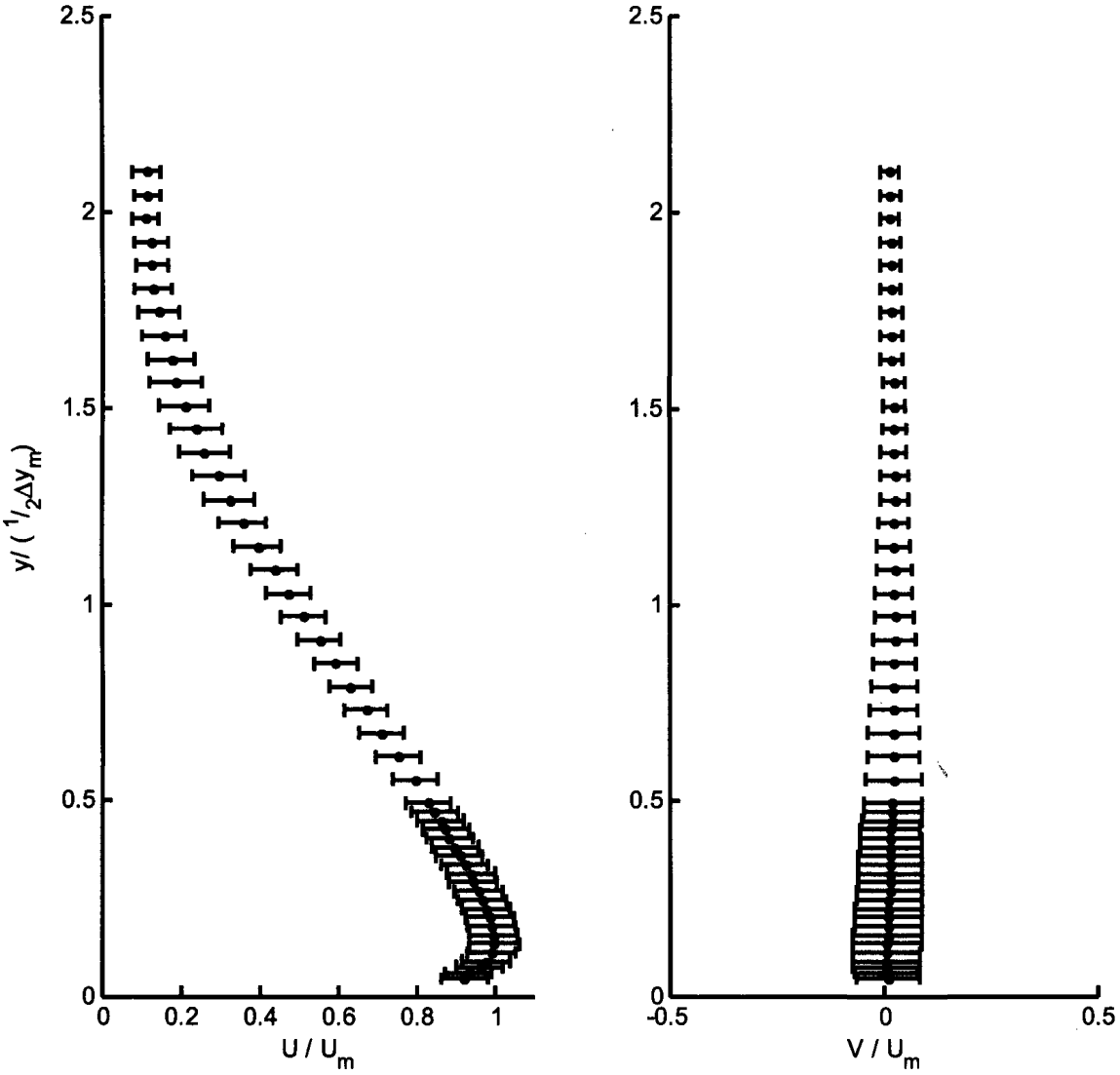

Figure 116: x = 40b, t = 0.125b, B = 10b, note the difference in velocity scales.

The vertical Velmex traverse is rated at an accuracy of 0.18 mm over a 254 mm distance, Velmex (2008). The stepping motor and lead screw assembly allows a resolution of 0.003175 mm/step. The sample volume of the Dantec 55P0611 cross hot-wire probe is 0.8 (mm) x 0.8 (mm), the area perpendicular to the probe axis. The size of the measurement volume is larger than any inaccuracies from the traverse system. The first

measurement, in a vertical profile, is taken with the probe holder located in contact with the wall boundary, refer to **Section 2.7** for additional set-up information. If the probe holder is pushed against the wall boundary, in setting up for the first point, the probe holder springs the probe upward and the probe springs back down when the traverse moves to the second location. The bias error in height because of the springing was estimated to be ± 0.5 (mm).

Sources of error exist in the determination of the half-height and of the integral length scale L. Both of these length scales are based on a velocity scale. The half-height was determined through the vertical location that the velocity is half of the maximum velocity, refer to **Figure 1**. The integral length scale was determined from the integral time scale multiplied by velocity; refer to **Equation 28** in **Section 2.8**. The error in half-height was estimated in the manner of **Figure 117**, where the variation due to U_m determined the error of the half-height. A more rigorous estimation of error would be preferable, but the current one shows that the error in the half-height is not great due to the slope of the velocity profile in the half-height region. In **Table 18** a list of downstream errors is listed for half-height.

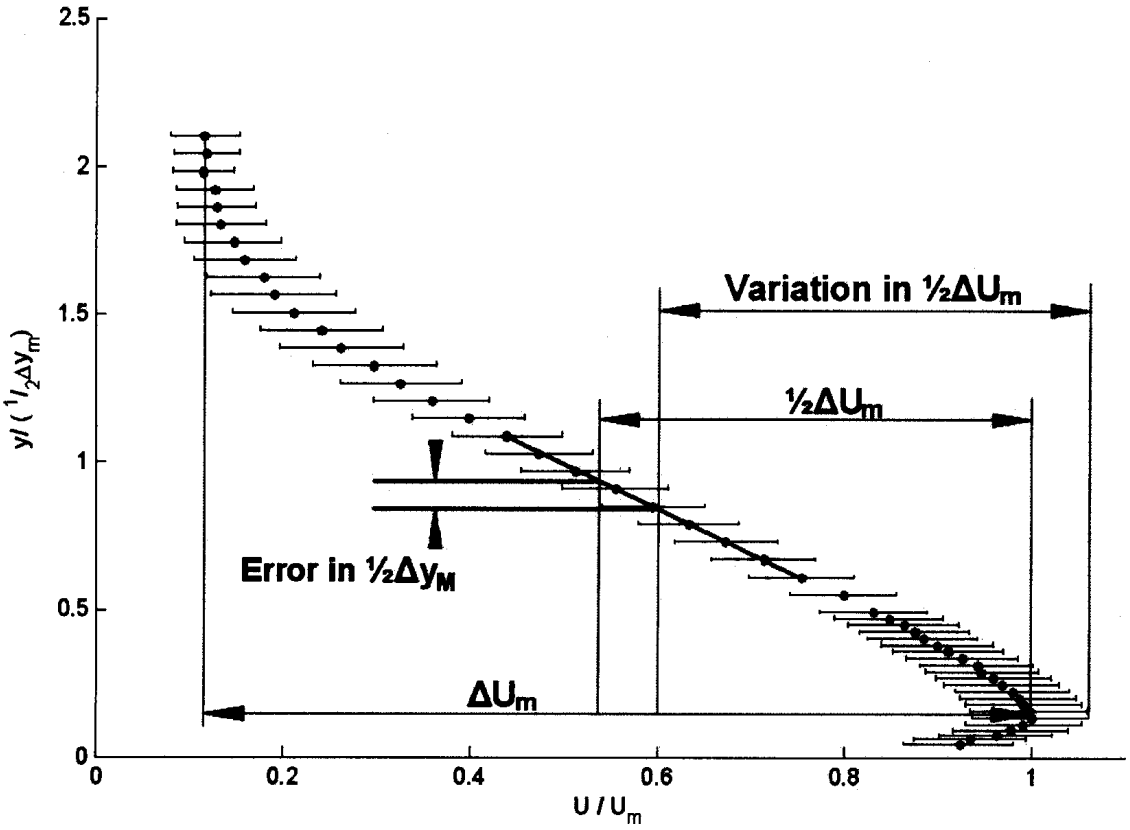

Figure 117: Determining half-height error

Table 18: Error in half-height and maximum velocity

x	$\frac{1}{2}\Delta y_{M\ error}$ ± (mm)	$U_{m\ error}$ ± (m/s)
10*b*	1.4	2.1
20*b*	2.4	1.8
40*b*	4.6	1.5
60*b*	6.8	1.3
80 *b*	8.5	1.2
100*b*	10.8	1.1
120*b*	11.7	1.0
140*b*	13.0	0.9
160*b*	15.0	0.8

In order to estimate the error in the integral length scale **Equation 58** was used.

Equation 58: Error in integral length scale

$$L_{error} = T_E U_{error}$$

Appendix E Cone building

Figure 118: High-density fiber board stacked to roughly shape the inlet cone mould

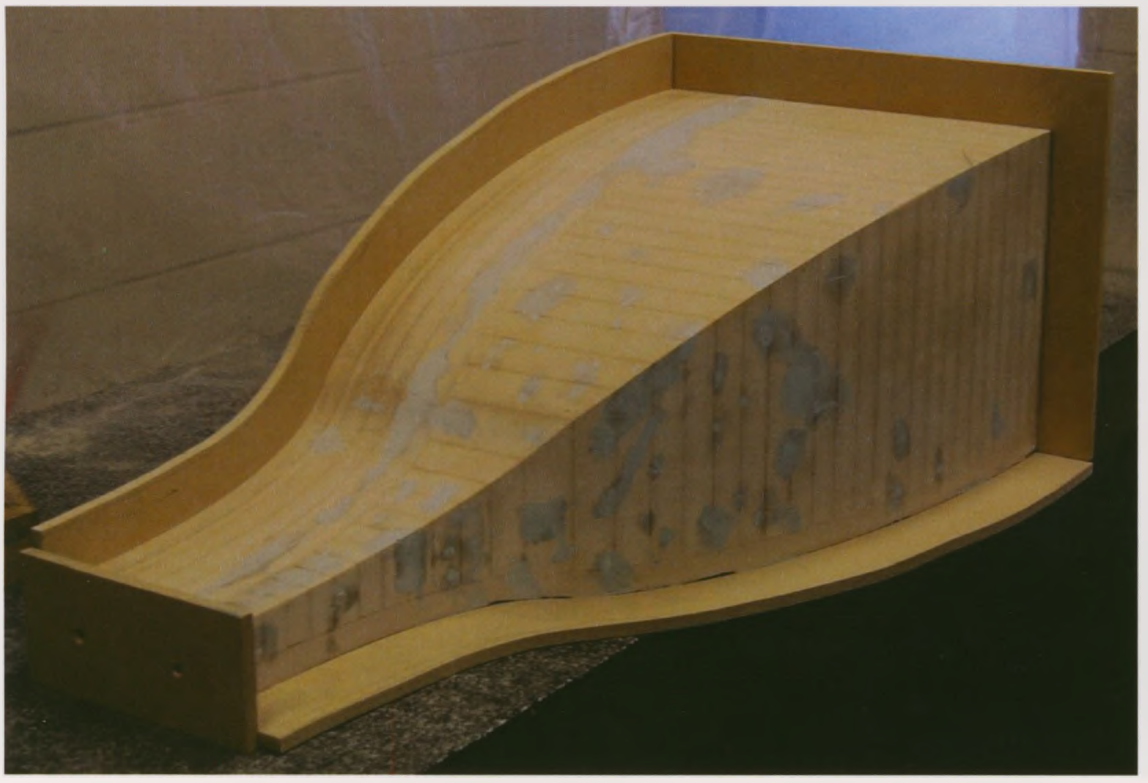

Figure 119: Machined inlet cone mould

Figure 120: Fiberglass portions of the inlet cone with imperfections smoothed with automotive body filler

Figure 121: Finished fiberglass halves of inlet cone

Appendix F Inlet conditions for the current study

Table 19: Jet velocities

	B = 10b	B = 13b	B = 16b	B = 20b
t = 0.125b	42.04	41.64	40.48	40.68
t = 0.5b	41.38	41.17	40.24	41.45
t = 1b	42.07	40.14	40.83	40.47
t = 2b	42.46	40.61	40.65	40.51

Table 20: Co-flow velocities

	B = 10b	B = 13b	B = 16b	B = 20b
t = 0.125b	5.88	5.47	4.55	4.49
t = 0.5b	5.84	5.36	4.83	4.46
t = 1b	5.87	5.42	4.68	4.71
t = 2b	6.06	5.51	4.4	4.37

Table 21: Velocity ratio

	B = 10b	B = 13b	B = 16b	B = 20b
t = 0.125b	0.14	0.13	0.11	0.11
t = 0.5b	0.14	0.13	0.12	0.11
t = 1b	0.14	0.14	0.11	0.12
t = 2b	0.14	0.14	0.11	0.11

Appendix G Additional plots from parametric analysis

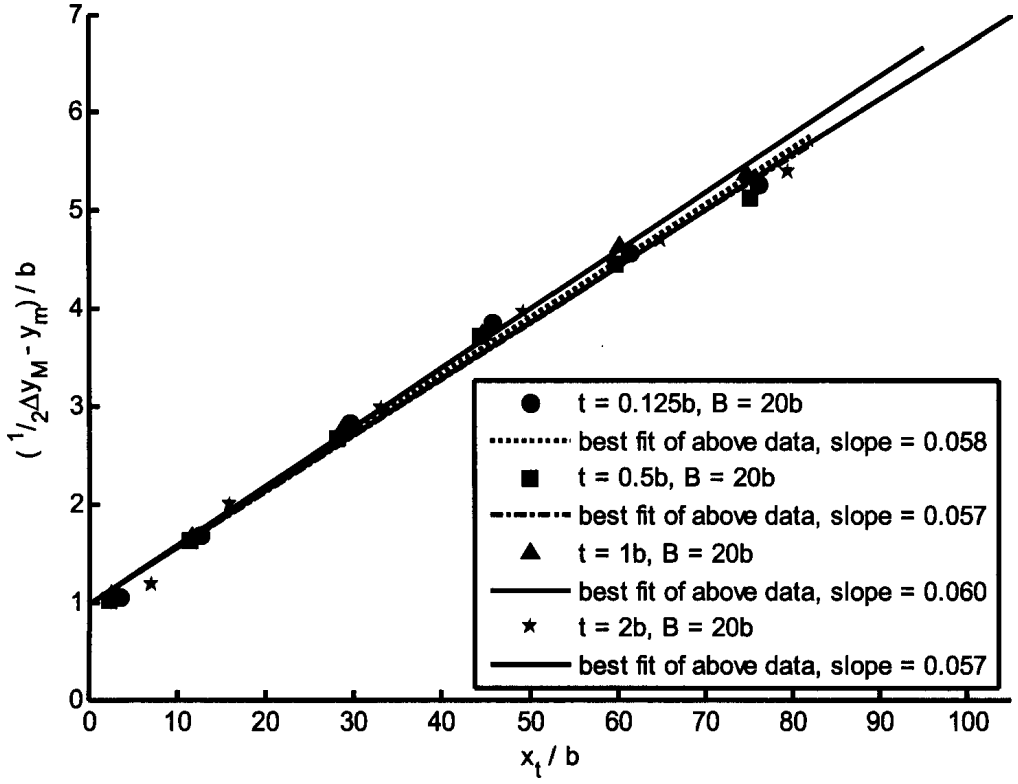

Figure 122: Scaling method for $\frac{1}{2}\Delta y_M - y_m$ of Kruka & Eskinazi (1964) for constant tunnel height

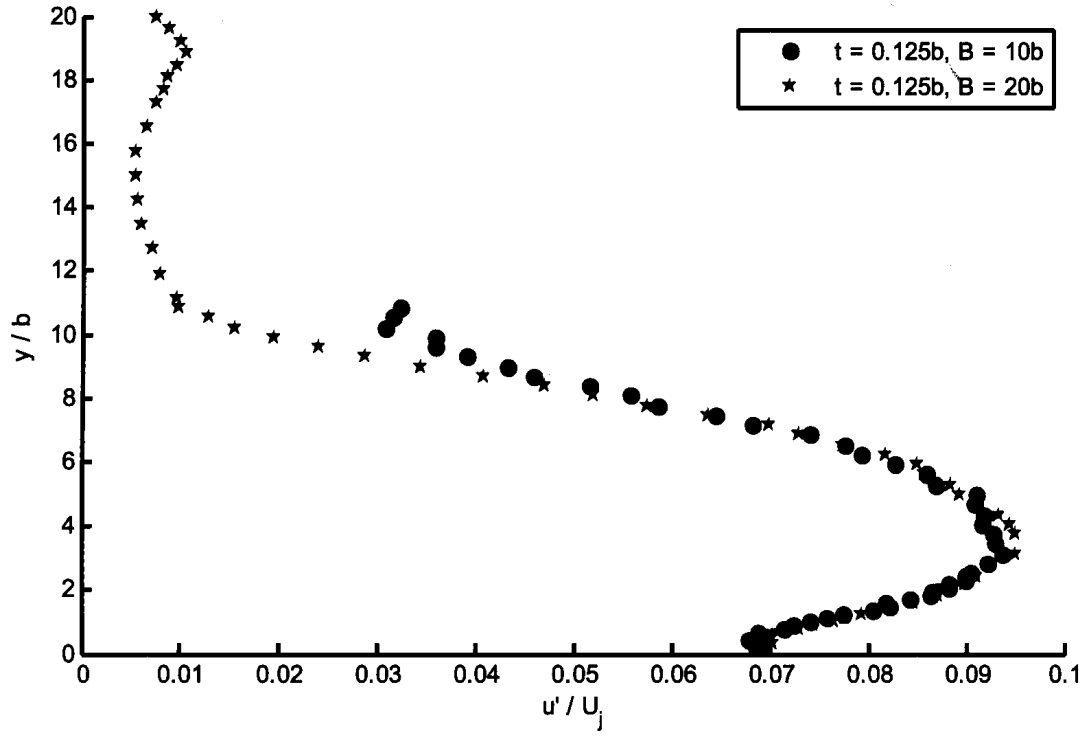

Figure 123: Turbulence intensity, x = 60b

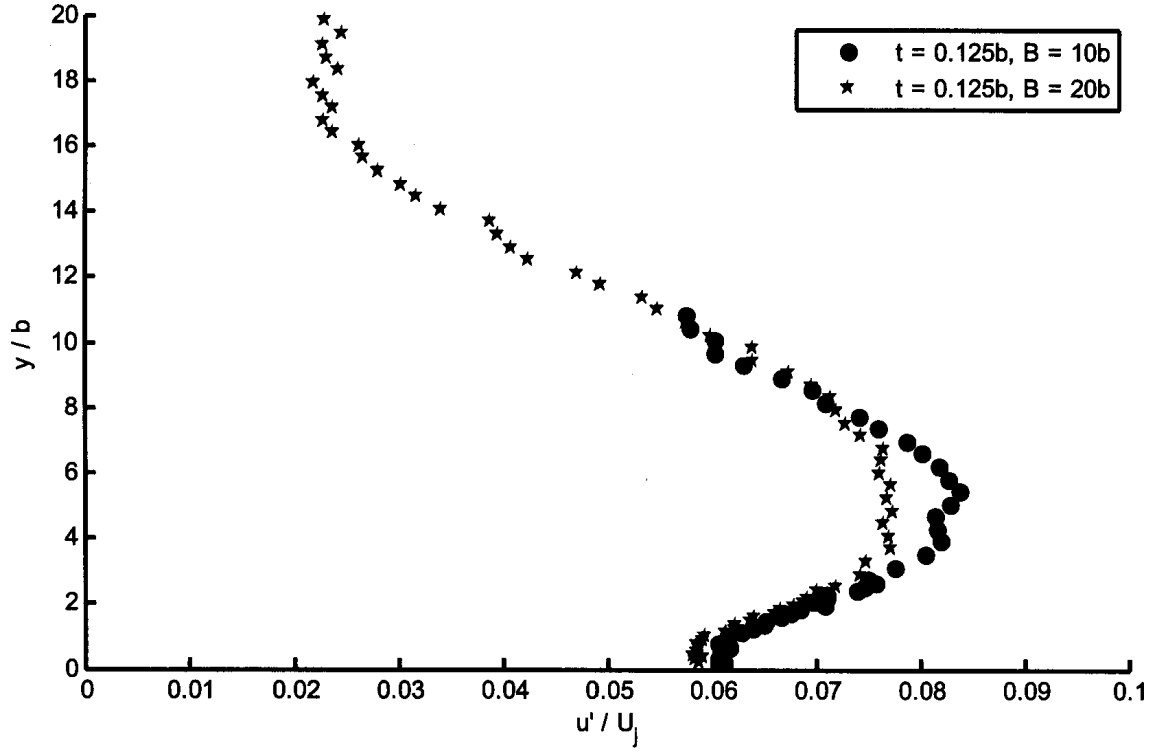

Figure 124:Turbulence intensity, x = 100b

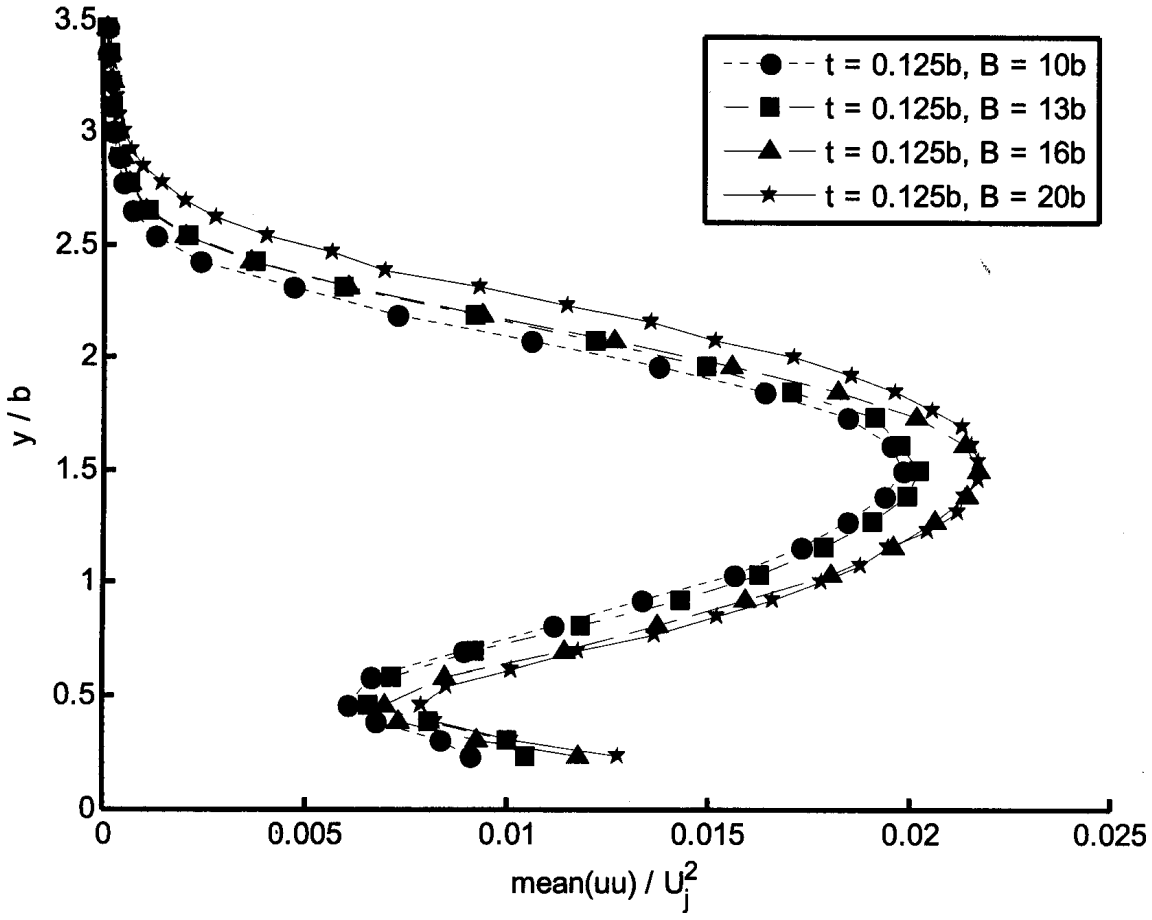

Figure 125: uu normal stress, x = 10b

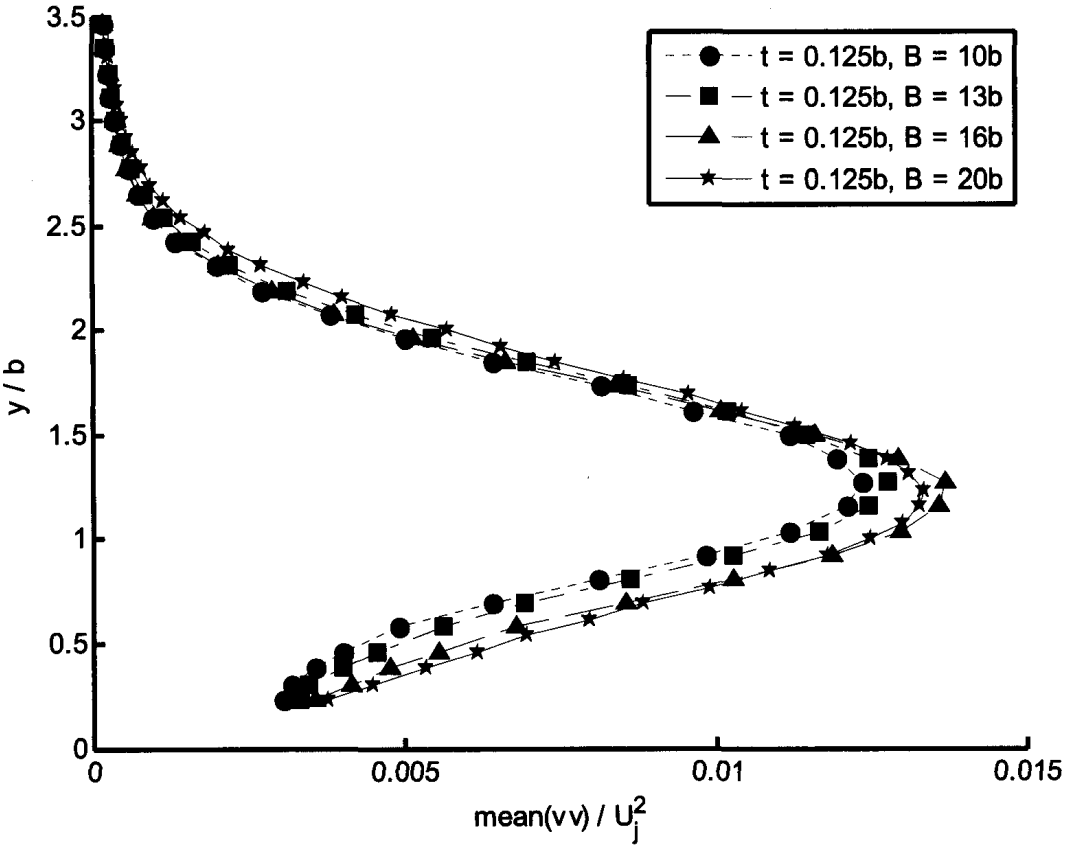

Figure 126: vv normal stress, x = 10b

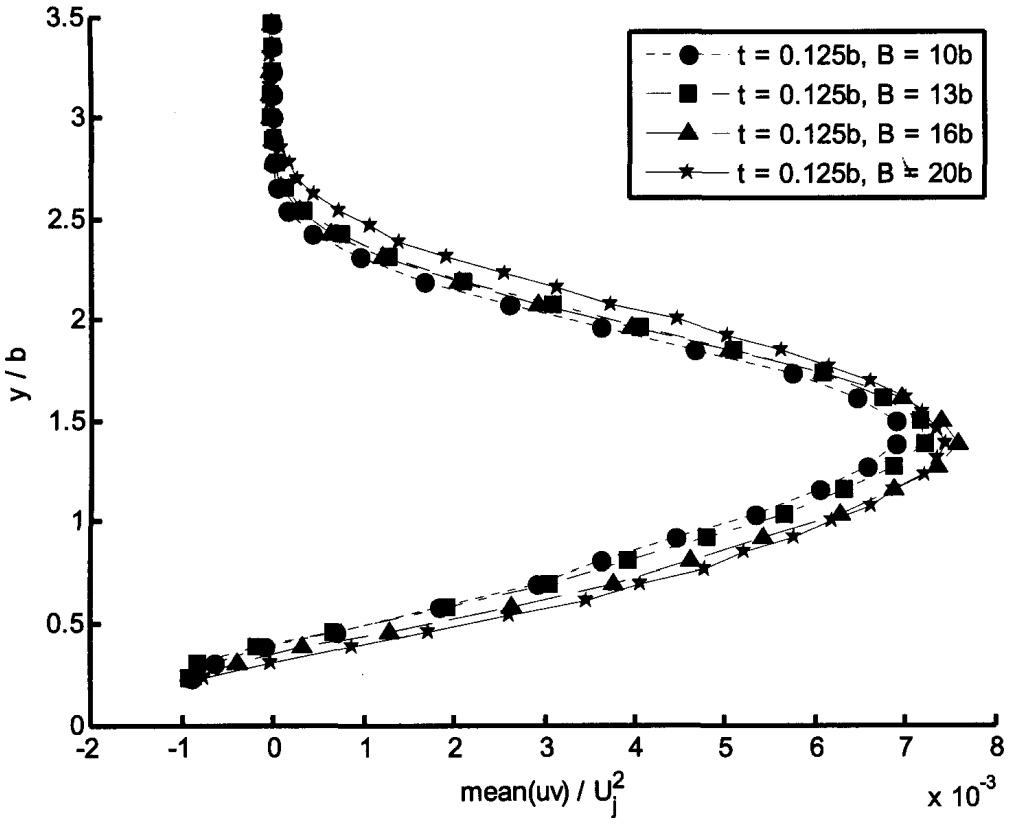

Figure 127: uv shear stress, x = 10b

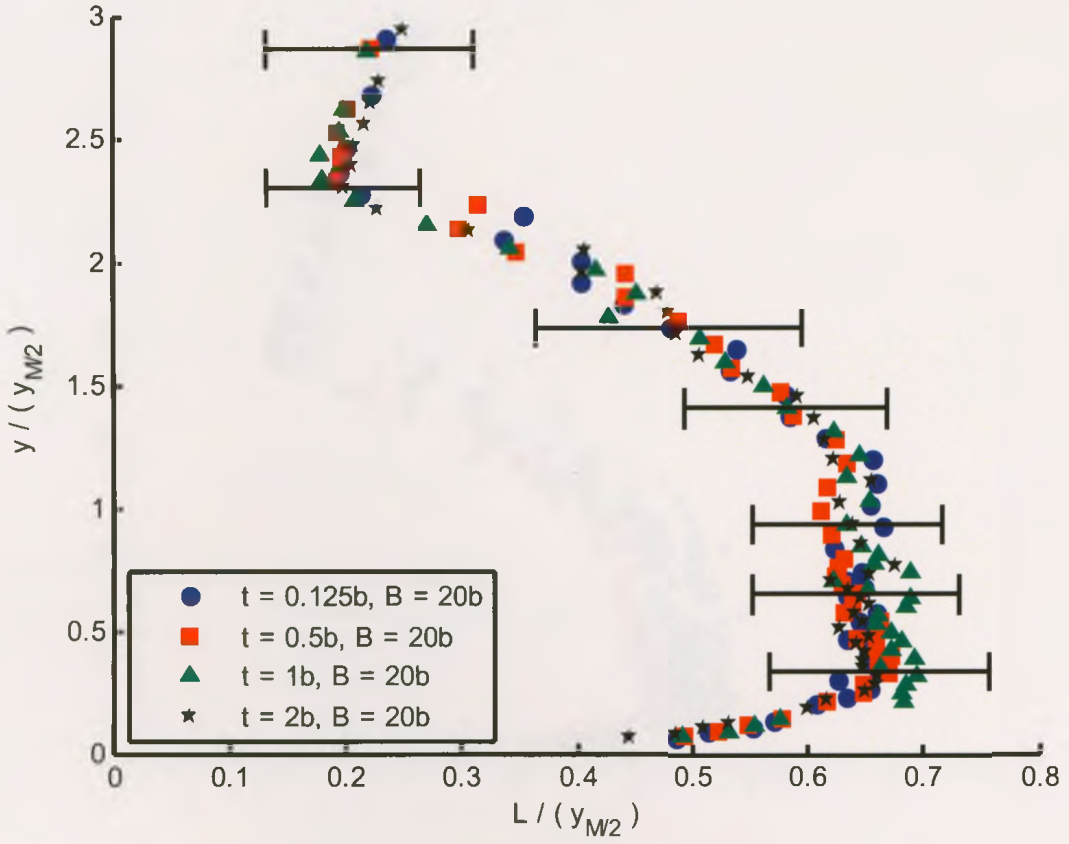

Figure 128: Integral length scale, x = 40b

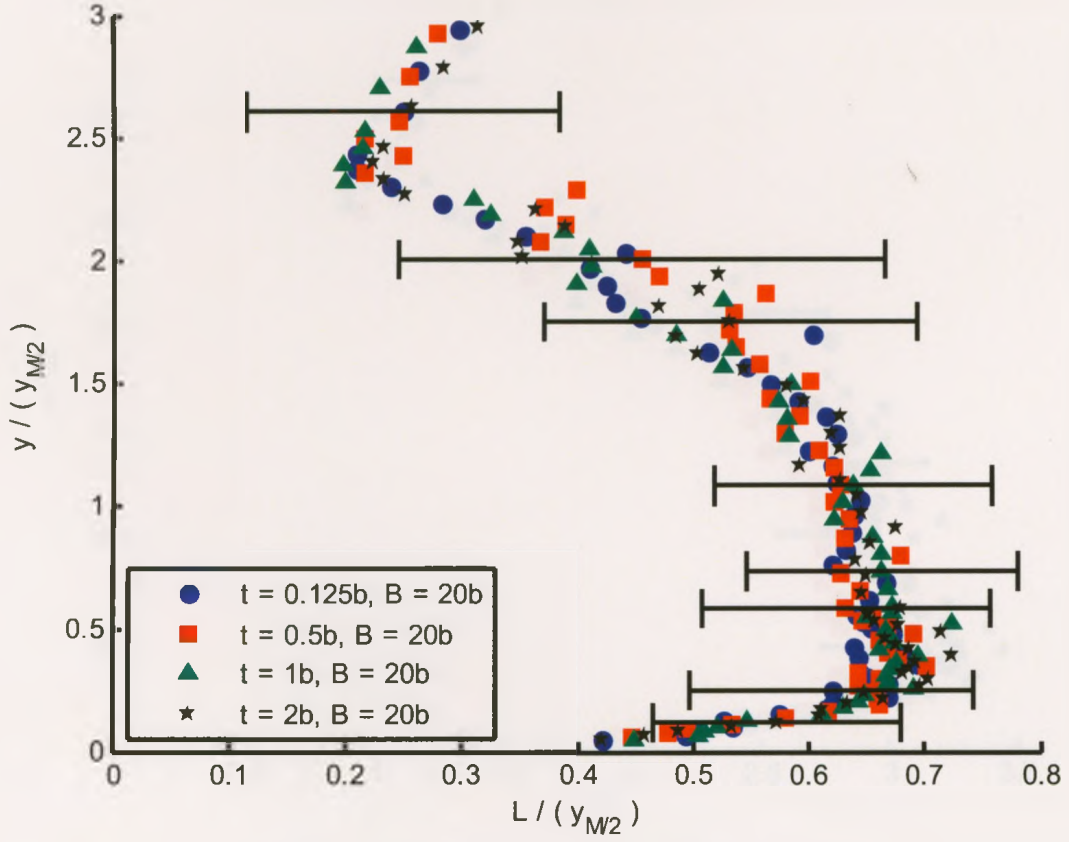

Figure 129: Integral length scale, x = 60b

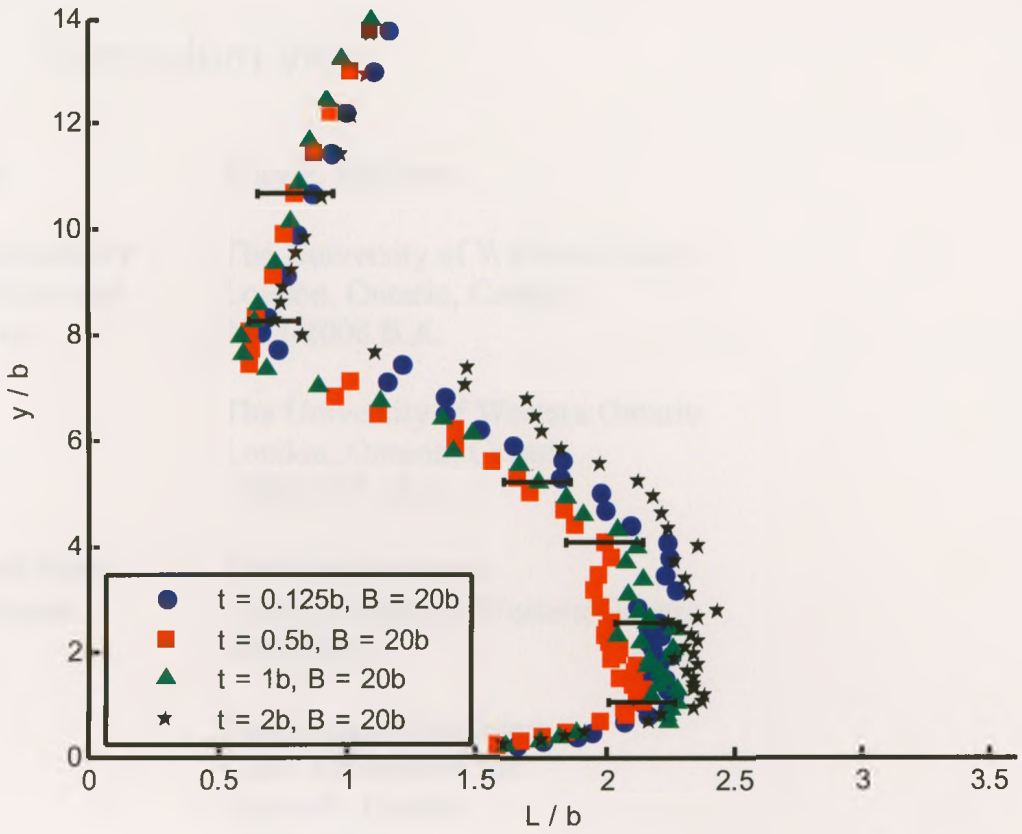

Figure 130: Integral length scale, x = 40b

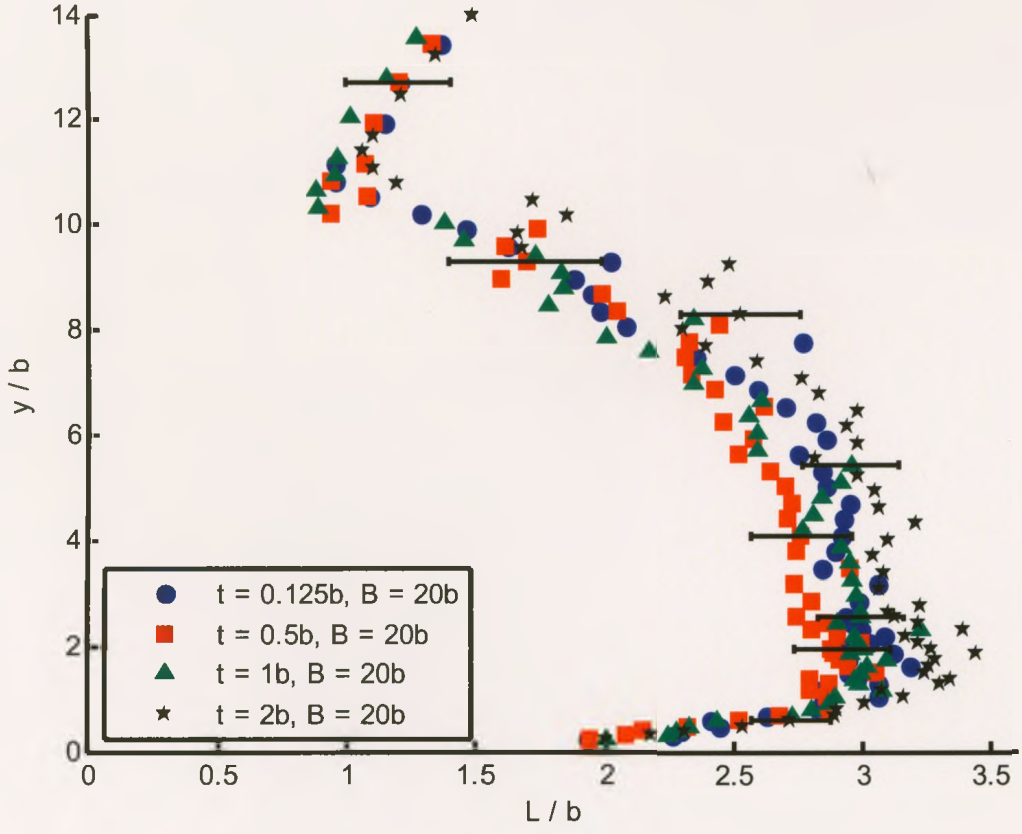

Figure 131: Integral length scale, x = 60b